Mathematical Modelling of Calcium Signalling

A thesis submitted to the University of East Anglia for the degree of Doctor of Philosophy

Matthew J. Evans

John Innes Centre
Norwich
March 24, 2017

Abstract

Calcium (Ca^{2+}) plays an integral role in a vast array of signalling pathways within both animals and plants. The study of these pathways has proven to be a fruitful avenue of research for experimental biologists and mathematical modellers. While the signalling processes have been well studied in animals, the same cannot be said of plants. This work takes a mathematical look at two important Ca^{2+} signalling pathways in plants, with a focus on how these signals are generated.

Nuclear Ca^{2+} oscillations in legumes occur at a key step in the development of symbioses. The oscillations occur both inside the nucleus and in the perinuclear cytoplasm, and are temporally coordinated. We present and develop a model for simulating diffusion on the surface of the nucleus and relate the properties of this signalling to behaviour in the bulk. We show that diffusion of Ca^{2+} through the nuclear pore complexes provides a possible mechanism for this coordination and that this mechanism is robust to differences in Ca^{2+} diffusion rates in the two compartments or to different numbers of Ca^{2+} channels.

Ca^{2+} has also been seen to propagate a wave travelling systemically through the root in response to salt stress. This wave is essential to the transcription of stress response genes in the leaves. We examine a range of different models for propagation of the wave, demonstrating that a combined reactive oxygen species (ROS) and Ca^{2+} wave cooperatively propagate the signal. The presence of this accompanying ROS wave was confirmed in experiments by our collaborators.

The present study highlights two very different Ca^{2+} signals and demonstrates the value of mathematical modelling for interpreting, understanding and furthering experimental investigations.

Contents

Abstract **3**

List of Figures **7**

List of Tables **8**

List of Publications **9**

Acknowledgements **10**

1 Stuff what other people did **13**

1.1 The Role of Calcium in Nature 14

1.1.1 Calcium in animals 14

1.1.2 Plant calcium in development 14

1.1.3 Plant calcium responses to abiotic stress 15

1.1.4 Plant calcium responses to biotic stress 15

1.2 Symbiosis Signalling 16

1.2.1 Root Nodule Symbiosis 17

1.2.2 Nuclear Calcium Oscillations - the SYM pathway 20

1.3 Modelling 21

1.3.1 Spatial models 22

1.3.2 The Fire-Diffuse-Fire Model 23

1.3.3 Models of Root Nodule Symbiosis Signalling 25

1.3.4 Models of Systemic Signalling 27

1.4 Summary 28

2 Calcium Oscillations across the Nuclear Envelope **29**

2.1 Simulating Ca^{2+} Signals Throughout the Nuclear Volume 32

2.1.1 Deriving an Analytical Solution 33

2.1.2 Variability of the Signal through the Nucleus 36

2.1.3 Microdomain Structure 37

2.2 Simulating Ca^{2+} Signals at the Nuclear Surface 39

2.2.1 Deriving an Analytical Solution . . . 40
2.3 The Surface Model Captures the Average Behaviour of the Volume Model . . . 41
2.4 Microdomain Structure can be Captured in the Surface Model . . . 46
2.5 Incorporating Nuclear Pores into the 2D model . . . 50
2.5.1 Simplified model and simulation speed . . . 51
2.5.2 Threshold Criteria . . . 54
2.6 The role of NPCs in nuclear calcium signalling . . . 55
2.6.1 Signal Saturation and membrane transparency . . . 55
2.6.2 Diffusion through pores can prevent nuclear Ca^{2+} signalling . . . 57
2.6.3 Diffusion through pores can enable coordination of signals across NE . . . 58
2.6.4 Relative channel abundance affects spike amplitude but not simultaneity 60
2.6.5 Simultaneous signals can occur in non-identical compartments . . . 62
2.6.6 Without pores, signals are uncoordinated . . . 65
2.7 Discussion . . . 67
2.7.1 Decoding of nuclear Ca^{2+} oscillations . . . 67
2.7.2 2D vs 3D model comparison . . . 68
2.7.3 Spike width and coordination . . . 69
2.7.4 Ca^{2+} permeability of the NPC . . . 70
2.7.5 Transparency and coordination . . . 72
2.7.6 The role of the nucleoporin mutants . . . 73

3 Propagation of Systemic Signals 75
3.1 Variation Potentials and Passive Signal Propagation . . . 78
3.1.1 Model of chemical diffusion with vascular flow can recapitulate VP propagation in wheat . . . 79
3.1.2 Hydraulic model predicts velocity of electrical signals varies with radius 80
3.1.3 Summary . . . 82
3.2 Feasibility of active propagation models to explain systemic Ca^{2+} signals . . . 82
3.2.1 Calcium Induced Calcium Release Models . . . 83
3.2.2 Vesicle Transport . . . 85
3.2.3 Mitochondrial RIRR . . . 85
3.2.4 Electrical Signalling . . . 85
3.2.5 ROS induced Calcium release . . . 86
3.2.6 Summary . . . 88
3.3 Calcium Induced Calcium Release waves in physiological cells . . . 88
3.4 TPC1 clustering cannot explain wave speeds . . . 92
3.5 Cytoplasmic streaming cannot explain wave speeds . . . 95
3.6 Experimental validation . . . 97
3.6.1 Blocking ROS production validates predictions of the ROS-assisted CICR model . . . 97

3.6.2 Imaging of extracellular ROS wave . . . 101
3.7 Full ROS and Calcium Model . . . 102
3.7.1 Model Description . . . 104
3.7.2 Ca^{2+} wave propagation in the *rbohD* mutant: a role for the plasmodesmata? . . . 104
3.7.3 Full model can reproduce behaviour in WT and OxTPC1, but not in *tpc1-2* backgrounds . . . 108
3.8 Discussion . . . 112
3.8.1 A chemical model of variation potential propagtion . . . 113
3.8.2 The interaction between ROS and Ca^{2+} in response to salt stress . . . 114
3.8.3 Comparisons with other systemic signals . . . 116

4 General Discussion **118**
4.1 The Fire-Diffuse-Fire Model . . . 118
4.2 Nuclear Ca^{2+} Oscillations . . . 119
4.3 Systemic Signalling . . . 120
4.4 Future Perspectives . . . 121
4.4.1 CNGCs and Ca^{2+} channel identity . . . 121
4.4.2 ROS and Ca^{2+} cross-talk . . . 121
4.4.3 Experiment and Theory . . . 122

List of Abbreviations **123**

Bibliography **125**

List of Figures

1.1 Bacterial invasion of the legume root hair 18
1.2 Symbiosis signalling components in *Medicago truncatula* 19
1.3 Wave propagation in the fire-diffuse-fire model 23
1.4 Compartment model of symbiosis signalling 26

2.1 Symbiotic Ca^{2+} spikes occur simultaneously on INM and ONM 30
2.2 Model of nuclear Ca^{2+} signalling 31
2.3 Variation of the Ca^{2+} spike in the 3D model 37
2.4 Ca^{2+} microdomains dominate the surface signal 38
2.5 The 2D model can capture the behaviour of the 3D model 43
2.6 The 2D surface model is able to fit multiple 3D parameter sets 45
2.7 The 2D model and 3D model diffusion constants are linearly related 46
2.8 The best fit to the average signal does not reproduce the channel microdomain 47
2.9 The surface model can produce a good fit to the microdomain structure of the 3D model 48
2.10 The 2D model can fit the either microdomain or the averaged signal 49
2.11 Boundary free solution provides a good fit to full periodic solution 52
2.12 The increase in simulation time with pore number 53
2.13 Threshold for wave propagation in the 2D model 54
2.14 Transmission of Ca^{2+} through NPCs increases with pore number, and then saturates 56
2.15 Diffusion through nuclear pores across the NE can kill Ca^{2+} spiking 57
2.16 Flux through pores alone is not sufficient to generate Ca^{2+} spikes 59
2.17 Amplitude on ONM decays with fewer ONM channels 60
2.18 Ca^{2+} signals on the ONM and INM are coordinated even with different channel numbers 61
2.19 Ca^{2+} signals in compartments with different properties are coordinated 62
2.20 Initiation side doesn't affect simultaneous signals 63
2.21 Without pores, signals are not simultaneous 64
2.22 Difference in diffusion constants that give rise to non-simultaneous signals . . . 66
2.23 Spatially inhomogeneous nature of nuclear Ca^{2+} oscillations 69

2.24 Comparing elicitor induced Ca^{2+} signals in the cytosol and nucleus 71
2.25 The number of channels on the ONM has only a minor effect on the INM Ca^{2+} signalling 73

3.1 Conceptual models for the propagation of systemic signals 77
3.2 A model of chemical diffusion in a background flow fits VP propagation data from wheat 80
3.3 Model of electrical signal propagation in response to hydraulic waves 81
3.4 CICR model captures velocity of Ca^{2+} waves 84
3.5 Ca^{2+} wave propagation between cells 90
3.6 The CICR model of wave propagation is sensitive to d but not to D 91
3.7 Clustering of TPC1 on the tonoplast reduces efficiency of Ca^{2+} wave transmission 94
3.8 Cytoplasmic streaming does not improve the fit for CICR propagated Ca^{2+} waves 96
3.9 DPI and ascorbate significantly reduce Ca^{2+} wave amplitude 98
3.10 Ca^{2+} wave has a reduced velocity in the *Atrbohd* mutant 99
3.11 Apoplastic ROS wave accompanies the Ca^{2+} wave 100
3.12 Conceptual model of propagation of the salt stress induced Ca^{2+}/ROS waves . 103
3.13 Fit to wave velocity in the *rbohD* mutant is dependent upon D_{Ca} 105
3.14 Presence of plasmodesmata located Ca^{2+} channels improves model fit 106
3.15 The original ROS model analysis produces a reasonable description of the full model 107
3.16 The model is able to capture the velocity in WT and OxTPC1 108
3.17 Ca^{2+} and ROS waves propagate in WT and OxTPC1 but not in *tpc1-2* 110

List of Tables

1.1 Key symbiotic signalling genes 17

3.1 Measured systemic waves and their velocities 76
3.2 Parameters used in CICR model 84
3.3 Testing clustering of TPC1 93
3.4 Calcium wave velocities in various *Arabidopsis* lines in response to salt 97
3.5 Parameters used in the full Ca^{2+} and ROS model 102

List of Publications

The following manuscripts include material from this thesis and have been published or are in preparation.

Chapter 1

T. Vaz Martins, **M. J. Evans**, H. Woolfenden, and R. J. Morris, "Towards the Physics of Calcium Signalling in Plants," *Plants*, vol 2, pp. 541-588, 2013.

Chapter 2

T. Vaz Martins, **M. J. Evans**, D. B. Wysham, and R. J. Morris, "Nuclear pores enable sustained perinuclear calcium oscillations", *BMC Systems Biology*, vol 10, pp 1-12, 2016.

Chapter 3

M. J. Evans, and R. J. Morris, "Re-examining the mechanisms of variation potential propagation in response to wounding", 2016. *In Preparation.*

M. J. Evans*, W. G. Choi*, S. Gilroy, and R. J. Morris, "A ROS-assisted calcium wave dependent on the AtRBOHD NADPH oxidase and TPC1 cation channel propagates the systemic response to salt stress," *Plant Physiology*, vol 171, pp. 1771-84, 2016.
*These authors contributed equally

Acknowledgements

I would first like to thank my supervisors, Richard Morris and Giles Oldroyd. Richard did a passable job - just kidding! Richard has been a fantastic supervisor whose good humour and enthusiastic support has carried this project through both its successes and its more trying periods. His advice on scientific and non-scientific matters has always been greatly appreciated. And lets not forget the regular deliveries of cake for group meetings. Giles was always on hand to provide fantastic feedback on the project and to keep my mind on the real, practical importance of my work.

I also want to thank the various members of the Computational and Systems Biology for their companionship and assistance. Teresa Vaz Martins, in particular, contributed so much to this project in terms of ideas, discussions and always ensured I had to thoroughly understand the subject at hand. Nick Pullen was a gold mine for coding tips and tricks. He, Robert Iestwaart, Marc Jones and Alex Calderwood made the office a great place to work. And of course, Matthew Hartley and, later, Tjelvar Olsson provided endless help and advice when code and computing systems chose to make life difficult.

From the scientific side I wish thank our collaborators from across the pond, Won-Gyo Choi and Simon Gilroy from the University of Wisconsin Madison. Their enthusiastic support and diligence turned an interesting side project into a great success and a major part of this thesis.

I also wish to thank Gordon Jamieson and Jonathon Clark for the opportunity to work with them during my 3 month internship at the Knowledge Exchange and Communications department. It was an incredibly valuable experience that has helped to significantly broaden my horizons. I learnt so much about so many subjects it would be impossible to list them all here. Thank you for your help and advice.

Likewise I would like to thank those who organised and gave me the opportunity to attend the Undergraduate Summer School program during the summer of 2011, in particular Derin Wysham, Enrico Coen and, again, Richard, without whom I would likely have never discovered the joys of Ca^{2+} signalling.

Of course, no PhD can be successful without beer, so my thanks go to Ben Hall, Thomas Vincent, Alex Calderwood, Dan Knevitt, Jonathon Cocker and Lizzie Thursby for helping me to keep Norwich's pubs flourishing for four years. Additional thanks to the 'JIC board game club' for many fun evenings! Special thanks to Chris Judge for everything you've done.

My heartfelt thanks to my family. You've always been there to support me and I know I wouldn't be who I am today if it weren't for your love and encouragement. And finally, thank you to my partner, Anna, for your patience, determination, and love in everything, always.

Matthew Evans
September 2016, Norwich.

Chapter 1

Stuff what other people did

With four parameters I can fit an elephant, and with five I can make him wiggle his trunk.

- by Enrico Fermi, attributed to John von Neumann [1]

Biology is messy[citation needed]. Even a relatively simple plant like *Arabidopsis* has some 25,000 genes [2], whose proteins, if they could each interact with one another, would give rise to $10^{10^{28}}$ possible interactions. Since the development of genetic analysis tools, biologists have focused on identifying 'what' genes give rise to what properties of the organism. Studying how groups of genes and the proteins they encode co-operatively give rise to these properties has typically been restricted to the identification of genetic pathways and qualitative models. What is required is the development of a systematic approach to the understanding of not only 'what' but also 'how' biological elements give rise to the phenological effects we observe and measure. Mathematical models are a key tool in unravelling the multi-layered complex nature of biological systems [3].

The early development of techniques for detecting and imaging calcium led to the establishment of a huge body of literature studying its role in a wide variety of organisms and signalling pathways. Systems biologists soon followed and the ongoing development of mathematical models to describe these various Ca^{2+} signals began [4]. Fewer examples of quantitative work exist in plants [5], in part due to the relative difficulties of obtaining high resolution Ca^{2+} images in these systems. The development of genetically encoded ratiometric Ca^{2+} sensors in plants [6, 7, 8] has enabled the field to advance rapidly over the last few years, to where spatio-temporal models can be of value.

Complex systems with non-intuitive effects can arise with merely three or more variables for non-linear interactions. As the famous quote from John von Neumann insinuates [1], with very few parameters it is possible to capture a great deal of complexity. It is our approach in this thesis to bring relatively simple models, with few parameters, to bear on outstanding questions regarding Ca^{2+} signalling in plants.

1.1 The Role of Calcium in Nature

The substantial difference in calcium concentration between the cytoplasm ($\sim 100\,\mathrm{nM}$) and regions outside the Plasma Membrane (PM; $0.3 - 1\,\mathrm{mM}$), or within internal compartments like the Endoplasmic Reticulum (ER; $0.05 - 2\,\mathrm{mM}$) or the vacuole ($0.2 - 80\,\mathrm{mM}$) creates the ideal conditions for allowing dynamic changes in state [9]. However, ionic calcium, Ca^{2+}, is toxic to the cell [10] so its concentration is carefully regulated. Thus the release of Ca^{2+} from storage compartments is mediated by gated channels in the relevant membranes that open only in response to certain stimuli. Once in the cytoplasm, the concentration of Ca^{2+} is buffered by Ca^{2+}-binding proteins. When concentrations in the cytoplasm get too high, ATP-driven Ca^{2+} pumps activate to take Ca^{2+} back across the membrane against the concentration gradient [11].

The activity of these signalling elements gives rise to a huge variety of different Ca^{2+} behaviours, from simple transients to waves and oscillations with periods varying from seconds to hours. The localised concentration varies in duration, amplitude, frequency and spatial distribution, and these observations gave rise to the "Ca^{2+} signature" hypothesis [11], which states that signal information is encoded in the spatio-temporal pattern of cytosolic Ca^{2+} signatures. Many Ca^{2+}-binding proteins can transduce the changes in local Ca^{2+} concentration into changes within the cell. Thus Ca^{2+} is able to form a key signalling link, and is widely recognised as one of the most important secondary messengers in both plants [12, 13, 14] and animals [15, 16].

1.1.1 Calcium in animals

Ca^{2+} as a signal is ubiquitous in animals, from the initial moment of fertilisation, through every stage of development and cell differentiation, it drives the rapid contractions of muscle and vascular tissue, is essential to the establishment of memory in nerve cells, and signals cell death. The most thoroughly studied signalling elements in animals are the PM-localised voltage-operated channels that mediate rapid Ca^{2+} fluxes during muscle contraction or synaptic signalling, and the Ca^{2+}-sensitive Inositol-1,4,5-triphosphate receptors (IP_3R) and Ryanodine receptors (RyR) [4, 16]. These last two channels are localised to the ER (or the Sarcoplasmic Reticulum in excitable cells) and mediate a process known as Calcium-Induced Calcium Release (CICR), a process of positive feedback allowing Ca^{2+} to self-propagate as a wave. While IP_3R-like channels exist in plants, they do not have as significant a role in signalling. Animal Ca^{2+} signals are detected by proteins such as calcium and calmodulin-dependent protein kinase II (CaMKII) or protein kinase C [16]. In animal systems, both amplitude and frequency signal encoding have been described [17].

1.1.2 Plant calcium in development

Tip-focused Ca^{2+} gradients occur in growing tip structures of root hairs, pollen tubes and fungal hyphae [18]. At the tip, oscillations in Ca^{2+} lead periodic growth phases by about 5 s

[6]. The Ca^{2+} gradient and oscillations in this system are believed to target the cytoskeleton and secretary apparatus to the growing tip. A key interaction in this signalling is the role of Reactive Oxygen Species (ROS). A Nicotinamide Adenine Dinucleotide Phosphate (NADPH)-oxidase, RBOHDC in *Arabidopsis thaliana*, produces ROS that stimulates Ca^{2+} release from hyper polarisation activated Ca^{2+} channels. There is a putative positive feedback loop in which the Ca^{2+} activates the RBOHDC to stimulate the next phase of the oscillation [6].

Slower oscillations in basal Ca^{2+} concentration occur as part of the molecular circadian oscillator [19]. There is a sinusoidal variation in Ca^{2+} concentration with a period of 24 hours that reaches a peak concentration of 300-700 nM [20]. Perturbation of these oscillations alter the circadian clock function, implying a feedback loop within the clock. The role of Ca^{2+} within the clock has an important effect on other pathways due to the extensive cross-talk that exists between circadian and stress signalling networks [19].

1.1.3 Plant calcium responses to abiotic stress

Ca^{2+} elevations with stimulus-specific properties are evoked by extracellular sodium, osmotic stress, low temperature, ozone, ROS, and mechanical stress [11, 21]. NaCl-induced Ca^{2+} spike amplitude in *Arabidopsis* roots showed a dose-dependency [22], demonstrating that information about the strength of the stimulus is encoded in the Ca^{2+} signal. More recently, salt stress has been shown to trigger a systemic wave of Ca^{2+} through the root cortex and endodermis that propagates at a speed of around $400\,\mu ms^{-1}$ [21]. This Ca^{2+} wave is essential for activating salt stress related gene expression in the leaves. A key role in the propagation of this wave is played by the Two Pore Channel 1 (*At*TPC1) gene, encoding a vacuole localised non-selective cation channel [21, 23, 24]. Ca^{2+} also plays an important role in systemic wounding signals [25] and action potential generation [26].

Abiotic (as well as biotic) stimuli such as CO_2 concentration, water availability and light conditions [27], often via abscisic acid (ABA), regulate the opening and closing of stomata, pores in the leaves that mediate transpiration. These stomata are formed from two kidney-shaped guard cells that are able to change their osmotic status to expand and shrink to close/open the stomatal pore. Ca^{2+} plays a key role in regulating this process [28]. Oscillations in Ca^{2+} are sufficient to close stomata, with frequency and amplitude determining the aperture [29]. As with tip-growth, an important role is played by ROS produced by NADPH-oxidases (this time *At*RBOHD and *At*RBOHF) [30]. Original imaging on stomatal Ca^{2+} indicated a single Ca^{2+} transient response. The oscillating signal was only identified once higher resolution imaging became available [31]. The single transient was a result of averaging over several unsynchronised Ca^{2+} oscillations [31].

1.1.4 Plant calcium responses to biotic stress

Raised cytosolic Ca^{2+} is one of the earliest responses to biotic stress [32, 33], triggered by detection of pathogen-associated molecular patterns (PAMPs) by PM-localised detector proteins.

This is essential for triggering the full suite of disease responses culminating in cell death. The cytosolic response is often followed by a much longer lasting nuclear Ca^{2+} transient [32]. Again, the Ca^{2+} response is intimately connected to a ROS burst [33] via RBOHD in *Arabidopsis* with a degree of feedback involved. Much like the stomatal Ca^{2+} signals, the PAMP-triggered Ca^{2+} burst was also shown to be an imaging artefact, with the true Ca^{2+} response in a single cell being an oscillating signal [8, 34] with a period of around 5 minutes. A more positive interaction occurs with symbiotic fungi and bacteria (see the next section for more details). Detection of species specific signal molecules give rise to nuclear Ca^{2+} oscillations that activate development of specialised structures for the internalisation of the symbiotic bacteria/fungi [35, 36, 37].

1.2 Symbiosis Signalling

The development of root symbioses presents one of the best studied systems for Ca^{2+} signalling in plants. Some 80% of plant species form a symbiotic interaction with the Arbuscular Mycorrhizae (AM) fungi [38], and the evolution of this symbiosis some 460 million years ago is acknowledged as one of the key steps in the colonisation of land by plant life [39]. In the absence of a plant host, the AM exist as spores in the soil [40], but after detecting plant strigolactones they germinate and undergo a process of directed hyphal growth towards the plant [41, 42]. After a signalling exchange with the plant that includes nuclear Ca^{2+} spikes in the plant cells, the AM is allowed to penetrate the plant through a specially constructed infection pathway and to colonise the root cortex cells where arbuscules are formed to allow for the exchange of nutrients. The extended hyphael structures of the AM fungi form an exceptionally efficient system for the uptake of less common nutrients such as phosphorus, copper and zinc, which are transferred through the arbuscules to the plant [40]. In return, the plant provides the fungi with carbohydrates [40].

A second important root symbiosis is that formed between legumes and rhizobium bacteria. This symbiosis evolved much later than AM symbiosis [43] and appears to have co-opted much of the signalling pathway used by AM symbiosis [44]. Like AM, the development of this symbiosis begins with a chemical exchange in the rhizosphere, nuclear Ca^{2+} oscillations, and the internalisation of the symbiont in specially constructed structures in the root, in this case nodules [36]. Root Nodule Symbiosis (RNS) creates the ideal anaerobic conditions in which the terminally differentiated bacteroids can "fix" atmospheric nitrogen, N_2, into biologically accessible ammonia, NH_3, which is again transferred to the plant in return for carbohydrates [45].

While crop plants can form AM symbiosis, none of the worlds largest crops can form RNS. Atmospheric nitrogen remains inaccessible to them due to the strength of the N_2 triple bond. Instead, agriculture relies on the application of chemical fertiliser that includes ammonia produced chemically through the Haber-Bosch process. The development of this technique led to a revolution in agriculture and enabled the dramatic increase in world population

Table 1.1: The key symbiotic signalling genes. A list of the name and function of genes important to early symbiosis signalling in *Lotus japonicas* and *Medicago truncatula*, and whether they have a role in Root Nodule (RNS) or Arbuscular Mycchorizal (AM) symbioses. We have focussed on genes that give rise to and decode the symbiotic Ca^{2+} signalling. The localisation of these proteins is illustrated in Figure 1.2.

Lotus	Medicago	Function	RNS	AM	Refs
NFR1	LYK3/4	Nod Factor detectors	✓		[50, 51]
NFR5	NFP	Nod Factor detectors	✓		[48, 50, 51, 52]
SYMRK	DMI2	Receptor-like kinase	✓	✓	[53, 54]
POLLUX	DMI1	Nuclear K^+ channel	✓	✓	[55, 56, 57, 58]
CASTOR	-	Nuclear K^+ channel	✓	✓	[58]
NUP85	-	Nucleoporin	✓	✓	[59]
NUP133	-	Nucleoporin	✓	✓	[60]
NENA	-	Nucleoporin	✓	✓	[61]
-	MCA8	Nuclear Ca^{2+} pump	✓		[62]
-	CNGC15	Nuclear Ca^{2+} channel	✓	✓	[63]
CCAMK	DMI3	Nuclear Ca^{2+} and Calmodulin binding kinase	✓	✓	[64, 65]
CYCLOPS	IPD3	Coiled-coil protein	✓	✓	[66, 67]
NSP1	NSP1	Transcription factor	✓		[68]
NSP2	NSP2	Transcription factor	✓	✓	[68, 69]
RAM1	RAM1	Transcription factor		✓	[69]

over the last century. However, this process is extremely energy intensive, a full 1% of the world's energy resources are expended on producing ammonia for fertilisers [46]. With the increasing demand from a growing population as well as pressures from climate change and other ecological consequences of fertiliser use [47], new approaches are required to ensure sustainable agriculture throughout the 21st Century.

The close genetic similarities between the symbiosis pathways for AM fungi and RNS open up the possibility for using genetic engineering to reconstruct the RNS pathway in crop plants, for which much of the underlying AM genetic pathway is already present [48, 49]. To achieve such a goal, a thorough understanding of the signalling pathways that give rise to these symbioses is required. Our work on symbiosis signalling presented in this thesis is focussed on the RNS, but many of the results and conclusions apply to AM symbiosis as well.

1.2.1 Root Nodule Symbiosis

The first stage of RNS begins when rhizobia bacteria detect flavonoid molecules secreted by plant roots. This causes them to produce their own signalling molecules, Nod Factors (NF, Figure 1.1A). NFs are lipochitooligosaccharides (LCO) [36, 70], diffusible molecules with a

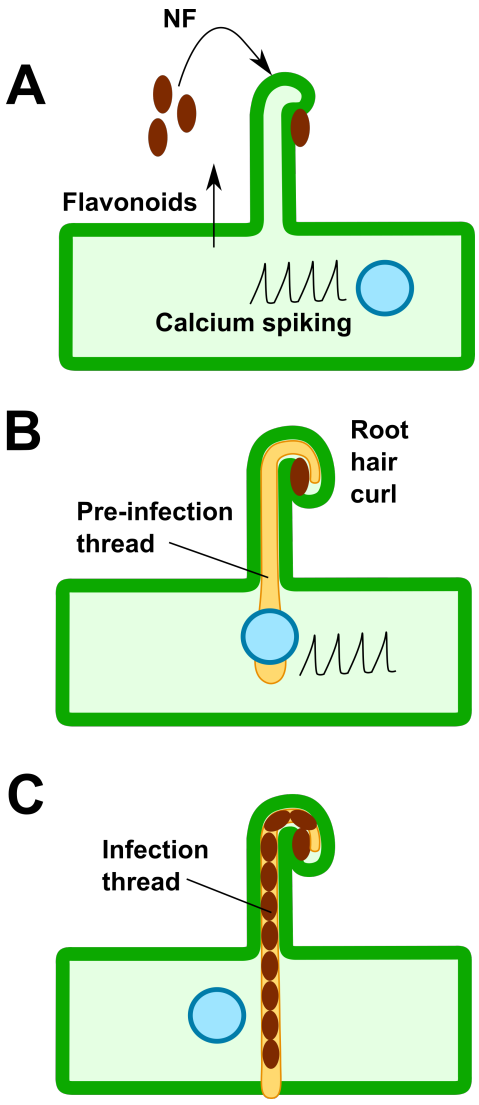

Figure 1.1: Bacterial invasion of the legume root hair. **(A)** Flavanoids released by the plant root signal to rhizobia, which in turn produce Nod factors (NF) that are recognised by the plant. This recognition gives rise to Ca^{2+} oscillations in the nucleus and nuclear localised cytoplasm. **(B)** Rhizobia gain entry into the plant via the root hair which curls around a pocket of bacteria attached to the root surface, trapping them inside a root hair curl. The calcium oscillations activate gene transcription leading to the development of the invasive structures. **(C)** The infection thread is an invagination of the plant cell that is initiated at the root curl, into which the bacteria grow and divide. This thread will go on to pierce multiple cell layers, ending in the early nodule structures that are developing within the root cortex.

chitin backbone and a variety of chemical side groups. Interestingly, AM also produce LCO-type signalling molecules (termed Myc Factors) [69], supporting the hypothesis that RNS evolved by adaptation of the AM pathway. The LCO side groups are the key determinant of host specificity [71]. Root hair cells are able to detect NF at concentrations of 10^{-12} M, implying the binding to a high affinity receptor. The presence of NF alone induces formation of pre-infection structures [72, 73], Figure 1.1B, but full infection (Figure 1.1C) requires the presence of actual bacteria, suggesting further signalling is required.

To detect NF, the plant has a number of specialised detectors in the plasma membrane. In the model legume *Lotus japonicus*, *Lj*NFR1 and *Lj*NFR5 encode receptor-like kinases with LysM domains, known to bind chitin [74], which form a heterocomplex to detect NF [51]. In the second symbiosis model organism *Medicago truncatula*, the gene *Mt*NFP has a strong homology to *Lj*NFR5 [48], and several candidate receptor-like-kinases with homology to *Lj*NFR1, including *Mt*LYK3 and *Mt*LYK4. Only *Mt*NFP is required for the initial signalling response, but both *Mt*NFP and *Mt*LYK3 are required for the full infection process [52, 75, 76]. The specificity of NF recognition is linked to these LysM domains, in particular of *Lj*NFR5 and *Mt*NFP [77, 78].

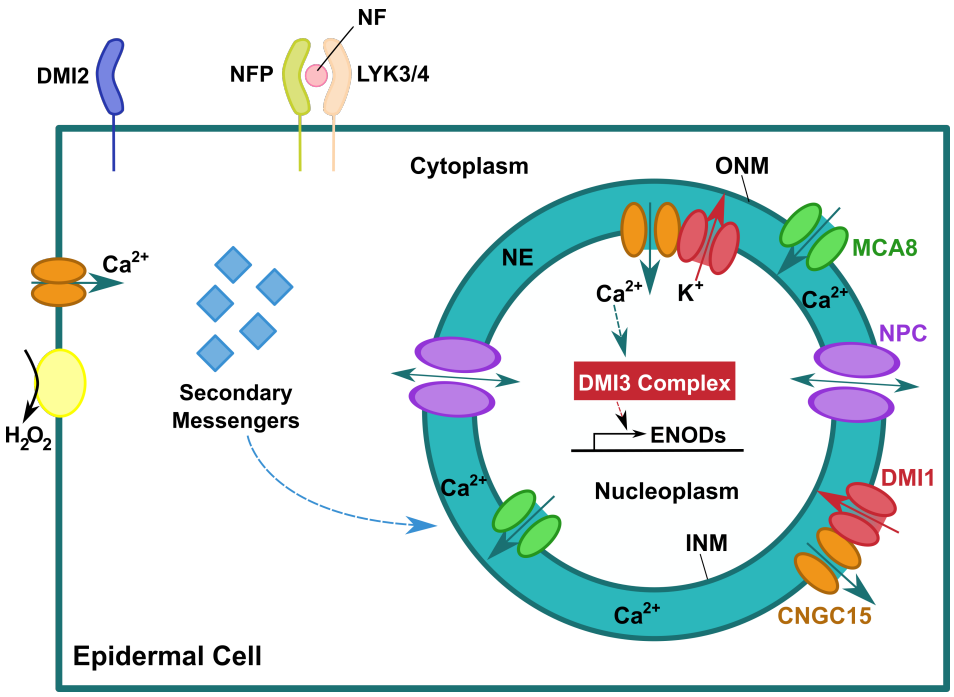

Figure 1.2: Symbiosis signalling components in *Medicago truncatula* during RNS. Symbiosis signalling is triggered when Nod Factor (NF) is bound to detector proteins NFP/LYK3/4. These along with DMI2 trigger the generation of some as yet unidentified secondary messengers in the cytosol that trigger Ca^{2+} oscillations in the nucleus, via a Ca^{2+} channel, CNGC15, a K^+ channel, DMI1 and a Ca^{2+} pump, MCA8. These oscillations are decoded by a complex of DMI3, IPD3 and NSP1/2 that causes transcription of the ENOD genes, amongst others.

Detection of NF and Myc Factors leads to the activation of a common symbiotic (SYM) pathway [79] that involves a number of genes and Ca^{2+} signalling. This pathway precedes the physiological changes that characterise the two symbioses. The Ca^{2+} signal is formed from two separable responses [80], nuclear Ca^{2+} oscillations [81] (to be discussed in the following section) and a rapid Ca^{2+} influx at the plasma membrane [82]. This influx occurs within one minute of NF application and is concomitant with efflux of Cl^- and K^+, and alkalinization of the cytoplasm [83, 84, 85].

While it might be simple to assume this Ca^{2+} influx triggers nuclear Ca^{2+} spiking, the two can be uncoupled. It is possible to activate nuclear Ca^{2+} spiking without a detectable Ca^{2+} influx and the Ca^{2+} flux requires higher concentrations of NF than the nuclear response [80]. The signal that connects NF perception and nuclear Ca^{2+} spiking is still unknown [36, 86]. Inhibitors of phospholipase C and D, producers of inositol phosphates, block NF-induced Ca^{2+} oscillations [87, 88], but there is no evidence for a role of inositol phosphate regulated channels in symbiosis signalling [36, 86]. At the plasma membrane, *Mt*DMI2 and *Lj*SYMRK are receptor-like kinases that are hypothesised to form complexes with the NF and Myc Factor receptors [53] and could give rise to the secondary messenger that activates nuclear Ca^{2+} oscillations, either through a mitogen-activated protein kinase kinase [89] or a 3-hydroxy-3-methylglutaryl-CoA reductase [90]. The recent identification of the symbiotic Ca^{2+} channel [63] suggests a role for cyclic nucleotides as another plausible signal. The genes *Mt*DMI2 and *Lj*SYMRK represent the first components of the SYM pathway.

1.2.2 Nuclear Calcium Oscillations - the SYM pathway

At the core of the SYM pathway are oscillations in Ca^{2+} concentration in the nucleoplasm and perinuclear cytosol [79, 81, 91] that occur around 10 minutes after NF application [92] and can last for several hours, with a period commonly lying between 60 and 120 seconds after a initial burst of rapid oscillations [80, 93, 94]. Each spike has a characteristic asymmetric shape formed by a rapid release of Ca^{2+} from an internal store, followed by a slower Ca^{2+} uptake [94, 93]. High resolution imaging and localisation of the key Ca^{2+} signalling components to the Nuclear Envelope (NE) identified the nuclear lumen, which is contiguous with the ER, as the Ca^{2+} store for symbiotic Ca^{2+} oscillations [62, 63, 94].

A number of key genes are required for generating these Ca^{2+} signals (Table 1.1). These are: a transmembrane cation channel, located preferentially to the inner nuclear membrane (*Mt*DMI1, *Lj*CASTOR and *Lj*POLLUX) [55, 56, 57, 58, 62], three components of the nuclear pore complex (*Lj*NUP85, *Lj*NUP133 and *Lj*NENA) [59, 60, 61] and recently a Cyclic Nucleotide Gated Channel *Mt*CNGC15 has been shown to mediate Ca^{2+} release in response to NF and Myc Factor [63]. Additionally, a sarcoplasmic/endoplasmic reticulum calcium ATPase (SERCA)-type Ca^{2+}-ATPase *Mt*MCA8 was shown to be required for NF-induced Ca^{2+} signalling [62]. *Mt*DMI1 encodes a putative K^+ channel that may counterbalance the change in membrane voltage during Ca^{2+} release. The two *L. japonicus* channels CASTOR

and POLLUX, together perform the same role as *Mt*DMI1 [58, 95].

Downstream of the Ca^{2+} oscillations is the decoding complex formed by *Lj*CCaMK/*Mt*DMI3 [64, 65] and *Lj*CYCLOPS/*Mt*IPD3 [66, 67]. CCaMK is a Ca^{2+} and Calmodulin (CaM) binding protein kinase, featuring 3 EF-hand domains that stabilise the inactive state of the protein [96]. Binding of Ca^{2+}-bound CaM releases that inhibition and enables phosphorylation of downstream targets, including CYCLOPS. CYCLOPS is required for rhizobial infection, but not nodule formation [67]. CCaMK marks the point at which the SYM pathway diverges. It interacts with transcription factors NSP1 and NSP2 in the RNS pathway [68], or RAM1 and NSP2 in the AM pathway [69], that lead to the expression of symbiosis specific gene signalling including the ENOD genes (Figure 1.2).

Ca^{2+} signalling and the activation of CCaMK is a core step in the signalling process, and a minimum number of Ca^{2+} spikes are required for this activation [80]. Activated CCaMK makes upstream components of the symbiosis pathway redundant [97] meaning activation of CCaMK must be the primary role of the nuclear Ca^{2+} oscillations. Despite both RNS and AM pathways utilising this same pathway, the plant must still discriminate between the two to activate the correct developmental processes. Auto-active CCaMK induces nodulation [98], but when CCaMK is activated in AM signalling nodules are not formed. It is plausible that different Ca^{2+} signatures could encode specificity [11, 99, 100], but nuclear Ca^{2+} signatures were later shown to have a similar shape and frequency in both RNS and AM [100, 101]. This suggests specificity of symbiosis signalling is transmitted through an independent pathway to Ca^{2+} signalling.

Ca^{2+} oscillations occur across a broad number of cells around the root hair and, at later stages of symbiotic entry into the root, within the cortical cell layer as well [94]. Non-synchronous nuclear Ca^{2+} oscillations occur in adjacent cells [94, 100], and the structure of oscillations also differs between cells [81, 94, 100]. The path of infection through the root is predicted by a preinfection structure [102] (Figure 1.1B) that is always directed through cells that exhibit high frequency Ca^{2+} oscillations [101]. Thus, while the Ca^{2+} oscillations may not provide specificity regarding the type of symbiosis, they may provide positional information for coordinating development of downstream responses.

1.3 Modelling

The identification of Ca^{2+} signals occurred relatively recently compared to the discovery of many biological phenomena. This coincided with the rise of computational methods, enabling those methods to drive both intracellular imaging and mathematical modelling approaches in tandem. The many diverse forms of Ca^{2+} signal have given rise to an equally diverse range of mathematical models to describe them (see [103] for a comprehensive review).

Much of the theoretical literature analysing Ca^{2+} signals has been performed in animal systems where the focus has been on understanding the core role of the IP_3R channel [4]. The conductance of the IP_3R depends on both IP_3 and Ca^{2+} and thus it positively contributes

to its own opening. This, as well as its ubiquitousness in animal systems, has made it a rich subject of study. However, in plants IP_3Rs were not chosen during evolution as such a dominant signalling pathway and in most situations we have discussed above (Section 1.1) the identity of the Ca^{2+} channel is not known [12], let alone understood to the level that would allow detailed modelling of its gating properties. Thus, only those models that focus on general release units, rather than specific channel types, are of significant value to the development of models in plant systems.

1.3.1 Spatial models

Ca^{2+} can form propagating waves across cells [104] and tissues [21, 105]. Approaches to describe these signals start with incorporating diffusion of Ca^{2+} using the standard reaction-diffusion formalism:

$$\frac{\partial c}{\partial t} = D_c \nabla^2 c + g(\mathbf{r}, t), \tag{1.1}$$

where c is the concentration of Ca^{2+}, D_c is the diffusion constant for Ca^{2+}, and $g(\mathbf{r}, t)$ is a function defining all the relevant reactions of Ca^{2+}. These reactions include transport of Ca^{2+} between compartments, mediated by channels or pumps, and reactions with buffering species. Buffering of Ca^{2+} has a major impact on calcium's ability to mediate signalling in the cell. A large proportion of Ca^{2+} is bound after release from a channel, and this dramatically restricts the diffusion of free Ca^{2+}. Buffers can be either stationary or mobile, and the relative binding properties of these two Ca^{2+} pools determines the transport properties of Ca^{2+} within the cytoplasm. The mobile buffers carry Ca^{2+} along with themselves, the stationary buffers immobilise it. Thus, the full dynamics of cytosolic Ca^{2+} signalling should take into account the dynamics of buffers.

Fortunately, this complexity can be absorbed into the definition of an effective diffusion constant as long as we assume the buffers bind Ca^{2+} quickly (compared to diffusion), and are linear and stationary. Under these circumstances, Wagner *et al.* [106] showed it was possible to obtain an effective diffusion constant

$$D_{\text{eff}} = \frac{K}{K + [B_s]_T} D_c, \tag{1.2}$$

where $K = \frac{k_s^-}{k_s^+}$, the ratio of the association and dissociation constants for the stationary buffer, B_s, under the condition of rapid buffering. This valuable result allows us to focus only on the dynamic behaviour resulting from Ca^{2+} transport processes,

$$\frac{\partial c}{\partial t} = D_{\text{eff}} \nabla^2 c + g'(\mathbf{r}, t), \tag{1.3}$$

where $g'(\mathbf{r}, t)$ now only describes the interaction of Ca^{2+} with channels and pumps. These elements can be incorporated into models as either discrete elements or as having a continuous distribution throughout the signalling environment. The appropriateness of which model to consider typically depends on the length scales of interest; the tissue level waves in pancreatic

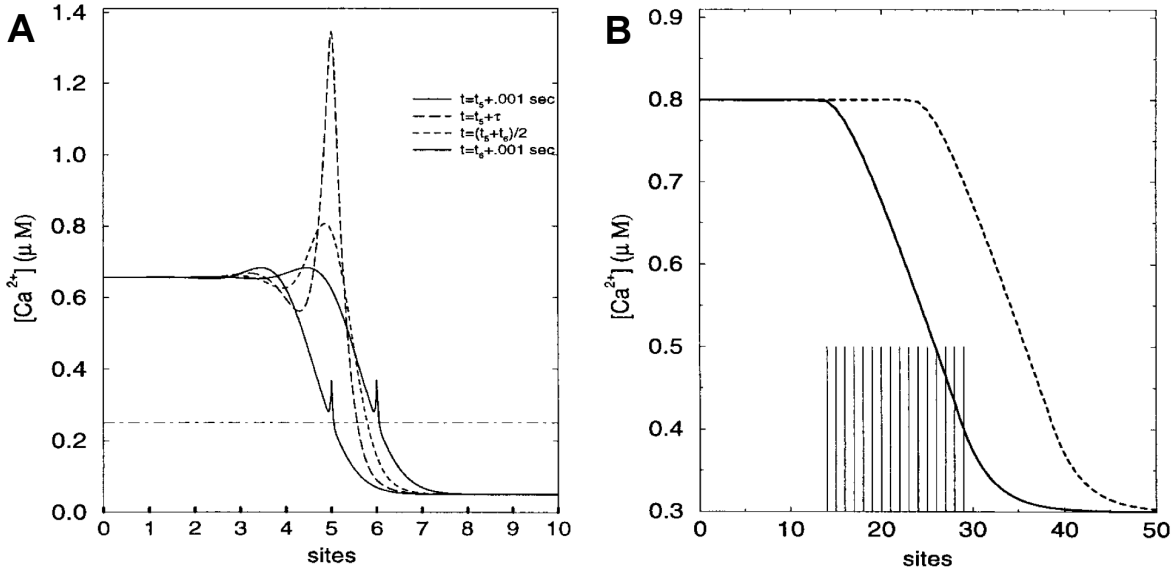

Figure 1.3: Saltatory and continuous wave propagation in the fire-diffuse-fire model. (A) Four snapshots of a rightward propagating saltatory wave. One site is firing at a time, and so the shape of the wave changes with time. **(B)** Two snapshots of a rightward propagating continuous wave. The vertical lines indicate sites that are simultaneously firing to contribute to the first snapshot (solid line). Taken from Ponce-Dawson *et al.* [109].

or ventricular tissues are well described by continuous models, whereas channels are known to exist as discrete elements or clusters whose separation is much larger than their individual size. On a sub-cellular resolution, it might typically be more appropriate to look at discrete descriptions. Both discrete and continuous frameworks can be considered as limits of the Fire-Diffuse-Fire (FDF) model developed by Keizer, Pearson and Ponce-Dawson [107, 108, 109].

1.3.2 The Fire-Diffuse-Fire Model

The FDF model was developed as a simple means of capturing the dynamics of CICR waves without worrying about the details of channel behaviour [107]. Individual release sites are considered at points $x = nd$ $(n = 0, \pm 1, \pm 2, ...)$ in 1-dimension and instantaneously release a fixed quantity, σ, of Ca^{2+} when the concentration of Ca^{2+} at the site exceeds a threshold amount, $c = c_{\text{th}}$. After release, the site enters a refractory period during which it will not fire. The released Ca^{2+} diffuses and will activate neighbouring channels under the right conditions. If a channel remains open for a time τ, then we have a formalism in which both saltatory and continuous wave propagation can be considered [109]. The FDF model can then be described by the diffusion equation,

$$\frac{\partial c}{\partial t} = D\frac{\partial^2 c}{\partial x^2} + \frac{\sigma}{\tau}\sum_{n=-\infty} \delta(x - nd)H(t - t_n)H(t_n + \tau - t), \tag{1.4}$$

where t_n is the firing time of the nth channel, $\delta(x)$ is the Dirac δ-function, and $H(t)$ is the Heaviside step function ($H(t) = 0$ for $t < 0$, $H(t) = 1$ for $t \geq 0$).

When channels are far apart, the shape of the wavefront changes as the wave passes between channels, and individual releases can be picked out during propagation [109], giving rise to a wave that appears to be made up of a discrete series of releases (Figure 1.3A). This so-called "saltatory" wave corresponds to the case where individual releases are quick (τ is small) and the separation between channels, d, is large. In the discrete limit, with $\bar{x} = x/d$, $\bar{t} = tD/d^2$, $\bar{c} = c/c_{\text{th}}$,

$$\frac{\partial \bar{c}}{\partial \bar{t}} = \frac{\partial^2 \bar{c}}{\partial \bar{x}^2} + \frac{1}{\alpha} \sum_{n=-\infty} \delta(\bar{x} - n)\delta(\bar{t} - \bar{t}_n), \tag{1.5}$$

where $\alpha = dc_{\text{th}}/\sigma$. The criteria for wave propagation is that if all previous channels have fired, then the concentration at the first unfired site reaches c_{th}. Assuming the time intervals between successive releases, Δ, is constant, propagation occurs if [107]

$$\alpha \leq g(\Delta) = \sum_{n=1}^{\infty} \sqrt{\frac{1}{4\pi\Delta n}} e^{-(n/4\Delta)}. \tag{1.6}$$

This has a single root [107], giving a steady velocity

$$v = D/d\Delta \tag{1.7}$$

showing that the velocity of waves in such systems is proportional to D, in contrast to the $\sqrt{D}$ dependence of continuous waves [110]. For small α, $\Delta = 1/[4 \log 1/\alpha]$ so

$$v = \frac{4D}{d} \log\left(\frac{\sigma}{dc_{\text{th}}}\right), \tag{1.8}$$

a valuable result we will make use of in Chapter 3. We assumed Δ takes a single value, and for $\alpha < 0.5$ this is true. For higher values, wave propagation can still occur where the combined Ca^{2+} released from multiple sites is necessary to activate a channel. Propagation failure in the FDF model occurs by a period doubling bifurcation for $0.512 < \alpha < 0.535$ [108, 107]. These observations further hold when release is not instantaneous [108]. This analysis was extended by Coombes *et al.* [111, 112, 113] to incorporate pumps. In agreement with the above, there is a single propagating solution for $\tau = 0$, but they found that decreasing τ with non-zero pumping can switch the system from propagation failure to supporting wave propagation. Hence, it is most efficient for cells to use large single channel currents and brief release events to propagate signals while exposing the cytosol to as little Ca^{2+} as possible.

The continuous case occurs for high τ, small d systems in which typically multiple releases contribute to the formation of the wavefront (Figure 1.3B). The wave front is then able to maintain it's shape as it propagates through the system, which it does with velocity [108]

$$v \approx \sqrt{\frac{\sigma D}{dc_{\text{th}}\tau}}. \tag{1.9}$$

The transition from saltatory to continuous propagation was illustrated by simulations of waves in cardiac myocytes [107].

1.3.3 Models of Root Nodule Symbiosis Signalling

Different hypotheses have been put forward to explain the generation of perinuclear calcium oscillations. In Granqvist *et al.* [114] a three-component ordinary differential equation (ODE) system is presented containing a Ca^{2+}-activated K^+ channel (DMI1 [95]), a voltage-gated Ca^{2+} channel and a Ca^{2+}-ATPase (MCA8 [62]), see Figure 1.4A. Within their model,

$$\dot{v} = \frac{1}{C_m}(I_{\mathrm{Ca}} + I_{\mathrm{K}}), \tag{1.10}$$

describes the change in membrane voltage v due to currents I_{Ca} through the Ca^{2+} channel and I_{K} through the K^+ channel, with C_m being the membrane capacitance. The concentration of Ca^{2+} in the cytoplasm obeyed

$$\dot{c} = E_{ps}(\alpha I_{\mathrm{Ca}} - \mu c) + \sum_{i=1}^{N} R_i, \tag{1.11}$$

where μ is the pump rate and E_{ps} and α are scaling constants. With this two-ODE system, and appropriate definitions for I_{Ca} and I_{K} [114], the model was able to reproduce the shape and frequency of nuclear Ca^{2+} oscillations (Figure 1.4). By including calcium-buffering species through the reactions R_i, the authors aimed to explain several experimental observations on the nature of the calcium signal that could not be accounted for within the buffer-free system. Firstly, that different spike shapes are observed when using different experimental techniques, secondly that the initial calcium spikes occur at a higher frequency than the later spikes, and finally that the oscillations terminate.

By changing the buffer dissociation constant to known values [115] the model could reproduce the various observed spike shapes for the different buffers used experimentally. The period of high frequency spiking observed initially could be explained by the presence of large quantities of unbound buffer at the start. By hypothesising that the perception of the symbiont signalling molecule causes an increase in buffering capacity within the nucleus, possibly by the migration of calmodulin to the nucleoplasm from the cytosol as is observed in animal systems [116], the model predicted that a period of rapid oscillations would occur if additional quantities of the signalling molecule were added during existing oscillations. This was indeed observed, demonstrating that components beyond those identified in previous genetic studies play an essential role in determining the calcium signal.

This model was later extended by Charpentier *et al.* [86] to study the relationship between DMI1 and the Ca^{2+} channel in more depth. This showed that Ca^{2+} spiking required the simultaneous opening of both DMI1 and the Ca^{2+} channel. The Ca^{2+} release appears to occur in two steps, an initial release that equilibrates the electropotential gradient across the membrane, but in doing so binds to DMI1's EF-hands [117] to allow K^+ to flow across the membrane. This steady flux drives further flow of Ca^{2+} creating the full spike in the model. This localised feedback suggested DMI1 and the Ca^{2+} channel would need to be closely localised on the nuclear envelope, and the later identification of the symbiotic Ca^{2+} channel

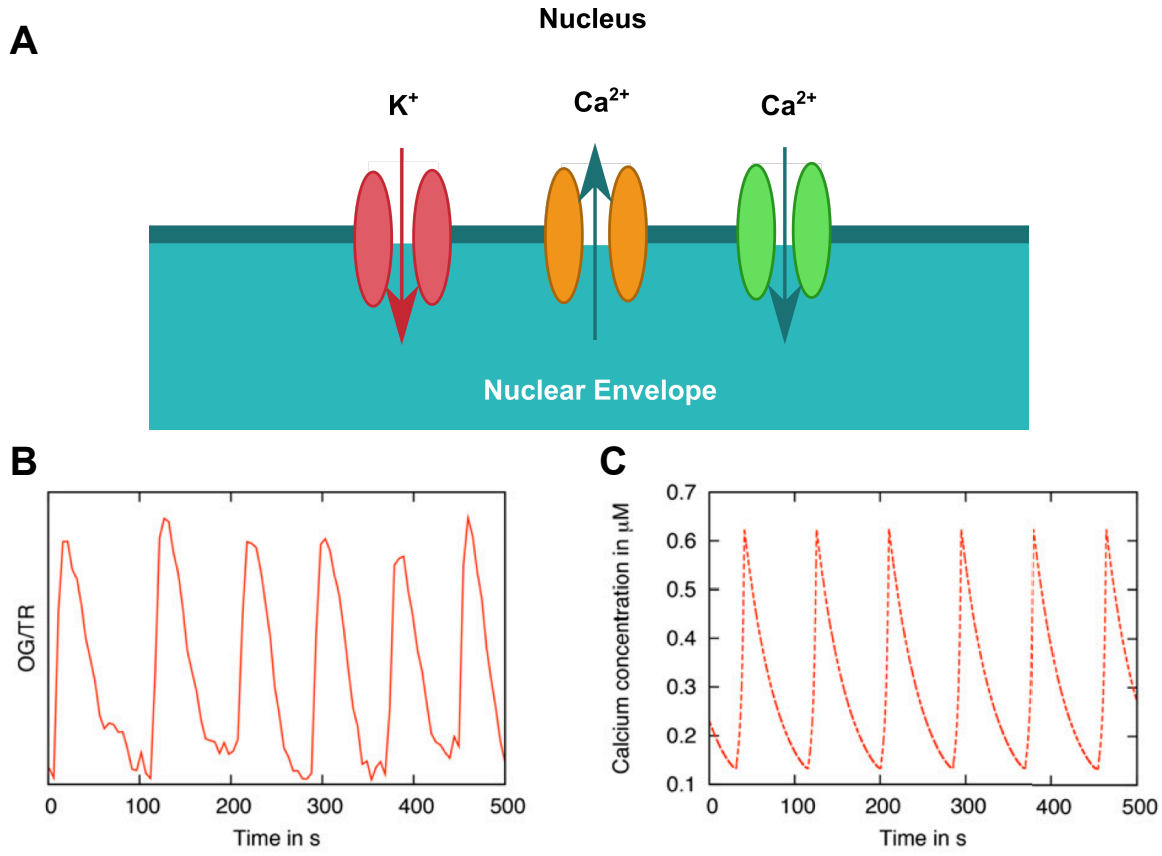

Figure 1.4: Compartment model of symbiosis signalling. **(A)** Illustration of the basic symbiosis signalling model from Granqvist *et al.* [114], featuring the 3 key transporters, the Ca^{2+}-activated K^+ channel, DMI1 (red), a voltage-activated Ca^{2+} channel (orange) and the Ca^{2+}-ATPase, MCA8 (green) on the inner nuclear membrane. **(B)** Experimental Ca^{2+} oscillations using microinjection of the dyes Oregon Green (OG) and Texas Red (TR) into a *M. truncately* root hair cell. **(C)** Simulated Ca^{2+} oscillations from the model illustrated in A. B&C taken from Granqvist *et al.* [114].

(CNGC15, Table 1.1) confirmed this [63]. The description of the Ca^{2+} channel (I_{Ca}) was updated here to include the known behaviour of CNGC channels [12]. Any time delay between DMI1 and CNCG15 activation in this model terminated oscillations.

A more unconventional approach to modelling calcium signalling was presented by Sciacca *et al.* [118] utilising a methodology referred to as the Calculus of Wrapped Compartments (CWC) [119]. At its heart the CWC model is a term rewrite system [120], in which the biological system is described by a "term" and the evolution of the system is modelled by the application of a set of "rewrite rules". The form of the terms and rules considered within the CWC allows the description of membrane wrapped compartments, and can simulate the interaction of elements localised to membranes and within the compartmental volumes, e.g. proteins, ions, channels, etc. They described the flow of Ca^{2+} across the nuclear membrane through channel and uptake by a Ca^{2+}-ATPase. The channel opened via binding of an

external signalling molecule (the unknown secondary messenger). A decaying concentration of this signalling molecule results in a Ca^{2+} trace with decreasing frequency, recreating the information content of the spikes [121]. The CWC method is extremely versatile; within the same mathematical framework, the authors have been able to study the spatial interaction between the Mychorrizal hyphae and the plant root [122], a technique that could be extended to the interaction of rhizobia and the plant within infection thread growth/formation, for example. Within the sphere of calcium modelling, it is simple to add additional rules to incorporate different gating models, particularly with the recent identification of the symbiotic Ca^{2+} channel [63] and buffering effects.

Work on symbiosis signalling has so far concentrated on the temporal behaviour of the calcium signal. However, the spatial nature of the system can have important implications on the signals generated [94, 123]. The signal within the nucleus is spatially inhomogeneous [94], and it is important to understand how the decoding protein perceives, and is affected by, the signal. In Capoen *et al.* [62], an early spatial model was used to highlight the necessity of having signalling components on both sides of the NE in order to generate Ca^{2+} oscillations in both the cytosol and nucleosol. Diffusion of Ca^{2+} through the Nuclear Pore Complexes (NPCs) was insufficient to explain spiking on both sides. In Chapter 2 we examine this model in much more detail, extending the work to look at signal generation in both compartments in more detail.

1.3.4 Models of Systemic Signalling

Systemic signals are generated in response to a range of biotic and abiotic stimuli and are a means of rapid communication eliciting responses far from the original stimulus. Modelling in plants has so far ben restricted to electropotentials: action potentials (APs) and variation potentials (VPs) [26, 124]. The generation of an electropotential is associated with the passive fluxes of the ionic species Ca^{2+}, Cl^- and K^+ [26, 124, 125]. An initial influx of Ca^{2+} triggers a Cl^- efflux through voltage-dependent anion channels, resulting in a rapid depolarisation of the membrane, which is the electropotential. APs and VPs are responses to different stimuli. An action potential is triggered by a non-damaging stimulus (e.g., cold, pH changes, salt stress), and is propagated by voltage-dependent Ca^{2+} channels, whereas a VP occurs in response to damaging stimuli (e.g., wounding, chewing insects) and may be generated by mechanosensitive [126] or ligand-gated [127] Ca^{2+} channels.

Sukhov *et al.* [128] proposed a model for AP development, incorporating the key ionic species and PM ion transporters in a series of ODEs based on the work of Gradmann *et al.* [129, 130]. They focus on the interaction of Ca^{2+} with a H^+-ATPase that they show to be important to the generation of the AP. In a follow up paper, Sukhov *et al.* [131] study the propagation of APs through plant tissue, presenting the first detailed model of AP propagation in plants. Cells from the previous paper were connected together to form a grid, allowing electrical conductivity and diffusion of apoplast ions between nearest neighbours. The model

is able to capture the quantitative details of experimental AP propagation when examining behaviour of the membrane potential. Sukhov *et al.* [131] go on to test the effects of cell-to-cell conductivity and the activity of the H^+-ATPase on signal propagation. Interestingly, it is seen that properties that result in good AP propagation are generally bad for AP generation.

The only VP model to date was also presented by Sukhov *et al.* [132], which extended the authors' AP work. The authors consider a ligand-gated Ca^{2+} channel that is triggered by the binding of some "wounding substance" that diffuses from the wounding site through the plant xylem. The model was able to simulate VP propagation and showed qualitative agreement with their experiments. The decaying ligand concentration away from the site within the model results in a decreasing VP as has been observed [133]. This ligand-based model is, however, in conflict with current perspectives on VP propagation in the field, in which it is believed a pressure wave through the xylem is the underlying signal behind VP propagation [134, 135]. In Chapter 3 we take a closer look at both of these qualitative descriptions of VP propagation.

1.4 Summary

In this thesis we examine two main areas in which Ca^{2+} signalling plays a major role in plants. Our approach is to identify the minimum signalling elements required to reproduce observed behaviour. In this way we are able to provide an intuitive understanding of the underlying processes, and guide future experimental work.

We study the generation of Ca^{2+} oscillations in the nucleus during the establishment of symbiosis in Chapter 2. We first compare applications of the FDF model in the spherical environment of the nucleus in 3D and in a 2D model in which Ca^{2+} is restricted to the nuclear surface. We then apply our model to study the possible role of the nuclear pores in signal generation, validating and extending the work of Capoen *et al.* [62]. By allowing Ca^{2+} to diffuse through pores in our model, we examine how signals on the inside and outside of the NE are temporally co-ordinated.

In Chapter 3, we again apply the FDF model, this time to study the propagation of systemic Ca^{2+} signals in plant roots. We discuss and examine systemic signalling in a general context, then focus on the Ca^{2+} wave observed by Choi *et al.* [21] in response to salt stress. We examine various mechanistic models of its propagation via modelling. This modelling work was confirmed in experiments performed by our collaborators in the Gilroy lab in the University of Wisconsin, Madison.

Chapter 2

Calcium Oscillations across the Nuclear Envelope

The nucleus represents a unique signalling environment within the cell, separated from the cytoplasm by the NE. As the site of transcription, signals within the nucleoplasm have the opportunity to directly effect gene expression, without that signal needing to be transduced across the NE. Nuclear Ca^{2+} signals are able to regulate physiological processes like cell proliferation [136] or protein translocation [137] and it has been widely observed that the nucleus contains its own calcium signalling machinery [138, 139, 140]. However, the presence of nuclear pores may enable connectivity between cytoplasmic and nucleoplasmic Ca^{2+} signals and how the two are related remains an ongoing question in both plant and animal fields.

The NPC is a large protein complex that sits at holes in the NE through which the nucleoplasm and cytoplasm are connected. At these points, the Outer Nuclear Membrane (ONM) and the Inner Nuclear Membrane (INM) are contiguous. The NPC acts as a gateway for the transport of proteins between the cytoplasm and the nucleoplasm [141]. Given the size of the central channel, proteins and molecules with a diameter smaller than 9 nm should be able to pass through without restriction [142], although the central channel can become occluded when transporting a large protein or in response to some stimuli [143]. Even when the central channel is blocked, it has been shown that small molecules are able to pass through small pores that exist in each of the 8 subunits making up the NPC [144, 145]. While some studies have shown that the NPC can attain a conformation preventing all ion transport [146, 147], these were performed under non-physiological conditions and later experiments on animal nuclei have reinforced the conclusion that the NPC is permeable to Ca^{2+}, under normal conditions [148, 149, 150].

The limited studies in plant nuclei, however, do not yet support NPC mediated Ca^{2+} movement across the NE [138]. Experiments on isolated nuclei suggested the nuclear compartment was not passively permeable to Ca^{2+} [147]. Tobacco cells show a stimulus dependent delay between cytosolic and nuclear Ca^{2+} peaks that vary from a few seconds up to an hour [32, 147, 151, 152, 153, 154, 155]. Such observations suggest nuclear Ca^{2+} changes in

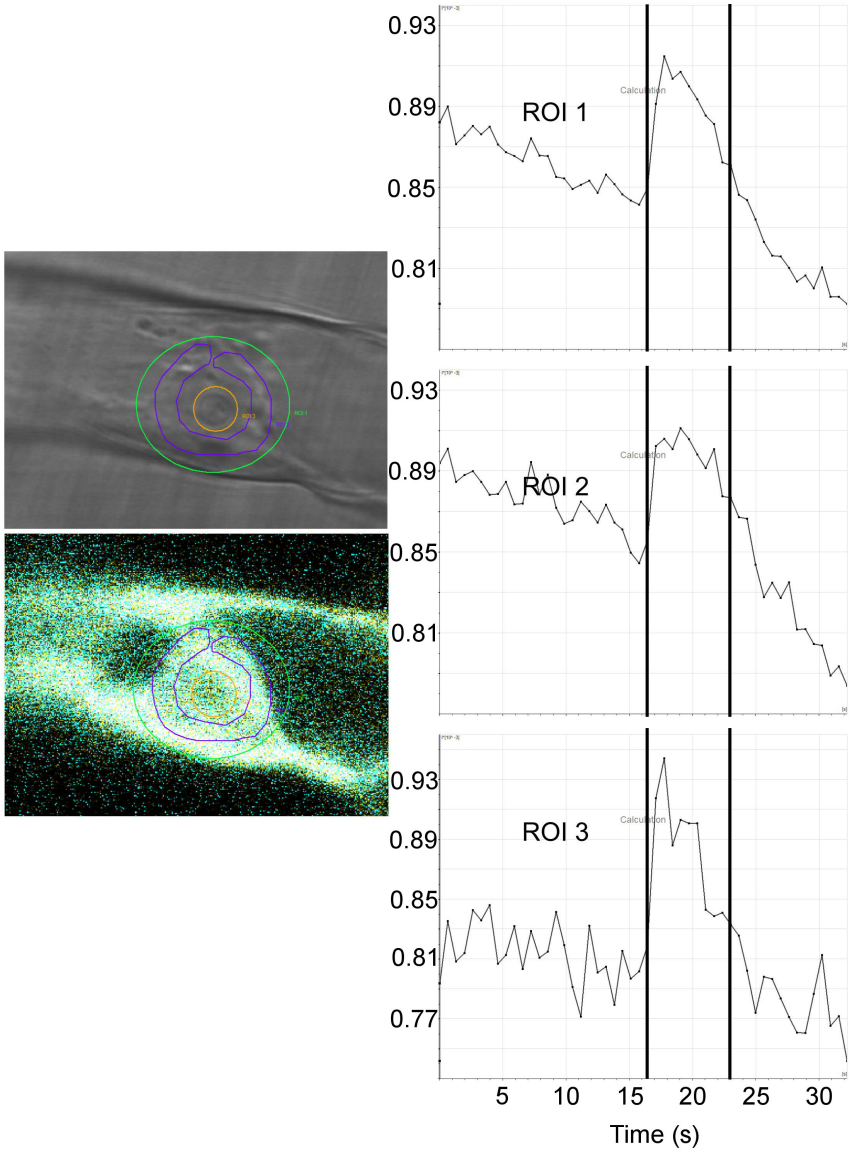

Figure 2.1: Symbiotic Ca^{2+} spikes occur simultaneously on INM and ONM. Concentration of Ca^{2+} during nuclear Ca^{2+} oscillations in legume root hairs upon stimulation by Nod Factors, calculated from confocal images generated every 0.66 s. Traces show fluorescence intensity ($I \times 10^{-3}$). Images were divided into three regions of interest (ROI)) indicated in the left hand images. ROI 1 is limited to the interior of the nucleus (orange circle), ROI 2 is taken to be an annular region around the outside of the nucleus (purple annulus), and ROI 3 is a larger region encapsulating the nucleus and perinuclear cytoplasm (green circle). We see that the Ca^{2+} spike is generated at the same time in all three regions. *Data and Figure produced and analysed by our collaborators Jongho Sun from the lab of Prof Giles Oldroyd, Department of Cell and Developmental Biology, John Innes Centre, Norwich, UK.*

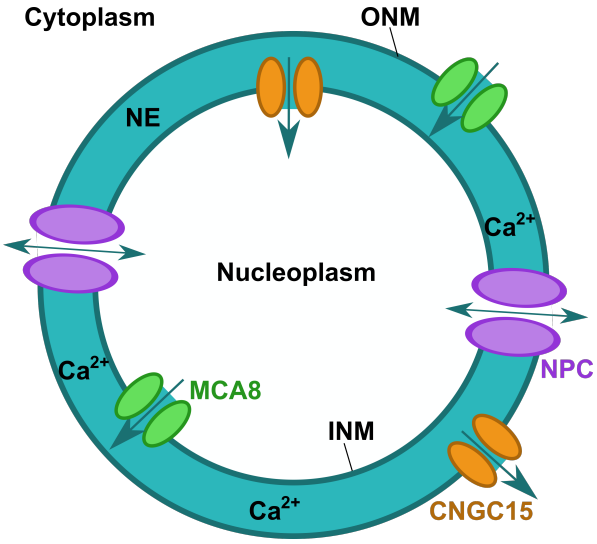

Figure 2.2: Model of nuclear Ca^{2+} signalling. Ca^{2+} is released from the NE store through CNGC15 Ca^{2+} channels, present on the INM and ONM. The activation of these channels is dependent on the DMI1 potassium channel, but this has not been explicitly modelled, the complexities of channel activation are instead encapsulated in the FDF framework. Ca^{2+} is pumped back into the NE by MCA8 pumps, likewise present on both membranes, and Ca^{2+} is able to passively diffuse between the INM and ONM through the NPCs.

plants are generated independently of cytosolic Ca^{2+} changes, in contrast to the animal field [150, 142, 139].

The symbiosis between legumes and rhizobial bacteria or mychorrizal fungi is the best studied example of nuclear Ca^{2+} signalling in plants [36, 80, 81, 86, 94, 100]. Perception of diffusable signal molecules, Nod Factors from rhizobia and Myc Factors from mychorrizal fungi, by plasma membrane localised receptors triggers a signalling cascade that results in nuclear Ca^{2+} oscillations followed by symbiosis specific gene expression [36, 50, 99], Figure 2.1. While Ca^{2+} is not believed to transmit this specificity [101], it is essential for triggering symbiotic gene expression, with a minimum number of spikes required to activate downstream responses [80]. This signalling process has been dissected in the model legumes *Lotus japonicus* and *Medicago truncatula*. A number of nuclear localised proteins required upstream of the Ca^{2+} signal in both symbioses have been identified, including a transmembrane cation channel, DMI1 in *M. truncatula* [55, 57] and CASTOR/POLLUX in *L. japonicus* [58, 95], the SERCA-type Ca^{2+}-ATPase MCA8 in *M. truncatula* [62], three components of the nucleoporin (NUP85, NUP133 and NENA in *L. japonicus*) [59, 60, 61], and, most recently, a cyclic nucleotide-gated Ca^{2+} channel, CNGC15 [63].

The Ca^{2+} oscillations in this system occur not only in the nucleoplasm, but also in the perinuclear cytoplasm, providing an excellent system to study Ca^{2+} signalling across the NE in plants. The perinuclear cytosolic signal is temporally coordinated with the nucleoplasmic

signal, in that Ca^{2+} spikes occur simultaneously on both sides of the NE (Figure 2.1) and the signal frequency is the same [62], which raises the question: how does this coordination occur? We have developed a spatial model of Ca^{2+} diffusion that allows investigation of the involvement of NPCs in generating these signals [62]. This model, illustrated in Figure 2.2, is based on the FDF framework and uses a CICR mechanism to describe channel activation. By focussing on signal generation, we demonstrate that a Ca^{2+} permeable NPC is a robust mechanism for generating simultaneous Ca^{2+} spikes. While we focus our attention primarily on symbiosis signalling, many of our results here are of general application to a number of fields and systems.

2.1 Simulating Ca^{2+} Signals Throughout the Nuclear Volume

To model the dynamics of nuclear Ca^{2+} signals, we utilise the FDF framework [62, 107, 109, 111, 113, 156, 157, 158, 159], as it provides a simple way to capture the effect of spatially localised channels on Ca^{2+} signalling. As illustrated in Figure 2.2, we focus on a core subset of the symbiotic Ca^{2+} signalling machinery, the minimum components required to generate a Ca^{2+} spike, namely the Ca^{2+} channel, CNCG15 [63] and the Ca^{2+} pump MCA8 [62]. For simplicities sake, we do not include the potassium channel DMI1 that is responsible for activation of the Ca^{2+} channel [86] since the FDF model is able to encapsulate such complicated channel activation into a single threshold parameter [103]. In later models (see Section 2.5) we will incorporate the NPCs to couple the INM and ONM.

The concentration of calcium, $c(\mathbf{r}, t)$ obeys the diffusion equation with a diffusion constant, D, which describes the properties of the medium and takes into account rapid buffering of Ca^{2+} [106]. We do not explicitly incorporate buffering proteins into the model. The nuclear volume is taken to be free from Ca^{2+} initially and Ca^{2+} is released from the NE store [62, 94] via channels described by the source term

$$g(\mathbf{r}, t) = \sigma \sum_{i=0}^{N} \sum_{k=1,2,\ldots} \delta(\mathbf{r} - \mathbf{r}_i)\delta(t - t_i^k), \tag{2.1}$$

for source strength σ, and N sources firing at locations $\mathbf{r}_i$ and at times t_i^k. The sum over k is the sum over all Ca^{2+} releases from a given channel. For a nucleus of radius $R = 8$ μm, we typically use 24 channels, which matches the separation of the focal release sites measured in *Xenopus laevis* [160]. It makes sense to consider the spatial extent of the calcium sources to be delta functions in space because channels are typically on the order of 10^{-2} μm in size while the radius of the nucleus is several μm. We also incorporate pumps on the nuclear surface with an uptake rate k_s, which act to take calcium from the nucleoplasm and return it to the membrane store. In a three dimensional model, these add a surface flux term, giving

a set of equations

$$\frac{\partial c}{\partial t} = D\nabla^2 c + g(\mathbf{r}, t), \tag{2.2a}$$

$$D\left.\frac{\partial c}{\partial r}\right|_{\text{surface}} = -k_s c, \tag{2.2b}$$

to describe the concentration dynamics. A single source releases a fixed quantity, σ, of Ca^{2+} when the concentration, c, of Ca^{2+} at that site exceeds a threshold value, c_{th}. This determines the firing times t_i^k in (2.1). After release, the channel enters a refractory period of length, T. In our system, this represents the depletion of the NE store of Ca^{2+} in the local region around the channel, and the time required for the store to recover. We determine this refractory period as the time required for the concentration at a recently fired source to fall below some fraction, α, of the threshold, independent of any other sources.

In the FDF model all the firing times must be computed and stored. To limit the number of times we must store, we compute the time that the contribution from a single release falls bellow 10^{-4} μM at that source, a negligible concentration. Any t_i^k such that $t - t_i^k$ is greater than this quantity will be removed from memory. To avoid precalculating the firing times t_i^k, we step forward by some fixed time step, Δt, and let t_i^k be the first time for which $c \geq c_{\text{th}}$ and $t_i^k \geq t_i^{k-1} + T$. We must choose this time step to be sufficiently small that we do not incorrectly have sources firing simultaneously when they should not, but large enough that we do not do more time consuming calculations than we need to. Generally we chose to step forward in time on the order of ms.

2.1.1 Deriving an Analytical Solution

The system of equations in (2.2) must be solved to allow us to analyse the model. A system of this form can be solved numerically using established techniques [161], typically involving large numbers of time consuming calculations. Under certain rare conditions, we are able to derive an analytical solution which dramatically aids analysis. An analytical solution here provides the mathematical form of the Ca^{2+} signal at all points in space and time. If we know when each channel fires (which can be calculated, as described above), we only need to perform one calculation to calculate the concentration at a position. In contrast, numerical techniques require we follow the complete dynamics of Ca^{2+} release and diffusion throughout the entire region at a high enough temporal resolution to limit the effects of numerical errors.

Within the spherical geometry of the nucleus, the FDF model can be solved analytically using Green's functions. Our derivation here follows the work of Skupin *et al.* [162], extending their work to incorporate a surface uptake. The Green's function in 3D satisfies

$$\frac{\partial G}{\partial t} = D\nabla^2 G + \frac{1}{r'^2 \sin\theta'}\delta(r - r')\delta(\theta - \theta')\delta(t - t'), \tag{2.3a}$$

$$D\left.\frac{\partial G}{\partial r}\right|_{r=R} = -k_s G(R, \theta, t|r', \theta', t'), \tag{2.3b}$$

$$G(r, \theta, t|r', \theta', t') = 0, t \geq t'. \tag{2.3c}$$

After Laplace transformation with respect to t, the governing equation of the transformed Green's function $\tilde{G}(r,\theta,s|r',\theta',t')$ is

$$s\tilde{G} = D\nabla^2\tilde{G} + \frac{1}{r'^2\sin\theta'}\delta(r-r')\delta(\theta-\theta')e^{-st'}. \tag{2.4}$$

We first solve the homogeneous problem, readily identified as the Helmholtz equation, which in spherical polar coordinates reads

$$\frac{\partial^2\psi}{\partial r^2} + \frac{2}{r}\frac{\partial\psi}{\partial r} + \frac{1}{r^2\sin\theta}\frac{\partial}{\partial\theta}\left[\sin\theta\frac{\partial\psi}{\partial\theta}\right] = -\lambda^2\psi, \tag{2.5}$$

which can be solved by a standard separation ansatz. The radial part leads to Bessel's differential equation, while the angular part obeys Legendre differential equations. Due to convergence restrictions, the solution to the Helmholtz equation has the form

$$\psi_{lp}(r,\theta) = \frac{J_{l+1/2}(\lambda_{lp}r)}{r^{1/2}}P_l(\cos\theta), \qquad p = 1,2,3,\dots \;\; l = 0,1,2,\dots \tag{2.6}$$

$$\psi_{00}(r,\theta) = \begin{cases} 1 & \text{if } k_s = 0 \\ 0 & \text{otherwise,} \end{cases} \tag{2.7}$$

where $J_{l+1/2}(x)$ denotes the Bessel function of the first kind and $P_l(\cos\theta)$ is the Legendre polynomial. The λ_{lp} are determined by the positive roots of the boundary equation (2.3b), which for $k_s = 0$ is

$$lJ_{l+1/2}(\lambda_{lp}R) - \lambda_{lp}RJ_{l+3/2}(\lambda_{lp}R) = 0. \tag{2.8}$$

We then consider the ansatz

$$\tilde{G}(r,\theta,s|r',\theta',t') = \sum_{l,p=0}^{\infty}\beta_{lp}\psi_{lp}(r,\theta), \tag{2.9}$$

which only satisfies (2.3b) for $k_s \neq 0$ if $\psi_{00} = 0$ (note that $\tilde{G}$ satisfies the boundary equation if and only if G does). Then, for $k_s \neq 0$, the λ_{lp} are given by the solutions to

$$\frac{\partial}{\partial r}\left.\frac{J_{l+1/2}(\lambda_{lp}r)}{r^{1/2}}\right|_{r=R} = -\frac{k_s}{D}\frac{J_{l+1/2}(\lambda_{lp}R)}{R^{1/2}}, \tag{2.10}$$

which can be expressed as

$$\left(l + \frac{k_sR}{D}\right)J_{l+1/2}(\lambda_{lp}R) - \lambda_{lp}RJ_{l+3/2}(\lambda_{lp}R) = 0. \tag{2.11}$$

We can then solve (2.4) by inserting our ansatz (2.9) leading to

$$s\sum_{l,p=0}^{\infty}\beta_{lp}\psi_{lp}(r,\theta) = -D\sum_{l,p=0}^{\infty}\beta_{lp}\lambda_{lp}^2\psi_{lp}(r,\theta) + \frac{1}{r'^2\sin\theta'}\delta(r-r')\delta(\theta-\theta')e^{-st'}. \tag{2.12}$$

We apply the integral operators

$$\vartheta_1 f : f \mapsto \int_{-1}^{+1} d\mu P_m(\mu)f(\mu) \tag{2.13a}$$

$$\vartheta_2 g : g \mapsto \int_0^R dr r^{3/2}J_{m+1/2}(\lambda_{lp}r)g(r) \tag{2.13b}$$

to obtain (via orthogonality)

$$s\beta_{mq} = -\beta_{mq}\lambda_{mq}^2 D + \frac{1}{\mathcal{N}(m)\mathcal{N}(\lambda_{mp})}\psi_{mq}(r',\theta')e^{-st'}, \tag{2.14}$$

where the norms $\mathcal{N}$ are given by

$$\mathcal{N}(l) = \int_{-1}^{+1} d\mu P_l^2(\mu) = \frac{2}{2l+1} \tag{2.15a}$$

$$\begin{aligned}\mathcal{N}(\lambda_{lp}) &= \int_0^R dr r^2 \left[\frac{J_{l+1/2}(\lambda_{lp}r)}{r^{1/2}}\right]^2 \\ &= \frac{R^2}{2}\left[J_{l+1/2}^2(\lambda_{lp}R) - J_{l-1/2}(\lambda_{lp}R)J_{l+3/2}(\lambda_{lp}R)\right]\end{aligned} \tag{2.15b}$$

$$\mathcal{N}(\lambda_{00}) = \int_{-1}^{+1} d\mu \int_0^R dr r^2 = 2R^3/3. \tag{2.15c}$$

The unknown components, β_{lp}, are determined by (2.14). The solution in Laplace space is

$$\tilde{G}(r,\theta,s|r',\theta',t') = \sum_{l,p=0}^{\infty} \frac{1}{\mathcal{N}(l)\mathcal{N}(\lambda_{lp})(s+D\lambda_{lp}^2)}\psi_{lp}(r',\theta')e^{-st'}\psi_{lp}(r,\theta). \tag{2.16}$$

It can be transformed back to time by the residue theorem since we have first order poles, $s+D\lambda^2$, along the negative real axis only. The Green's function of the inhomogeneous problem (2.3a) without the ϕ dependence is

$$\begin{aligned}G(r,\theta,t|r',\theta',t') = \sum_{l=0,p=1}^{\infty} &\frac{1}{\mathcal{N}(l)\mathcal{N}(\lambda_{lp})}\frac{J_{l+1/2}(\lambda_{lp}r')}{r'^{1/2}}P_l(\cos\theta')e^{\lambda_{lp}^2 Dt'} \\ &\frac{J_{l+1/2}(\lambda_{lp}r)}{r^{1/2}}P_l(\cos\theta)e^{-\lambda_{lp}^2 Dt} + \frac{3}{2R^3},\end{aligned} \tag{2.17}$$

in the case where $k_s = 0$ and

$$\begin{aligned}G(r,\theta,t|r',\theta',t') = \sum_{l=0,p=1}^{\infty} &\frac{1}{\mathcal{N}(l)\mathcal{N}(\lambda_{lp})}\frac{J_{l+1/2}(\lambda_{lp}r')}{r'^{1/2}}P_l(\cos\theta')e^{\lambda_{lp}^2 Dt'} \\ &\frac{J_{l+1/2}(\lambda_{lp}r)}{r^{1/2}}P_l(\cos\theta)e^{-\lambda_{lp}^2 Dt},\end{aligned} \tag{2.18}$$

otherwise. For simulation purposes, the assumption of spherical symmetry is not valid and we must reintroduce explitly the ϕ dependence in the Green's function. This only depends on the cosines of the angles between $P(\mathbf{r})$ and $P(\mathbf{r}')$, and hence we can rotate the coordinate system such that one of the angles is zero. The angle Θ between the points is given by

$$\cos\Theta = \cos\theta\cos\theta' + \sin\theta\sin\theta'\cos(\phi-\phi'). \tag{2.19}$$

The final form of the Green's function is therefore

$$\begin{aligned}G(r,\theta,\phi,t|r',\theta',\phi',t') = \sum_{l=0,p=1}^{\infty} &\frac{J_{l+1/2}(\lambda_{lp}r')J_{l+1/2}(\lambda_{lp}r)}{2\pi\mathcal{N}(l)\mathcal{N}(\lambda_{lp})r'^{1/2}r^{1/2}}P_l(\cos\Theta)e^{-\lambda_{lp}^2 D(t-t')} \\ &+ \frac{3}{4\pi R^3},\end{aligned} \tag{2.20}$$

for $k_s = 0$ and

$$G(r,\theta,\phi,t|r',\theta',\phi',t') = \sum_{l=0,p=1}^{\infty} \frac{J_{l+1/2}(\lambda_{lp}r')J_{l+1/2}(\lambda_{lp}r)}{2\pi\mathcal{N}(l)\mathcal{N}(\lambda_{lp})r'^{1/2}r^{1/2}} P_l(\cos\Theta)e^{-\lambda_{lp}^2 D(t-t')}, \tag{2.21}$$

otherwise, where the ϕ dependence has given another normalization factor of $1/2\pi$. The resulting concentration can be derived from (2.21) by considering Green's second identity, which for scalar fields u and v defined in a volume V enclosed by a surface S is

$$\int_V \left(u\nabla^2 v - v\nabla^2 u\right) dV = \oint_S \left(u\frac{\partial v}{\partial n} - v\frac{\partial u}{\partial n}\right) dS, \tag{2.22}$$

where $\partial v/\partial n$ is the directional derivative of v in the direction of the outward pointing normal $\mathbf{n}$ to the surface element dS

$$\frac{\partial v}{\partial n} = \nabla v.\mathbf{n}. \tag{2.23}$$

Now consider (2.22) with $u = c$ and $v = G$ for our system. For the specified boundary conditions (2.3b), the surface term

$$\oint_S \left(c\frac{\partial G}{\partial r} - G\frac{\partial c}{\partial r}\right) dS \tag{2.24}$$

vanishes, and by inserting the diffusion equation into the volume term, we obtain the solution

$$c(\mathbf{r},t) = \sigma \sum_{i=0}^{N} \sum_{k=1,2,\ldots} G(\mathbf{r},t|\mathbf{r_i},t_i^k). \tag{2.25}$$

2.1.2 Variability of the Signal through the Nucleus

To examine how the Ca^{2+} signal varies throughout the nucleus in this model, we simulated the generation and recovery phase for a single Ca^{2+} spike. At the nuclear surface ($r = R = 8$ μm), the concentration of Ca^{2+} is calculated at 1000 points, placed with approximately uniform spacing across the surface using a golden section spiral [163]. At all other radii, n points were similarly placed across the spherical shell of radius r, with n scaling according to the radius of the shell, $n = (1000 * r/R + 1)$. The average Ca^{2+} signal was calculated at each radial shell from these n points, and a volume average was calculated from the total of all points across all shells. Figure 2.3 shows an illustrative case for a single parameter set (see the figure legend for details). The majority of the signal variation occurs at the nuclear surface (Figure 2.3B), with the signal throughout the bulk volume, away from the surface, remaining fairly uniform (Figure 2.3A). Indeed, the volume average (that we might expect to measure with a calcium sensitive dye [164]) is very similar in shape and magnitude to the Ca^{2+} signal at the centre of the nucleus (Figures 2.3C&D). While the volume average shows the characteristic transient shape of a Ca^{2+} spike, the surface signal is substantially different. Proteins that respond to Ca^{2+} signals do not measure the volume average, only the local signal. Figure 2.3 illustrates how important the localisation of these detector proteins are, the Ca^{2+} signal at the centre of the nucleus is very different to that in a region close to one of the release sites.

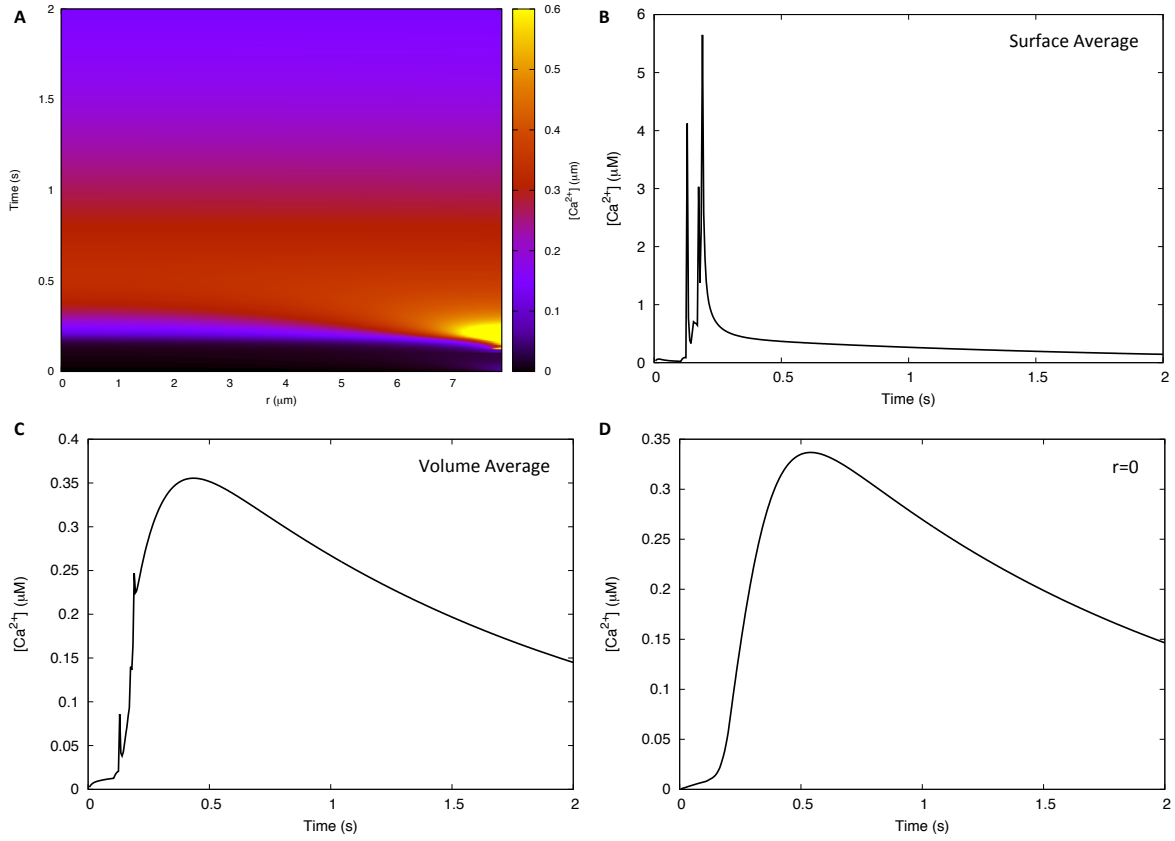

Figure 2.3: Variation of the Ca^{2+} spike in the 3D model. Generating a single spike in the 3D model. **(A)** For each radial shell at distance, r, from the centre, the average calcium concentration over that shell is calculated, and then plotted against time, t. **(B)** The average Ca^{2+} concentration measured across the nuclear surface, $r = 8\,\mu$m. **(C)** The Ca^{2+} concentration averaged over the entire volume of the nucleus. **(D)** The concentration measured at the centre of the nucleus, $r = 0\,\mu$m. Parameters: $D = 20\,\mu\text{m}^2\text{s}^{-1}$, $\sigma = 40 \times 10^{-21}$ mol and $k_s = 0.05\,\mu\text{ms}^{-1}$.

2.1.3 Microdomain Structure

The release sites are localised to the nuclear surface, so the high concentrations around individual release sites are likely to be dominating the surface average. To test this, I defined a circular area around each channel and removed any averaging points that fell within this area. The resulting peak amplitude and the number of points removed is plotted in Figure 2.4A. For small areas around the channel, there is a rapid drop in the maximum amplitude of the Ca^{2+} signal, for only a small number of removed averaging points. As the area increases, the number of points excluded likewise increases, but the rate at which the peak amplitude falls slows considerably, suggesting that the simulation signal is no longer varying substantially across the nuclear surface. In Figure 2.4B, we compare the average surface signal using the full calculation (as in the previous section; black) with the average signal when regions around each channel of area 0.28 μm^2 are ignored. Despite only corresponding to 8 averaging points

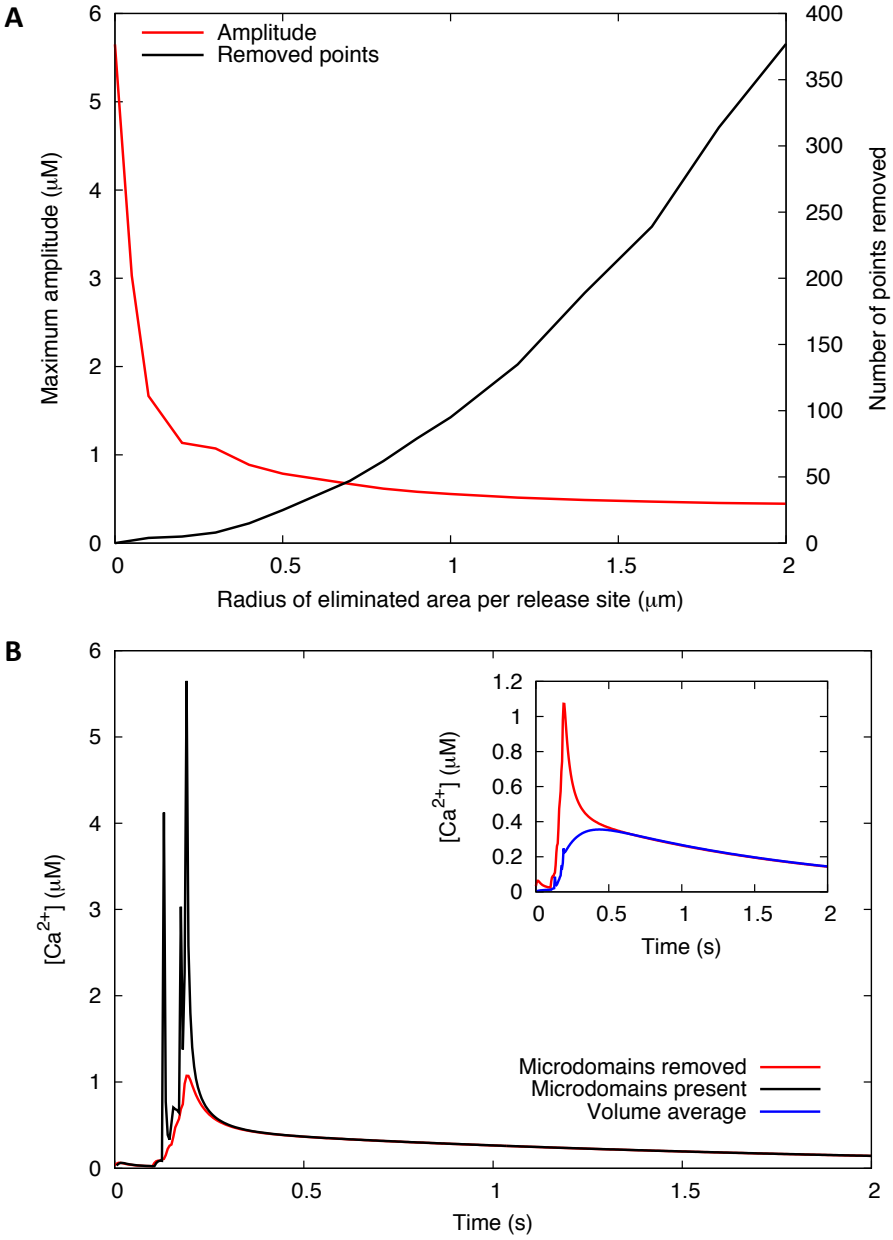

Figure 2.4: Ca^{2+} microdomains dominate the surface signal. (A) Eliminating a circular region around each channel from the calculation of the average calcium concentration removes an increasing number of points (black), and results in a decreasing peak amplitude (red). **(B)** Comparing the original average Ca^{2+} signal across the surface (black) with the signal when a region of size $0.28\,\mu\text{m}^2$ is ignored from the average calculation (red). The area eliminated contained 8 points, yet these are responsible for the large spikes in Ca^{2+} concentration observed. The inset compares this signal with the volume averaged signal (blue), as in Figure 2.3C. Parameters: $D = 20\,\mu\text{m}^2\text{s}^{-1}$, $\sigma = 40 \times 10^{-21}$ mol and $k_s = 0.05\,\mu\text{ms}^{-1}$.

(out of 1000) being excluded, the peak amplitude has dropped by a factor of 5 and the rough spiky nature of the trace has been reduced to a smoother transient. While similar to the volume average of Figure 2.3C (see inset of Figure 2.4B), the signal amplitude is on average substantially larger at the nuclear surface than throughout the volume. We conclude that microdomains exist around the firing sites whose contribution dominates the surface average. These small areas of high concentration are not representative of the behaviour across the surface.

The surface signal shows a much higher amplitude than the overall volume. These different signal strengths would be capable of activating proteins with different equilibrium dissociation constants, and has relevance for where the key symbiotic decoding protein, CCaMK, might be activated. CCaMK features 3 EF hands for binding Ca^{2+} as well as a calmodulin (CaM) binding domain, which itself has 4 Ca^{2+} binding sites [96]. The dissociation constants for Ca^{2+} of each of these proteins have been measured [165]. The highest for CCaMK itself is approximately $0.2\,\mu$M, suggesting it could bind calcium anywhere in the volume during spike generation. The CaM EF hands, however, have dissociation constants of $1\,\mu$M and $15\,\mu$M [165]. Assuming activation requires complete binding, our simulations here suggest CaM could only really be activated at the nuclear surface, perhaps even only near the Ca^{2+} channels themselves.

2.2 Simulating Ca^{2+} Signals at the Nuclear Surface

The 3D model is a powerful tool for simulating Ca^{2+} signalling within the nucleus. However, to study the influence of nuclear pores in a complex signal generation process like this, we also need to describe the spatial behaviour of Ca^{2+} outside the nucleus, which would necessitate the derivation of a second Green's function for the exterior volume. The 3D model has the distinct disadvantage of taking a long time to simulate the process without pores. Including the pores as discrete sources or sinks as we intend to (see Section 2.5), would be impractical. It would require an additional N_p evaluations of (2.20) every time step.

The key signalling elements responsible for generating the Ca^{2+} signal are all localised to the NE. Therefore, the use of a 2D model in which Ca^{2+} is restricted to moving across the surface of the nuclear membrane might allow us to study the signalling process in a more efficient way, and model the INM and ONM using the same mathematical framework. Following the same modelling approach as before (Section 2.1), the calcium concentration, $c(\mathbf{r}, t)$, on the surface of the nucleus evolves as

$$\frac{\partial c}{\partial t} = D\nabla^2 c - k_s c + \sigma \sum_{i=1}^{N} \sum_{k=1,2,\ldots} \delta(\mathbf{r} - \mathbf{r}_i)\delta(t - t_i^k), \tag{2.26}$$

for diffusion constant, D, uptake rate, k_s, and release strength, σ. There are N sources at position $\mathbf{r}_i$ releasing at times t_i^k, $k = 1, 2, \ldots$. Aside from its dimensionality, such a model contains all the same elements as the 3D model (Figure 2.2). Since the surface represents

the whole space here, the uptake by pumps is included as a global effect. The form of this diffusion equation again allows us to again derive an analytic solution using Green's method, as we shall do in the following subsection. In later sections we will demonstrate the relevance of this model to simulating the generation of Ca^{2+} signals in a 3 dimensional environment.

A note on concentrations used in this model: rather than treat the concentration as a true 2D concentration, for easier comparison we treat c as having units of μM by assuming the Ca^{2+} is confined to a thin spherical shell.

2.2.1 Deriving an Analytical Solution

This follows a similar process to the derivation of the Green's function for the 3D model in Section 2.1.1. On the surface of a sphere of radius, R, Green's function satisfies

$$\frac{\partial G}{\partial t} = D\nabla^2 G - k_s G + \frac{1}{R^2 \sin\theta'}\delta(\theta-\theta')\delta(t-t'), \tag{2.27a}$$

$$G(r,\theta,t|r',\theta',t') = 0, t < t' \tag{2.27b}$$

where, as before, we neglect the ϕ dependence for now, including it later via trigonometric properties [162]. After Laplace transform with respect to t, the governing equation of the transformed Green's function $\tilde{G}(\theta, s|\theta', t')$ is

$$s\tilde{G} = D\nabla^2\tilde{G} - k_s\tilde{G} + \frac{1}{R^2\sin\theta'}\delta(\theta-\theta')e^{-st'}. \tag{2.28}$$

The homogeneous problem

$$\frac{1}{R^2\sin\theta}\frac{\partial}{\partial\theta}\left[\sin\theta\frac{\partial\psi}{\partial\theta}\right] = -\frac{l(l+1)}{R^2}\psi, \tag{2.29}$$

is the well known Legendre differential equation, whose solution are the Legendre polynomials

$$\psi_l(\theta) = P_l(\cos\theta). \quad l = 0, 1, 2, \ldots \tag{2.30}$$

We then consider the ansatz (2.9),

$$\tilde{G}(\theta, s|\theta', t') = \sum_{l,p=0}^{\infty} \beta_l \psi_l(\theta), \tag{2.31}$$

which, upon substitution into (2.28), yields

$$s\sum_{l=0}^{\infty}\beta_l P_l(\cos\theta) = -D\sum_{l=0}^{\infty}\beta_l\frac{l(l+1)}{R^2}P_l(\cos\theta) - k_s\sum_{l=0}^{\infty}\beta_l P_l(\cos\theta) + \frac{1}{R^2\sin\theta'}\delta(\theta-\theta')e^{-st'}. \tag{2.32}$$

To determine the normalisation β_l, we again apply the integral operator

$$\vartheta_1 f : f \mapsto \int_{-1}^{+1} d\mu P_m(\mu) f(\mu) \tag{2.33}$$

to obtain

$$s\beta_m = -\beta_m \frac{l(l+1)}{R^2} D - k_s \beta_l + \frac{1}{R^2 \mathcal{N}(m)} P_l(\cos\theta') e^{-st'}, \tag{2.34}$$

where

$$\mathcal{N}(l) = \int_{-1}^{+1} d\mu P_l^2(\mu) = \frac{2}{2l+1}. \tag{2.35}$$

Using (2.34) to find β_l, we find the solution in Laplace space

$$\tilde{G}(\theta, s|\theta', t') = \sum_{l=0}^{\infty} \frac{1}{\mathcal{N}(l)(s + Dl(l+1)/R^2 + k_s)} P_l(\cos\theta') e^{-st'} P_l(\cos\theta). \tag{2.36}$$

This can be transformed back using the inverse Laplace transform and the residue theorem, since we have first order poles, $s+Dl(l+1)/R^2+k_s$ along the negative axis only. Reintroducing the ϕ dependence to consider multiple sources using (2.19) as before, we obtain the final form of the 2D Green's function,

$$G(\theta, \phi, t|\theta', \phi', t') = \sum_{l=0}^{\infty} \frac{P_l(\cos\Theta)}{2\pi R^2 \mathcal{N}(l)} e^{-l(l+1)D(t-t')/R^2 - k_s(t-t')}. \tag{2.37}$$

The corresponding concentration due to a set of sources at $\mathbf{r}_i$, $i = 1, \ldots, N$ firing at times t_i^k for the ith location is

$$c(\theta, \phi, t) = \sigma \sum_{i,k} \sum_{l=0}^{\infty} \frac{P_l(\cos\Theta)}{2\pi R^2 \mathcal{N}(l)} e^{-l(l+1)D(t-t_k^i)/R^2 - k_s(t-t_i^k)}, \tag{2.38}$$

with

$$\cos\Theta = \cos\theta\cos\theta_i + \sin\theta\sin\theta_i\cos(\phi - \phi_i). \tag{2.39}$$

2.3 The Surface Model Captures the Average Behaviour of the Volume Model

A model in which Ca^{2+} diffusion is restricted to the surface of nucleus neglects a number of properties of the full 3 dimensional nuclear system. In the volume model (Section 2.1), Ca^{2+} is free to diffuse away from the surface, raising the concentration throughout the volume (Figure 2.3). If we restrict Ca^{2+} to the surface, not only would the concentration profile be different, the reduced degrees of freedom would result in more rapid channel activation. The time taken to diffuse a distance, x, in a space of dimension, d,

$$t \sim \frac{\langle x^2 \rangle}{2Dd}, \tag{2.40}$$

shows that the time to activate a channel, if all other things are equal, is inversely proportional to the dimension. Within the enclosed space of the nucleus, this is further complicated by the existence of shorter paths through the volume between channels at different positions on the surface. There are more complicated effects that have been observed in systems, like ours,

in which release sites are localised to a surface of one dimension less than the full signalling space. Under these circumstances, Pando *et al.* [166] showed that the velocity of the wave can be independent of the diffusion constant, or even fail to propagate entirely when D is large enough. Since the surface model is so much more efficient for simulation, we investigated whether it might still be able to approximate the behaviour of a full 3D model.

As illustrated above, we would not expect using the same parameter values in the surface model would reproduce the behaviour of the 3D model, but a different parameter set might. If we required the time to diffuse a set distance in both models to be the same, (2.40) would suggest the diffusion constant in the 2D model, D_2, would be related to the diffusion constant in the 3D model, D_3, by

$$D_2 \sim \frac{3}{2} D_3. \tag{2.41}$$

The loss of Ca^{2+} from the surface into the bulk could be captured by an enhanced uptake rate, k_s, also potentially capturing the behaviour observed by Pando *et al.* [166], since uptake processes were neglected in their model. However, (2.41) doesn't take into account the geometry of the system, and so neglects the effect of shortcuts in the 3D model between neighbouring channels (which would mean different $\langle x^2 \rangle$ in the two models). We therefore took a numerical approach to find the best possible fit.

Since we wish to study simultaneous spike generation on either side of the nuclear envelope, the time taken for the concentration in the model to peak, a property we refer to as the spike width, is the most important property of the system to capture. At the resolution of typical experiments studying nuclear Ca^{2+} signalling (seconds), the overall Ca^{2+} spikes and not the individual channel releases are relevant. Using the firing time of the final channel in the nucleus as a convenient measure of the full spike width, we tested a wide range of parameters in the 2D model and compared them to an example 3D parameter set ($D = 20\,\mu\text{m}^2\text{s}^{-1}$, $\sigma = 40 \times 10^{-21}\,\text{mol}$ and $k_s = 0.05\,\mu\text{ms}^{-1}$, as used in Section 2.1). To avoid any artefacts from channel distribution we used a roughly uniform spacing between 24 channels in both models using the golden section method [163]. The 2D parameter sets that produce the same spike width are shown in Figure 2.5A. This shows a band of parameter space within which all the simulations produce the same width. As we would expect from the behaviour of the FDF model [111], decreasing the release strength, σ, shifts D to higher values. Likewise, increasing k_s requires we increase D and/or σ to maintain the same overall spike width.

We notice a number of gaps in the fitting region of Figure 2.5A. These arise due to the resolution with which we explored the D, k_s and σ parameters (only to a resolution of 10^0 in each). Exploring at a higher resolution in the 2D model would be expected to find a smooth surface in parameter space. We note that there is further a limit on this imposed by the discrete time step and the threshold nature of the firing condition. The time step will always introduce some finite error into the firing time of each channel, which is then multiplied by the number of channels activated in the generation of an overall spike.

Not all of these parameter sets will produce spikes that show the same kind of amplitude

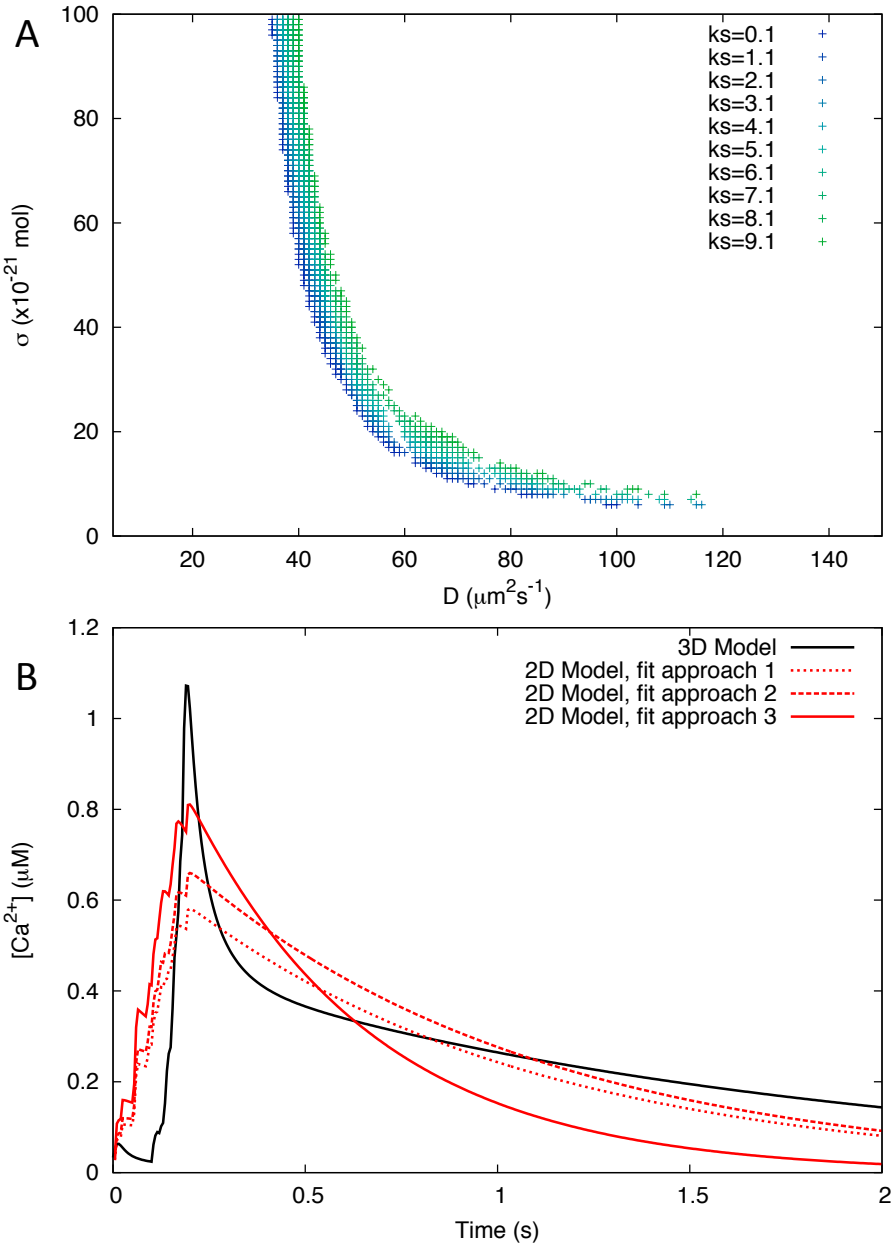

Figure 2.5: The 2D model can capture the behaviour of the 3D model. **(A)** 2D model parameter sets that result in the same spike width as the 3D model with parameters: $D = 20\,\mu\text{m}^2\text{s}^{-1}$, $\sigma = 40 \times 10^{-21}\,\text{mol}$ and $k_s = 0.05\,\mu\text{ms}^{-1}$. **(B)** Identifying 2D parameter sets (red) that are also a good fit to the full Ca^{2+} spike in the 3D model (black). The different 2D models correspond to the different fitting functions specified in the main text (2.43). Fit approach 1 (2.43a) $D = 47\,\mu\text{m}^2\text{s}^{-1}$, $\sigma = 22 \times 10^{-21}\,\text{mol}$ and $k_s = 1.1\,\text{s}^{-1}$. Fit approach 2 (2.43b) $D = 45\,\mu\text{m}^2\text{s}^{-1}$, $\sigma = 25 \times 10^{-21}\,\text{mol}$ and $k_s = 1.1\,\text{s}^{-1}$. Fit approach 3 (2.43c) $D = 42\,\mu\text{m}^2\text{s}^{-1}$, $\sigma = 34 \times 10^{-21}\,\text{mol}$ and $k_s = 2.1\,\text{s}^{-1}$.

behaviour as the 3D model. We took all the parameter sets in Figure 2.5A and compared their $[Ca^{2+}]$ v time curves to that of the 3D model. We had a number of options to consider when doing this. We could compare to the volume average (Figure 2.3C), the surface average (Figure 2.3B) or to the surface average without microdomains (Figure 2.4B). We chose to compare the 2D model to the surface average with microdomains removed because the microdomain contribution to the average 3D signal prevents a clear spike from being seen for easy comparison (Figure 2.4B), and the magnitude of this average is dominated by the very high concentrations around individual channels. The average containing these microdomains is therefore not a good representation of what is happening on the rest of the surface. We explore the ability for the 2D model to capture the microdomain behaviour in the following section.

Figure 2.5B shows some of the fits obtained. An important decision to make is the form of the error function to minimise, and Figure 2.5B illustrates that different fits are obtained for different error functions. We considered 3 similar functions based on the standard method of least squares regression [167], in which we aim to find the point at which the sum, S, of squared residuals

$$S = \sum_{i=1}^{N_R} r_i^2 \tag{2.42}$$

is minimum. We considered 3 different definitions for our residual,

$$r_i = (y_2 - y_3)_i \tag{2.43a}$$

$$r_i = \left(\frac{y_2 - y_3}{\sqrt{y_3}} \right)_i \tag{2.43b}$$

$$r_i = \left(\frac{y_2 - y_3}{y_3} \right)_i \tag{2.43c}$$

where y_2 and y_3 are the concentrations of Ca^{2+} at time step i of the 2D and 3D models, respectively. Residual (2.43a) corresponds to the standard least squares residual. Figure 2.5B shows that this standard residual provides a good fit to the overall curve, but the fit is biased by the long slow tail off in the 3D model. This shallower decay is due to the presence of Ca^{2+} in the bulk, that must first return to the surface to be taken up by pumps. Using residual (2.43c), we bias the fit around the peak, resulting in the fitting process choosing a parameter set with a stronger peak, but a worse fit to the decay slope than (2.43a).

We note that the firing times of individual channels are not the same in the two models. This can be seen most clearly in the early time behaviour of the two models in Figure 2.5B. The 3D model has a single release and then a delay before many channels fire in quick succession. The channels of the 2D model fire more regularly as the Ca^{2+} wave propagates around the surface. This is an effect of the bulk volume in the 3D model: Ca^{2+} diffuses into this bulk, but this contributes to channel activation at distant sites. It is an effect of the "shortcuts" available to Ca^{2+} diffusing through the bulk.

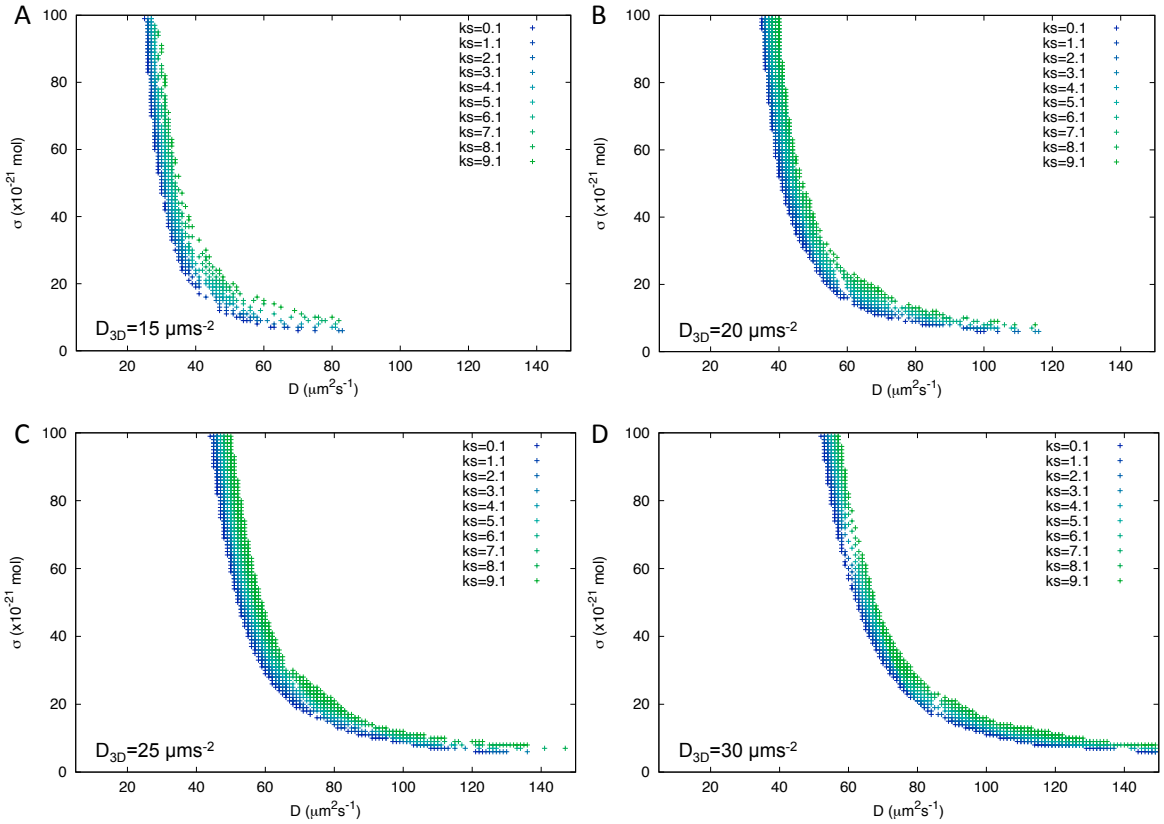

Figure 2.6: The 2D surface model is able to fit multiple 3D parameter sets. 2D model parameter sets that result in the same spike width as the 3D model. Increasing D in the 3D model shifts the 2D fits to higher D. **(A)** $D_{3D} = 15\,\mu\text{m}^2\text{s}^{-1}$, **(B)** $D_{3D} = 20\,\mu\text{m}^2\text{s}^{-1}$ as in Figure 2.5, **(C)** $D_{3D} = 25\,\mu\text{m}^2\text{s}^{-1}$, **(D)** $D_{3D} = 30\,\mu\text{m}^2\text{s}^{-1}$. Other 3D model parameters: $\sigma = 40 \times 10^{-21}$ mol and $k_s = 0.05\,\mu\text{ms}^{-1}$.

Figure 2.6 shows that we can find fits to the spike width for a range of D values in the 3D model. We consider 10 $\mu\text{m}^2\text{s}^{-1} \leq D \leq 30$ $\mu\text{m}^2\text{s}^{-1}$ in the 3D model as corresponding to the measured range of diffusion constants in the cytoplasm ($D = 5 - 20\,\mu\text{m}^2\text{s}^{-1}$ [168]) as well as some larger, to account for the observed higher rate of diffusion for Ca^{2+} in the nucleoplasm [139, 142]. We see from Figure 2.6 that increasing D in the 3D model shifts the fits within the 2D model to higher D values. Identifying the best fit to the full curve as in Figure 2.5B (for all definitions of the residual) allows us to examine how the 2D model varies in comparison to the 3D model, Figure 2.7. This shows that there is an approximately linear relationship between the diffusion constants in the two models. The slope of the fit is, for the most part, independent of which residual we use to obtain these fits (indicated by the different coloured lines). The shorthand estimate for the scaling (2.41) is an overestimate for the slope we observe in Figure 2.7, due to the effect of geometry and the values of the other parameters, σ and k_s. For the fits in Figure 2.7, the values of k_s in the 2D model are constant

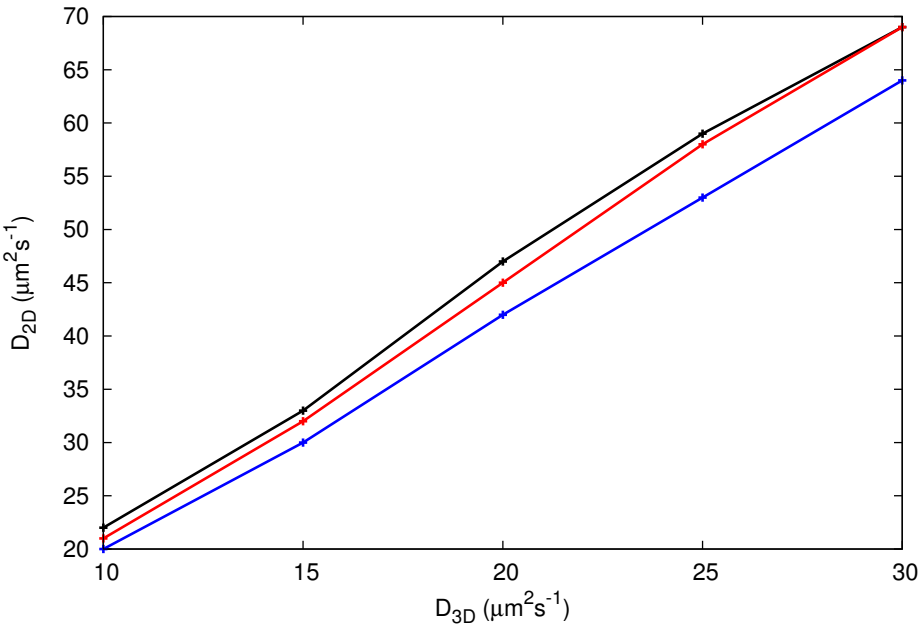

Figure 2.7: The 2D model and 3D model diffusion constants are linearly related. Plotting the diffusion constant in the 2D model, D_{2D}, for those parameter sets that fit the 3D model, for different values of the 3D diffusion constant, D_{3D}. Repeated for each of the fitting approaches (2.43): black line (2.43a), red line (2.43b), blue line (2.43c). Other 3D model parameters: $\sigma = 40 \times 10^{-21}$ mol and $k_s = 0.05\,\mu\text{ms}^{-1}$.

within each line, while the value of σ varies over a range of $5 - 10\%$ within each line, a much smaller degree of variation than with D.

We conclude that using a surface-restricted model we are able to capture the average behaviour of the full 3 dimensional Ca^{2+} signalling process on the INM. We have further been able to relate the diffusion constant within the 2D model to the diffusion constant within the bulk nucleoplasm, which will be of value when we study the impact of nuclear pores on Ca^{2+} signalling (see Section 2.6). This work allows us to greatly enhance the computational efficiency of the simulations.

2.4 Microdomain Structure can be Captured in the Surface Model

We have found parameters for the surface model that are able to capture the average behaviour of Ca^{2+} spiking on the INM, but to do this we purposefully neglected the contribution to the 3D model signal from microdomains around the channels. As we have seen (Figure 2.4) the microdomains make a significant contribution to the overall signal at the surface. We therefore ask how well the 2D model is able to capture the behaviour of these microdomains.

To do this, we look at the profile produced by a single channel release within the 3D

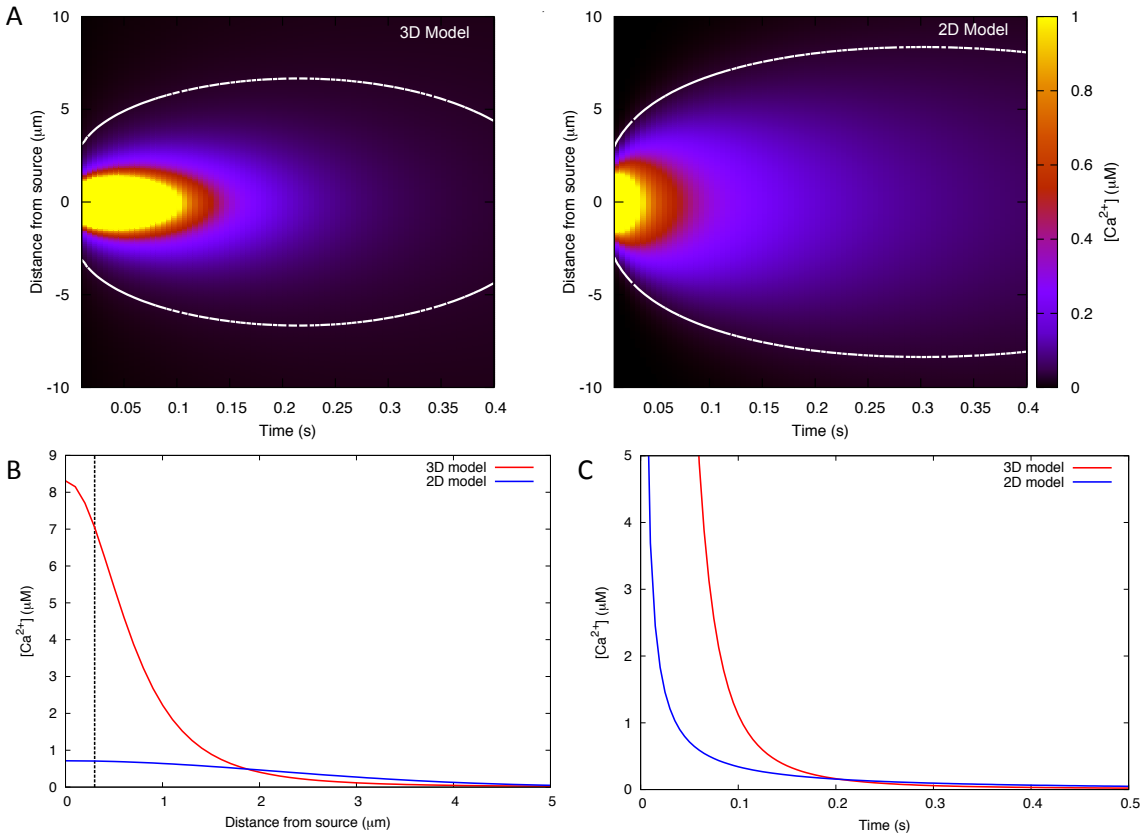

Figure 2.8: The best fit to the average signal does not reproduce the channel microdomain. We simulated the Ca^{2+} profile generated by a single Ca^{2+} channel release. **(A)** The Ca^{2+} profile in space and time in the 3D (left) and 2D (right) models. Distance from source along INM surface calculated as $R\Theta$, where Θ is the angle between source and measurement point, as in (2.19). We note that the spatial profile across the surface is circularly symmetric. The white line indicates the position at which $[Ca^{2+}]= c_{\text{th}}$, the threshold for channel activation. **(B)** Spatial profiles at a single time step, $t = 0.05\,\text{s}$. Dashed line indicates the size of the microdomain (within $0.3\,\mu\text{m}$ of the channel). **(C)** Variation of Ca^{2+} at the channel ($\Theta = 0$) with time, t. 2D model (blue line) parameters: $D = 47\,\mu\text{m}^2\text{s}^{-1}$, $\sigma = 22 \times 10^{-21}\,\text{mol}$ and $k_s = 1.1\,\text{s}^{-1}$. 3D model (red line) parameters: $D = 20\,\mu\text{m}^2\text{s}^{-1}$, $\sigma = 40 \times 10^{-21}\,\text{mol}$ and $k_s = 0.05\,\mu\text{ms}^{-1}$.

model. We use our usual illustrative parameter set within the 3D model, $D = 20\,\mu\text{m}^2\text{s}^{-1}$, $\sigma = 40 \times 10^{-21}\,\text{mol}$ and $k_s = 0.05\,\text{s}^{-1}$, for all work in this section. In Figure 2.8, we compare this with a single channel profile from a 2D parameter set that fit the average signalling profile in Figure 2.5B. It is clear from Figure 2.8 that this parameter set fails to capture the amplitude (Figure 2.8B) and the persistence (Figure 2.8C) of the 3D model microdomain. The overall shape of the peak in the 2D model profile (Figure 2.8A, yellow region) is also different. The white contour in Figure 2.8A corresponds to the position at which the Ca^{2+} concentration is equal to the Ca^{2+} threshold required to activate channels. This contour is broader in the 2D

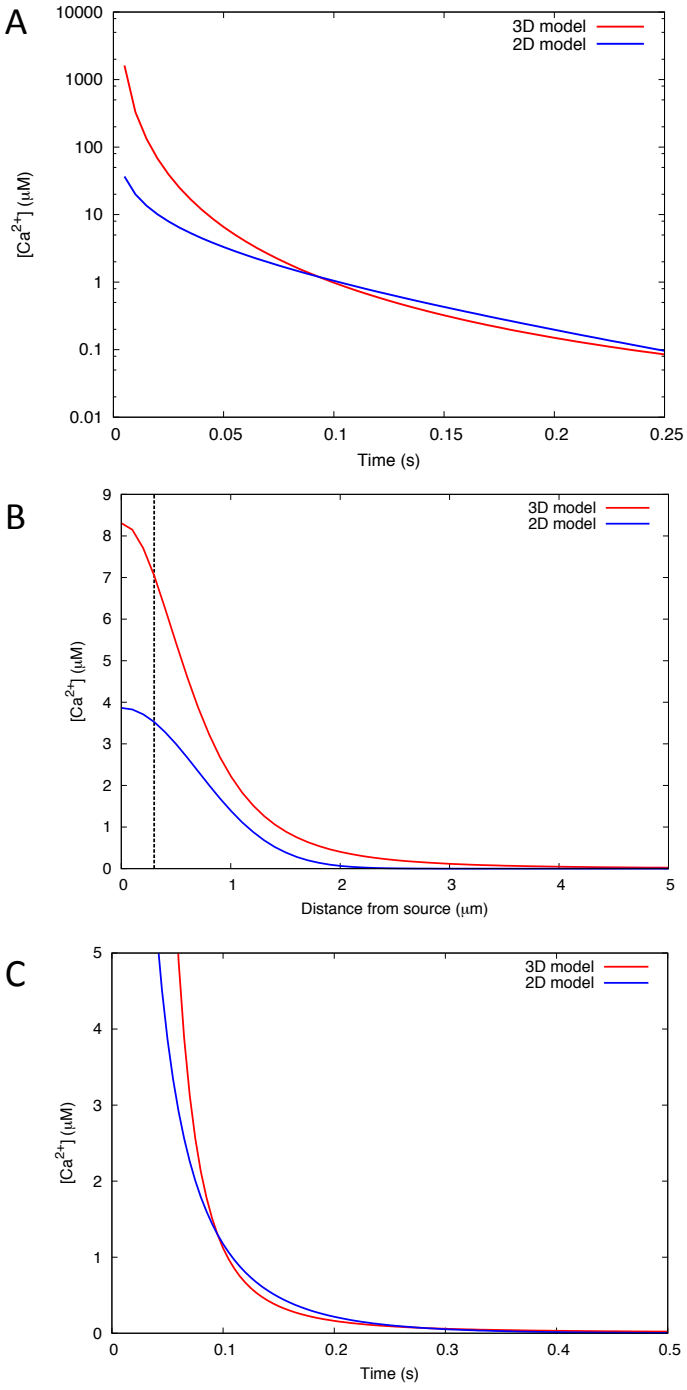

Figure 2.9: The surface model can produce a good fit to the microdomain structure of the 3D model. Structure of the 2D model microdomain, from parameters fitted to the average microdomain concentration. **(A)** Average Ca^{2+} concentration across the microdomain (defined as within $0.3\,\mu$m of the channel). **(B)** Spatial profiles at a single time step, $t = 0.05\,$s. Dashed line indicates the size of the microdomain **(C)** Variation of Ca^{2+} at the channel ($\Theta = 0$) with time. 2D model (blue line) parameters: $D = 5\,\mu\text{m}^2\text{s}^{-1}$, $\sigma = 20 \times 10^{-21}\,$mol and $k_s = 10\,\text{s}^{-1}$. 3D model (red line) parameters: $D = 20\,\mu\text{m}^2\text{s}^{-1}$, $\sigma = 40 \times 10^{-21}\,$mol and $k_s = 0.05\,\mu\text{ms}^{-1}$.

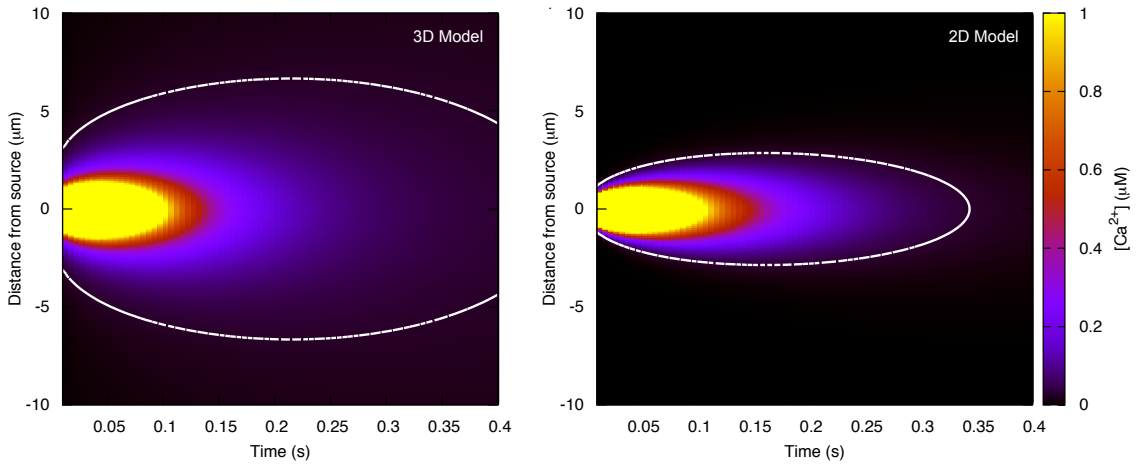

Figure 2.10: The 2D model can fit either the microdomain or the averaged signal. Comparison of the spatio-temporal profile of the single channel release in the 3D (left) and 2D (right) models. Distance from source along INM surface calculated as $R\Theta$, where Θ is the angle between source and measurement point, as in (2.19). We note that the spatial profile across the surface is circularly symmetric. The white line indicates the position at which $[Ca^{2+}]= c_{\text{th}}$, the threshold for channel activation. The spatial extent of the 2D model is significantly restricted in comparison to the 3D model, resulting in the failure of this parameter set to propagate a signal in a full simulation. 2D model parameters: $D = 5\,\mu\text{m}^2\text{s}^{-1}$, $\sigma = 20 \times 10^{-21}\,\text{mol}$ and $k_s = 10\,\text{s}^{-1}$. 3D model parameters: $D = 20\,\mu\text{m}^2\text{s}^{-1}$, $\sigma = 40 \times 10^{-21}\,\text{mol}$ and $k_s = 0.05\,\mu\text{ms}^{-1}$.

model than in the 3D model, which gives rise to the difference in individual channel firings in the two models, as discussed in the previous section.

To find whether the 2D model can describe the microdomain structure, we sampled a large range parameters in the 2D model and scored their fit to the full 3D simulation using (2.42) and (2.43a). To provide an easy to use comparison that contained information on both the spatial and temporal evolution of the signal, we calculated the average concentration across the microdomain, defined as the region within $0.3\,\mu\text{m}$ of the channel, and used this as the basis of our fitting function; y_3 and y_2 in (2.43a). None of the parameters were able to produce a perfect fit. One of the best is illustrated in Figure 2.9. This fits the microdomain average well after $t = 0.05\,\text{s}$, but fails to reach the full amplitude seen in the 3D model. From the spatial profile (Figure 2.9B) and on source behaviour (Figure 2.9C) plots, we see that this parameter set is able to produce a much better fit to the microdomain than the previous parameter set (Figure 2.8). The full spatial extent of this channel release is, however, strongly restricted outside of the microdomain (Figure 2.10). This parameter set fails to propagate a wave in a full simulation (see also, Figure 2.13). Producing a better fit to the microdomain compromises the capacity for the 2D model to fit the full Ca^{2+} signalling process.

Using much larger values for the release strength, σ, and correspondingly large values for the uptake rate, k_s, can result in closer fits to the high amplitude, early microdomain signal,

yet this comes at the price of poor fits at other time periods. We cannot get a good fit to the behaviour of the microdomain at all times, but we have been able to capture some of its features. These parameters are not then able to correctly fit the average behaviour across the surface. This, combined with the work of the previous section, demonstrates that it is possible to use the 2D model to describe the behaviour of a 3D signalling process in terms of either the average behaviour at the surface, or the microdomain structure, but not both simultaneously.

2.5 Incorporating Nuclear Pores into the 2D model

During symbiosis signalling, Ca^{2+} oscillations are observed in the nucleus and the peri-nuclear cytoplasm [35, 62]. Individual spikes are generated simultaneously on both sides of the NE [62], Figure 2.1. Since the number of Ca^{2+} spikes [80] and their frequency [96] are key to the activation of decoding proteins present in the nucleoplasm [96], or brought in from the cytoplasm [114], this coordination could have physiological importance. Three mutants in nucleoporin proteins NUP85, NUP133 and NENA in the model legume *Lotus japonicus* are deficient in Ca^{2+} spiking, highlighting the possible important role the NPC has in Ca^{2+} signal generation. We therefore used our diffusion models to study the influence of pores on nuclear calcium signalling. We assume that the NPC is permeable to Ca^{2+}, but see the discussion (Section 2.7) for more on this.

We model pores as additional point sources [62]. Typically, pores have a diameter, p_d, of approximately 9 nm, but can dilate to a maximum width of 39 nm in order to allow for movement of larger proteins. Even at this maximum extension, they are orders of magnitude smaller than the distances between channels. Any perturbation due to their finite size will be on a spatial scale much less than we are interested in. Each of these pores therefore adds a source term to the diffusion equation (2.27)

$$\sum_{j=1}^{N_p} \Omega_j(t)\delta(\mathbf{r}-\mathbf{r}_j), \tag{2.44}$$

for N_p pores at positions $\mathbf{r}_j$ for $j = 1, \ldots, N_p$, each of which has a flux through them of $\Omega_j(t)$. The pores are considered to be either closed, in which case $\Omega_j(t) = 0$, or open.

To compute how much calcium crosses through each open pore, we denote $c_o(\mathbf{r}, t)$ and $c_i(\mathbf{r}, t)$ to be the calcium concentrations on the outer and inner sides of the nuclear envelope, respectively, and use Fick's law of diffusion. At each time step we approximate the gradient across each pore by a simple difference formula, giving a flux

$$\Phi(\mathbf{r}_j, t) = -(c_o(\mathbf{r}_j, t) - c_i(\mathbf{r}_j, t))D/\Delta m \tag{2.45}$$

for membrane thickness, $\Delta m = 0.01\,\mu$m. If the concentration is larger on the exterior, $c_o > c_i$, then $\Phi < 0$ and calcium leaves the exterior through the pore. For a time step of size Δt, we

say a pulse of size

$$\Omega = |\Phi(\mathbf{r}_j, t)|(p_d/2)^2\pi\Delta t, \tag{2.46}$$

enters the nucleus when $\Phi < 0$, or a pulse of the same size exits the nucleus if $\Phi > 0$. Since the pores are open pathways between the two surfaces, the flux $\Phi(\mathbf{r}_j, t)$ through each pore must be evaluated at every time step, and we therefore have a source term from every pore for every time step that we evaluate the model. Thanks to the action of the pumps, the effect of an individual release within the model is only felt for a period of time, τ_p, after which we can ignore that release during the simulations, as discussed in Section 2.1. For all simulations with pores, even a moderate N_p substantially increases simulation time.

2.5.1 Simplified model and simulation speed

To further improve the efficiency of our algorithm, we ignore the higher order terms in the summation over the Legendre polynomials, l (2.39). It is likely that the dynamics of diffusing calcium on the nuclear surface are such that the dominant contribution from a single source at some point of interest (another channel, say) will be due to calcium that has performed less than one journey around the surface. That is, although strictly speaking the sphere has periodic boundary conditions, on the time scales of interest, and over the range of parameters we are using, diffusion is not sufficient to allow the periodicity to have an observable effect. It might be reasonable to treat the surface as being without a boundary. On the surface of a sphere then, we believe the concentration due to sources at $\mathbf{r}_i$ for $i = 1, \ldots, N$ firing at times t_i^k at the ith location to be well approximated by the free space solution

$$c(\mathbf{r}_j, t) = \sigma \sum_{i,k} \frac{1}{4\pi D(t - t_i^k)} \exp(-\Delta\mathbf{r}_{ij}^2/4D(t - t_i^k) - k_s(t - t_i^k)), \tag{2.47}$$

where $\Delta\mathbf{r}_{ij}$ is the length of the great arc connecting the points $\mathbf{r}_i$ and $\mathbf{r}_j$ on the surface of the nucleus,

$$\Delta\mathbf{r}_{ij} = R\cos^{-1}(\cos\Theta), \tag{2.48}$$

in accordance with (2.39). In the long time limit, this gives a vanishing calcium concentration regardless of whether an uptake rate, k_s, is included, but since we always consider pumps to be present this will not become an issue. In Figure 2.11A we compare (2.47) with the full 2D solution (2.38) by calculating the calcium profile for a single point source at $\phi = 0$, for a number of time points. This clearly shows that any difference between the full solution (2.38; points) and the approximate solution (2.47; lines) is small. Figure 2.11B calculates the ratio of the full solution to the approximate solution at the source, where the error is largest, for a variety of diffusion constants. While the relative error grows with time, and grows faster with larger diffusion constants, the absolute amplitude falls even faster, preventing this effect from becoming an issue during simulations. The timescale over which these relative errors grow large is greater than the timescales of signal generation that we will be studying here.

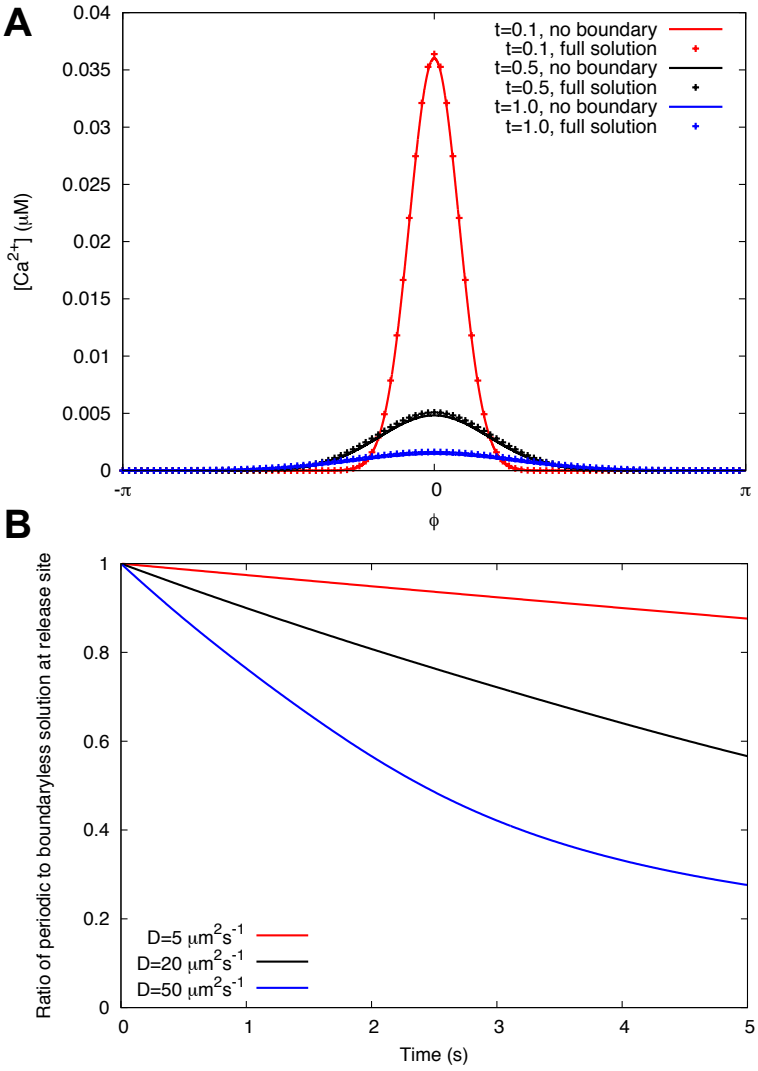

Figure 2.11: Boundary free solution provides a good fit to full periodic solution. Comparing the full periodic solution to the 2D diffusion equation on a spherical surface (2.38) with the free space solution in 2D (2.47). **(A)** Ca^{2+} profiles in cross section ($\theta = \pi/2$). A single channel at $\phi = 0$ releases Ca^{2+} at $t = 0$ and the concentration of Ca^{2+} is calculated at points around the equator of the sphere at different times, $t = 0.1\,\mathrm{s}$ (red), $t = 0.5\,\mathrm{s}$ (black) and $t = 1.0\,\mathrm{s}$ (blue). Lines show the boundary free solution, points are for the periodic solution. Parameters $D = 20\ \mu\mathrm{m}^2\mathrm{s}^{-1}$, $k_s = 1.0\ \mathrm{s}^{-1}$, $\sigma = 1 \times 10^{-21}$ mol. **(B)** Relative on peak ($\phi = 0$) amplitude in the periodic compared to the boundary free solution against time, and for different diffusion constants. While there can be a large relative shift in amplitude between the two models, the absolute amplitude in both models at these times is very small, as illustrated in (A).

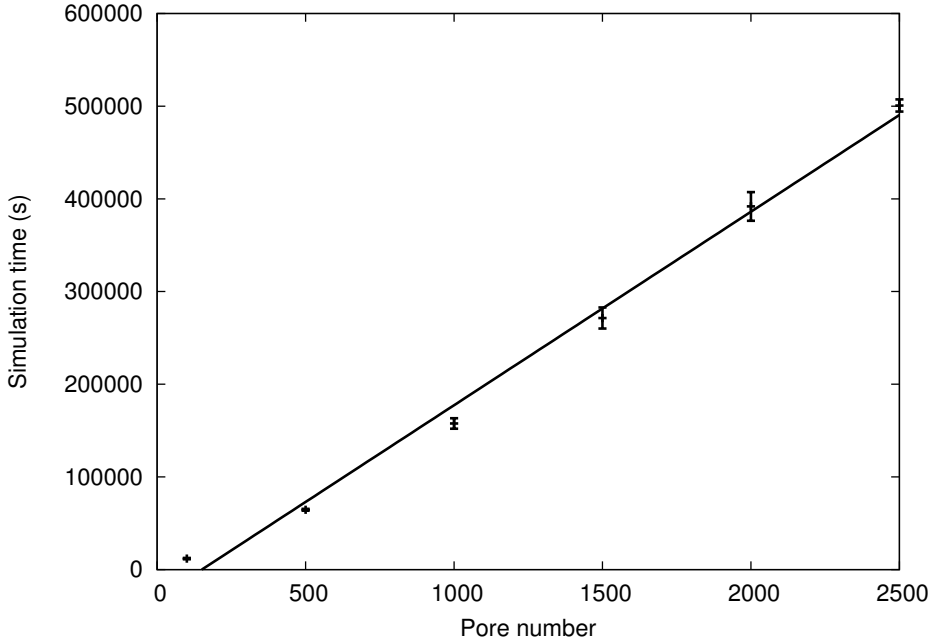

Figure 2.12: The increase in simulation time with pore number. Using the simplified model (2.47), we ran simulations with 24 Ca^{2+} channels on the INM and the relevant number of pores, for 1 s of simulated time. Each point represents an average of 10 different pore distributions, with the standard deviation of those measurements shown. A linear fit was performed using Gnuplot.

Using this simplified model, the pores contribute an additional term,

$$c_{pore}(\mathbf{r}_j, t) = \sum_{i,k} \frac{\Omega_i}{4\pi D(t - t_i^k)} \exp(-\Delta \mathbf{r}_{ij}^2 / 4D(t - t_i^k) - k_s(t - t_i^k)), \tag{2.49}$$

to the evaluation of each concentration via (2.47), where the sum over k is now over every time step since the pores are continuously mediating the passage of Ca^{2+} within our model. Ω_i is as defined in (2.46).

This approximate solution offers at least a 4-fold improvement in the speed of simulation over the full 2D simulation, tested in a system without pores. To see how important of an effect this is, we demonstrate how the simulation time of this algorithm varies for different numbers of pores in Figure 2.12. Each point represents the average time over 10 repeats to account for different, random, distributions of the pores, for 1 s of simulated time (corresponding to 500 time steps). We observe a linear increase in simulation time with pore number. Even at small pore numbers, the simulation can take several hours in this simplified model. The simulation time is expected to grow on the order of N_p^2 with time simulated, up until τ_p, limiting our ability to simulate large time periods within this model.

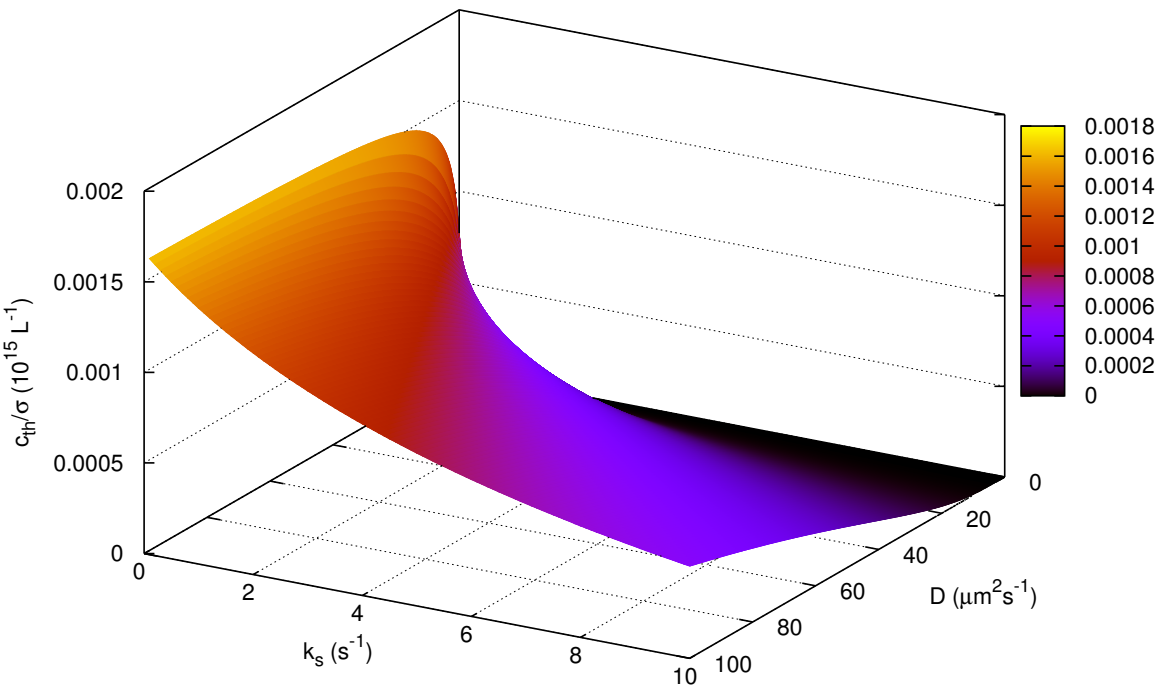

Figure 2.13: Threshold for wave propagation in the 2D model. For any D or k_s, if the ratio of the threshold to the firing strength is above the pictured surface, then a travelling wave will not propagate across the entire surface. Conversely if below the surface, a single release event is guaranteed to initiate a wave that activates every other channel. $\bar{\mathbf{r}} = 5.65\,\mu$m corresponding to 24 equally spaced channels on a sphere of radius $8\,\mu$m.

2.5.2 Threshold Criteria

Within this model, a global spike in which all channels on the nuclear surface release Ca^{2+} can be generated by causing a single channel to open. From that first release, Ca^{2+} will diffuse across the surface of the nucleus. When the concentration of Ca^{2+} builds above the firing threshold, c_{th}, at a release site, that channel will also fire, making it's contribution to the global spike. A global spike is therefore formed by a wave of Ca^{2+} propagating throughout the nucleus.

The ability for the nucleus to propagate a Ca^{2+} wave depends upon the signalling capacity of the nucleus. Too many buffers present in the nucleoplasm, or channel releases that are too weak (due to a nuclear envelope and ER that are depleted of Ca^{2+}, perhaps) may result in a wave that initiates, but is unable to propagate. A single channel or group of channels may fire, but a global spike is not observed.

Within our simplified model, the conditions for propagation can be easily determined. If

propagation occurs there is a time t at which

$$c(\bar{\mathbf{r}}, t) = c_{\text{th}}, \tag{2.50}$$

where $\bar{\mathbf{r}} = \max_i \{\min_{j\neq i} \Delta\mathbf{r}_{ij}\}$, with $\Delta\mathbf{r}_{ij}$ as in (2.48) is the largest separation of nearest neighbour channels. When calcium is released from a channel it spreads with circular symmetry away from the point of release. The distance from the channel at which the concentration is equal to c_{th} grows as a ring across the surface, then contracts back to the release site (illustrated in one dimension in Figures 2.8A and 2.10). This means there is a maximum distance r_{max} beyond which a release cannot activate a channel. The limiting case of propagation failure occurs when this $r_{max} = \bar{\mathbf{r}}$. By differentiating the condition (2.50) with respect to time, we can show that this occurs at time

$$t = -\frac{1}{2k_s} + \frac{1}{2k_s}\sqrt{1 + \bar{\mathbf{r}}^2 k_s/D} = \frac{1}{2k_s}\beta. \tag{2.51}$$

Hence the condition for the critical surface for propagation in terms of our model parameters is

$$\frac{c_{\text{th}}}{\sigma} = \frac{k_s}{2\pi D\beta} \exp\left[-\frac{\bar{\mathbf{r}}^2 k_s}{2D\beta} - \frac{1}{2}\beta\right]. \tag{2.52}$$

A graphical representation of the parameter choices for which travelling wave solutions exist appears in Figure 2.13. We considered 24 evenly spaced channels on a nucleus with a radius of 8 μm, which results in a $\bar{\mathbf{r}} \approx 5.65\,\mu$m. This value is consistent with the value of $\bar{\mathbf{r}} \approx 5.5\,\mu$m seen in oocytes [160].

2.6 The role of NPCs in nuclear calcium signalling

2.6.1 Signal Saturation and membrane transparency

If NPCs allow passage of Ca^{2+}, they will have an effect on the generation of Ca^{2+} signals in the nucleus. Different species and cellular stages can have different pore numbers and distributions [169, 170, 171, 172, 173, 174, 175], with pore densities varying between 1 and 60 pores/μm^2 [142]. To study how much Ca^{2+} is transmitted across the NE, we asked how much Ca^{2+} spreads across the NE from a single release for different pore densities, Figure 2.14. We place one channel on the INM which releases an amount of Ca^{2+}, σ, at time $t = 0$. We measure the maximum concentration of Ca^{2+} reached at a point on the ONM, relative to this release amount. This measurement point is placed at a greater distance from the channel, measured as the arc length, $R\Theta$, with Θ as defined in (2.19), than the size of the microdomain around that channel.

We observe in Figure 2.14 that Ca^{2+} transmission increases with pore density before saturating at relatively low pore densities. The addition of pores does not increase the transmission further. For $D = 20\,\mu\text{m}^2\text{s}^{-1}$ (red line) this density is around 4 pores/μm^2, or around 3000 pores in our model nucleus. To understand the meaning of this saturation, we asked what would happen if our measurement point was instead on the same side as the channel.

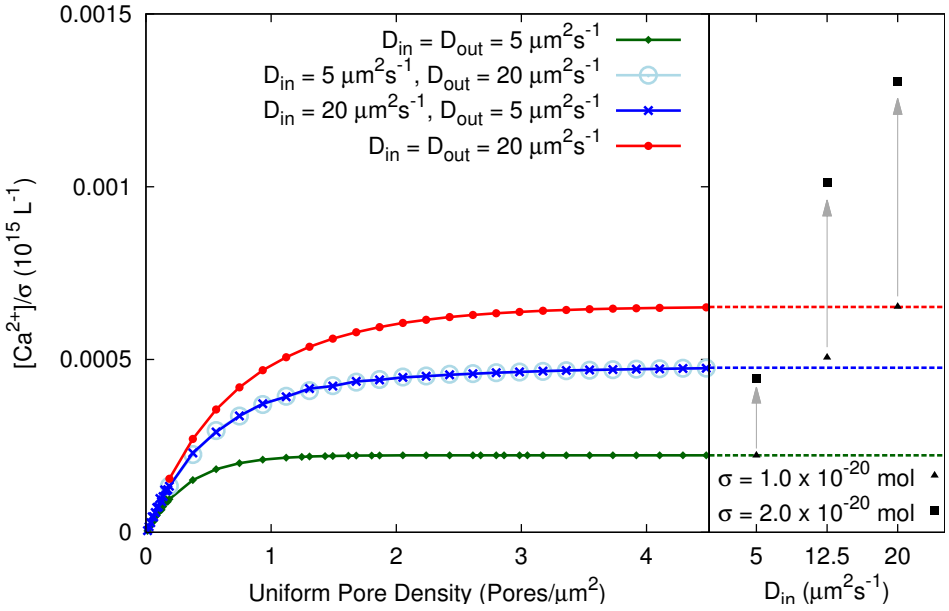

Figure 2.14: Transmission of Ca^{2+} through NPCs increases with pore number, and then saturates. Left panel: maximum Ca^{2+} concentration measured at a reference point on the ONM, in response to single channel release on the INM, relative to the Ca^{2+} release strength, $\sigma = 2.0\times10^{-20}$ mol. The pores are distributed evenly across the surface. In general, a larger transmission is achieved for a larger number of pores. For the numbers and positions of pores represented, larger diffusion constants lead to larger transmissions. Right panel: maximum Ca^{2+} transmission measured at a point at the same distance from the channel on the INM, in a nucleus without pores, for the σ values as labelled. *This data was produced by Teresa Vaz Martins, a Post Doc in my lab. The data was interpreted jointly by myself and Teresa.*

On the right hand panel of Figure 2.14, we consider the situation without pores, and with an equivalent measurement point on the same side as the channel, for 3 different diffusion constants, D_{in}. When $\sigma = 1.0 \times 10^{-20}$ mol (triangular points), the maximum concentration measured is the same value as measured at saturation pore densities on the left hand panel of Figure 2.14, when the measurement point is on the opposite side of the ONM. The dashed lines illustrate this point. When $\sigma = 2.0\times10^{-20}$ mol (square points), the measured concentration is, as we would expect, twice the concentration as before (grey arrows). However, the simulations showing saturation with pore density (left hand panel of Figure 2.14) were performed with $\sigma = 2.0\times10^{-20}$ mol. Thus, at saturation pore densities, half the Ca^{2+} that would have reached a point on the same side as the channel has passed on to the other side of the NE. This is equivalent to comparing diffusion in a half-space with that of a full space, without a barrier. It confirms that as far as diffusing Ca^{2+} is concerned, beyond a certain pore density the NE provides no barrier to passage of Ca^{2+} between the two sides. We refer to this as the NE becoming transparent.

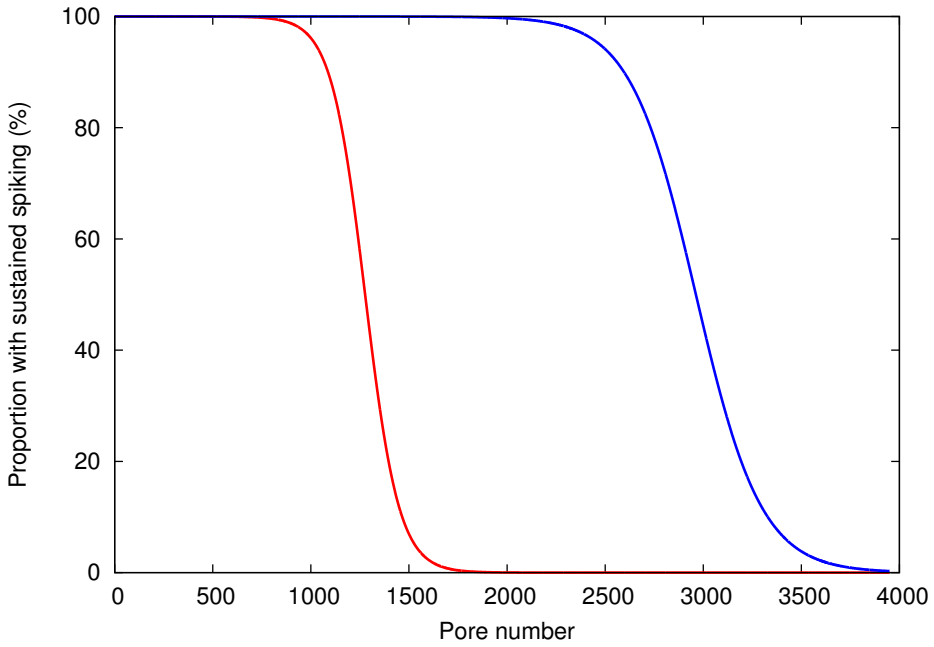

Figure 2.15: Diffusion through nuclear pores across the NE can kill Ca^{2+} spiking. The proportion of 50 simulations in which a full Ca^{2+} spike is generated for different numbers of pores. 24 equally spaced Ca^{2+} channels are placed on the INM, and pores are placed randomly, with a uniform distribution. No channels are placed on the ONM. Parameters: $k_s = 2.5\,s^{-1}$, $\sigma = 85.1 \times 10^{-21}$ mol, $c_{th} = 0.1\,\mu M$, $\alpha = 0.642$, and (red curve) $D = 15\,\mu m^2 s^{-1}$, (blue curve) $D = 20\,\mu m^2 s^{-1}$.

Slower diffusion hinders propagation over long distances by giving pumps time to take significant amounts of Ca^{2+} back into the NE. This limits the maximum amount of Ca^{2+} that can be transmitted for a smaller diffusion constant, D. However, when the NE becomes transparent, the two surfaces combine their Ca^{2+} propagation abilities to behave as a single surface with an intermediate diffusion constant for Ca^{2+}. This can be seen in Figure 2.14 by comparing the transmission between surfaces for $D = 5$ and $20\,\mu m^2 s^{-1}$ (blue lines), with the transmission on a single surface with $D = 12.5\,\mu m^2 s^{-1}$.

Transparency of the NE means that when transmitting Ca^{2+} over distances larger than the calcium microdomain, such as the distance between neighbouring channels, larger release strengths are required than if the nuclear membranes were isolated. The pore density at which transparency occurs, although increasing with D, is considerably less than the 50 pores/μm^2 observed in Tobacco nuclei, for example. This has implications on the capacity of the nucleus in different systems to generate their own Ca^{2+} oscillations.

2.6.2 Diffusion through pores can prevent nuclear Ca^{2+} signalling

Transparency of the NE means that Ca^{2+} has a significantly greater volume to diffuse into than just the nucleoplasm, and this will have an effect on the systems ability to generate Ca^{2+} spikes. Even in our 2D model, the total space has effectively doubled, and Ca^{2+} moving

to the other surface is not contributing to the activation of neighbouring channels. We would expect that increasing the number of pores would eventually cause Ca^{2+} signalling to fail (in a similar way to Figure 2.13).

We place a realistic number of channels (24) on one side of the NE [160] and initiate the system by triggering one of these channels to fire. We include a varying number of pores placed randomly across the nuclear surface with a uniform distribution. For certain parameter sets, the presence of too many pores can kill nuclear Ca^{2+} oscillations (Figure 2.15). Increasing D within these simulations shifts the curve to higher pore numbers, but this is always for fewer pores than those observed in tobacco nuclei (50 NPCs μm^{-2}) [176]. In the model legume *Lotus japonicus*, the pore density is substantially lower (1-2 NPCs μm^{-2}) [177]. For our model nucleus with a radius of 8 μm, this gives roughly 1000 NPCs across the NE and the termination of spiking by this effect will not be an issue.

This also places the symbiosis signalling system below the point at which the nucleus becomes transparent, for $D \geq 20\,\mu m^2 s^{-1}$. Interestingly, the half max activity curve for $D = 20\,\mu m^2 s^{-1}$ in Figure 2.15 corresponds to a density of around $3.5\,\text{pores}/\mu m^2$, around the saturation point for transmission in Figure 2.14. This, however, is a coincidence, as the position of the decay curves in Figure 2.15 also depends upon the values of k_s and σ. Since transmission through the pores reaches a saturation point, for sufficiently high D and σ, Ca^{2+} signalling will likely occur for any number of pores.

2.6.3 Diffusion through pores can enable coordination of signals across NE

The number of pores in *Lotus japonicus* means that nuclear Ca^{2+} signals could be generated despite the presence of pores. During legume symbiosis, there are also Ca^{2+} signals observed in the perinuclear cytoplasm (Figure 2.1). If we only have Ca^{2+} channels on the INM, Figure 2.16A shows that the overall concentration on the ONM is increased by a mere $0.05\,\mu$M, by diffusion through the NPCs, much less than the corresponding changes seen on the INM. This was for the realistic case of 1000 pores [177]. The INM signal does not mimic spiking behaviour. Even if we increase the number of pores by a factor of 4, going well beyond the experimentally observed density in this system, the INM still fails to produce spiking behaviour (Figure 2.16B).

If we add an equal number of channels to the ONM, but still initiate by releasing Ca^{2+} through a single channel on one side, the signalling in each compartment is now almost perfectly coordinated (Figure 2.16C). The channel positions are generated by the same method as the INM channels, but are shifted relative to the INM channels so that they are not directly opposite each other across the NE. This confirms earlier work that Ca^{2+} oscillations on both sides of the NE requires Ca^{2+} channels on both nuclear membranes [62]. We note that this result is independent of which side the initial release occurs (see Figure 2.20).

The two signalling compartments are identical in the analysis of Figure 2.16C. Despite this, the signalling process in the two compartments is different. Diffusion of Ca^{2+} through

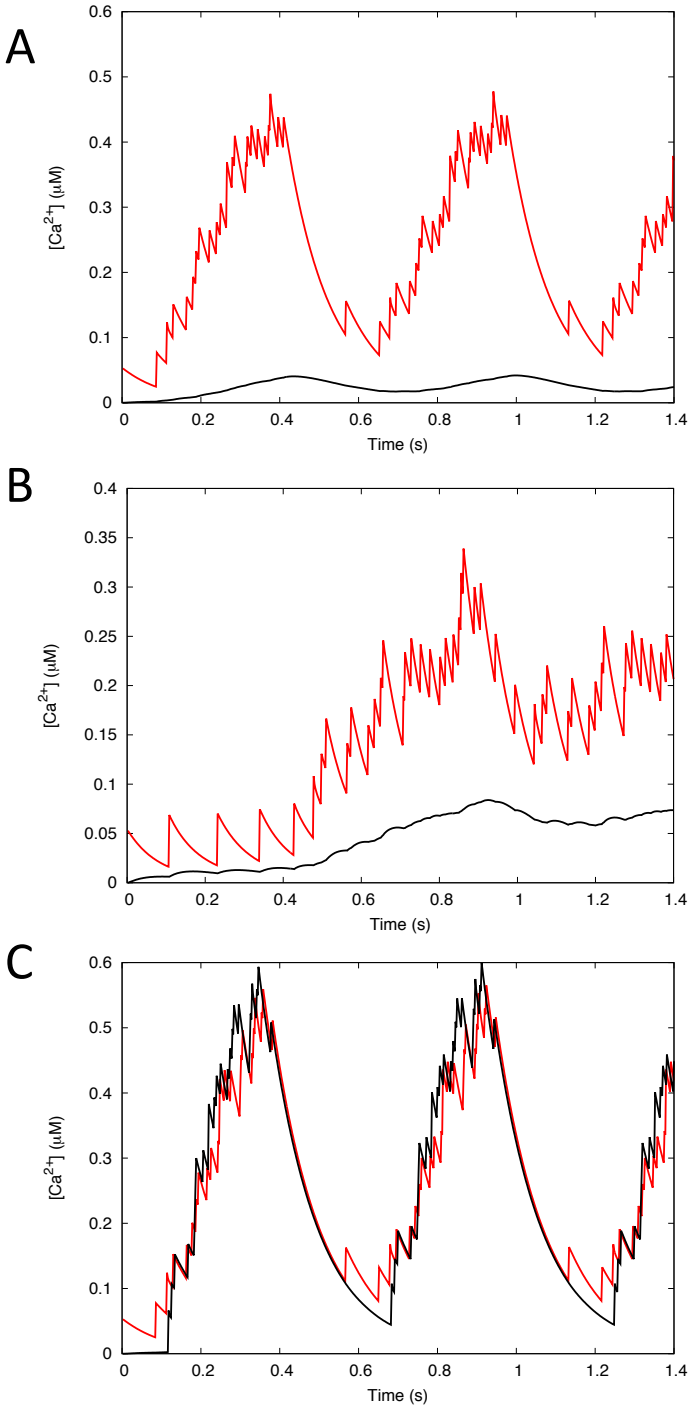

Figure 2.16: Flux through pores alone is not sufficient to generate Ca^{2+} spikes. With calcium channels on one side of the membrane only, diffusion through the pores is insufficient to give the appearance of spiking on the other side of the membrane. Lines show average concentration of Ca^{2+} across the INM (red) or ONM (black). **(A)** with 1000 pores, **(B)** with 4000 pores. **(C)** When channels are present on both side of the membrane signalling is coordinated. Image shows the case of 1000 pores. Parameters: $D = 27.9\,\mu\mathrm{m}^2\mathrm{s}^{-1}$, $k_s = 7.9\,\mathrm{s}^{-1}$, $\sigma = 43.2 \times 10^{-21}\,\mathrm{mol}$, $c_{\mathrm{th}} = 0.025\,\mu\mathrm{M}$, $\alpha = 0.77$.

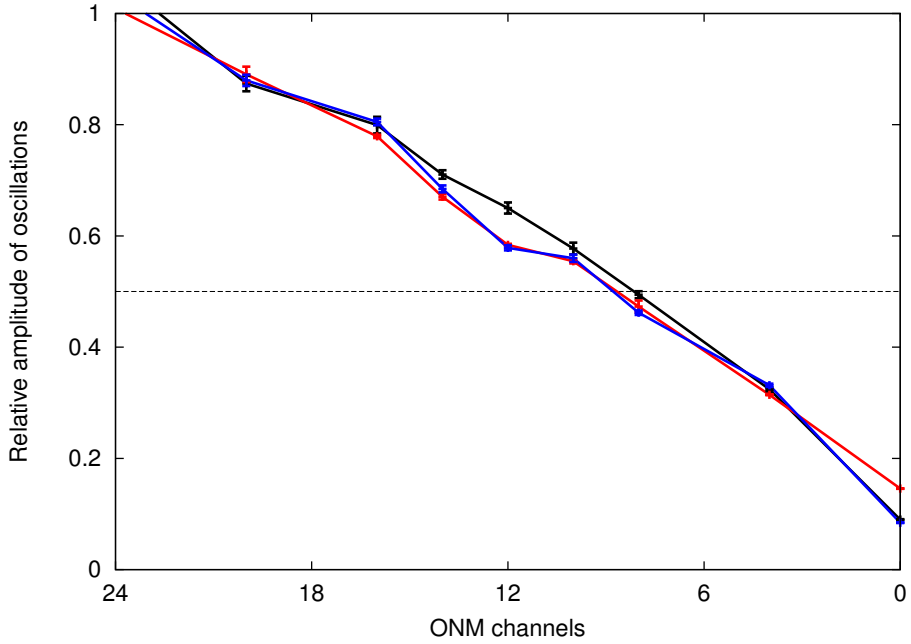

Figure 2.17: Amplitude on ONM decays with fewer ONM channels. Decreasing the number of Ca^{2+} channels on the ONM reduces the amplitude of ONM signals compared to the INM signal. 24 channels are placed approximately equidistantly on the INM and a varying number are placed on the ONM. The horizontal line indicates where the ONM signal falls to less than half the amplitude of the INM signal, which for both parameter sets occurs for around 9-10 ONM channels. Points are averages over 10 random distributions of 1000 pores. Parameters: $D = 27.9\,\mu\mathrm{m}^2\mathrm{s}^{-1}$, $k_s = 7.9\,\mathrm{s}^{-1}$, $\sigma = 43.2\times10^{-21}$ mol, $c_{\mathrm{th}} = 0.025\,\mu$M, $\alpha = 0.77$ (black line); $D = 45.2\,\mu\mathrm{m}^2\mathrm{s}^{-1}$, $k_s = 5.5\,\mathrm{s}^{-1}$, $\sigma = 45.2\times10^{-21}$ mol, $c_{\mathrm{th}} = 0.025\,\mu$M, $\alpha = 0.5$ (red line); $D = 29.8\,\mu\mathrm{m}^2\mathrm{s}^{-1}$, $k_s = 8.9\,\mathrm{s}^{-1}$, $\sigma = 70.0\times10^{-21}$ mol, $c_{\mathrm{th}} = 0.025\,\mu$M, $\alpha = 0.81$ (blue line).

the NPCs initialises firing on the ONM, but also affects the spread of the calcium wave across the ONM, triggering channels to fire sooner than they otherwise would if no flux were present. This can be seen from the lag before the ONM signal initiates at the start of the simulation, compared to the simultaneous peak of both signals (Figure 2.16C). The coordination we observe here is due to diffusion through the pores, and not due to the identical properties of the compartments.

2.6.4 Relative channel abundance affects spike amplitude but not simultaneity

It is possible to obtain near perfect coordination between the nucleoplasmic and cytosolic signals when there are identical components on both membranes, but the actual abundance of the Ca^{2+} channel involved in symbiosis is presently unknown. The ONM and INM are known to have different protein abundances [176], and indeed a key component of the symbiosis pathway, the putative potassium channel *Mt*DMI1, is known to be preferentially located to

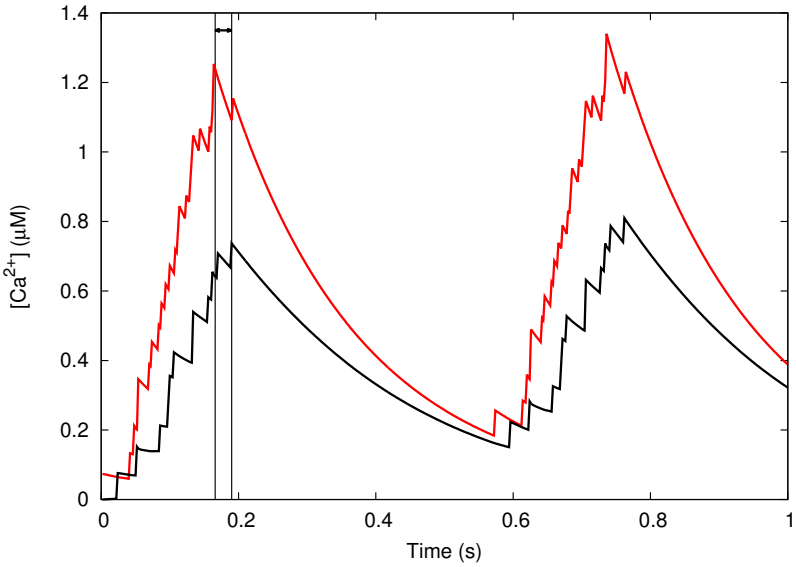

Figure 2.18: Ca^{2+} signals on the ONM and INM are coordinated even with different channel numbers. Average Ca^{2+} concentration across the INM (red) and ONM (black) with 24 and 12 channels respectively and 1000 pores. The arrow indicates the difference between peak concentrations. We see that the signals are well coordinated. Parameters: $D = 45.0\,\mu\text{m}^2\text{s}^{-1}$, $k_s = 4.0\,\text{s}^{-1}$, $\sigma = 60.0 \times 10^{-21}$ mol, $c_{\text{th}} = 0.025\,\mu$M, $\alpha = 0.77$.

the INM [62]. *Mt*DMI1 plays a key role in regulating the symbiotic Ca^{2+} channel [58, 86, 95, 114, 117] and these two components of the signalling pathway have recently been observed to co-localise [63]. We expect from this that the abundance of the symbiotic Ca^{2+} channel is likely to follow that of *Mt*DMI1.

To investigate the effect of this, we varied the number of channels (N_{Och}) on the ONM between 0 and 24 and simulated the average Ca^{2+} signal either side of the NE. As the number of ONM channels falls, the amplitude of the ONM spike falls (Figure 2.17), and for small numbers of channels the signal is just a series of Ca^{2+} releases with no observable global peak. When the numbers either side are similar, the signals on the two membranes do not differ significantly (Figure 2.16C). There is a smooth transition between identical spiking behaviour and the loss of recognisable spiking through which the signals either side of the NE become distinguishable. The use of different dyes in Capoen *et al.* [62] to distinguish between the cytosolic and nuclear signal means any difference in the amplitude of the two signals could not be interpreted in this context, but techniques exist that could detect such differences [178]. For the cases in which a global spike is observed on the ONM, the signals on the two membranes can be seen to be simultaneous (illustrated for the case of $N_{Och} = 12$ in Figure 2.18). In accordance with Figure 2.16, the flux between the membranes is small; Figure 2.25 shows how the average INM signal is hardly affected at all by changing the ONM channel abundance.

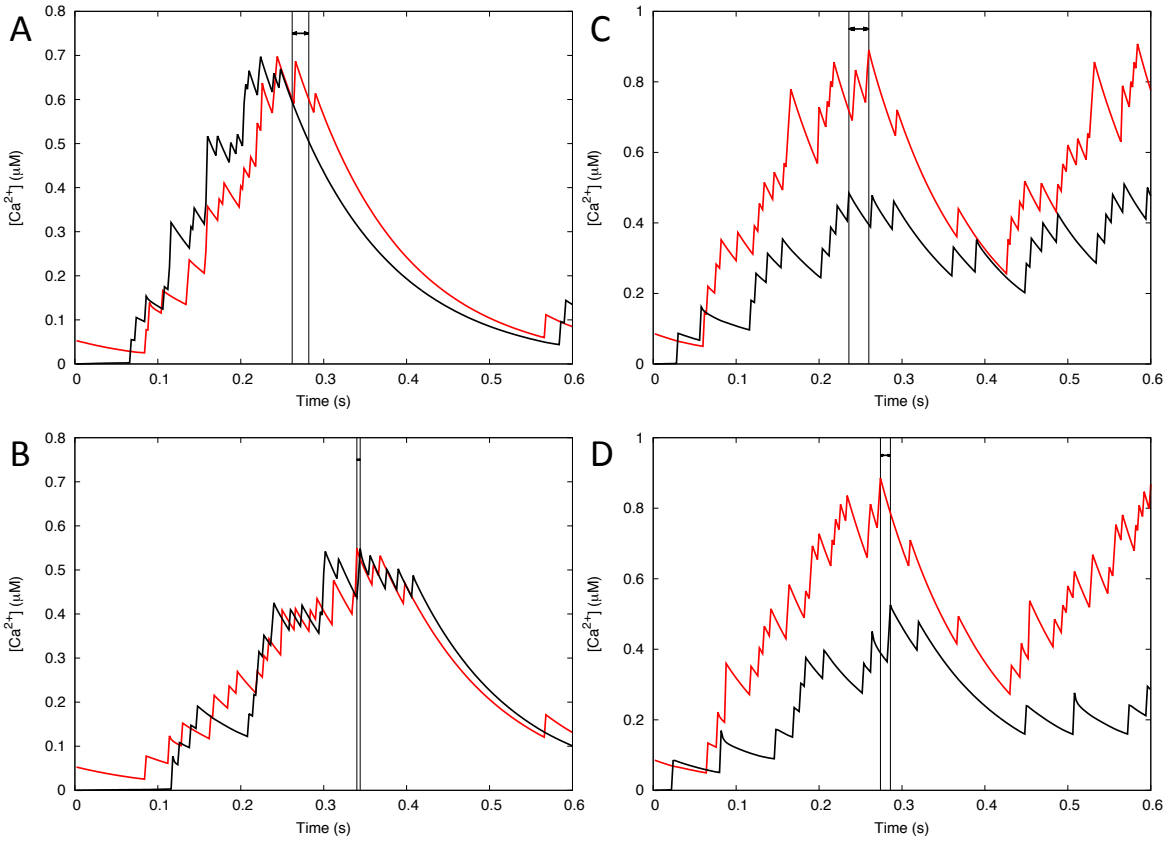

Figure 2.19: Ca^{2+} signals in compartments with different properties are coordinated. Average Ca^{2+} signals across the INM (red) and ONM (black) with different diffusion constants. **(A)** $D_{\text{in}} > D_{\text{out}}$, **(B)** $D_{\text{in}} < D_{\text{out}}$, both with 24 channels on each side. **(C)** $D_{\text{in}} < D_{\text{out}}$, **(D)** $D_{\text{in}} > D_{\text{out}}$ with 12 channels on ONM, 24 on INM. The signals on the two membranes peak roughly simultaneously in all cases. Parameters: **(A&B)** $k_s = 7.9\,\text{s}^{-1}$, $\sigma = 43.2 \times 10^{-21}$ mol, $c_{\text{th}} = 0.025\,\mu$M, $\alpha = 0.1$, **(A)** $D_{\text{in}} = 45.0\,\mu\text{m}^2\text{s}^{-1}$, $D_{\text{out}} = 27.9\,\mu\text{m}^2\text{s}^{-1}$, **(B)** $D_{\text{in}} = 27.9\,\mu\text{m}^2\text{s}^{-1}$, $D_{\text{out}} = 15.0\,\mu\text{m}^2\text{s}^{-1}$. **(C&D)** $k_s = 8.9\,\text{s}^{-1}$, $\sigma = 70.0 \times 10^{-21}$ mol, $c_{\text{th}} = 0.025\,\mu$M, $\alpha = 0.8$, **(C)** $D_{\text{in}} = 45.0\,\mu\text{m}^2\text{s}^{-1}$, $D_{\text{out}} = 29.8\,\mu\text{m}^2\text{s}^{-1}$, **(D)** $D_{\text{in}} = 29.8\,\mu\text{m}^2\text{s}^{-1}$, $D_{\text{out}} = 15.0\,\mu\text{m}^2\text{s}^{-1}$.

2.6.5 Simultaneous signals can occur in non-identical compartments

We have so far studied the case where the model parameters are the same on both the INM and the ONM. However, Ca^{2+} diffuses faster in the nucleus than in the cytosol due to the greater buffering capacity of the cytosolic compartment [139, 142]. The buffering capacity of the compartment is represented by an effective diffusion constant, D, in our model [106], so we investigated the influence of different diffusion constants on the system's ability to generate simultaneous signals. The Ca^{2+} pump, MCA8, has the same abundance either side of the NE [62] so the uptake rate, k_s, will not be varied, nor will the Ca^{2+} release strength, σ, and firing threshold, c_{th}, since we assume the same channel is involved on both membranes [62, 63].

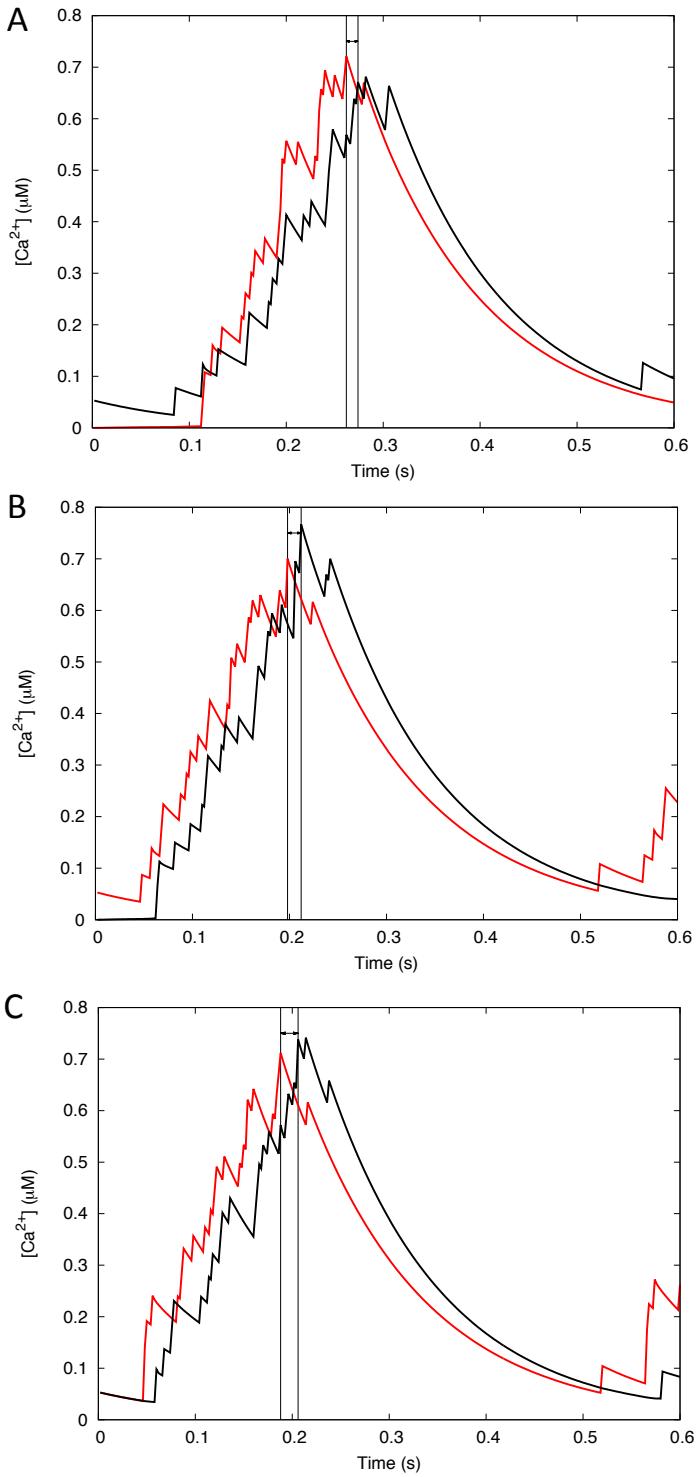

Figure 2.20: Initiation side doesn't affect simultaneous signals. Average Ca^{2+} signals across the INM (red) and ONM (black) with $D_{\text{in}} > D_{\text{out}}$. The simulation is initialised by opening one channel on **(A)** the ONM, **(B)** the INM, **(C)** both sides. The signals on the two membranes occur simultaneously in all cases. Parameters: $k_s = 7.9\,\text{s}^{-1}$, $\sigma = 43.2 \times 10^{-21}$ mol, $c_{\text{th}} = 0.025\,\mu$M, $\alpha = 0.1$, $D_{\text{out}} = 27.9\,\mu\text{m}^2\text{s}^{-1}$, $D_{\text{in}} = 45.0\,\mu\text{m}^2\text{s}^{-1}$

Simulations show that the spikes occur simultaneously on both sides of the membrane despite differences in the diffusion constants (Figures 2.19A&B). Due to how we define the refractory period in our model the frequencies of the signals do not match, as we will discuss in more detail later, but the key observation from the model is that a single spike can be generated simultaneously in both compartments. There are the same number of channels on both membranes in Figures 2.19A&B, but the results continue to hold when one membrane has

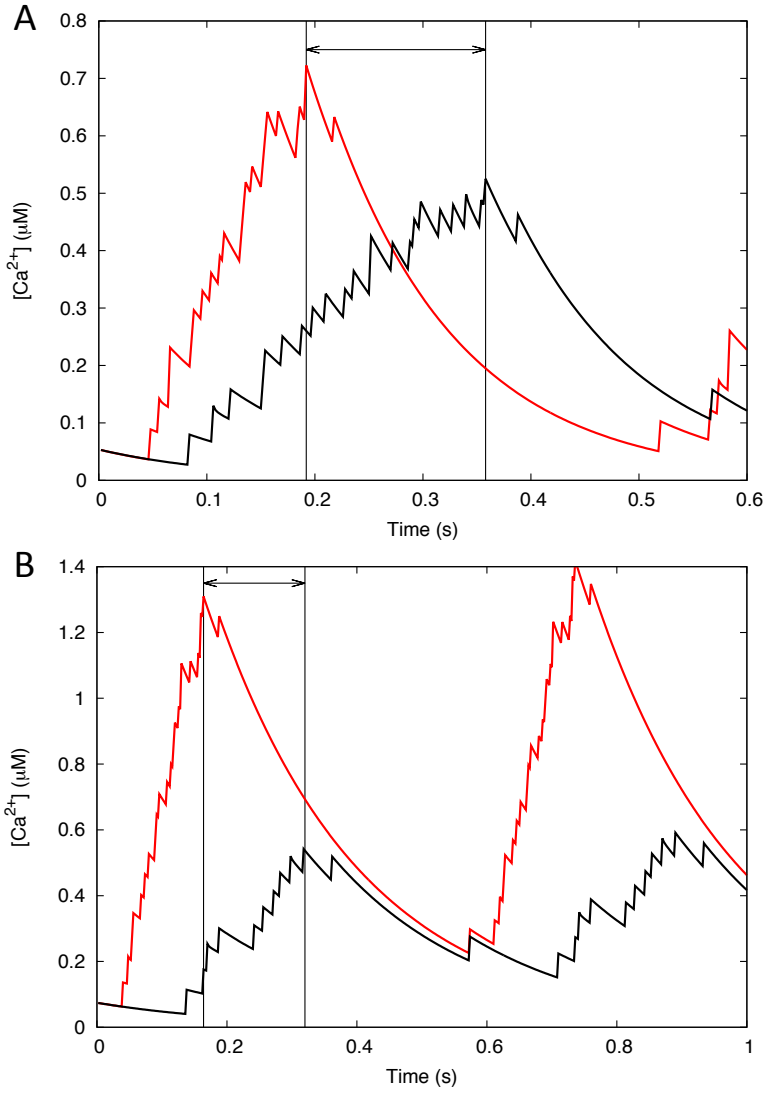

Figure 2.21: Without pores, signals are not simultaneous. Average Ca^{2+} signals across the INM (red) and ONM (black) with no pores. The arrow indicates the difference between peak concentrations. **(A)** 24 channels on both sides, $D_{\text{in}} > D_{\text{out}}$. **(B)** 24 channels on INM, 12 channels on ONM, same parameters. Parameters: **(A)** $D_{\text{out}} = 27.9\,\mu\text{m}^2\text{s}^{-1}$, $D_{\text{in}} = 45.0\,\mu\text{m}^2\text{s}^{-1}$, $k_s = 7.9\,\text{s}^{-1}$, $\sigma = 43.2 \times 10^{-21}\,\text{mol}$, $c_{\text{th}} = 0.025\,\mu\text{M}$, $\alpha = 0.1$. **(B)** $D = 45.0\,\mu\text{m}^2\text{s}^{-1}$, $k_s = 4.0\,\text{s}^{-1}$, $\sigma = 60.0 \times 10^{-21}\,\text{mol}$, $c_{\text{th}} = 0.025\,\mu\text{M}$, $\alpha = 0.77$.

fewer channels (Figures 2.19C&D). Furthermore, simultaneous signals occur independently of which side of the NE the signal is initiated (Figures 2.20).

2.6.6 Without pores, signals are uncoordinated

The diffusion constant is key to determining the speed of the Ca^{2+} wave that spreads across the nuclear surface during the generation of a spike [107, 109]. When there are no pores and the effective diffusion constants are different in the two compartments, there is a clear difference in the peak times of the signals either side of the membrane (Figure 2.21A). This is despite both sides being initiated at the same time. Allowing diffusion through the pores immediately coordinates the spikes (Figure 2.19A).

When there are different numbers of channels on the two membranes, the signals are again not simultaneous without pores (Figure 2.21B). This is to be expected as, with fewer channels, the average separation between channels increases and the resulting Ca^{2+} wave slows [107, 109]. A second observation from Figure 2.21B is the large difference in spike amplitudes on the two sides of the membrane, more than expected based purely on channel numbers alone. Adding pores immediately coordinates the signalling (Figure 2.18), and even improves the relative amplitude of the signals.

For large D, small k_s and large σ values, the match between signals improves even when no pores are present. For the large range of parameters tested there is never perfect agreement, but it is conceivable that the resolution of experiments is insufficient to resolve small differences. However, such parameter sets do not correspond to those that fit the 3D model (Figure 2.6) and are therefore not realistic. The illustrative trace of Figures 2.21B and 2.18 corresponds to the outer edge of the correlation plots in Figure 2.6, but the ONM/INM Ca^{2+} peaks are separated by almost the full INM spike width.

Figure 2.22 investigates this in more depth. It shows what differences in the peak time of ONM and INM Ca^{2+} spikes occur for a range of differences in the diffusion constants on the ONM and INM. Since the diffusion constant is believed to be smaller in the cytoplasm [142], we kept D_{out} fixed and increased the value of D_{in}. For both $D_{\text{out}} = 22\ \mu\text{m}^2\text{s}^{-1}$ (Figure 2.22A) and $D_{\text{out}} = 33\ \mu\text{m}^2\text{s}^{-1}$ (Figure 2.22D), increasing D_{in} increased the delay between peak Ca^{2+} on the ONM and the INM when no pores were present, but had no effect when pores were present.

In Figure 2.22 we specifically simulate parameter sets that correspond to those that fit the 3D model (Figure 2.7) so that we can compare the values of the diffusion constant with those measured experimentally. The 2D values of D_{out} correspond to $10\ \mu\text{m}^2\text{s}^{-1}$ in Figures 2.22A-C, and $15\ \mu\text{m}^2\text{s}^{-1}$ in Figures 2.22D-F, in line with measured diffusion constants in the cytosol [168], although we need to be careful of making comparisons between 2D and 3D parameters on the ONM (see Discussion). The resulting range of nucleosolic diffusion constants are noted in the figure. A difference of $10\ \mu\text{m}^2\text{s}^{-1}$ in the physiological diffusion constant can give rise to a difference in peak timing of at least the width of the INM peak (Figure 2.22C&F), while a

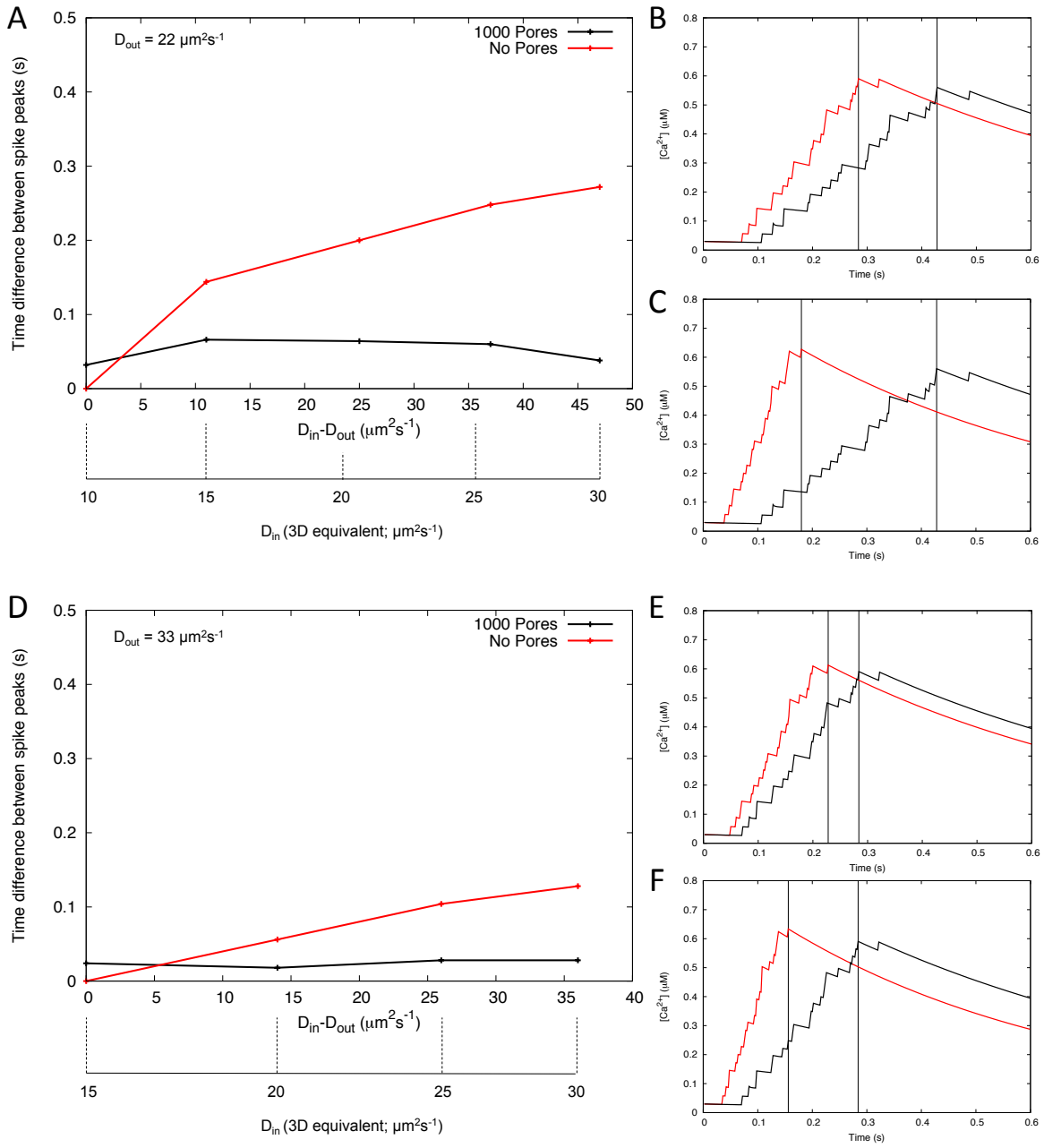

Figure 2.22: Difference in diffusion constants that give rise to non-simultaneous signals. **(A,D)** illustrate the time difference in spike peaks, for different D_{out} and D_{in} values. With 1000 pores (black lines), the time difference is fairly constant. With no pores, the time difference grows as the difference in diffusion constants grows. **(B,C,E,F)** show example spikes in the average Ca^{2+} concentration across the INM (red) and ONM (black) for a NE with no pores. **(A-C)** $D_{\text{out}} = 22\,\mu\text{m}^2\text{s}^{-1}$, equivalent to $D_{3\text{D}} = 10\,\mu\text{m}^2\text{s}^{-1}$. **(D-F)** $D_{\text{out}} = 33\,\mu\text{m}^2\text{s}^{-1}$, equivalent to $D_{3\text{D}} = 15\,\mu\text{m}^2\text{s}^{-1}$. **(B)** $D_{\text{in}} = 33\,\mu\text{m}^2\text{s}^{-1}$, **(C)** $D_{\text{in}} = 59\,\mu\text{m}^2\text{s}^{-1}$, **(E)** $D_{\text{in}} = 47\,\mu\text{m}^2\text{s}^{-1}$, **(F)** $D_{\text{in}} = 59\,\mu\text{m}^2\text{s}^{-1}$ Other parameters: $k_s = 1.1\,\text{s}^{-1}$, $\sigma = 24.0 \times 10^{-21}$ mol, $c_{\text{th}} = 0.025\,\mu\text{M}$, $\alpha = 0.1$.

difference of 5 $\mu m^2 s^{-1}$ gives rise to a smaller difference in peak time that may be detectable, depending on D_{out}. The difference in Figure 2.22B is of a similar size to that of Figure 2.22F, while Figure 2.22E has an obviously smaller gap. Standard imaging techniques are already able to sample at rates 5-10 times per Ca^{2+} peak during symbiotic Ca^{2+} signalling [94], so any such differences would be easily detectable.

With different channel numbers, the signals could be made to coordinate when the other parameters on the two membranes are different. Since the relative abundance of DMI1 on the two membranes [62] would suggest the ONM has fewer active Ca^{2+} channels than the INM, to obtain simultaneous signals the cytosol would need a larger Ca^{2+} diffusion constant than the nucleoplasm. However, this is inconsistent with our understanding of the relative buffering capacities of the two compartments [142].

2.7 Discussion

In this chapter we have investigated mathematical models for simulating nuclear Ca^{2+} signals and applied them to study the effect of nuclear pores on the generation of Ca^{2+} spikes. We extended the solution of the FDF model in a spherical volume presented by Skupin *et al.* [162] to include the effect of Ca^{2+} pumps on the INM (Section 2.1) and simulated spike generation in this model (Figures 2.3 & 2.4). Since the core signalling components are confined to the nuclear surface, we developed more efficient algorithms by restricting ourselves to a 2-dimensional model of the nuclear surface (Sections 2.2 & 2.5). We showed that this model was able to capture either the shape and width of the Ca^{2+} spike (Section 2.3) or the behaviour of the Ca^{2+} microdomain around a channel (Section 2.4) but not both at the same time. We then incorporated pores into the model (Section 2.5), connecting two copies of our nuclear surface model, one tracking Ca^{2+} on the INM, the other on the ONM. We showed in Section 2.6 that diffusion through the NPCs could coordinate signals even if the number of channels or the signalling capacities (represented by the diffusion constant) in the two compartments were different. Without Ca^{2+} diffusion through the NPCs, this coordination would not necessarily occur. Pores provide a robust mechanism by which signals in the nucleoplasm and peri-nuclear cytoplasm may be coordinated.

2.7.1 Decoding of nuclear Ca^{2+} oscillations

Our work here has illustrated how the concentration in Ca^{2+} microdomains near channels can be substantially larger than the concentration in other parts of the nucleus. Figure 2.4 demonstrated that a substantial part of the surface averaged Ca^{2+} concentration was contributed by just a few measurement points close to Ca^{2+} release sites. This has implications for how the Ca^{2+} signal is decoded. Decoding proteins are only able to detect the Ca^{2+} concentration within their local region, and the binding constants for Ca^{2+} of these proteins means they can only be activated in specific regions of the nucleus where the Ca^{2+} concentration is sufficiently high.

In symbiosis signalling, the protein CCaMK in cooperation with CaM, detects the Ca^{2+} signal [64, 96] and, by forming a complex with various transcription factors and other proteins inside the nucleus [67], triggers expression of symbiosis specific genes [179]. The EF-hands of CCaMK when bound to Ca^{2+} maintain an auto-inhibited state, but binding of Ca^{2+}-activated CaM activates CCaMK [96]. As discussed in Section 2.1.3, the binding constants of CCaMK and CaM to Ca^{2+} are such that CCaMK would remain auto-inhibited throughout the nucleus, but that CaM would likely only be activated at or near the NE. Modelling work from Granqvist *et al.* [114] suggested that CaM might migrate into the nucleus in response to Nod factor detection, as has been observed in animal systems [116], placing it at or near the NE during spiking. Indeed, raised cytosolic Ca^{2+} has been shown to mediate such movement in animals [142, 180, 181, 182], raising a putative role for the perinuclear cytoplasmic Ca^{2+} oscillations. One of the key transcription factors required for symbiotic gene transcription, NSP2, is initially localised to the NE, only entering the nuclear volume upon Nod factor stimulation [183]. Therefore, not only are the key Ca^{2+} signal generating components located at the NE, so too may be a number of the key downstream decoding proteins as well, further highlighting the importance of the nuclear surface in this signalling system.

2.7.2 2D vs 3D model comparison

We demonstrated that the 2D surface model could be related to the behaviour of Ca^{2+} in the 3D volume of the nucleus, in particular showing how the diffusion constant changes between models (Figure 2.7). The 3D solution for the exterior would, however, have a different form to that of the interior due to the different boundary conditions. We did not perform this analysis for the ONM, partly due to the time it would require, but also uncertainty in how best to approach such a model. We could treat the cytoplasm as an open system on the length scale of Ca^{2+} diffusion, but there are numerous other structures in the cytoplasm such as the ER and mitochondria that not only act as obstacles to Ca^{2+} diffusion, but also interact with Ca^{2+} through pumping and even further release. However, the Green's function framework would require us to neglect these elements.

In terms of signal generation there is one key difference between the 3D Ca^{2+} signalling processes on the ONM and the INM. On the INM, the spherical geometry means that Ca^{2+} paths between two points on the surface through the bulk are shorter than the corresponding paths that are restricted to the surface. On the ONM, however, the shortest paths are those restricted to the surface. If we neglect pores, for the same signalling parameters (in particular, the same D) in 3D we would expect the ONM spike width to be broader than the INM spike, as it would take longer to activate individual channels. In the living system the diffusion constants differ on either side of the NE [142], $D_{\text{out}} < D_{\text{in}}$, exacerbating these differences in spike width. Likewise, as discussed in Section 2.6.4, the number of Ca^{2+} channels on the ONM in legumes is predicted to be smaller than on the INM, again making the ONM a less efficient signalling system. Therefore, the differences between ONM and INM models would act to

increase the differences between ONM and INM Ca^{2+} signals in isolated nuclei, strengthening the results of our pore analysis.

2.7.3 Spike width and coordination

In our analysis we focussed on the development of a single Ca^{2+} spike, since these are observed to develop simultaneously in the two signalling compartments [62]. Ca^{2+} spikes typically last for around 50 s, with the time between initiation and peak lasting (what we have termed the spike width) around 10 s [93]. In all our simulations, the spike width is less than 1 s. Even without pores, there are no parameter sets below the critical surface of Figure 2.13 that produce a spike width of greater than 1 s. This is true for the 3D model as well. This is a fundamental limitation of our FDF model. In order to activate neighbouring channels, the Ca^{2+} release from a single channel needs to be sufficiently large, but that combined with realistic diffusion constants propagates a Ca^{2+} wave across the entire surface too quickly. While this is unfortunate, it will not affect the conclusions of our analysis.

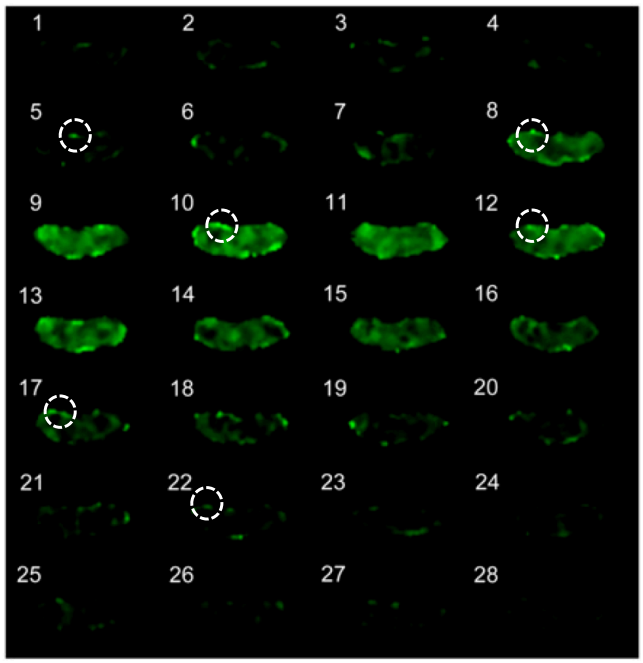

Figure 2.23: Spatially inhomogeneous nature of nuclear Ca^{2+} oscillations. Spatio-temporal changes in Ca^{2+} concentration during a single nuclear Ca^{2+} spike, adapted from Sieberer *et al.* [94]. Frame-by-frame imaging sequence with 1 s intervals. Added dashed white rings highlight repeated local increases in Ca^{2+} concentration at the nuclear surface that seem to be due to repetitive releases from Ca^{2+} channels in that small region of the INM.

With a broader spike width, Ca^{2+} has more time to diffuse through NPCs and we would

expect the influence of pores on the generation of a spike to be stronger. Therefore, with physiological Ca^{2+} spikes the pores will be more able to coordinate spikes than in our model. Since we've already demonstrated NPCs can coordinate spikes, our conclusions regarding coordination can still be applied to physiological spikes. Likewise, the effect of different diffusion constants or channel numbers in two isolated compartments would be stronger if spike generation occurred over a longer period of time. This holds as long as Ca^{2+} is able to diffuse through the NPCs (see next section) and that Ca^{2+} can regulate the activation of channels.

Experimental data and earlier models certainly suggests Ca^{2+} regulates its own channel. The essential symbiotic protein DMI1 encodes a K^+ channel that co-localises with the symbiotic Ca^{2+} channel, CNGC15 [58, 63], and modelling indicates it is key to the activation of the Ca^{2+} channel [86, 114]. DMI1 contains a putative Ca^{2+} binding domain [117], while CNGCs contain CaM binding domains that render the channel inactive. Therefore both activation and de-activation of the symbiotic Ca^{2+} channel could be regulated by Ca^{2+}, offering numerous ways through which Ca^{2+} from neighbouring channels could act to stimulate release.

What is the feature missing in our model? In Figure 2.23 we have highlighted a number of confocal images of nuclear Ca^{2+} signalling from Sieberer *et al.* [94] that appear to show multiple releases from a single region of the INM, suggesting that channels fire multiple times in the generation of a single Ca^{2+} spike. In our model a single channel only fires once. The signalling shown in Figure 2.23 and in Sieberer *et al.* [94] are reminiscent of the generation of Ca^{2+} spikes in animal systems, in which a global spike represents the coordination of stochastic releases from multiple Ca^{2+} channels, where this coordination occurs via diffusion [113]. Future modelling work in this system should explore this possibility further.

2.7.4 Ca^{2+} permeability of the NPC

The degree to which nuclear Ca^{2+} is independently regulated has been a controversial topic for many years [138, 142, 149]. This conflict stems from the cytosol and nucleosol being connected by nuclear pores. The NPC is a large protein complex capable of allowing up to 30 kDa molecules and ions to passively diffuse between the cytoplasm and nucleoplasm [139, 184]. In the animal field (see reviews [139, 142, 149]), it was generally believed that the presence of the NPCs would naturally cause cytoplasmic and nucleoplasmic Ca^{2+} levels to equilibriate by passive diffusion. Even when signals were generated in the vicinity of the NE, it was not clear whether nuclear Ca^{2+} was released from the INM, or was initially released from the ONM and diffused into the nucleus through the NPCs [139]. As we have shown here (Figure 2.16) the generation of Ca^{2+} signals on both nuclear membranes requires active signalling components on both sides. In plants (see the reviews of [138, 185, 186, 187]) the opposite viewpoint has been taken. Early experiments showed stimulus dependent delays between cytoplasmic Ca^{2+} elevations and the corresponding nuclear Ca^{2+} response [32, 138, 147, 151, 152, 153, 154, 155] implying the NPC is not permeable to Ca^{2+}.

Our results (Figure 2.16) indicate that active signalling components are needed on the INM to generate large variations in nuclear Ca^{2+}, even when the NPC density is such that the NE is effectively transparent (Figure 2.16B). The failure of cytoplasmic Ca^{2+} oscillations in pollen tip growth to elicit similar fluctuations in the nucleus [188, 185] can be understood in this context. The delays between nuclear and cytoplasmic responses to the biological elicitors cryptogein, harpin and flg22 [32, 152], reproduced in Figure 2.24, are believed to show that INM Ca^{2+} channels respond to downstream secondary messengers, not that cytoplasmic Ca^{2+} diffuses into the nucleus directly. However, our results suggest raised cytoplasmic Ca^{2+} need not correspond to a similarly strong peak in nuclear Ca^{2+} concentration.

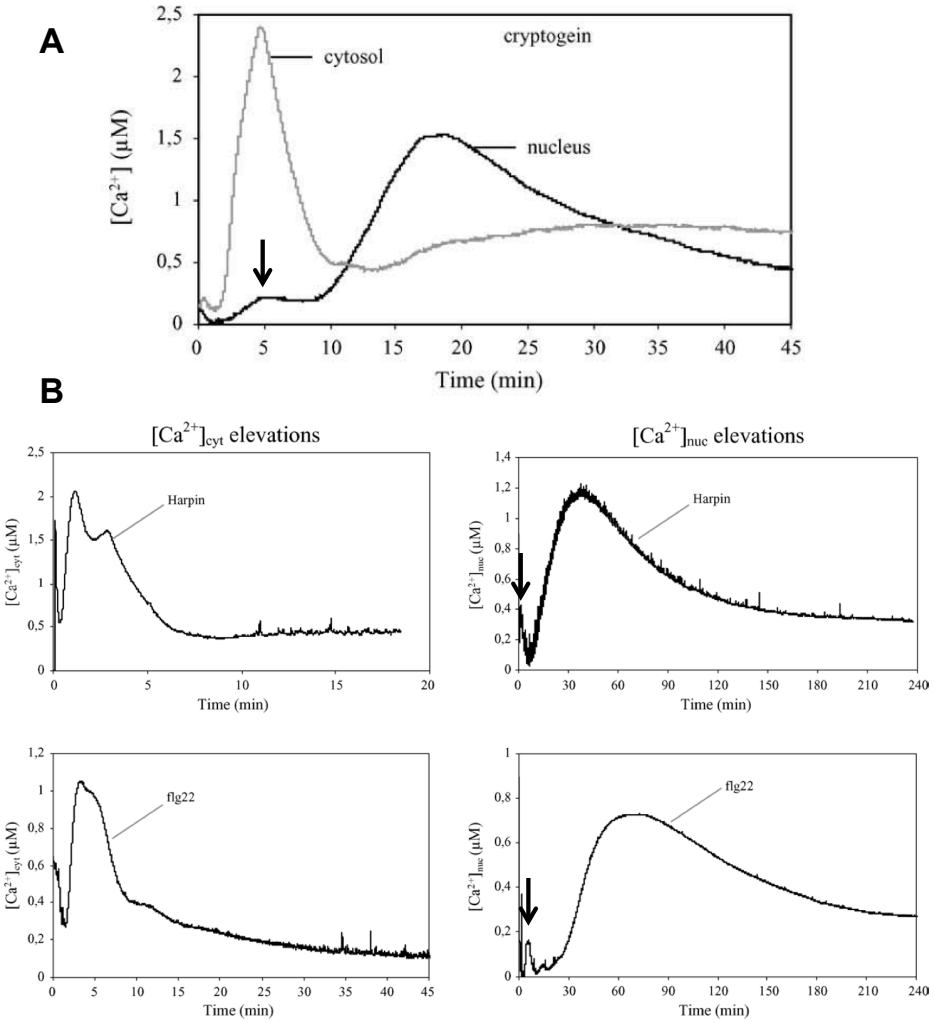

Figure 2.24: Comparing elicitor induced Ca^{2+} signals in the cytosol and nucleus. Tobacco plants expressing aequorin in either the nucleus or cytoplasm, taken from Lecourieux *et al.* [152]. Arrows indicate peaks in the nuclear signal that appear correlated with the cytoplasmic peak. **(A)** Comparison of changes in nuclear and cytosolic Ca^{2+} concentration induced by 100 nM cryptogein. **(B)** Comparison of changes in nuclear and cytosolic Ca^{2+} concentration induced by $10\,\mu g\,mL^{-1}$ harpin or 50 nM flg22. Left column are the cytosolic responses, right column are the nuclear responses.

Figure 2.16B indicates that even when the NE is effectively transparent to Ca^{2+}, only a relatively shallow peak might be observed on the INM. Looking closely at the data of Lecourieux *et al.* [32, 152], we see early peaks in the nuclear Ca^{2+} signal that could correspond to the small amount of Ca^{2+} that does diffuse through the NPCs (indicated by arrows in Figure 2.24). The sub-cellular localisation of the cytoplasmic Ca^{2+} signal is also of importance when interpreting these cell-averaged Ca^{2+} signals. If generated far from the NE, the actual Ca^{2+} concentration that reaches the nucleus will most often be far less than the cell or tissue-averaged Ca^{2+} concentration measured in these experiments. Recent experiments indicate that the biological elicitors used by Lecourieux *et al.* generate highly localised changes in cytoplasmic Ca^{2+} [8]. Furthermore, aequorin data represents the average over many cells, and such transients can be due to the average over many oscillating signals [31]. The latest data from experiments with flg22 show that at least the cytosolic signals are also due to underlying Ca^{2+} oscillations at the single cell level [8].

2.7.5 Transparency and coordination

A question that arises from our analysis is why, if the NPC density is high enough for the NE to be considered "transparent" (Figure 2.14 and Section 2.6.1), can different Ca^{2+} signals be observed on the two nuclear membranes? The key to this lies in the Ca^{2+} microdomains that surround Ca^{2+} channels. The analysis of transparency in Figure 2.14 used a measurement point that was sufficiently far from the channel microdomain. Even if the NE is transparent, the limited quantity of Ca^{2+} that is able to diffuse away from the Ca^{2+} microdomain around channels ensures the signal observed is different on the two sides of the membrane.

Coordination occurs not because a large amount of Ca^{2+} is crossing the NE, but because the small amount that does is able to trigger activation of Ca^{2+} channels much faster. When considering different diffusion constants in the cytoplasm and nucleoplasm, the coordination arises because the wave in the high D environment travels across the nuclear membrane faster, leaking through to the regions of the slow D environment where the Ca^{2+} wave hasn't yet reached, accelerating the activation of Ca^{2+} channels in those regions. Figure 2.20 demonstrates this effect. Since $D_{\text{in}} > D_{\text{out}}$, when the system is initialised on the ONM (Figure 2.20A), when the ONM tries to drive the INM, the peak occurs later than when the INM drives the ONM (Figure 2.20B&C).

The wave across a membrane with fewer Ca^{2+} channels also travels slower because the gaps between neighbouring channels are larger, and waves in the FDF model travel at a speed inversely proportional to channel separation [109]. Thus, the side with more Ca^{2+} channels drives the side with fewer channels. Figure 2.25 shows that the Ca^{2+} concentration on the driving side is almost completely unchanged by the number of Ca^{2+} channels on the other side. This is because the amount of Ca^{2+} crossing the NE is virtually unchanged. Most of that Ca^{2+} comes from the leading edge of the wave where the concentration difference across the NE is largest. In this region the concentration of Ca^{2+} on that far side is negligible whether

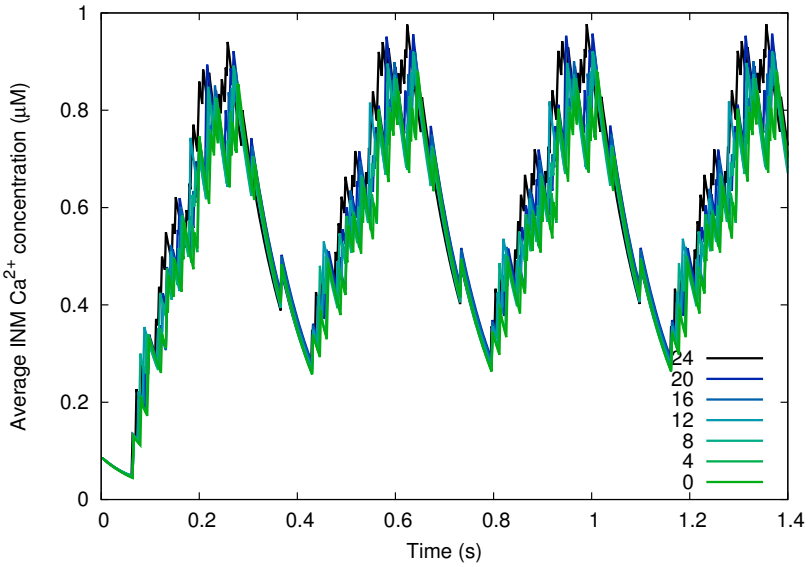

Figure 2.25: The number of channels on the ONM has only a minor effect on the INM Ca^{2+} signalling. Showing the INM signal for different numbers of ONM channels. 24 channels are placed on the INM. 1000 pores. Parameters: $D = 29.8\,\mu\text{m}^2\text{s}^{-1}$, $k_s = 8.9\,\text{s}^{-1}$, $\sigma = 70.0 \times 10^{-21}\,\text{mol}$, $c_{\text{th}} = 0.025\,\mu\text{M}$, $\alpha = 0.81$.

there is a full complement of channels or none. Figure 2.25 also highlights how little overall Ca^{2+} is flowing across the NE to give rise to coordination.

Even if the plant NPC is permeable to Ca^{2+}, there may be other ways in which coordination is possible across the NE. One possibility is that signals are coordinated directly through the NE. The release of Ca^{2+} from a channel in either membrane will deplete the NE of Ca^{2+} in a localised region around that channel. A channel on the other membrane that is sufficiently close to that depleted region could then have its behaviour affected. A combination of modelling and imaging work in animal systems demonstrated that the size of these depleted regions in the ER (to which the NE is contiguous) is less than $0.5\,\mu$m, and that they last on the order of ms [189, 190]. Identification of the symbiosis Ca^{2+} channel allowed for immunogold labelling of the channel by Charpentier *et al.* [63] which showed these channels are only occasionally within this distance of one another. Our model suggests that all channels are affected by Ca^{2+} from pores, and thus coordination is due to a combined influence on all channels. We also note that depletion of Ca^{2+} from the NE would act to negatively affect coordination, as those channels on the other side of the NE would be unable to release Ca^{2+} from the depleted region, thus delaying their release.

2.7.6 The role of the nucleoporin mutants

Three mutants in *Lotus japonicas* nucleoporins are deficient in Ca^{2+} spiking and nodulation, *Lj*NUP133 [59], *Lj*NUP85 [60] and *Lj*NENA [61]. There are few other physiological effects

observed in these mutants, although the double mutant *nup85/nup133* exhibited severe developmental phenotypes [177]. What their role is in the generation of nuclear Ca^{2+} signals is not clear. They could be directly involved in regulation of Ca^{2+} movement through the NPC, or play an indirect role in correctly mediating the transport of key components to the INM.

Our results here show that while diffusion of Ca^{2+} through the NPC might aid coordination of signals, it is not essential for generating symbiosis Ca^{2+} oscillations. With different diffusion constants and fewer ONM Ca^{2+} channels, both sides of the NE are still able to generate Ca^{2+} signals (Figure 2.21). This suggests that if the nucleoporin mutants only prevented passage of Ca^{2+} through the NPC, we might still expect to see Ca^{2+} oscillations. As we showed in Figure 2.16, generation of Ca^{2+} signals on both sides of the NE requires signalling machinery on both sides of the NE. Therefore, if the NPC plays a role in the correct localisation of signalling machinery, this could explain the loss of detectable Ca^{2+} signals. Consistent with this, the three nucleoporins are believed to be part of the nuclear pore scaffold [177, 191] important to maintaining the structure of the NPC, and thus its ability to transport proteins across the NE.

Chapter 3

Propagation of Systemic Signals

Systemic signalling enables distant parts of plants and animals to respond to stimuli that only a small number of cells are exposed to. Within plants, biotic stresses from invading pathogens trigger Systemic Acquired Resistance (SAR) in which distal parts of the plant are primed for defence, protecting the plant from further attack. Systemic wound responses trigger the production of Jasmonic Acid (JA), a plant hormone, throughout the plant as a deterrent to herbivores. In response to abiotic stresses such as cold, salt and UV, Systemic Acquired Acclimation (SAA) is triggered resulting in the expression of relevant tolerance genes throughout the plant. Systemic responses occur to nearly all known stresses, yet unlike animals, plants have no dedicated central nervous system to transmit these responses.

Plant systemic signals appear to be propagated by a diverse array of mechanisms and with a large range of speeds, as summarised in Table 3.1. Hydraulic waves in the vasculature occur in response to drought stresses [192] and wounding [125]. Wounding, via mechanical damage and herbivory, also triggers electrical signals [26, 193, 194, 195], as well as waves of Ca^{2+} [25] and ROS [196]. Ca^{2+} is also involved in acclimation to salt stress [21, 197] and propagation of defence responses [198, 199]. Finally, the propagation of free radicals and small metabolites have also been suggested to play a role in SAR [200, 201, 202]. Despite the variety in measured signals, the field is still far from a clear understanding of the underlying mechanisms of signal propagation.

While the different signals have typically been studied in isolation, hypotheses are emerging that combine one or more signals into a single signalling framework. Hydraulic waves have been connected to electrical signalling [125, 134, 135] and so too have chemical signals [127, 203]. Ca^{2+} is thought to be an important player in electrical signalling [26], with wound induced electrical signalling requiring known Ca^{2+}-permeable channels [193]. But ROS and Ca^{2+} are also suggested to be able to form a linked, self propagating signalling system [198, 204, 205, 206], potentially independent from electrical signals. Electrical signals further come in different flavours, APs and VPs, that are distinguished by differences in speed and amplitude [26]. To make progress in understanding these interlinked systems, mathematical modelling can be a valuable tool, especially when quantitative data is available.

Table 3.1: Measured systemic waves and their velocities.

Ref	Stimulus	System	Wave Type	Velocity (μms^{-1})
[134]	Pressure step	Pea	Electrical	300-500
[207]	Drought	Arabidopsis	Pressure	> 300
[125]	Salt	Barley	Electrical	3000-5000
[196]	Wounding (stem)	*At* WT	ROS	1400
		Atrbohd		80
[194]	Wounding	*Vicia faba*	Electrical	1600
[208]	Wounding	Avacado	Electrical	1400-3500
[192]	Drought	Arabidopsis	Pressure	> 6000
[209]	Herbivory (leaves)	Arabidopsis	Electrical	300
[193]	Wounding (leaf lamina)	Arabidopsis	Electrical	400
	Wounding (leaf midrib)			1500
[195]	Herbivory (leaves)	Arabidopsis	Electrical	300, 1000
	Cutting (leaves)			2500
[197]	Salt	Arabidopsis	Ca^{2+}	60-300
[25]	Herbivory	Arabidopsis	Ca^{2+}	300-1100
[21]	Salt	*At* WT	Ca^{2+}	390 ± 30
		Attpc1-2		15 ± 2
		At OxTPC1		680 ± 70

In this chapter we explore the mechanisms that underly systemic signalling in plants. There are numerous phenomenological models that have been described previously to explain systemic signalling (Figure 3.1) [135, 198, 200, 204]. We choose to divide them into two broad categories: passive signals (Figures 3.1A&B) and active signals (Figures 3.1C-G). Passive signals are such that, once generated at the site of stress, they travel through the plant without being regenerated, possibly triggering other signalling pathways in nearby cells as they go past. Not needing to be regenerated means they can pass through regions of dead tissue (like the xylem) or those that have been poisoned [210]. Examples include hydraulic [192, 135] and chemical signals [200]. VPs are believed to be a downstream response of a passive signal, and these shall be explored in more detail in the next section (Section 3.1). Active signals, on the other hand, are continuously regenerated as they propagate, much like the nervous signals in animals [211]. Examples include action potentials [26], and waves of ROS and Ca^{2+} [21, 196, 198]. Since application of channel inhibitors in these systems are able to block propagation of the signals [21, 196], they need to be actively regenerated within each cell the signal passes through. The mechanisms underlying propagation of these active signals is the focus of the rest of the chapter (Sections 3.2 onwards).

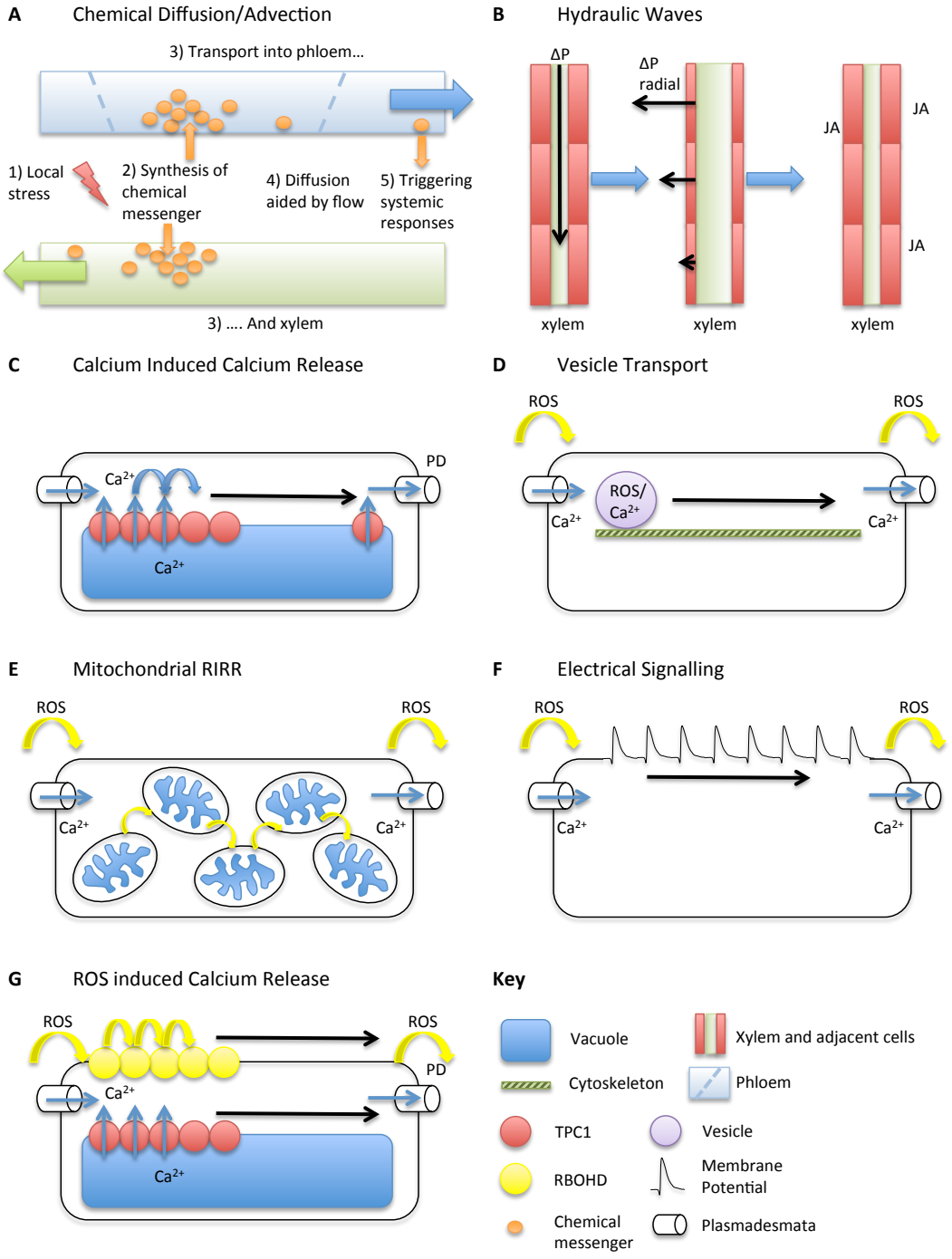

Figure 3.1: Conceptual models for the propagation of systemic signals. (A) A local stress triggers the synthesis of chemical messengers that are transported to the xylem and phloem where they are carried throughout the plant by a combination of diffusion and advection. (cont.)

Figure 3.1: (cont.) Detection of the chemicals could trigger ion fluxes in surrounding tissues to produce the detected electrical/ROS/Ca^{2+} signals. **(B)** The Squeeze Cell hypothesis [135] for systemic signalling. A hydraulic wave propagates through the xylem, squeezing the adjacent cells (in red). Mechanosensitive channels in these cells initialise a signalling cascade that induces JA production, in response to wounding. **(C)** Calcium Induced Calcium Release between neighbouring TPC1s and passage of Ca^{2+} through the plasmodesmata (PD) might explain the waves observed by Choi *et al.* [21]. **(D)** ROS and/or Ca^{2+} could be packed into vesicles to be transported through cells. **(E)** A process of ROS induced ROS release may propagate a ROS signal through a network of mitochondria/chloroplasts. **(F)** Electrical signals may mediate the spread of a signal from one end of a cell to the other. **(G)** Micro-propagation as in (C) but also utilising the ROS producing capabilities of RBOHD. ROS triggers Ca^{2+} influx which triggers ROS production in a self propagating system.

3.1 Variation Potentials and Passive Signal Propagation

Wounding a plant generates a systemic electrical signal known as a Variation Potential [26]. VPs are unique amongst electrical signals in that they appear able to propagate past regions of dead or poisoned tissue that would block APs [210]. The mechanism propagating VPs must be capable of passively propagating through these regions of dead tissue, a mechanism that is distinct from the self-propagating ionic species of APs and ROS or calcium waves [21, 26, 196]. The measured VP therefore reflects the generation of successive depolarisations of each cell in sequence, which appear as an electrical propagation, but are in effect electrically uncoupled [26]. Preventing generation of the electrical signal in one cell, does not prevent generation of the electrical signal in later cells.

It has been widely suggested that passage of hydraulic waves triggers VPs [26, 134], plausibly through activation of mechano-sensitive ion channels [192]. An alternative hypothesis, originally proposed by Ulrich Ricca a century ago [212], is that a chemical substance, released into the vasculature upon wounding, triggers electrical signals in nearby cells [127, 203]. Such a signal may propagate because the chemical diffuses through the vasculature. However, neither of these models can directly explain the speed of apparent VP propagation. VPs typically propagate at speeds on the order of 1 mms^{-1}, but the diffusion of chemical species is typically 2 orders of magnitude slower [213], while hydraulic waves travel at around 1500 ms^{-1}, the speed of sound in water [127, 192].

A number of hypotheses arose to understand the discrepancies between VP and other signal speeds. Malone [127] examined how flow within the vasculature, directed away from the site of wounding, could be responsible for propagating a chemical signal at speeds in excess of those achievable by diffusion alone. Stahlberg *et al.* [134], on the other hand, showed how application of small pressure changes to the roots of pea plants generated VPs with a delay that depended on distance from the roots and on the size of the applied stress. They proposed that a xylem hydraulic signal mediated radially propagating turgor pressure changes that were

responsible for the electrical signals in the epidermis. However, Vodeneev *et al.* [203] showed in wheat that excision of the leaf tip within 1 s of burning prevented transmission of the VP, whereas later excisions had no effect, putting an upper limit on the speed of the signal that is much less than expected for a hydraulic wave.

In this section, we examine both hydraulic and chemical hypotheses through the use of simple mathematical models based on the underlying physical processes.

3.1.1 Model of chemical diffusion with vascular flow can recapitulate VP propagation in wheat

One way in which VPs might be propagated is through the movement of a chemical signal [127, 203, 212], as illustrated in Figure 3.1. The migration of molecules from the wounding site could trigger electrical reactions in cells adjacent to the vasculature, which could propagate radially to the epidermis in the same way that an AP propagates [26], or the chemicals themselves could diffuse from the xylem through the apoplastic space, initiating electrical signalling in neighbouring cells. Furthermore, such a model is consistent with the ability of VPs to pass across regions of dead tissue [210].

Vodeneev *et al.* [203] suggested a model in which a chemical species diffuses through the vasculature, but to fit their model to VP propagation data required a diffusion constant of $4.5 \times 10^6\,\mu\mathrm{m}^2\mathrm{s}^{-1}$, orders of magnitude greater than that observed experimentally [213]. This estimate, however, did not take into account the flow through the xylem. Xylem flow could carry any chemical messengers through the plant and trigger electrical signals in nearby cells. For a flow rate, u, and diffusion rate, D, the flux of a chemical species obeys

$$J = D\nabla c + uc, \tag{3.1}$$

where c is the concentration of the species. Triggering generation of a VP within a cell in this model would require some threshold concentration of the chemical, which we denote c_{th}, representing the quantity of the species required to activate sensitive channels. The distance from the wounding site at which the chemical has just reached this concentration, r, therefore obeys

$$r = ut + \sqrt{-4Dt \log \frac{2c_{\mathrm{th}}\sqrt{\pi Dt}}{c_0}}, \tag{3.2}$$

where c_0 is the initial concentration of the chemical. For a small molecule, a typical diffusion rate is $100\,\mu\mathrm{m}^2\mathrm{s}^{-1}$ [213]. Using this we can fit to the available data from Vodeneev *et al.* [203] with a background flow velocity of $1.7\,\mathrm{mms}^{-1}$ (Figure 3.2). The xylem flow rate in wheat has been measured as $0.8\,\mathrm{mms}^{-1}$ [214], which is the same order of magnitude as the model. The failure of the model to fit the final points of the data is likely due to our assumption of a constant flow velocity, which is likely to be an oversimplification as the flow away from the wound site will slow as the fluid from the wound site is drawn into the xylem [127].

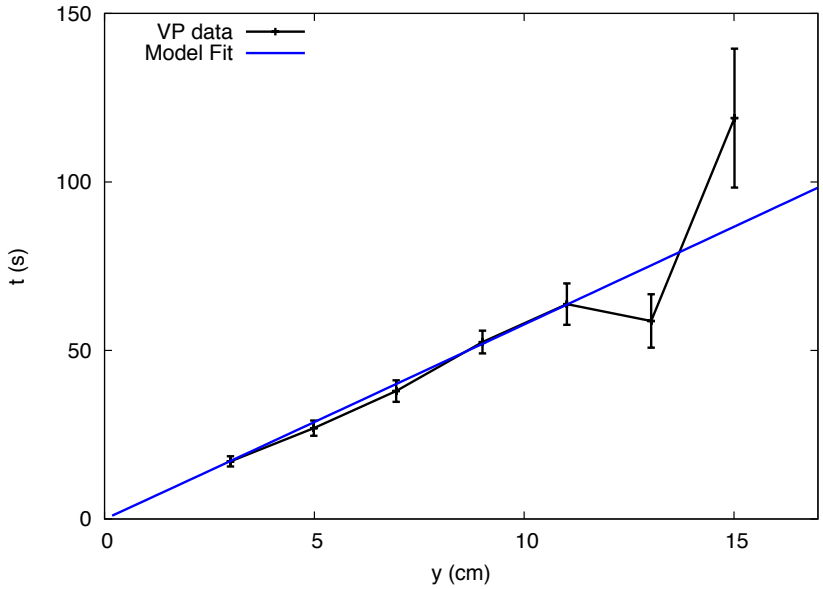

Figure 3.2: A model of chemical diffusion in a background flow fits VP propagation data from wheat. Experimental measurement of surface electrical changes (black line) in response to burning leaf tips of wheat, reproduced from Vodeneev *et al.* [203]. A model of chemical diffusion in the presence of background xylem transport (blue line) produces a good fit to this data for realistic parameters (see main text for details). Distance along the longitudinal axis of the leaf (y, as in Figure 3.3) is plotted against the time after burning, t.

3.1.2 Hydraulic model predicts velocity of electrical signals varies with radius

Axial hydraulic waves within the xylem might give rise to electrical signals at the epidermis and within the phloem by means of a radially propagating pressure wave [134, 135]. This signalling process is illustrated in Figure 3.1B, and in more detail in Figure 3.3. The axial hydraulic wave, travelling with velocity, v_{xylem}, triggers radially propagating signals which travel at velocities, $v(y)$, depending on the position, y, along the plant axis. When this radial disturbance reaches a cell, it causes the generation of the electrical signal. The delay time between passage of the hydraulic wave and possible detection of an electrical signal at a radial distance, r, from the xylem is $t^d(r, y) = r/v(y)$.

If the behaviour of the radially propagating disturbance did not depend on position, $v(y + \Delta y) = v(y)$, then the surface electrical signal would appear to travel at the same speed as the axial hydraulic wave. Stahlberg *et al.* [134] proposed that the decreasing amplitude of the hydraulic wave might trigger slower radial disturbances. In this case, radial disturbances initiated further from the wounding site would propagate with a slower velocity, $v(y + \Delta y) <$

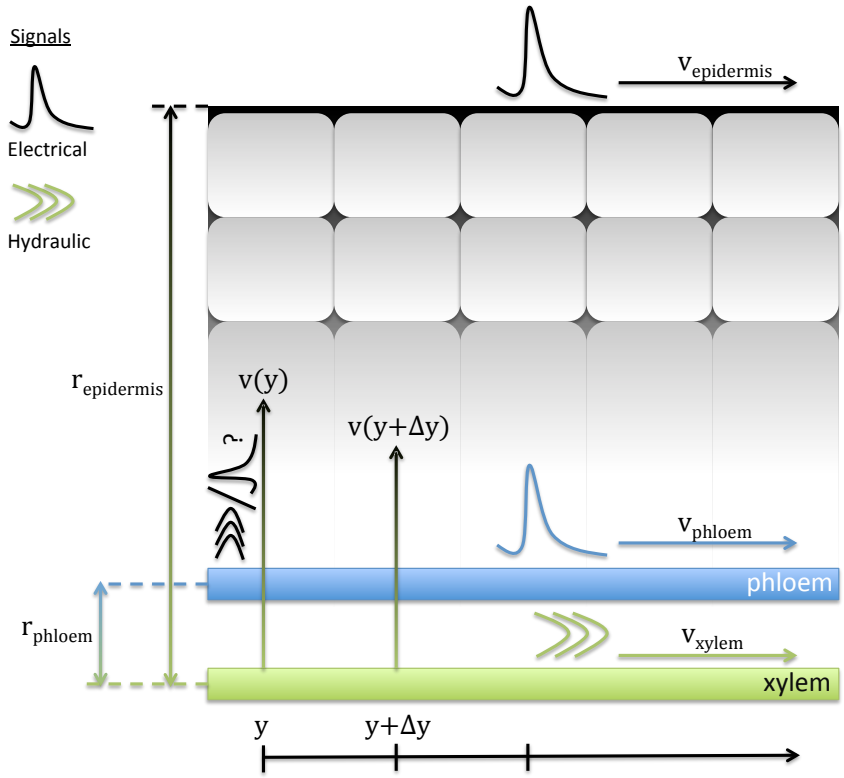

Figure 3.3: Model of electrical signal propagation in response to hydraulic waves. Propagation of an axial hydraulic wave through the xylem (with velocity v_{xylem}) has been proposed to trigger electrical signalling at the plant epidermis and within the phloem. These electrical signals appear to travel at velocities of $v_{\text{epidermis}}$ and v_{phloem} respectively. Differences in these velocities will occur if the signal propagating radially from the xylem varies with position, $v(y) \neq v(y + \Delta y)$, see main text for details. The phloem and epidermis are at a distance r_{phloem} and $r_{\text{epidermis}}$ from the xylem, respectively.

$v(y)$, and delay times would increase with distance, y.

In this model, in which the driving wave propagates through the vasculature and activates radial disturbances that propagate towards the epidermis, the expected delay time also depends on r, the radial position at which the electrical signal is measured. Electrical signals in response to wounding have been measured on both the epidermis [193] and in the phloem [195]. Since the delay time scales with distance from the xylem, the delay time that would be measured in the phloem should be less than the delay time measured at the epidermis,

$$t^d_{\text{phloem}} = \frac{r_{\text{phloem}}}{r_{\text{epidermis}}} t^d_{\text{epidermis}}, \tag{3.3}$$

assuming the radial velocity is constant. If there is a decay in the velocity of the radial disturbance during its propagation, the difference in delay times would be further exaggerated. From this we would expect a faster signal to be measured in the phloem compared to the surface. Based on the model in Figure 3.3, the velocities would be expected to scale according

to the relative radial distances,

$$v_{\text{phloem}} = \frac{r_{\text{epidermis}}}{r_{\text{phloem}}} v_{\text{epidermis}}. \tag{3.4}$$

Within the *Arabidopsis* stem and root, the value of $r_{\text{epidermis}}/r_{\text{phloem}}$ is in the region of 5-10 [215, 216], while in the rosette leaf petiole, $r_{\text{epidermis}}$ is at least 10 times r_{phloem} [216]. The hydraulic wave hypothesis would therefore predict velocities for electrical signals in the phloem that are 5-10 times the speed of VPs measured at the epidermis. This estimate assumes that the radial disturbances travel at constant velocity. Stahlberg *et al.* [134] suggested that it is changes in cell turgor that trigger the VP. These changes take longer to occur the further from the xylem they are measured [217]. There is a decay in radial propagation, therefore. However, this decay would *increase* the difference between phloem and xylem signal speeds.

Experimental measurements of VP speeds in *Arabidopsis* do not support the predicted differences [193, 195]. Mousavi *et al.* [193] measured surface VPs that propagated at speeds of 0.8-1.5 mms^{-1} in response to excision of the leaf tip. Salvador-Recatala *et al.* [195] measured the velocity of electrical signals in the phloem in response to chewing insects (1 mms^{-1}) and cutting (2.5 mms^{-1}). In order for phloem and epidermal electrical signals to have approximately the same apparent velocity, the radial signal velocity must be the same at all points along the plant axis, $v(y + \Delta y) = v(y)$. However, this would require them to propagate at the same speed as the underlying xylem signal, and no delay would be observed.

3.1.3 Summary

In this section we have shown that a chemical signal, aided by wound-induced flow [127, 218] through the xylem is consistent with measured VP propagation [203], but a hydraulic signal, that propagates faster than the VP, is inconsistent with measured data [193, 195]. The fact that phloem and epidermis VPs appear to propagate at approximately the same velocity indicates the radial signal is constant and independent of position along the plant axis ($v(y + \Delta y) = v(y)$), which further requires them to be propagating at the same speed as the underlying xylem signal. A hydraulic signal could not propagate this slowly, but we have shown a chemical signal could be propagated at the correct speed. We therefore favour a chemical model for transmission of VPs in response to wounding.

3.2 Feasibility of active propagation models to explain systemic Ca^{2+} signals

Active signals require regular regeneration. Typically the measured signal is generated within a cell (or part of a cell), and that signal then causes the generation of the signal in an adjacent cell (or region of a cell). These self-propagating signals are the basis of action potential propagation in animal nerve cells [211] and intra-cellular Ca^{2+} waves. In plants, similar signals propagate using active mechanisms [21, 26], but the absence of dedicated nervous systems and

different signalling machinery means that these mechanisms are different to those of animals. As with studies in animals, mathematical modelling can provide valuable insights into the processes underlying systemic signals.

The Ca^{2+} wave in response to local salt stress has been particularly well defined in the root system of Arabidopsis [21], with velocities measured under a number of different conditions (Table 3.1). The wave propagates through the root cortical and endodermal cells at a velocity of 390 ± 40 μms^{-1} and induces a range of stress response genes in the leaves. Inhibition of Ca^{2+} release pathways with pharmacological agents blocked propagation of the wave, indicating that it had a self-propagating mechanism. Disruption of the *Two Pore Channel 1* (TPC1) gene resulted in a substantial drop in wave speed, while overexpression of TPC1 increased the speed of the wave by a factor of 1.7 (Table 3.1). Recent work has further demonstrated that knockouts of TPC1 also disrupted a Ca^{2+} wave triggered by herbivory [25]. TPC1 in Arabidopsis encodes the slow vacuolar (SV) channel [24, 219] that has been shown to be permeable to Ca^{2+} (and other ions) and has been proposed to mediate Ca^{2+} release from the vacuole [220]. This set of wave speeds means the TPC1 mediated Ca^{2+} wave offers an ideal situation for mathematical analysis, and will be the focus of the remainder of this chapter.

A number of possible models were proposed by Gilroy *et al.* [204] to explain the propagation of the Ca^{2+} wave (Figure 3.1C-G). These possibilities include CICR via TPC1, vesicle transport [221] with Ca^{2+} and ROS linking neighbouring cells, mitochondrial ROS-induced ROS release (RIRR) [222], electrical signalling (involving Ca^{2+} and possibly ROS) [26], and ROS induced Ca^{2+} release (RICR). In this section, we apply simple models to test these possible mechanisms and identify which we will take forward for future analysis.

3.2.1 Calcium Induced Calcium Release Models

The existence of self-propagating Ca^{2+} waves [21, 25, 197] suggests the possibility of a CICR mechanism via the vacuolar channel TPC1 (Figure 3.1C). TPC1 is gated by both voltage and by binding of calcium [219, 223, 224, 225], but for the purposes of a model it is sufficient to consider a series of calcium induced calcium releases. Calcium diffuses through the cytosol and activates TPC1 that causes (directly or indirectly) the release of calcium from the vacuole. This released calcium will diffuse to trigger the next channel, generating a saltatory wave through the cell [108]. At the end of the cell, the calcium could diffuse through plasmodesmata to trigger channels in adjacent cells.

We consider the diffusion of calcium in one dimension. We will assume the calcium sources are distributed equally throughout the plant with separation, d, and that they fire with strength, σ, when the calcium concentration at the source location is greater than some threshold value, c_{th}. Under these circumstances, the wave velocity is given by [108],

$$v \sim \frac{4D}{d} \log \frac{\sigma}{dc_{\text{th}}}, \tag{3.5}$$

as described in Section 1.3.2, for diffusion constant, D. Values for the release strength, σ, and firing threshold, c_{th}, are not well defined, but we can use the wild type velocity (Table 3.1)

Table 3.2: Parameters used in CICR model

Symbol	Value	Units	Ref
D	20	μms^{-2}	[168]
d_{WT}	1	μm	[226]
d_{OxTPC1}	0.6	μm	[24]

along with the parameters in Table 3.2 to restrict the value of the ratio to $\sigma/c_{\text{th}} = 139.42\,\mu$m. We can use (3.5) to predict how the velocity of such a wave would vary with channel separation, d (Figure 3.4).

In the TPC1 overexpressor, we expect the density of channels to increase. Peiter *et al.* [24] measured the average numbers of TPC1 channels in vacuolar membrane patches in wild type and the overexpressor, and with the average channel density measured by Pottosin *et al.* [227], we would expect the channel separation d in the overexpressor to be about $0.6\,\mu$m. The model therefore predicts a wave speed of $v_{\text{OxTPC1}} = 726\,\mu\text{ms}^{-1}$, well within experimental errors, as illustrated in Figure 3.4.

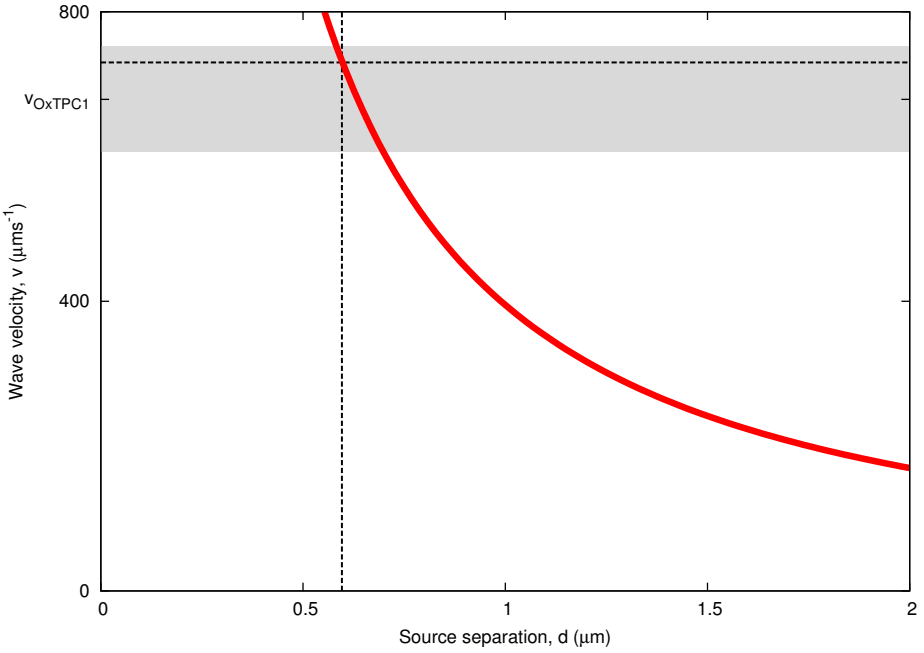

Figure 3.4: CICR model captures velocity of Ca^{2+} waves. Variation of predicted Ca^{2+} wave velocity with channel separation, d, using (3.5). The system is fitted to wild type velocity $395\,\mu\text{ms}^{-1}$ at $d = 1\,\mu$m. For OxTPC1, Peiter *et al.* [24] suggests a value of $d \approx 0.6\,\mu$m, giving a predicted velocity of $726\,\mu\text{ms}^{-1}$ (dashed lines), well within 1 standard error of the measured value v_{OxTPC1} (grey region).

We conclude that a CICR mechanism could propagate the Ca^{2+} waves observed by Choi *et al.* [21]. This is not the full story, however. Application of the Ca^{2+} channel inhibitor Lanthanum Chloride (La^{2+}) completely blocks propagation of the Ca^{2+} wave, yet a (dramatically reduced) Ca^{2+} wave is still present in the *tpc1* mutant. There is likely to at least be a plasma membrane localised Ca^{2+} channel involved in propagation of this wave (since La^{2+} acts on PM-localised channels). Additionally, we have neglected in this simple treatment any influence of a cell wall. In future sections, we shall explore this model in more depth.

3.2.2 Vesicle Transport

To mediate rapid signal transmission, another possible mechanism involves vesicle transport (Figure 3.1D) [204]. In this model, ROS and/or Ca^{2+} might be packed into vesicles, directly or through binding proteins, that are transported along the cytoskeleton. The use of vesicles to transmit intracellular signals has been observed in animal neurons [221], allowing these signals to be maintained over long distances. At their best, vesicle speeds have reached 2-4 μms^{-1} in mice cells [228], which is interestingly faster than the speeds of purified molecular motors like kinesin or dynein [229]. In plants, vesicle trafficking has been measured in pollen tubes, 1.1 μms^{-1} [230] to 1.9 μms^{-1} [231], and *in vitro* with Golgi vesicles, 1.8 μms^{-1} [232]. The speed of this transport is much too low to be the driving force behind the comparatively rapid systemic signalling that has been observed.

3.2.3 Mitochondrial RIRR

In animal cells, mitochondrial stress can be propagated between neighbouring mitochondria through a process of ROS-induced ROS release [222], of particular importance to function, and disfunction, of mammalian heart cells. These waves propagate through the mitochondrial network through a whole cell. A similar signalling process could occur in plant cells (Figure 3.1E) involving mitochondria and perhaps chloroplasts given their similar roles as intracellular signalling hubs [233]. However, the speed of such waves in human cardiac muscle cells, containing particularly large numbers of mitochondria, are only around 0.31 μms^{-1} [222]. It is unlikely that plant cells would be able to propagate such signals at the rates required for mitochondrial RIRR to be the underlying mechanism for propagation.

3.2.4 Electrical Signalling

Electrical signals were the first directly measured systemic signals in plants. Since then, multiple types of electrical signal have been identified in response to multiple stimuli [26, 124]. Electrical signals are categorised into either action potentials, variation potentials [26, 134, 124] or the recently proposed system potentials [194] and are distinguished by their kinetic properties. APs show all-or-nothing response kinetics, whereas VPs have an amplitude dependency on the stimulus. APs also propagate at a constant speed, where as VPs have a decaying velocity. However, it is becoming clear that such distinctions are difficult to

maintain in many circumstances [26]. The electrical response to leaf wounding shows a mixture of AP and VP dynamics [195], and its velocity varies over the course of its transmission, slowing in the centre of the plant but accelerating again within the receiving leaf [193]. There are also clear connections between electrical signals and Ca^{2+} and ROS dynamics [26]. The velocity of the ROS wave is the same as measured electrical signals (Table 3.1), and the same stimulus that triggers electrical signals has been shown to further trigger a (TPC1-dependent) Ca^{2+} wave [25]. The propagation of Ca^{2+} and ROS waves through a plant could potentially be driven by the changes in membrane potential that result from the release or generation of these species, and systemic electrical signals may also be self-propagating.

The propagation of an electrical signal (Figure 3.1) is mediated by movement of ionic species. The opening of channels triggers a flux of ions between cellular compartments that results in a change in membrane potential that can trigger other channels to open. Since the potential varies spatially across the membrane, the potential change can be propagated across a membrane by the opening of successive channels in a channel array. The propagation of membrane voltage, V, obeys the cable equation [234],

$$\frac{\partial V}{\partial t} = \frac{\partial^2 V}{\partial x^2} + f(V), \tag{3.6}$$

where $f(V)$ is some expression accounting for the current due to the ion channels. This system has wave like solutions of the form $V(x,t) = U(x+vt) = U(\xi)$ for some value of the velocity, v. The new variable, ξ, is a coordinate system that moves with fixed speed, v. It has the advantage of converting (3.6) to an ordinary differential equation

$$U_{\xi\xi} - vU_{\xi} + f(U) = 0. \tag{3.7}$$

The form of any solution will depend on the functional form of the various currents in the system, $f(U)$, which can be highly complicated, the resulting system typically being intractable analytically. However, there are valuable scaling relationships that we can use [234]. If the number of channels is changed by a factor α, then the new system propagates a potential wave

$$\bar{U}'' - s\bar{U}' + \alpha f(\bar{U}) \tag{3.8}$$

at speed s. By performing the substitution, $\bar{U}(\xi) = U(\sqrt{\alpha}\xi)$, we transform (3.8) into (3.7) with speed $s = v\sqrt{\alpha}$. If the stress response to salt [21] is propagated by an electrical signal, we would expect the increase in TPC1 number to result in an increase in wave speed according to $v_+ = v_{\mathrm{WT}}\sqrt{\alpha}$ where α is the ratio of TPC1 in the overexpressor to TPC1 in WT, $\alpha = 24.2/8.6$ [24]. Using this simple model, and the wild type velocity (Table 3.1), predicts an overexpressor velocity of $v_+ = 663\ \mu\mathrm{ms}^{-1}$, well within the experimentally determined value. Hence an electrical signal could be responsible for propagating the observed Ca^{2+} wave.

3.2.5 ROS induced Calcium release

Rapid propagation of an increase in ROS produced by the NADPH oxidase AtRBOHD (Respiratory Burst Oxidase Homolog D) has been reported in response to stress signals [196].

RBOHD is ubiquitously expressed throughout Arabidopsis plants and is localised to the plasma membrane of cells [235]. It is responsible for production of reactive oxygen species such as H_2O_2 in the apoplast and is involved in a range of signalling processes, such as defence [236, 237] and the opening and closing of stomata [30, 238]. Furthermore, it has been shown to be essential to the propagation of the ROS waves of Miller *et al.* [196]. How RBOHD and ROS fit into the picture of systemic signalling mechanistically is yet to be understood, however.

ROS and Ca^{2+} signalling pathways are known to overlap, and there is potential for waves of Ca^{2+} and ROS to act together in propagating the systemic signal (Figure 3.1G). A conceptual model for ROS wave propagation was produced by Dubiella *et. al.* [198] where Ca^{2+} acting via the Calcium-dependent Protein Kinase family member 5 (CPK5) stimulates ROS production from the plasma membrane NADPH oxidase RBOHD and ROS is able to trigger Ca^{2+} influx across the plasma membrane into cells via ROS regulated plasma membrane Ca^{2+} channels [239]. This provides a self-propagation mechanism in which ROS triggers plasma membrane Ca^{2+} influx into the cell potentially triggering CICR from the vacuole. The cellular Ca^{2+} rise in turn activates RBOHD that then produces more apoplastic ROS. This ROS could travel through the apoplast and trigger the same process in the neighbouring cell.

We will summarise this process by a ROS-induced ROS release model, allowing us to re-use the formalism from Section 3.2.1. Now, c is the concentration of ROS in the apoplast. ROS does not activate the neighbouring RBOHD directly, but via triggering increased Ca^{2+} in the cytoplasm, which in turn activates RBOHD. The critical threshold parameter c_{th} incorporates the indirect nature and complexity of this activation process in one variable and so provides a mathematical means through which changes in Ca^{2+} behaviour can feedback on ROS propagation without needing to parameterise the detailed molecular mechanisms behind this process.

ROS diffusion in the apoplast is predicted to be faster than that of Ca^{2+} in the cytoplasm as cytoplasmic Ca^{2+} buffering and sequestration mechanisms limit the cytoplasmic movement of this ion [11, 168]. RBOHDs also exist at a higher density than TPC1 [240]. Therefore, the velocity of the ROS-assisted wave has a different functional form than from a purely CICR-driven process,

$$v_{\text{WT}} \sim \sqrt{\frac{\sigma D}{d u_c \tau_R}}. \tag{3.9}$$

If more calcium is being produced in a cell (because of TPC1 overexpression), then we would expect the RBOHDs to be activated more quickly, which can be represented in the model by a decreased c_{th} irrespective of the precise molecular mechanism responsible for the Ca^{2+}-dependent activation. Therefore, in the TPC1 overexpressor we would expect a velocity

$$v_+ \sim \sqrt{\frac{\sigma D}{d c_{\text{th}} \tau_R \alpha}} = \frac{1}{\sqrt{\alpha}} v_{\text{WT}}, \tag{3.10}$$

where α is the decrease in the firing threshold, c_{th}, due to the increase in TPC1 channels in the overexpressor. The number of channels increases by a factor of 24.2/8.6 [24]. The

rate of activation of RBOHD should therefore increase, and c_{th} should decrease, by this ratio. Therefore, $\alpha = 8.6/24.2$ and the model predicts $v_+ = 662.6\ \mu\text{ms}^{-1}$, which is well within the experimental uncertainty of the measured value from the overexpressor. Hence this Ca^{2+} assisted ROS model is able to produce a very good fit to the data.

3.2.6 Summary

In this section we have explored possible mechanisms of propagating a systemic Ca^{2+} wave as observed by Choi *et al.* [21]. Since the wave can be blocked by local application of a Ca^{2+} channel blocker, La^{2+}, it must utilise an active mechanism (Figures 3.1C-G). By examining simple mathematical models or analogous systems in animal systems, we conclude that vesicle transport or mitochondrial RIRR are unlikely mechanisms, whereas CICR, voltage driven propagation or RICR are plausible mechanisms for the propagation of this wave.

It is commonly perceived that self propagating electrical signals are transmitted via the vasculature due to the optimal conditions for signal propagation that they provide [124, 26]. However, the systemic Ca^{2+} signal of Choi *et al.* [21] is restricted to the cortex and endodermis cells within the roots, and is not present in the vasculature. We choose therefore to focus our attention on the CICR and RICR models, but we note that the use of the FDF model and threshold activation mechanisms does not exclude electrical/voltage based mechanisms for channel activation. The flow of Ca^{2+} ions across the tonoplast will shift the membrane potential, and the threshold value, c_{th}, might be represent the build up of charge as well as the direct binding to channels. This is particularly applicable here as activation of TPC1 involves both Ca^{2+} binding and voltage changes [223, 224, 225]. The FDF model has the advantage over the voltage model of Section 3.2.4 of making it easy to examine different channel distributions, as we shall do in the following sections.

3.3 Calcium Induced Calcium Release waves in physiological cells

We previously showed that with a regular, one dimensional array of TPC1 Ca^{2+} channels, we could reproduce the Ca^{2+} wave speeds measured by Choi *et al.* [21] (Section 3.2.1). However, TPC1 is localised to the vacuole and within a cell the vacuole typically occupies 50-90% of the interior volume [241], leading to two distinct regions needing to be modelled to describe propagation of the wave. In the first, the Ca^{2+} wave is propagating through the cytoplasm surrounding the vacuole, and propagation can be modelled as before (Section 3.2.1). In the second region, the wave must move between neighbouring cells. If the mechanism behind propagation is a self-propagating wave of CICR from the vacuole mediated by TPC1, the Ca^{2+} must passively diffuse between the vacuoles in these adjacent cells, probably through the plasmodesmata. In this section, we will incorporate this feature into our earlier CICR model.

With the vacuole containing approximately uniformally distributed TPC1 channels involved in releasing Ca^{2+}, the wave in the first region has a velocity given by (3.5). When crossing between vacuoles, a distance d_v, we assume the plasmodesmatal coupling poses no obstacle to diffusion so that the model has the best chance of propagating a wave at maximal speed. The Ca^{2+} moving from the previous cell takes a time, T, to activate the first channel on the next vacuole. The concentration profile for a single release evaluated at the time of activation of the next channel (when $c = c_{\text{th}}$) would then satisfy the expression

$$c_{\text{th}} = \frac{\sigma}{\sqrt{4\pi DT}} \exp\left[-d_v^2/4DT\right]. \tag{3.11}$$

We assume that the activation of the first channel in the neighbouring cell is dominated by calcium released from one channel, which we will later find to be a reasonable approximation. The velocity of a Ca^{2+} wave that would be observed experimentally would then be the average velocity across these two regions. The spatial and temporal resolution of the empirical experiments measuring these rates is insufficient to robustly distinguish transmission through each cell versus the cell-to-cell component crossing d_v, even using the high-spatial and temporal resolution afforded by confocal microscopy. Therefore, the transit speed between the two regions cannot be separated and so is averaged in the empirical measurements. For a cell of length L this average speed is given by

$$v_{\text{predicted}} = \frac{L}{\frac{L-d_v}{v} + T}. \tag{3.12}$$

The time taken to cross the cell wall region (3.11), and the velocity in the cytoplasm surrounding each vacuole region (3.12), both depend on the parameter ratio σ/c_{th}. This dependency leads to the conclusion that in order to decrease time spent crossing the cell wall region the cell must change the release properties of the channels, but this has a corresponding effect on how quickly the wave crosses the cytoplasm in the vacuolar region. We used the measured velocity in the wild type, $395\,\mu\text{ms}^{-1}$, to calculate a value for this parameter ratio, σ/c_{th}. We then used this value to determine if this model can recapitulate the velocity in the TPC1 overexpressor, $680 \pm 70\,\mu\text{ms}^{-1}$. Using the channel separation in the overexpressor, d_{OxTPC1}, (Table 3.2) and the ratio σ/c_{th} calculated from the wild type data, we calculated the expected velocity in the TPC1 over-expressor for a range of cell lengths and inter-vacuolar distances, d_v, covering those found in the regions of the Arabidopsis root where empirical wave speed determinations have been made (Figure 3.5B).

We see that the model can only recapitulate the velocity in the overexpressor when d_v is sufficiently small. This result did not depend on our choice of diffusion constant (Figure 3.6A), but could be affected by changes in the channel separation, d (Figure 3.6B). Since our chosen value for d came from TPC1 channel density data from mesophyll cells [226] and the wave travels through the root, different expression levels of TPC1 could result in different densities of TPC1 on the vacuolar membrane. Our collaborators tested for such potential differences with QPCR analysis of roots and shoots dissected from plants grown as for the Ca^{2+} imaging.

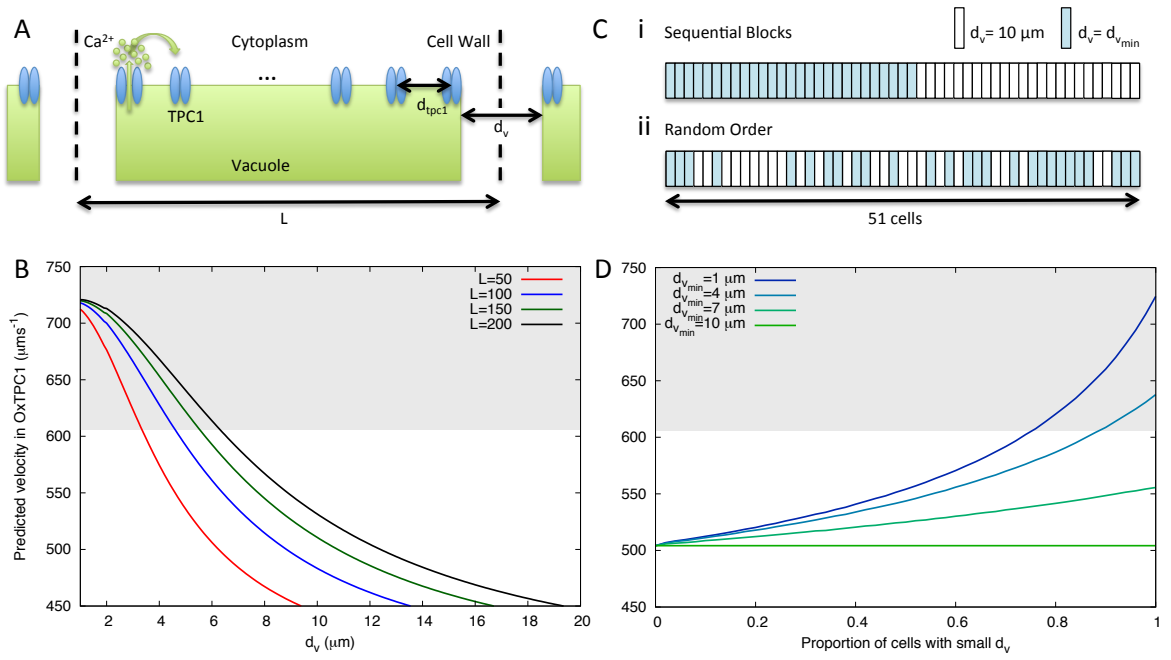

Figure 3.5: Ca^{2+} wave propagation via CICR and Ca^{2+} diffusion through the plasmodesmata can explain observed velocities only under limited circumstances. (A) Scheme of the model. Calcium is released through activated TPC1, it diffuses through the cytoplasm a distance d_{tpc1} to activate neighbouring TPC1 channels. At the end of a cell (length, L), the signal diffuses passively to activate the neighbouring cell (a distance d_v) through the plasmodesmata. **(B)** Predicted wave speeds for the TPC1 overexpressor (OxTPC1) for a range of L and d_v using equations (3.5), (3.11 and (3.12), where the model parameters are chosen to fit the wild type velocity (Table 3.1). The grey region indicates one standard deviation in the observed velocity. **(C)** To account for distributions in d_v, two simple schemes were tested. A 1-dimensional array of cells with either $d_v = 10\,\mu$m (white) or $d_v = d_{v_{\min}}$ (blue) were set up in sequential order (i) or in random order (ii). **(D)** The result of varying the proportion of cells within (Ci) with $d_v = d_{v_{\min}}$, as described in (B), and utilizing a full simulation (see full text).

This analysis showed no statistically significant difference between root and shoot expression in wild type. In the overexpressor, shoots showed 1.9 fold higher transcript level than the roots of the same plants. Any change in actual channel density between roots and shoots will likely be small.

Measurements of cell wall thickness [242], and imaging of tonoplast intrinsic proteins (TIPs) [243, 244, 245, 246] suggest values of d_v that range from $1 - 2\,\mu$m up to $10\,\mu$m and even $60\,\mu$m. Due to the variability in such parameters drawn from the literature, our collaborators used the Green Fluorescent Protein (GFP) signals in the images from the Ca^{2+} measurement data to visualise the cytoplasm of the cells used for Ca^{2+} wave speed measurement (see Section 3.6) and so define where the vacuoles within each cell likely ended. They then measured the distance between the vacuole (where the Yellow Fluorescent Protein

(YFP) signal was < 2 s.d. above background) in one cell to the vacuole in the adjacent cell using ImageJ [247]. As the Ca^{2+} wave speed is constant throughout the root at $\sim 400\,\mu\text{ms}^{-1}$ in wild type [21], we concentrated on making these measurements in images taken at the $1000\,\mu$m region from the root tip to allow direct comparison with the data in Figures 3.9 and 3.10 which focus on Ca^{2+} wave responses at this point in the root. Using this approach, average cytoplasmic lengths between vacuoles in adjacent cells were: $4.4 \pm 1.2\,\mu$m (epidermis, mean $\pm$ s.d., $n = 29$), $5.4 \pm 1.5\,\mu$m (cortex, $n = 38$) and $4.9 \pm 1.4\,\mu$m (endodermis, $n = 41$). It is

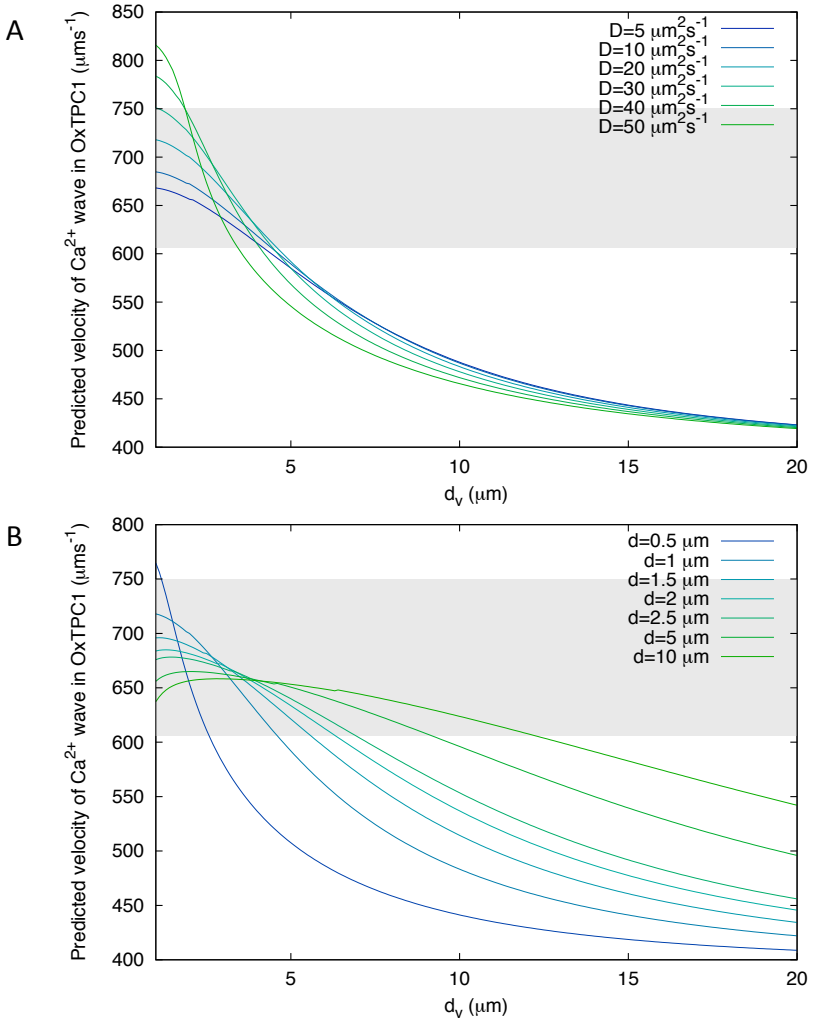

Figure 3.6: The CICR model of wave propagation is sensitive to d but not to D. Extended analysis of the results of Figure 3.5B. If the CICR model can capture the WT Ca^{2+} wave velocity, it can also capture the overexpressor velocity for different values of **(A)** diffusion constant, D, with $d = 1\,\mu$m, but not so consistently for **(B)** TPC1 separation in WT, d, with $D = 20\,\mu\text{ms}^{-2}$. In (B), d is scaled by α to give a OxTPC1 channel separation. For both cases, $L = 100\,\mu$m.

important to note that vacuoles are dynamic organelles and so these measurements should be viewed as a time-averaged value of vacuolar behaviour as they are taken from random images across multiple independent experiments.

To assess the sensitivity of the model to d_v and how well the measured inter-vacuolar distances could support a model that recapitulates measured wave speeds, we extended our modelling to consider an array of cells with two different values for d_v, distributed either as two blocks of cells (Figure 3.5Ci), or randomly amongst the array (Figure 3.5Cii). In this case we fully simulate the FDF process (1.4). A full simulation of the CICR model, illustrated in Figure 3.5A, uses equation (1.4) assuming a fast Ca^{2+} release. Under this assumption, each release site, x_i, firing at time, t_i, contributes

$$c_i = \frac{\sigma}{\sqrt{4\pi D(t-t_i)}} \exp\left[-(x-x_i)^2/(4D(t-t_i))\right] \tag{3.13}$$

to a reference point at position, x, and at time, t. The total concentration is the sum of these terms over all Ca^{2+} releases, i, $c(x,t) = \sum_i c_i$. This method requires calculation of the firing times of all releases, and therefore places an upper limit on the temporal step size of the algorithm. We typically used a step size $\Delta t = 1 \times 10^{-6}\,\mathrm{s}$. As before, we use the measured velocity in the wild type to determine the unconstrained parameter ratio, σ/c_{th}, then increase the TPC1 channel density to evaluate whether the model can recapitulate the measured velocity in the overexpressor. We ask what proportion of the array must have a small d_v value, if the largest value of d_v is $10\,\mu$m. Figure 3.5D shows how even with an inter-vacuole separation of $1\,\mu$m (the smallest value suggested in the literature [243, 244, 245, 246]) more than 75% of the cells must have this value to reproduce the empirically determined wave speed. Figure 3.5D has the cells organized according to the scheme in Figure 3.5Ci, but the choice of cell distribution has no effect on the velocities predicted.

Thus, with such inter-vacuolar distances, Ca^{2+} diffusion would not be sufficiently rapid to recapitulate experimentally determined wave speeds. We emphasis that this model has not included any kind of obstruction to propagation the plasmodesmata may produce. While the true distribution of vacuolar separations is unknown, the range of separations present in the available literature together with our analysis suggests it is unlikely that calcium alone is responsible for propagating the observed signal.

3.4 TPC1 clustering cannot explain wave speeds

The analysis outlined above assumes that TPC1 is uniformally distributed across the vacuolar membrane. However, clustering of signalling components may provide a mechanism for selective amplification and channelling of signals that could, in theory, contribute to increased signal propagation rates. Indeed, the observed distribution of channels [24] suggests that TPC1 may show a degree of clustering. The data from which we took the average TPC1 channel density in the overexpressor gives the distribution of TPC1 counts in vacuolar membrane patches. The distribution of random independent events on some fixed interval of space

Table 3.3: Testing clustering of TPC1 χ^2-test of data in Peiter *et al.* [24] with the null hypothesis that TPC1 channel counts from membrane patches have a Poisson distribution.

Line	Best fit Poisson mean	χ^2
WT	5.14288	7.2×10^8
OxTPC1	23.6695	1.54×10^6

or time (such as the area of a membrane patch) follows the Poisson distribution [167]. If TPC1 channels occur randomly with a uniform distribution across the vacuole, we would expect the data [24] to obey a Poisson distribution.

In Figure 3.7, we compare the measured distribution of TPC1 channels [24] with the best fit Poisson distribution for both the wild type and overexpressor lines. We see that the Poisson distribution does not describe either of the experimental distributions well. Indeed, performing a χ^2-test with the Poisson distribution as a null hypothesis indicates that both the wild type and the overexpressor show strong evidence of clustering (Table 3.3).

However, we determined that possible clustering does not alter the conclusions of the modelling using a number of simulations to compare the velocity of a Ca^{2+} wave in systems with increased clustering. An initial wave was generated assuming equally spaced channels. Keeping the number of channels the same, the number of channels in a cluster was increased (initially one channel per cluster with separation, d, changing to two channels per cluster with separation $2d$, and so on). We simulated the system with an array of 51 cells (as in Figure 3.7C) with all d_v values the same and a cell length of $100\,\mu$m. This analysis showed that the speed of the wave falls with increased clustering (Figure 3.7). The optimal arrangement for most rapid signal propagation is therefore when channels are equally spaced (i.e., the assumption used in the initial modelling).

The expression for the wave velocity (3.5) explains this decrease in velocity with increased clustering. Increasing the degree of clustering as suggested above involves changing the channel separation $d \to d' = 2d$, and the release strength $\sigma \to \sigma' = 2\sigma$ (since we now have two channels at a release site). The resulting velocity v' is

$$v' = \frac{4D}{d'} \log \frac{\sigma'}{d' c_{\text{th}}} = \frac{4D}{2d} \log \frac{\sigma}{d c_{\text{th}}} = \frac{1}{2} v. \tag{3.14}$$

This captures the qualitative behaviour of the wave, as shown in Figure 3.7C. Since the model neglects the inter-vacuolar separation, the fit is best for $d_v = 1\,\mu$m. In our Ca^{2+} model, this optimal distribution of channels is unlikely to explain the speed of the observed Ca^{2+} waves. An increase in clustering between WT and the TPC1 overexpressor would lead to less efficient signal propagation than the equally spaced channels our model assumed. Therefore clustering does not explain the discrepancy between the CICR model and experiment identified in Section 3.3.

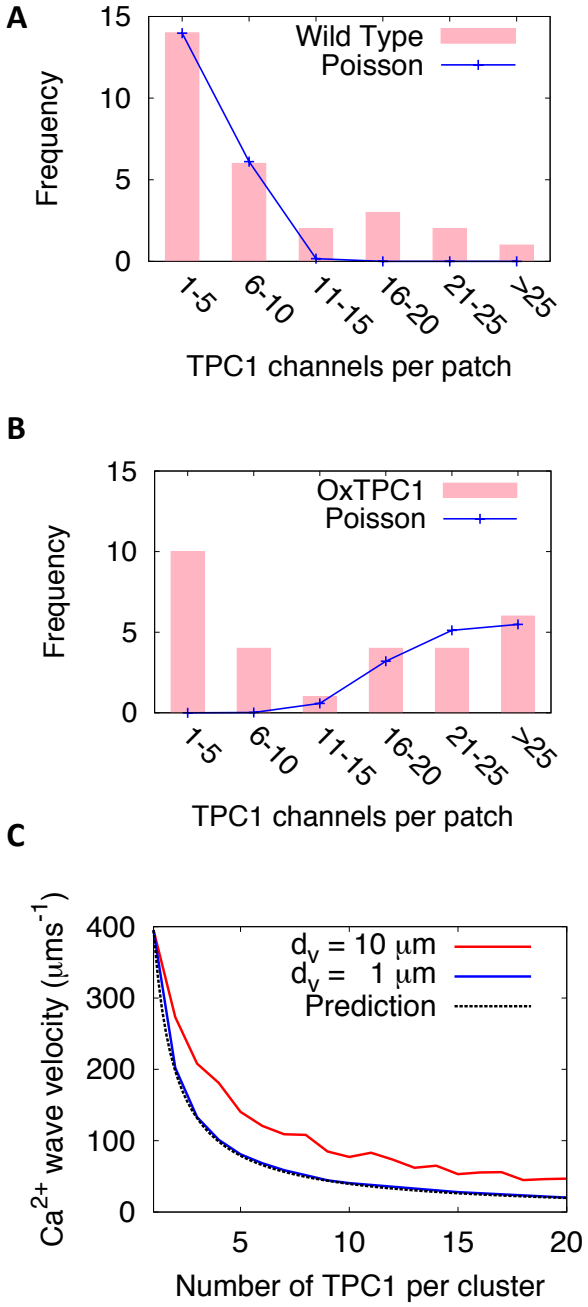

Figure 3.7: Clustering of TPC1 on the tonoplast reduces the efficiency of CICR mediated Ca^{2+} wave transmission. (A, B) Numbers of TPC1 channels observed in vacuolar membrane patches by Peiter *et al.* [24] (bars) compared to best fit Poisson distributions (lines) for wild type (A) and the TPC1 overexpressor (B). **(C)** How the velocity of a Ca^{2+} wave varies with increased clustering within the CICR model. Number of channels is kept constant as the number per cluster increases. Release strength, σ/c_{th}, was chosen so the velocity with equally spaced channels matched the wild type velocity ($395\,\mu\text{ms}^{-1}$). The dashed line shows the behaviour predicted by equation (3.14).

3.5 Cytoplasmic streaming cannot explain wave speeds

The movement of particles and organelles within the cell, mediated by myosin motor proteins along actin bundles, entrains the surrounding cytoplasm creating regions of bulk flow termed cytoplasmic streaming [248]. This flow has been proposed to be involved in aiding transport and mixing of molecular species in the cytoplasm, and can reach speeds of up to $100\,\mu\text{ms}^{-1}$ [249]. The presence of cytoplasmic streaming may present a mechanism through which CICR signalling can be enhanced.

To test whether cytoplasmic streaming enhances propagation of the Ca^{2+} wave, we included it in our CICR model. We will assume a steady flow in the direction of signalling (that which would enhance wave propagation by the greatest amount) of velocity, u. This adds an advective term to the one dimensional diffusion equation (1.4) giving

$$\frac{\partial c}{\partial t} = D\nabla^2 c + uc + \sum_{i=-\infty}^{+\infty} \frac{\sigma}{\tau}\delta(x - id)H(t - t_i)H(t + \tau - t_i), \tag{3.15}$$

for which the velocity derived by Pearson *et al.* [108] (equation 3.5) is no longer valid. Fortunately we are able to derive an equivalent expression. Firstly we assume the channels act as point sources in time ($\tau \to 0$) and then convert (3.16) to non-dimensional units using $x \to x/d$, $t \to tD/d^2$ and $c \to c/c_{\text{th}}$ giving

$$\frac{\partial c}{\partial t} = \frac{\partial^2 c}{\partial x^2} + \xi c + \frac{1}{\alpha}\sum_{i=-\infty}^{+\infty} \delta(x - i)\delta(t - t_i), \tag{3.16}$$

where $\alpha = c_{\text{th}}d/\sigma$ and $\xi = ud/D$. The concentration of Ca^{2+} then obeys

$$c = \sum_{i=-\infty}^{\infty} H(t - t_i)\sqrt{\frac{1}{4\pi\alpha^2(t - t_i)}}\exp\left(-\frac{(x - i - \xi(t - t_i))^2}{4(t - t_i)}\right). \tag{3.17}$$

If we assume that N sites have fired, and that N is large enough that we can neglect the terms with $i < 0$, then the firing time of the next channel in sequence, t_{N+1}, satisfies

$$c(x_{N+1}, t_{N+1}) = 1 = \sum_{i=0}^{\infty} \sqrt{\frac{1}{4\pi\alpha^2(t_{N+1} - t_i)}}\exp\left(-\frac{(N + 1 - i - \xi(t_{N+1} - t_i))^2}{4(t_{N+1} - t_i)}\right). \tag{3.18}$$

We define $\Delta_j = t_j - t_{j+1}$, for $j = 1, 2, ..., N + 1$. For a wave of constant velocity, we can express $v = 1/\Delta$ as long as such a solution exists (see Pearson *et al.* [108] for a thorough discussion of this). Under this assumption, we can take $t_{N+1} = t_N + \Delta$ and

$$\alpha = \sum_{i=0}^{N} \sqrt{\frac{1}{4\pi\Delta(N + 1 - i)}}\exp\left(-(N + 1 - i)\frac{(1 - \xi\Delta)^2}{4\Delta}\right). \tag{3.19}$$

For $\alpha \ll 1$, and in the limit $N \to \infty$, we find

$$\log\alpha = -\frac{1}{4\Delta}(1 - \xi\Delta)^2, \tag{3.20}$$

from which we can obtain an expression for the wave velocity that, in dimensional units, is

$$v = u + \frac{2D}{d}\log\frac{\sigma}{c_{\text{th}}d} + \frac{D}{2d}\sqrt{16\left(\log\frac{\sigma}{c_{\text{th}}d}\right)^2 + 8\frac{ud}{D}\log\frac{\sigma}{c_{\text{th}}d}}, \tag{3.21}$$

which holds for $\sigma/c_{\text{th}}d \gg 1$, and reduces to (3.5) in the limit $u \to 0$.

To investigate the effect of cytoplasmic streaming in a system of cells, we will assume that the effect of cytoplasmic streaming is present only along the vacuole, and that propagation of Ca^{2+} between the vacuoles of adjacent cells is purely diffusive. This approach allows us to apply the same method as in Section 3.3, replacing (3.5) in the vacuole region with (3.21). As in Section 3.3, we fit the model to the WT velocity, decrease the channel separation, d, and test whether the model can fit the velocity in the TPC1 overexpressor.

Figure 3.8 shows the resulting predictions for the velocity of the wave in the TPC1 overexpressor, given parameters that fit the WT velocity. This was tested for a range of possible inter-vacuolar distances, d_v, and measured cytoplasmic stream velocities $u = 1 - 100\,\mu\text{ms}^{-1}$ [249]. For all situations, the model with cytoplasmic streaming was less efficient at propagating a signal in the overexpressor than the original model (Section 3.3). This counter intuitive result is due to fitting the model to the WT velocity before simulating the overexpressor.

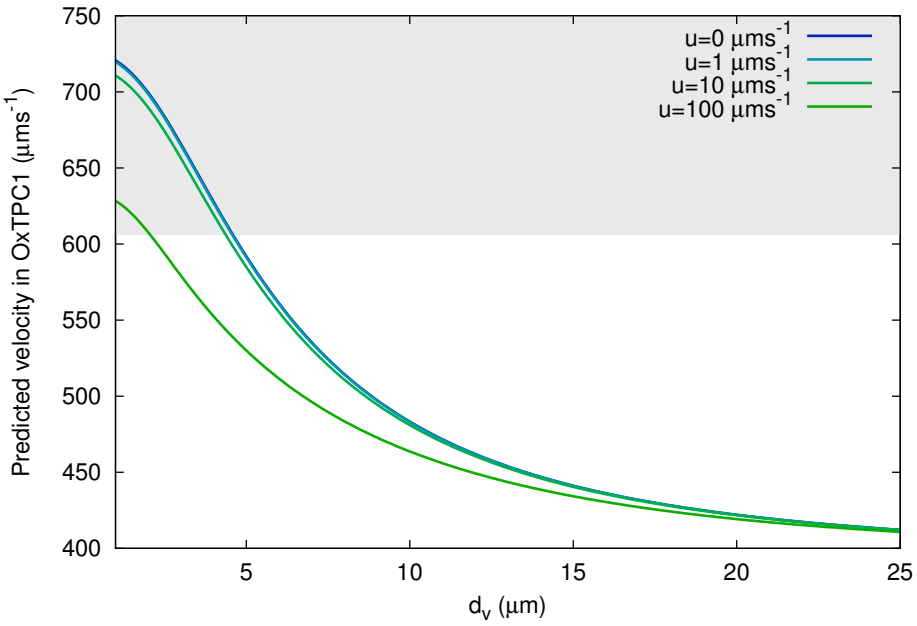

Figure 3.8: Cytoplasmic streaming does not improve the fit for CICR propagated Ca^{2+} waves. Predicted velocity in the TPC1 overexpressor (OxTPC1), for varying inter-vacuolar distance, d_v, and cytoplasmic streaming velocity, u. The grey region indicates the measured velocity in OxTPC1 with its experimental error (Table 3.1). Higher cytoplasmic stream velocities results in slower velocities in OxTPC1.

A stronger cytoplasmic stream results in a smaller contribution from TPC1 to propagate a signal at the WT velocity, so that increasing the TPC1 density to simulate the overexpressor does not have as large an effect.

3.6 Experimental validation

A self propagating Ca^{2+} wave is unable to travel at the observed velocities in model cells. Therefore, the mechanism underlying the wave observed by Choi *et al.* [21] must involve more components. Dubiella *et al.* [198] proposed a model for a joint Ca^{2+} and ROS propagated wave, that may unify the systemic signals observed by Miller *et al.* [196] and Choi *et al.* [21]. In this proposed model, raised cytoplasmic Ca^{2+} activates the NADPH oxidase RBOHD, via calcium binding kinases [198, 199]. The RBOHD generates ROS that can propagate through the apoplast to neighbouring cells, where they activate Ca^{2+} release, possibly via plasma membrane localised channels [239]. This creates a self propagating signal that requires both Ca^{2+} and ROS. We have already demonstrated the potential for a ROS/Ca^{2+} linked wave to effectively propagate a signal (Section 3.2.5), so in this section we present experimental work to test the hypothesis that a ROS wave is also involved in the salt stress induced Ca^{2+} wave.

All the experimental work in this section was performed by our collaborators Won-Gyu Choi in the lab of Simon Gilroy, Department of Botany, University of Wisconsin, Madison, WI, USA.

3.6.1 Blocking ROS production validates predictions of the ROS-assisted CICR model

To empirically test the prediction of a ROS-assisted mechanism for Ca^{2+} wave propagation, we attempted to dissect the involvement of ROS in the Ca^{2+} wave by treating the root with the ROS scavenger ascorbate and the NADPH oxidase inhibitor diphenyliodonium (DPI).

Table 3.4: Calcium wave velocities in various *Arabidopsis* lines in response to salt

Genotype	Wave velocity ($\mu ms^{-1} \pm SEM$)	Ref
WT	396 ± 28	[21]
+ 25 μM La^{3+}	0	[21]
+ 25 μM DPI	146 ± 40	This study
+ 10 mM Ascorbate	64 ± 16	This study
tpc1-2	15.5 ± 1.9	[21]
OxTPC1	679 ± 73	[21]
+ 25 μM DPI	134	This study
AtrbohD	73 ± 19	This study

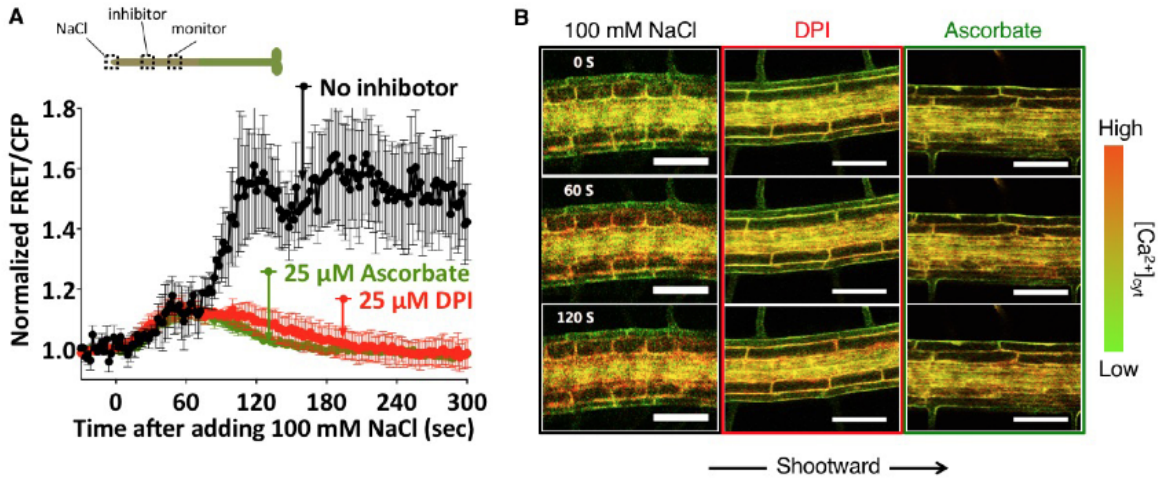

Figure 3.9: DPI and ascorbate significantly reduce Ca^{2+} wave amplitude. **(A)** Quantitative analysis of the Ca^{2+} response to local application of 100 mM NaCl to the root tip, with and without 25 μM DPI or ascorbate applied between the tip and the observation window. **(B)** Ratiometric images of the effect of DPI or ascorbate on the NaCl-induced Ca^{2+} wave. Results represent mean $\pm$ SEM of $n \geq 5$ (DPI and ascorbate) or $n = 17$ (wild type) monitored 1000 μm from the site of NaCl application. Scale bars = 100 μm. *This data and figures produced by Won-Gyu Choi in the lab of Simon Gilroy, Department of Botany, University of Wisconsin, Madison, WI, USA.*

To separate the effects of these compounds on the ability of the plant to propagate the wave versus the ability to initially trigger a stress response, we initiated a Ca^{2+} wave by locally treating the tip of the root with 100 mM NaCl in the absence of any inhibitor. The root system of the plant was growing through a Phytagel matrix and so the local treatment was applied by cutting an approximately 100 μm x 100 μm hole in the gel ahead of the root tip and letting the root apex grow into this window, which was subsequently filled with growth medium containing 100 mM NaCl. We have previously determined that this treatment localizes the salt stress to the very apex of the root and to reproducibly trigger a Ca^{2+} wave propagating shootward from the root apex [21]. Either 25 μM DPI, potassium ascorbate (dissolved in growth medium), or growth medium (negative control) were locally applied 10 min prior to the root tip NaCl stimulation to a similar window cut into the gel surrounding the mature region of the root >1000 μm shootward of the root tip. In all cases, the Ca^{2+} wave propagated at 400 μms^{-1} from root tip to the region treated with inhibitor but transit through the treatment region was altered depending on the pharmacological agent present. Calcium wave speed through the region treated with growth medium alone was maintained at 400 μms^{-1}. Treatment with either ascorbate or DPI slowed wave propagation to 64 μms^{-1} and 146 μms^{-1} respectively (Table 3.4, Figure 3.9A). These observations are consistent with a requirement for NADPH oxidase-mediated ROS production in Ca^{2+} wave transmission. Further, knockout of AtRBOHD slowed propagation of the Ca^{2+} wave to 73 μms^{-1} (Table 3.4, Figure 3.10).

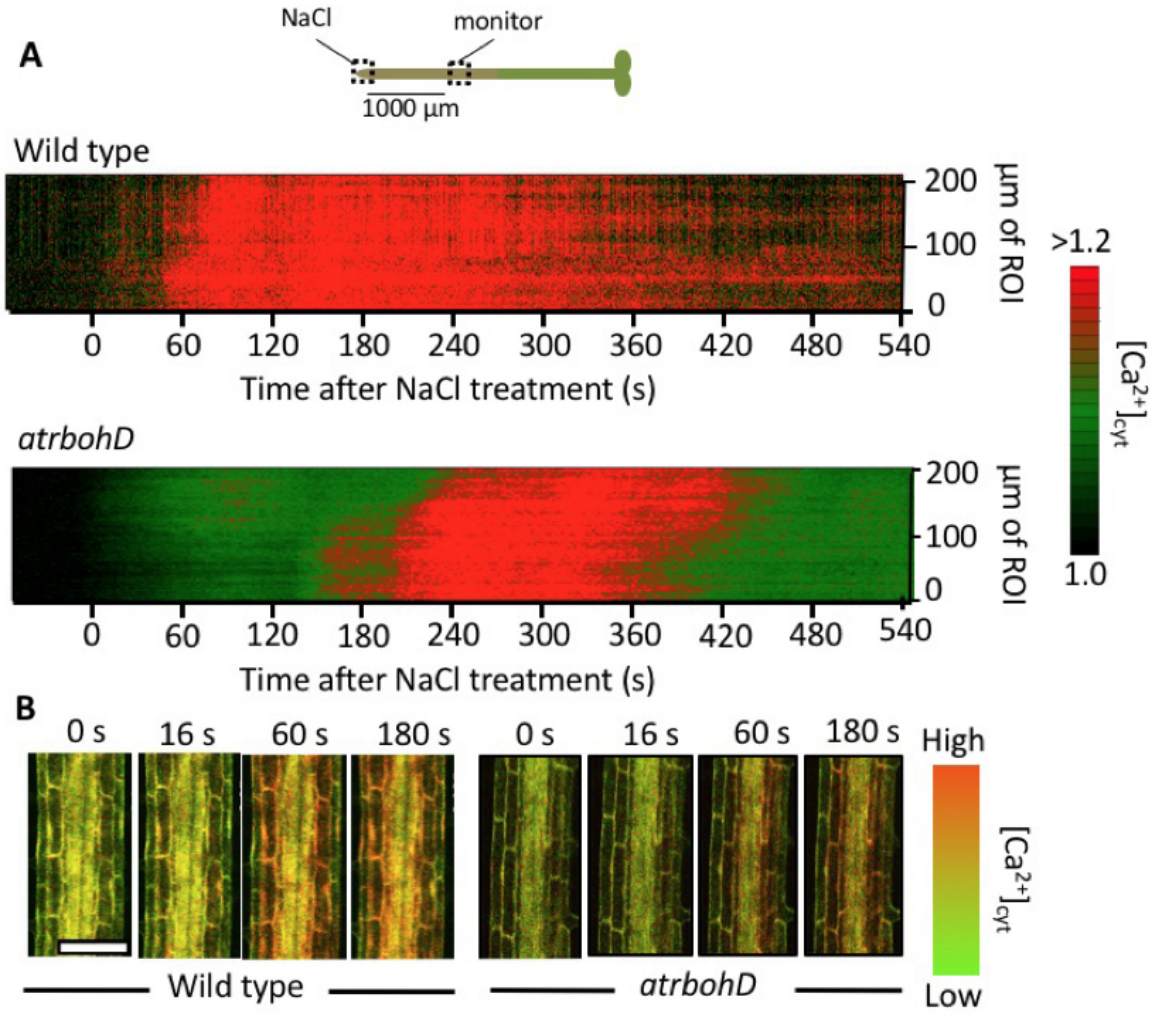

Figure 3.10: Ca^{2+} wave has a reduced velocity in the *Atrbohd* mutant. Ca^{2+} propagation in the mature root, 1000 μm shootward of site of NaCl application at the root tip. Quantitative ratiometric data was extracted from a region of interest (ROI) 5 μm long by 144 μm deep (1024 pixels of data) covering the cortex and endodermis for a 5 μm length of the root. This ROI was scanned along the root creating 92 sequential data points covering 460 μm of root length per image. Analysis was repeated on images taken every 2 s for 10.5 min (315 images) and then the data extracted from 5 roots was averaged and pseudo-colour-coded as shown. Performed on wild type and *atrbohD* lines. A wave speed of $73 \pm 19\,\mu\text{ms}^{-1}$ was calculated from the time for the ratio signal to increase significantly (P <0.05,>2 s.d.) above pre stimulus values. Increasing FRET:CFP signal represents an increase in Ca^{2+} levels. *This data and figures produced by Won-Gyu Choi in the lab of Simon Gilroy, Department of Botany, University of Wisconsin, Madison, WI, USA.*

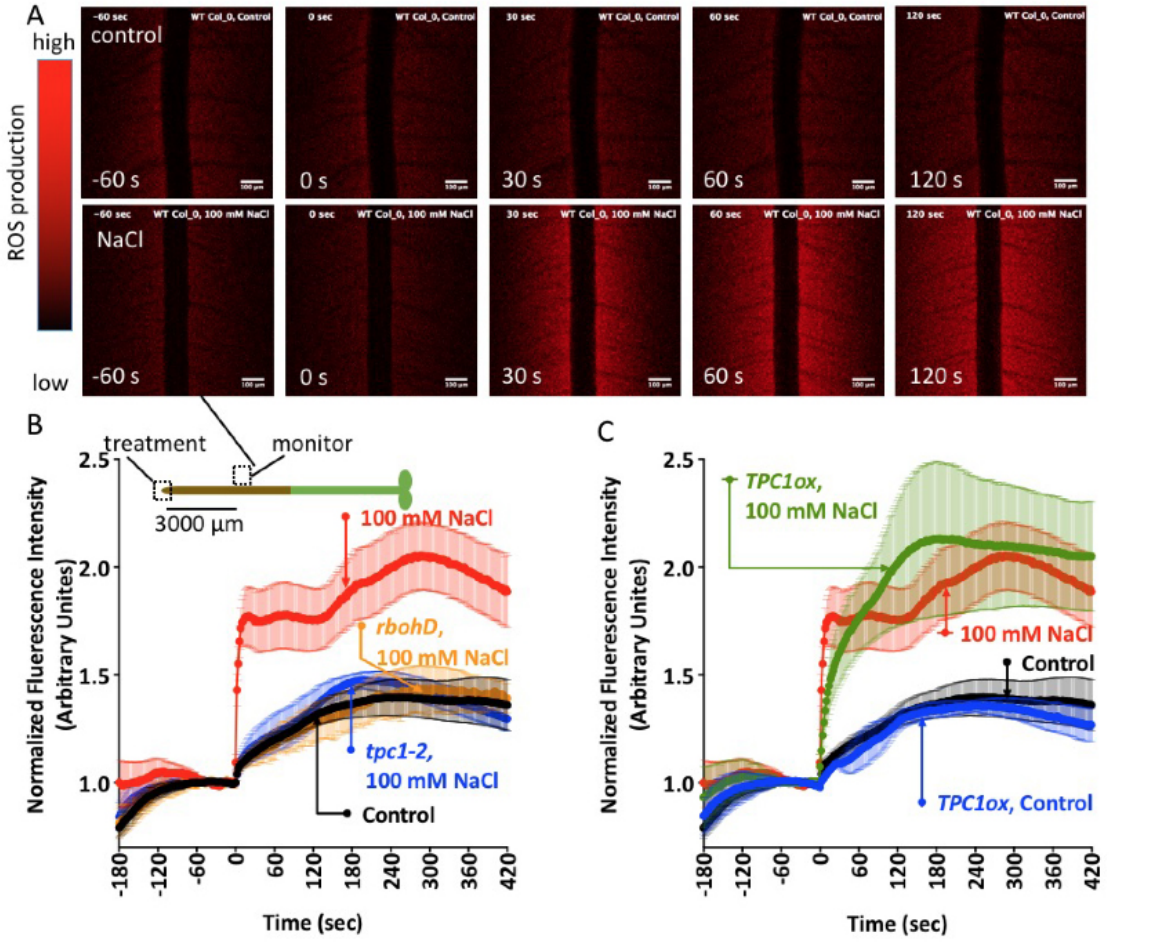

Figure 3.11: Apoplastic ROS wave accompanies the Ca^{2+} wave. **(A)** Apoplastic ROS monitored with OxyBurst Green-BSA measured 3000 μm shoot ward of root tip treated with medium (control) or 100 mM NaCl in wild type. **(B)** OxyBurst signal 3000 μm from the tip in wild type and mutants *atrbohD* and *tpc1-2*. **(C)** Response measured at 3000 μm shootward in OxTPC1 treated with medium (control) or 100 mM NaCl added to the root tip. Signals were normalised to the mean signal for 60 s prior to additions at 0 s. OxyBurst becomes irreversibly more fluorescent as it is oxidised. Results are mean ± SEM, $n \geq 5$. *This data and figures produced by Won-Gyu Choi in the lab of Simon Gilroy, Department of Botany, University of Wisconsin, Madison, WI, USA.*

One further prediction of the ROS-assisted CICR model is that loss of ROS production in the OxTPC1 background will slow wave propagation,

$$v_{\mathrm{rbohD/OxTPC1}} = \frac{1}{\sqrt{\alpha}} v_{\mathrm{rbohD}}, \tag{3.22}$$

with α as in Section 3.2.5. This suggests a velocity of $123\,\mu\mathrm{ms}^{-1}$. To test this prediction, we applied DPI to the OxTPC1 plants and monitored wave speeds. In the OxTPC1 background, a Ca^{2+} wave was still evident after pre-treatment with DPI but the rate of transmission was slowed to $134.4\,\mu\mathrm{ms}^{-1}$, which is in good agreement with the prediction.

3.6.2 Imaging of extracellular ROS wave

Implicit in the ROS-assisted CICR model of Ca^{2+} wave propagation is that the Ca^{2+} wave should be accompanied by a similarly propagating wave of apoplastic ROS production. Although the presence of a ROS wave has been inferred from the wave-like activation of the ROS-dependent transcriptional response (e.g [196]), direct measurement of the wave-like propagation of an apoplastic ROS signal has proven technically challenging. We used the ROS-sensing fluorescent dye OxyBurst Green H2HFF conjugated to bovine serum albumin to localize this ROS sensor to the apoplast of the root. OxyBurst becomes more fluorescent upon oxidation and so provides a measure of the kinetics of ROS increases [250, 251]. We therefore monitored OxyBurst fluorescence intensity before and after local NaCl stimulation of the root tip at points distant from the site of NaCl stimulation to try to capture the spread of a putative wave of ROS production. As OxyBurst shows an irreversible increase in fluorescence upon oxidation, the constitutive background ROS production by the root led to a slow increase in signal with time prior to treatment (Figure 3.11A, B). Addition of growth medium to the root tip (control) led to a slight increase in OxyBurst signal measured $3000\,\mu$m away from the root tip site of local medium addition (Figure 3.11A, B that may represent a small response to the mechanical signal generated by medium addition [250]. However, when NaCl was added to the tip, this distal region showed a rapid and significantly larger increase in OxyBurst fluorescence (Figure 3.11A, B). Calculation of the speed of movement of the signal triggering this response was made by monitoring the time for significant increase (>2 s.d. above pre-stimulated levels) in the mean OxyBurst signal monitored at 3000 and $5000\,\mu$m from the root apex in 14 replicate experiments. This analysis indicated a propagation speed of $374\,\mu\mathrm{ms}^{-1}$.

Consistent with the model of ROS-assisted CICR, these ROS increases distal to the site of NaCl stimulation were dependent on *At*RBOHD and TPC1, being attenuated in *AtrbohD* and *tpc1-2* mutants (Figure 3.11B). The ROS increase did not differ significantly (P >0.05, Anova) from WT response in the TPC1 overexpression line (Figure 3.11C).

Table 3.5: Parameters used in the full Ca^{2+} and ROS model.

Symbol	Description	Value	Units	Ref
D_{Ca}	Ca^{2+} diffusion constant	5 - 20	μms^{-2}	[168]
D_R	ROS diffusion constant	1000	μms^{-2}	
d_{PM}	PM Ca^{2+} channel separation	1	μm	assumed
d_{RBOHD}	RBOHD spearation	0.18	μm	[240]
d_{WT}	TPC1 separation in WT	1	μm	[226]
d_{OxTPC1}	TPC1 separation in OxTPC1	0.6	μm	[24]
d_v	Separation between vacuoles	1 - 10	μm	assumed
σ_T	TPC1 release strength		calculated	
σ_P	PM Ca^{2+} channel release strength		calculated	
σ_R	RBOHD release strength		calculated	
c_T	TPC1 activation threshold (Ca^{2+})		calculated	
c_P	PM Ca^{2+} channel activation threshold (ROS)		calculated	
c_R	RBOHD activation threshold (Ca^{2+})		calculated	

3.7 Full ROS and Calcium Model

Based on our combination of mathematical modelling and experimental analysis from the previous sections, we propose the following model for propagation of the systemic signal in response to salt. Locally, the application of salt triggers movement of ions between various compartments in the cell, and in particular the concentration of Ca^{2+} in the cytoplasm increases. This signal leads to the activation of RBOHD via its EF-hand domains and via phosphorylation by Ca^{2+}-binding kinases [198]. As illustrated in Figure 3.12A, local production of ROS by RBOHD is predicted to activate PM Ca^{2+} channels, such as the annexins [239] or another ROS-sensitive Ca^{2+} channel whose activities have been monitored at the electrophysiological level in *Arabidopsis* root cells [252, 253, 254]. This Ca^{2+} contributes to the activation of TPC1 resulting, directly or indirectly, in the release of more Ca^{2+} from the vacuole. Both ROS and Ca^{2+} diffuse within the apoplast and cytoplasm respectively, activating neighbouring channels until all the involved signalling proteins within a cell have been activated. The signalling molecules are able to diffuse between cells, ROS through the apoplast and Ca^{2+} through the plasmodesmata, where signalling in the next cell is activated. In the TPC1 overexpressor, the quantity of TPC1 channels is increased [24] resulting in more Ca^{2+} being released and faster activation of RBOHDs, and therefore a faster wave. Within the *tpc1-2* mutant background, RBOHD and the PM Ca^{2+} channel form a linked propagation system, Figure 3.12B, while in the *rbohD* mutant only TPC1 (and any associated vacuolar proteins) is responsible for release of Ca^{2+} from the vacuole, with systemic propagation being mediated by the plasmodesmata, Figure 3.12C. In this section, we develop a more complete mathematical model of this system.

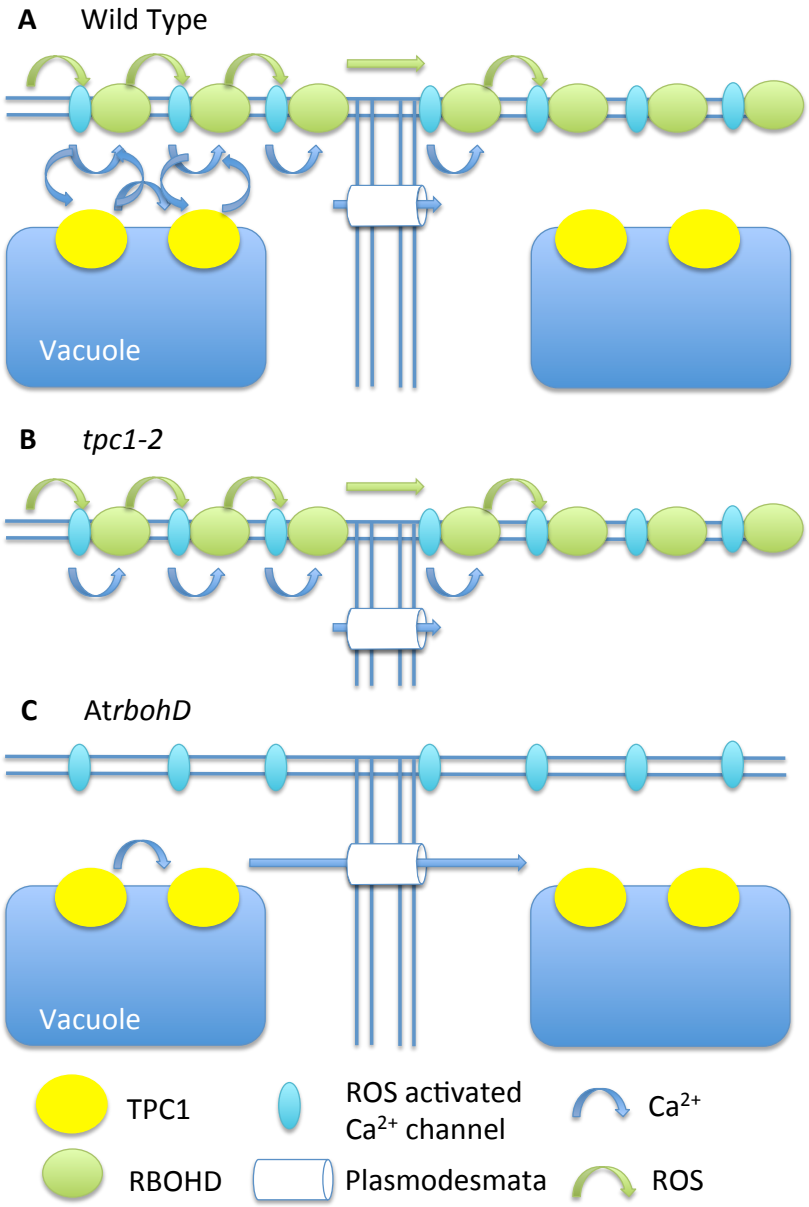

Figure 3.12: Conceptual model of propagation of the salt stress induced Ca^{2+}/ROS waves in (A) wild type and OxTPC1, (B) *tpc1-2* and (C) *AtrbohD*. **(A)** ROS (green arrows) is produced by RBOHD (green circles) and diffuses through the apoplast, activating ROS-sensitive Ca^{2+} channels in the plasma membrane (light blue ellipses). These channels release Ca^{2+} into the cytosol (blue arrows) that activate TPC1 proteins (yellow circles) that, directly or indirectly, mediate Ca^{2+} release from the vacuole. Combined, this Ca^{2+} activates further RBOHD proteins, giving rise to a self-propagating ROS/Ca^{2+} wave. Passage between cells may be mediated by either diffusion of ROS through the apoplast, or Ca^{2+} through the plasmodesmata. **(B)** In the *tpc1-2* mutant RBOHD and the ROS-activated PM Ca^{2+} channel form a less effective mutual propagation network. **(C)** In the *rbohD* mutant TPC1 acts as the only source of Ca^{2+}.

3.7.1 Model Description

We consider a model with 2 propagating species, Ca^{2+} in the cytoplasm and ROS in the apoplast (Figure 3.12), and 3 signalling units: RBOHD, to generate apoplastic ROS in response to raised cytoplasmic Ca^{2+}, TPC1 that releases Ca^{2+} from the vacuole, again in response to cytoplasmic Ca^{2+}, and a plasma membrane localised Ca^{2+} channel that responds to apoplastic ROS. We distribute these signalling units throughout the cell with regular separations as given in Table 3.5. We use the same approach as in Section 3.3 to describe the release and propagation of Ca^{2+}. Both the TPC1 and PM Ca^{2+} channels contribute an amount of Ca^{2+} to a measurement point, x, according to (3.13), with the total Ca^{2+} concentration at a point being the sum over these contributions. The release strength, σ, of the two channels may not be equal, however, nor will their thresholds for activation, c_{th}, necessarily be the same. We therefore must consider parameters, σ_T, c_T and σ_P, c_P as the release strength and activation threshold for TPC1 and the PM Ca^{2+} channel respectively. The PM channel is additionally responding to apoplastic ROS, so c_P is the threshold ROS concentration.

RBOHD is not an ion channel, it generates O_2^- free radicals via electron transfer across the plasma membrane. It is able to continuously produce these free radicals as long as it is active and the electron donor, NADPH, is available in the cytoplasm. However, fully simulating that process is computationally expensive and scales with the length of time of the simulation. While an RBOHD may be active for a long time after passage of the wavefront (while cytoplasmic Ca^{2+} remains raised), a single RBOHD only contributes to the generation of that wavefront for a comparatively short time. We therefore make the assumption that we can still treat ROS generation as a single release, and model the behaviour of RBOHD in an identical way to the Ca^{2+} channels. We assume it contributes a concentration of ROS to a point, x, as described by (3.13), using a release strength, σ_R. RBOHD will be activated by a concentration c_R of Ca^{2+} in the cytoplasm.

In this model, we therefore have 6 unknown parameters: the three release strengths σ_i and the three thresholds c_i. We first scale all the parameters relating to the Ca^{2+} concentration, σ_T, σ_P, and c_R, by c_T (TPC1 threshold). We also scale the ROS release strength σ_R by c_P, the ROS threshold for the PM-Ca^{2+} channel, leaving 4 unknown.

We start by analysing the *rbohD* mutant, which in this model requires just TPC1 (Figure 3.12), and should allow us to fit σ_T/c_T (Section 3.7.2). We would then use the measured behaviour in the WT and overexpressor to fit σ_P/c_T, σ_R/c_P and c_R/c_T (Section 3.7.3). Finally we will test whether these parameters are able to recapture the behaviour in the *tpc1-2* mutant.

3.7.2 Ca^{2+} wave propagation in the *rbohD* mutant: a role for the plasmodesmata?

We chose to fit the full model to the velocity of the rbohD mutant, $73 \pm 19\,\mu\text{ms}^{-1}$, first. In this case, the only active elements in the model are the TPC1 channels, and the process is

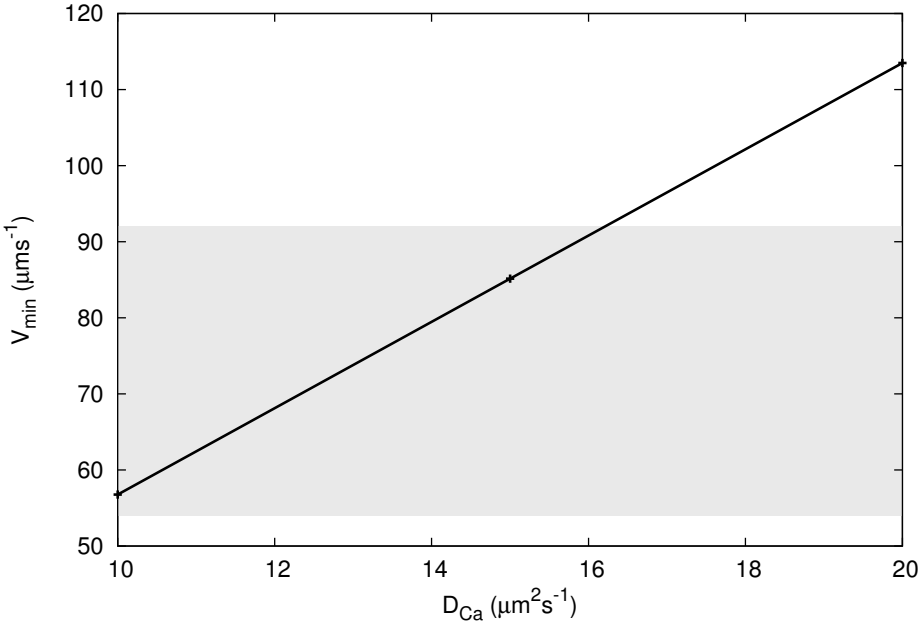

Figure 3.13: Fit to wave velocity in the *rbohD* mutant is dependent upon $D_{\mathbf{Ca}}$. Variation of the minimum possible velocity, $v_{\min}$, in the FDF model of *rbohD* (Figure 3.12B) with diffusion constant of Ca^{2+} in the cytoplasm, D_{Ca}. Calculated from (3.24), and thereby assumes $d_v = 1\,\mu$m. The grey region indicates the velocities within one standard error of the measured velocity (Table 3.4).

analogous to that of Section 3.3. The velocity we are aiming to achieve is so low that it runs into the theoretical limit of propagation within the system: where the amount of calcium released by a TPC1 is only just able to activate the next channel in sequence. This occurs when the maximum concentration at a neighbouring channel is equal to the threshold,

$$\max_t c(x_i + d_{\mathrm{WT}}, t) = \frac{\sigma_T}{\sqrt{4\pi D_{Ca} t}} \exp\left[-d_{\mathrm{WT}}^2/(4D_{Ca}t)\right] = c_T, \tag{3.23}$$

which occurs at a time $T = d_{\mathrm{WT}}^2/2D_{Ca}$. The minimum possible value of $\sigma_T/c_T = 4.13\,\mu$m, which is independent of the diffusion constant, D_{Ca}. For $d_v = 1\,\mu$m, the velocity most closely obeys (3.5), and the minimum possible velocity within this model of the *rbohD* mutant is

$$v_{\min} = \frac{4D_{Ca}}{d_{\mathrm{WT}}} \log \frac{\sigma_T}{d_{\mathrm{WT}} c_T} \tag{3.24}$$

We plot the variation of $v_{\min}$ with the diffusion constant, according to (3.24), in Figure 3.13. This shows that for $D_{Ca} > 16\,\mu\mathrm{m}^2\mathrm{s}^{-1}$ the minimum possible velocity in the model is greater than that measured experimentally. For higher values of d_v, larger values of σ_T will be needed to generate a propagating wave, and so may not be able to fit the observed velocity in the *rbohD* mutant.

In Figure 3.14 we fully simulate the propagation process for different values of the inter-vacuolar separation, d_v. As Figure 3.14A shows, even for low D_{Ca} values, the model fails

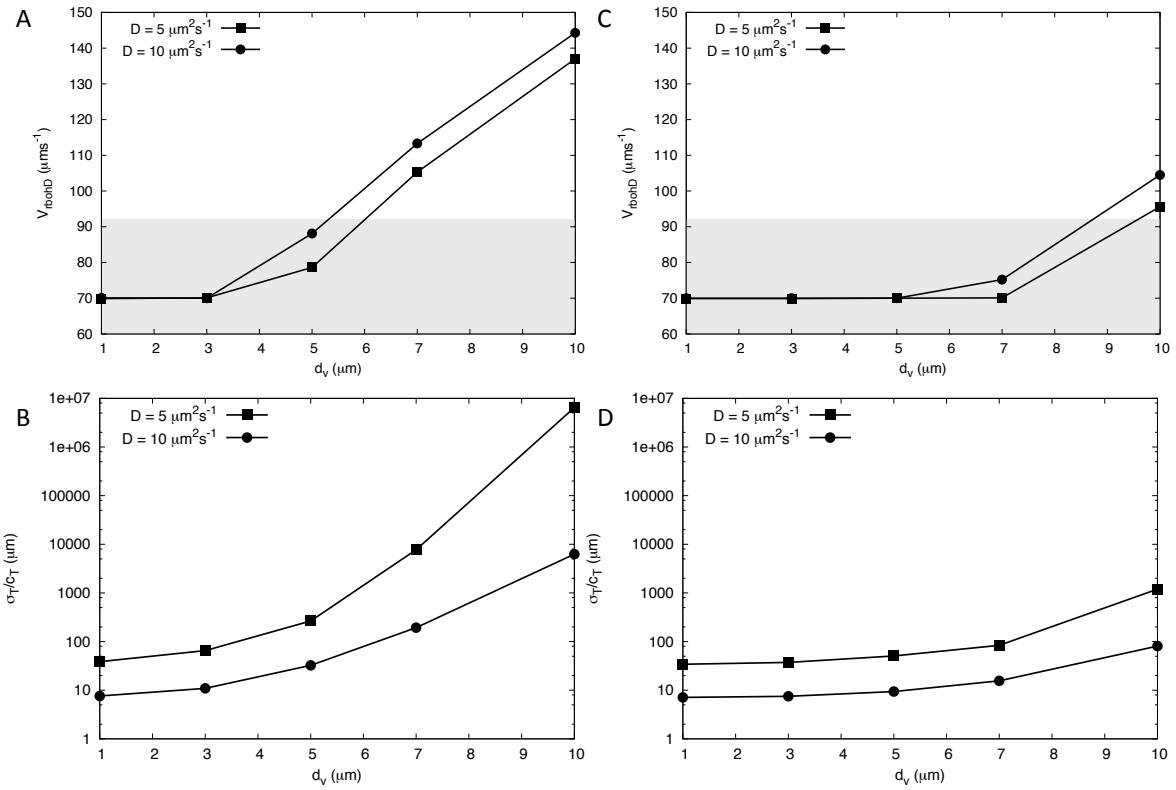

Figure 3.14: Presence of plasmodesmata located Ca^{2+} channels improves model fit. Attempts to fit the full model to Ca^{2+} wave velocities measured in an *rbohD* mutant background for different vacuolar separations d_v, and for different values of the diffusion constant, D_{Ca}. **(A)** Closest fit for the full model without a plasmodesmata Ca^{2+} channel. Failure to fit for $d_v > 5\,\mu$m for both D_{Ca}. **(B)** Corresponding values of σ_T/c_T to produce those wave speeds. **(C)** and **(D)**: as for (A) and (B), respectively, but with a single Ca^{2+} channel, with identical parameters to a TPC1, placed in the middle of the plasmodesmata. (A) and (C) Grey region indicates one standard deviation from the mean velocity measured experimentally (Table 3.4).

to reproduce the wave speed observed in the *rbohD* mutant background for $d_v > 5\,\mu$m. As indicated by Figure 3.13, for larger D_{Ca} the fits will be much worse. Figure 3.14B shows the necessary value of σ_T/c_T to obtain a fit. Activation of TPC1 is believed to require concentrations in the $10 - 100\,\mu$M range [224], whereas the concentration of Ca^{2+} in the vacuole is typically quoted at being in the $1 - 10\,$mM range [9]. We might therefore expect the ratio σ_T/c_T to be around $10 - 1000\,\mu$m, while for $d_v > 5\,\mu$m, Figure 3.14, we require far greater values to propagate a signal at all. This analysis can only be used as a rough guide, however, as vacuolar Ca^{2+} is also believed to inhibit the opening of TPC1 [255, 224], and so the precise relationship between σ_T and c_T is not clear. It is likely that more species are involved in the regulation of TPC1.

To transmit the signal between cells, we have assumed Ca^{2+} diffuses through the plasmodesmata (Figure 3.12C). The plasmodesmata are complex structures, containing many

unique proteins as well as enclosing part of the endoplasmic reticulum. The ER is known to contain Ca^{2+} signalling machinery in animals, and the plasmodesmata themselves may well contain Ca^{2+} signalling machinery [256]. We therefore asked how far a plasmodesmata localised Ca^{2+} channel might be able to rescue signalling within this model. To do so, we placed a single channel in the centre of the gap between adjacent vacuoles ($\frac{1}{2}d_v$ from each vacuole). For simplicity we assumed it had identical release strength and gating properties to the TPC1 channels in the model. As illustrated in Figure 3.14C, this substantially improves the velocity fit for all d_v at smaller D_{Ca} values. The σ_T/c_T values are also closer to what we might expect from the previous order of magnitude analysis (Figure 3.14D). Thus, in order to produce a good fit to the behaviour in the *rbohD* mutant, we need to include a plasmodesmata localised Ca^{2+} channel.

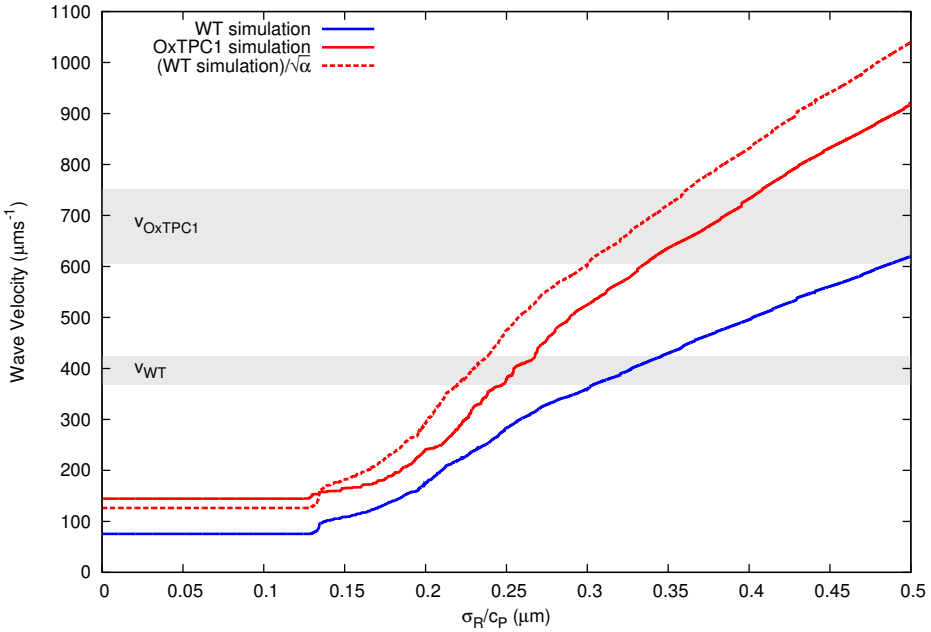

Figure 3.15: The original ROS model analysis produces a reasonable description of the full model. Comparing the full model simulation of the TPC1 overexpressor (solid red line) with the simple model (Section 3.2.5; dashed red line), a rescaling of the WT simulation (blue line) by a factor $\sqrt{\alpha}$, where $\alpha = 8.6/24.2$ is the relative increase in TPC1 channel numbers (see Section 3.2.5). The plot shows the velocities for a range of σ_R/c_P values. Simulated within a single cell (effectively $d_v = 1\,\mu$m). The upper and lower grey regions indicate the experimentally measured velocities in the TPC1 overexpressor and in WT respectively (Table 3.4). Parameters used for solid curves: $c_R/c_T = 0.9$, $\sigma_P/c_T = 1\,\mu$m, $\sigma_T/c_T = 38.6\,\mu$m, $D_{\mathrm{Ca}} = 5\,\mu\mathrm{m}^2\mathrm{s}^{-1}$.

3.7.3 Full model can reproduce behaviour in WT and OxTPC1, but not in *tpc1-2* backgrounds

The original model of ROS propagation (Section 3.2.5) assumed that the velocity in OxTPC1 could be modelled by merely a rescaling of the WT velocity by a factor $\sqrt{\alpha}$. With our full model, we can test this simple model. We set up a single cell (effectively $d_v = 1\,\mu$m) and simulated a range of σ_R/c_P values. Figure 3.15 shows the resulting velocity curves for the WT and OxTPC1 models, the only differences between the two being the separation between adjacent TPC1 channels (d_{WT} vs d_{OxTPC1}). From this we can immediately see that the WT

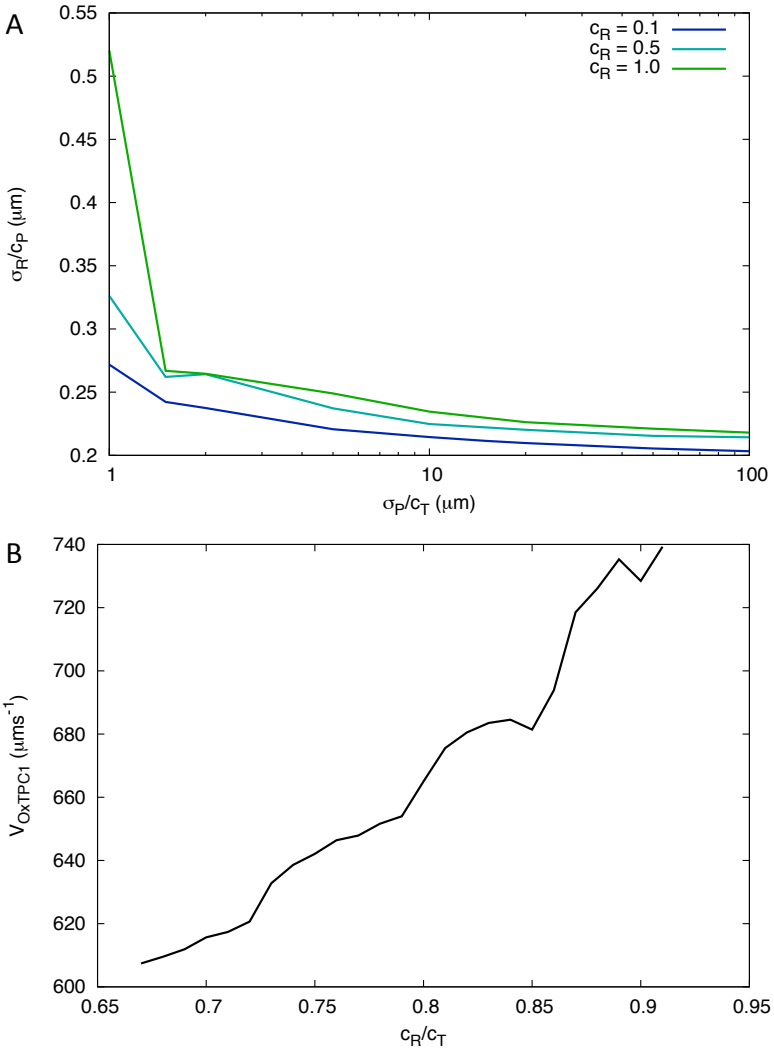

Figure 3.16: The model is able to capture the velocity in WT and OxTPC1. **(A)** Parameter sets that are able to fit WT velocity, using a model with a plasmodesmata localised Ca^{2+} channel, for $d_v = 5\,\mu$m. **(B)** Range of c_R/c_T for which velocity in the overexpresser model reproduces experimental velocity (Table 3.4), within one standard deviation of the mean. Other parameters, $\sigma_P/c_T = 1\,\mu$m, σ_R/c_P as appropriate to fit WT velocity.

simulation is able to fit the experimental WT velocity (lower grey region) for a certain range of σ_R/c_P values. The simple model (Section 3.2.5) predicts $v_{\mathrm{OxTPC1}} = \sqrt{\alpha} v_{\mathrm{WT}}$, and this is also plotted in Figure 3.15 (dashed red line). We see that the simple model gives a good qualitative description of the behaviour in the overexpressor but for most values of σ_R/c_P overestimates its value by around 50-100 $\mu\mathrm{ms}^{-1}$. This difference is enough that for this parameter set, a fit to experiment is obtained for the simple model (in the region where the WT simulation fits experiment, upper grey region), but not in the full simulation. For higher values of d_v, we would expect the OxTPC1 simulation to provide a worse fit (for example, Figure 3.5B). We note that the long plateau region region at low σ_R/c_P is where ROS production is too low to activate the PM Ca^{2+} channel, and therefore the RBOHDs do not contribute to propagation of the Ca^{2+} wave in this region. The speed in the OxTPC1 simulation in this region, however, is a close fit to the simple model and confirms the predicted velocity (Section 3.6.1) in an *rbohD*/OxTPC1 cross.

As illustrated in Figure 3.15, the full simulation is able to reproduce the WT velocity with certain parameter values. That model used a single cell (technically simulating the case of $d_v = 1\,\mu\mathrm{m}$) and only considers one value for the parameters c_R/c_T and σ_P/c_T. We therefore simulated with range of parameters, fitting each to the measured WT velocity (Table 3.4), using σ_R/c_P as the fitting parameter. Figure 3.16A shows how the fitted parameters are related. As we did in the previous section, we can evaluate how reasonable these parameter values are. The concentration of Ca^{2+} in the apoplast is around 1 mM [9] and, as discussed in the previous section, TPC1 requires Ca^{2+} in the $10 - 100\,\mu\mathrm{M}$ range [224], so the values of σ_P/c_T are reasonable. In our model, RBOHDs have a density of around 5 times that of the PM Ca^{2+} channel (Table 3.5), so a ratio of $\sigma_R/c_P < 1\,\mu\mathrm{m}$ is to be expected.

Taking these parameter sets forward (Figure 3.16B) we decreased the separation of TPC1 channels in the model to d_{OxTPC1} (Table 3.5) to simulate the TPC1 overexpressor. The model was only able to correctly reproduce the experimental velocity for a very restricted range of parameters. Figure 3.16B shows the values of c_R/c_T for which the model is able to reproduce the overexpressor velocity (within experimental errors, Table 3.4). RBOHD is known to be activated in response to pathogen attack induced Ca^{2+} transients, that typically reach average concentrations of $< 1\,\mu\mathrm{M}$ throughout the plant [33]. RBOHD is also activated by calcium dependent kinases [198, 257], whose Ca^{2+} binding behaviour has a half maximum value between 0.1 and 10 μM [258]. While it is not known how important each of these kinases are to the activation of RBOHD in this system, it suggests that our values of c_R/c_T are on the high end of what we might expect.

For all of these, $\sigma_P/c_T = 1\,\mu\mathrm{m}$. Higher values of this parameter underestimate the velocity in the overexpressor. This is because when fitting to the WT data, a stronger PM Ca^{2+} channel release means the model uses a weaker RBOHD release, decreasing the model's sensitivity to TPC1 (since RBOHD responds to raised Ca^{2+}, while the PM Ca^{2+} channel does not). Therefore, when TPC1 density is increased, it produces a smaller boost to the wave velocity.

With a full simulation we can image the propagation of the wave through a cell directly.

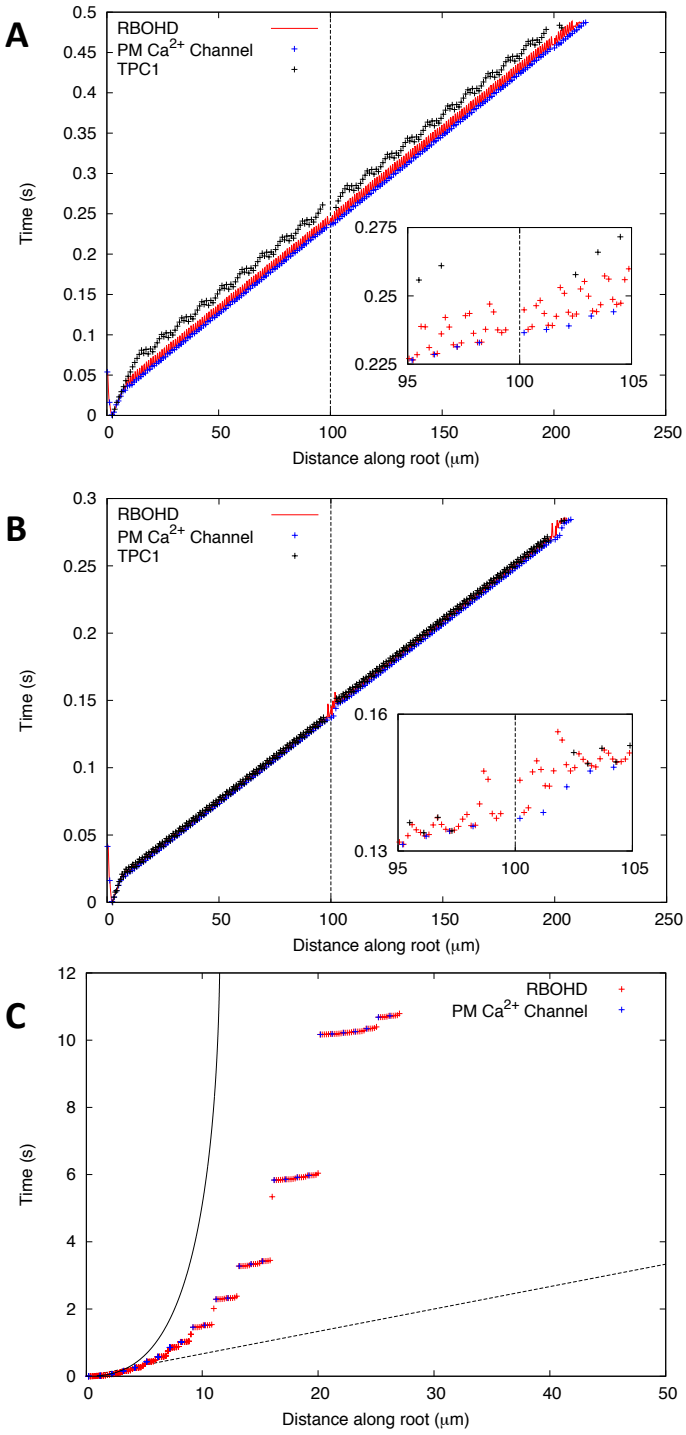

Figure 3.17: Ca^{2+} and ROS waves propagate in WT and OxTPC1 but not in *tpc1-2*. Propagation of the Ca^{2+} and ROS waves illustrated by way of channel activation times. Each point identifies a release site (TPC1, black, PM Ca^{2+} channel, blue) with its position measured from the centre of the first cell wall (at distance $= 0\,\mu$m), and the time at which that channel fires in (cont.)

Figure 3.17: (cont.) **(A)** WT, **(B)** OxTPC1, **(C)** *tpc1-2*. In (A) and (B), due to the density of RBOHDs, their release has been plotted as a continuous line (red), the dashed line at 100 μm indicates the position of the cell wall, and the inserts show a higher resolution plot of channel activation within 5 μm of the cell wall. (C) Dashed black line indicates the expected velocity (15.5 μms^{-1}), while the solid black line is the expected activation curve if driven purely by the plasmodesmata Ca^{2+} channel release. Parameters, $\sigma_P/c_T = 1\,\mu$m, $\sigma_R/c_P = 0.397\,\mu$m, $\sigma_T/c_T = 38.6\,\mu$m, $c_R/c_T = 0.81$, $D_{\mathrm{Ca}} = 5\,\mu\mathrm{m}^2\mathrm{s}^{-1}$, $d_v = 5\,\mu$m.

Figures 3.17A&B show this for WT and OxTPC1, respectively, by way of when channels activate. Each point within Figures 3.17A&B represent the release of the propagating species when that release site is activated. This is an indirect way of imaging the propagation of Ca^{2+} and ROS. Channels are only activated once the concentration climbs above some threshold amount, so this illustrates the time at which a particular wavefront reaches the positions of those channels. Interestingly, the different channels show differing behaviours in WT (Figure 3.17A), but more similar behaviour in OxTPC1 (Figure 3.17B).

In WT, the PM Ca^{2+} channels activate in sequence with a regular time between adjacent releases, indicating that the ROS wave is travelling at a constant speed through the apoplast. The RBOHDs, however, show an oscillating profile (most easily seen in the insert due to its spatial frequency of around 1 μm, equal to d_{PM}.) This occurs because the Ca^{2+} wave is travelling slower than the ROS wave; the next PM Ca^{2+} channel is being activated by ROS before Ca^{2+} has diffused through the cytoplasm to activate each of the intervening RBOHDs. The activation of TPC1 also oscillates, and is delayed in comparison with the RBOHD and PM Ca^{2+} channels. The system is initialised by release from the first TPC1, and initially the wave is driven by release from TPC1s. Once enough RBOHDs and PM Ca^{2+} channels have been activated, they form a more efficient signalling loop (with the aid of Ca^{2+} released by TPC1). TPC1, however, is slow to react to this because of the small value of σ_P/c_T. It requires the contribution from multiple PM Ca^{2+} channels to activate a TPC1 channel. In OxTPC1, the increased density of TPC1 channels results in faster propagation of the Ca^{2+} wave, and a tighter coupling between the ROS and Ca^{2+} signalling systems.

From the insets in Figures 3.17A&B, we can determine how the signal propagates between cells in the model. By looking at the channels that release immediately after the dashed line at 100 μm (insets), we can see whether an RBOHD or a PM Ca^{2+} channel fires first. Since they are activated by different species this tells us whether ROS or Ca^{2+} carries the signal between cells within the model. In both cases, a PM Ca^{2+} channel (blue) is the bottom left most point in both images, indicating that it is ROS that propagates the signal between cells in WT and OxTPC1. The presence of the plasmodesmatal Ca^{2+} channel is therefore not key to the propagation of the signal in WT, only being necessary for the *rbohD* mutant.

With parameter sets that fit both WT and OxTPC1, the next and final step was to see whether the model could reproduce the velocity of the *tpc1-2* mutant. Figure 3.17C shows that the models fails this challenge. The system is initialised by release from the

plasmodesmata Ca^{2+} channel, that we assume is still present in *tpc1-2*, and while this drives the initial RBOHD, and therefore PM Ca^{2+} channel releases, the signal propagates beyond the reach of Ca^{2+} from the plasmodesmata channel alone (black curve). However, the wave is unable to propagate at anything close to the velocity seen in experiments (dashed line), and after the releases shown, no further releases are observed in the model before 25 s, the end of the simulation.

The unusual stepped pattern in the releases is due to the discrete threshold of RBOHD within the model; the Ca^{2+} released is not quite able to trigger its activation. That it does is due to the eventual contribution of Ca^{2+} from the plasmodesmata channel. This alone is not able to trigger distant RBOHDs, but combined with previous PM Ca^{2+} channel releases is able to. The further from the start the wave travels, the larger the steps between firings become. This is because the Ca^{2+} diffusing from the plasmodesmata takes ever longer to travel that far, while more channels fire in each step because the Ca^{2+} profile will be more spatially uniform over this region. This is borne out in *tpc1-2* simulations without a plasmodesmata Ca^{2+} channel in which the system fails to propagate a signal over any distance. If the model had included some kind of pumps to remove Ca^{2+}, as are undoubtedly present in the plant, this effect would not have been observed.

We conclude that the failure of the model to simulate *tpc1-2* correctly indicates some feature is missing, and that more work needs to be done to understand the behaviour under these conditions.

3.8 Discussion

In this chapter we have explored some of the mechanisms of systemic signal propagation in plants and how they are inter-related. The concept of integrated signalling networks utilising multiple species and mechanisms is an area of growing interest (see the reviews of Gilroy *et al.* [204, 259], Hedrich *et al.* [260] and Mignolet-Spruyt *et al.* [261]). The variation potential in plants is a classic example of a signal whose underlying mechanism of propagation is of a quite different form to the signal being measured. The fact that VPs could be transmitted past regions of dead tissue [210] showed that the mechanism responsible for their propagation could not involve active regeneration of the signal, via electrical means or otherwise. Conceptual models [134, 135] suggested the underlying signal was hydraulic, however our work here has shown that this leads to contradictions with experiment (Section 3.1) and that a chemical signal is more likely. We also explored how the systemic Ca^{2+} wave observed by Choi *et al.* could be propagated, demonstrating that a CICR type mechanism was unlikely (Section 3.3), but that Ca^{2+} and ROS could form a coupled system. This was later borne out in experiments (Section 3.6). While new components, such as RBOHD, have been identified as propagating this Ca^{2+} signal, a more complete model showed that more components are required to fully explain the observed behaviour (Section 3.7).

3.8.1 A chemical model of variation potential propagtion

The hydraulic model of VP generation requires a radially propagating signal whose velocity decays with distance from the wound site. However, this would lead to significant differences in the velocity of epidermis and phloem VPs, which are not observed [193, 195]. The proposed mechanistic basis for a propagating radial disturbance that might have satisfied this criterion is a propagating increase in cell turgor [134]. Such responses would have an amplitude that depends on the size of the hydraulic pressure change, yet root excision experiments in maize show that increased xylem pressure changes (by means of NaCl addition to the bath medium) do not produce a corresponding change in the electrical signals [262]. It can take minutes for radially distant cells to complete their turgor response to a pressure change in the xylem [217]. However, ionic changes that are responsible for electrical signals in cells are thought to precede changes in cell turgor, since it is changes in ionic concentrations that give rise to the osmotic potential gradient [27]. Indeed, experiments in which cell turgor was artificially increased did not generate electrical signals [263]. We conclude that it is unlikely that changes in cell turgor are responsible for the electrical signals.

Vodeneev *et al.* [203] were able to put an upper limit on the speed of the axial signal by leaf sectioning post wounding. Sectioning the leaf 1 s after wounding prevented transmission of the VP, and suggests the axial signal cannot travel faster than $3\,\mathrm{cms}^{-1}$, much less than the speed of a hydraulic wave [192]. On the other hand, a model of xylem transported chemical signals fits VP propagation data in wheat with the correct order of magnitude, $0.17\,\mathrm{cms}^{-1}$ (model) vs $0.08\,\mathrm{cms}^{-1}$ [214] (experimental). Wounding cells makes large volumes of water and solute available to the xylem under atmospheric pressure. Given that the xylem is under tension, this can drive flow away from the wounding site [127]. The initial flow velocity under these circumstances may well be higher than rates measured in unwounded plants. Indeed, Vodeneev *et al.* [203] demonstrated enhanced translocation rates after wounding compared to without wounding through experiments with radioactive tracers, consistent with this model.

VPs can be propagated through a solution connecting two parts of a severed stem [212], and can be initialised by applying wound extract to the plant [264]. Such data are inconsistent with hydraulic waves, but suggestive of chemical messaging in which a component of the wound extract is acting as the chemical messenger. The requirement for plasmodesmata in systemic electrical signalling [209] further supports a chemical rather than hydraulic means of propagation since hydraulic disturbances can be transduced through mechanical stress of the cell wall. Chemicals indicating damage to the plant are known to trigger Ca^{2+} transients during pathogen attack [265], as well as suggested to underlie mechanical responses in *Mimosa pudica* [212, 266], while a large number of stress induced xylem proteins were recently identified in cotton [267]. Molecules suggested to be involved in wound signalling include oligosaccharides or plant hormones such as systemin [265, 268]. During wounding, ions and chemicals stored within the vacuole could be released into the surrounding tissue, and the vasculature, when the cell is damaged [127].

If VP propagation requires xylem flow rather than propagating pressure changes, as we have proposed, then we would expect xylem tension to be an important requirement for VP propagation. Wounding experiments performed under conditions of varying xylem tension, for example at night or under drought conditions, would be expected to show different rates of VP propagation. Malone [127] demonstrated an absence of VPs under very low xylem tension conditions. Xylem tension would not be expected to affect propagation of a hydraulic wave, nor a self-propagating ionic/ROS wave. Indeed, this has been observed [210].

The question remains, however, that non-wounding stresses are also able to induce VPs [134]. It is possible that the application of external pressure as was performed by Stahlberg *et al.* [134] is also able to induce chemical signals, that are then propagated through the xylem and responsible for the electrical signals observed. That turgor pressure changes do not trigger electrical signalling [263] could be interpreted by mechanosensors that distinguish the compressive force of external pressure from the internal pressure of increased turgor pressure on the cell wall. This is purely conjecture though. The different results regarding VP propagation in different systems [134, 193, 195, 203, 210, 218, 269] may be due to different organisms having different cellular responses to turgor pressure. Future experimental work to identify the different mechanisms at play, for instance simultaneous measurement of epidermal turgor pressure change and membrane potential in various systems, could once and for all settle the debate around VPs and their propagation.

3.8.2 The interaction between ROS and Ca^{2+} in response to salt stress

We applied the FDF model to explore mechanisms behind the plant-wide transmission of stress-induced Ca^{2+} waves, focusing on the salt-induced wave of the root. Our analyses suggest that a simple CICR-based mechanism relying upon a self-reinforcing Ca^{2+} release from the vacuole via TPC1-dependent Ca^{2+} efflux and diffusion of Ca^{2+} between cells is unlikely to account for the observed velocity of wave movement. Extending this CICR mechanism for Ca^{2+} wave transit through the cell with Ca^{2+}-dependent apoplastic ROS production to couple between cells, however, is able to support the observed velocities in a simple model. Experimental work further corroborated this model, identifying a key role of RBOHD as a source of ROS.

A comprehensive model (Figure 3.17) was able to recapture the behaviour in the *rbohD* mutant, WT, and OxTPC1 lines, but not in *tpc1-2*, indicating that model had not accounted for all important parts of the full system. Further experiments by our collaborators showed that an increased concentration of Ascorbate (100 μM) was able to completely terminate the wave. This suggests that ROS is required at all stages of wave transmission, and that additional sources of ROS are active even in the *rbohD* mutant. Since DPI did not have the same effect, it is likely this ROS originates from peroxidases active in the apoplast [270]. How they are activated in the absence of RBOHD, or when DPI has been applied however, is unclear. This suggests that rather than TPC1 acting alone in the *rbohD* mutant (Figure 3.12B), per-

oxidases are still generating ROS in the apoplast, that is activating the PM Ca^{2+} channels too. Adapting the model of Section 3.7 to account for this would be a valuable future step. Within WT, however, the contribution of these additional ROS sources would likely be minor in comparison to RBOHD, since the velocity falls by such a degree in the *rbohD* mutant. Our understanding of signal propagation in WT remains largely unchanged from Figure 3.12A.

The activity of TPC1 is known to be inhibited by ROS and activated by reducing agents [220, 271, 272] and this may at first sight appear contradictory to the ROS/TPC1-related propagation mechanism modelled above. However, since ROS is generated within the apoplast by RBOHDs it would be able to rapidly open ROS-activated channels in the plasma membrane. ROS would then need to cross the plasma membrane and the cytoplasm before interacting with TPC1. It can take 0.9 s to develop a stable gradient of ROS across plasma membranes [273] although the maximum theoretical rate could be much faster [274]. Given the speed of the Ca^{2+} wave in WT, it should take only 2.5 ms to activate each TPC1 in sequence, and thus it is unlikely that the ROS would have time to trigger a direct effect on TPC1's ability to mediate the initial propagation phase of the Ca^{2+} wave. The slower ROS-triggered inactivation of TPC1 may therefore have an important role to play in terminating the wave once it has moved through the cell. ROS-based TPC1 inactivation could also lead to a refractory period where the channel is unable to support further Ca^{2+} increases leading to the wavelike progression of the Ca^{2+} increase.

Inherent to the model presented above is rapid triggering of TPC1 by ROS-dependent cytosolic Ca^{2+} increases. Although the SV channel has long been identified as being activated by cytosolic Ca^{2+} [219], large concentrations of Ca^{2+} are required [224]. The ability for the SV channel to directly release Ca^{2+} is also a topic of some controversy [223] as large vacuolar Ca^{2+} concentrations inhibit activation of TPC1 [223, 224, 255]. The SV channel is known to be regulated by many other factors (reviewed in [223]). For example, recent structural data has indicated a number of potential phosphorylation sites on TPC1 [225] and the beet SV channel is activated by CaM [220]. Such alternate regulatory mechanisms provide a wide range of other means for activation of this channel as part of the Ca^{2+} wave transmission process. TPC1 could also be only indirectly responsible for the release of Ca^{2+} from the vacuole, possibly by controlling changes in membrane voltage that activate other channels [275]. Our modelling approach does not make any assumptions about TPC1's role in mediating Ca^{2+} release, merely requiring that activation of TPC1 leads to Ca^{2+} release, whether directly or indirectly.

While the full model (Section 3.7) predicts ROS propagation through the apoplast as the mechanism for intercellular signal transmission, we cannot exclude the possibility that Ca^{2+} diffusing through the plasmodesmata is responsible for transmitting the signal between adjacent cells, or indeed that the two species act in tandem. A TPC1 mediated CICR wave acting alone seems unlikely, and that motivated us to look at ROS propagation, but the requirement for a ROS activated PM Ca^{2+} channel means there could also be sources of Ca^{2+} influx within the plasmodesmatal plasma membrane itself that could contribute to a rapid transmission event. Likewise our full simulations (Section 3.7) suggested the presence

of such a component would be necessary to transmit a Ca^{2+} signal in the RBOHD mutant. Unfortunately, the resolution of current imaging techniques is unable to distinguish these possibilities.

TPC1 and AtRBOHD are ubiquitously expressed throughout the plant and so their distribution does not provide an obvious explanation as to why the salt-induced Ca^{2+} wave preferentially transits through the cortical and endodermal cell layers. Similarly, candidates for the putative ROS-activated Ca^{2+} release channels such as annexins and SKOR, [222, 239], are also expressed throughout the root [276]. Thus, identifying the ROS-regulated channels involved with this signalling process, as well as other components that provide regulatory roles, represents a key challenge for the future that may provide important insights into the tissue specific pattern of the Ca^{2+} wave.

3.8.3 Comparisons with other systemic signals

ROS have been repeatedly implicated in systemic signalling (e.g., [196, 277, 278, 279]) and while it is tempting to identify this and the Ca^{2+} wave we have studied here as two sides of the same coin, there are important differences that have yet to be explained. Firstly, the ROS wave in response to wounding travels at $1400\,\mu ms^{-1}$ [196], much faster than the Ca^{2+} wave we study here. This difference might be because the wound-induced ROS wave propagates through the vascular tissue, whereas the Ca^{2+} wave appears to be restricted to the cortex and endodermis [21]. The vasculature is well-suited for long distance transmission of signals [26], particularly electrical signals. Alternatively, the triggering stimulus may also impact on propagation speed/mechanism. Indeed, the velocity of the wound-related ROS wave is very similar to that of electrical responses to wounding [193] suggesting ROS and electrical signals may be acting together in the wounding response [26]. It is striking, however, that the signal velocity in the *rbohD* mutant is compromised in response to either salt stress or under wounding [196], and indeed the velocity in both cases is approximately the same, hinting at some possibly shared core components of the transmission machinery.

Before the electrical signal in response to wounding reaches the leaf mid-rib, it travels at a very similar speed to the Ca^{2+} wave we studied here [193]. After wounding occurs at the leaf tip, any signal must cross the leaf before it reaches the vasculature in the mid-rib. The fact that the wave speed in this region matches the salt stress Ca^{2+} wave suggests a similar mechanism might be involved in the region outside of the vasculature. The phloem electrical signals of Salvador-Recatalà *et al.* [195] show signs of both VP and AP behaviour, and may be a combination of both. We note that while the quickly propagating part of the wave travels at the same speed as that measured by Mousavi *et al.* [193], the slower part travels at around $300\,\mu ms^{-1}$, similar to the Ca^{2+} wave of Choi *et al.* [21]. Indeed, both the NaCl-triggered Ca^{2+} wave propagation [21] and wound-induced systemic Ca^{2+} increases [25] appear dependent on the TPC1, reinforcing the idea of conserved elements of the propagation system.

We identified in our early exploration of possible mechanisms (Section 3.2) that the Ca^{2+} wave could be propagated through an electrical mechanism. We note here that CICR and electrical models are not mutually exclusive. The use of a threshold variable, c_{th}, in the CICR model hides the exact mechanism of stimulation of TPC1 channels, which could be voltage dependent. Ca^{2+} is known to be involved in the generation of many electrical signals [26], although typically as a first step. The large depolarizations seen in action potentials, for example, are due to Cl^- ions moving through Ca^{2+}-gated channels. While the release of Ca^{2+} may not directly trigger adjacent signalling units, the overall behaviour can still be captured by a smaller c_{th} than might be expected for a direct Ca^{2+} interaction, say. Therefore, the FDF model is a valuable approach for analysing systemic Ca^{2+} signals, independent of the exact gating behaviour of the channels. A consequence of this generality is that we are unable to differentiate between detailed gating mechanisms within this framework. In the current case we have demonstrated that a ROS-Ca^{2+} system could reproduce the experimental observations but we can't exclude an underlying driving electrical signal being the cause.

Chapter 4

General Discussion

The aim of this thesis was to further understand Ca^{2+} signalling in plants. We were interested in the question of signal generation, and developed mathematical models to study this process in two particular systems: 1) nuclear Ca^{2+} oscillations during root nodule symbiosis in legumes [36], and 2) the propagation of the salt stress induced Ca^{2+} wave in *Arabidopsis thaliana* [21]. In both cases, we used simple models to aid formation of an intuitive understanding of the system.

4.1 The Fire-Diffuse-Fire Model

We have made extensive use of the Fire-Diffuse-Fire model throughout this thesis. The FDF model was developed as a means of capturing the dynamics of CICR without taking into account the complexities of channel activation [107]. This made it appropriate for our uses as, at the start of this project, the Ca^{2+} channels involved in our systems of interest were either unidentified [36] or mired in controversy [223]. By assuming CICR, the full channel activation mechanisms are wrapped up into the threshold value of activation, c_{th}. This threshold can represent the probabilistic binding of Ca^{2+} to Ca^{2+}-binding domains, the requisite build up of charged ions to activate a voltage-dependent channel, or indirect activation via Ca^{2+}-binding kinases or other proteins.

While the CNGC channel involved in symbiosis signalling is not likely to be directly activated by Ca^{2+}, DMI1 might be through its EF-hands [117]. The current model for symbiotic channel activation [63, 86] suggests that DMI1 aids release of Ca^{2+} through the open CNGC due to modulation of the local membrane potential (DMI1 allows K^+ to flow from the nucleoplasm into the NE [58], maintaining the electromotive force driving Ca^{2+} across the membrane [86]). The FDF model allows us to encapsulate the role of DMI1 into c_{th}. We note that this conceptual model is based on an ODE model, and has not yet been tested within a spatial model.

The activation and role of TPC1 in the generation of the salt stress-induced Ca^{2+} wave remains a source of much controversy [220, 223, 280, 281]. The original electrophysiological

characterisation of TPC1 showed it could be modulated by Ca^{2+} levels [219], and structural analyses indicate Ca^{2+} binding EF hands on the cytosolic side of the channel that aid channel activation [24, 223, 224, 225]. However, a domain on the vacuolar lumenal face shifts the channel's voltage activation towards more positive potentials [224, 255]. The recently published structure of TPC1 [224, 225] indicates several sites of phosphorylation and a possible role of dimerisation [282] that offers further scope for regulation. Thus, in our model the FDF process might represent direct activation of the channel, the requirement for activation of TPC1-regulatory proteins, or the activation of other channels that shift the tonoplast potential in order to activate TPC1.

Importantly, even if CICR is not the true underlying process for these systems, the application of the FDF model has allowed us to make valuable observations to direct future experimental work, as we shall now discuss.

4.2 Nuclear Ca^{2+} Oscillations

We applied a 2D FDF model to the surface of the nucleus to study generation of nuclear Ca^{2+} oscillations both inside and outside the nucleus in Chapter 2. We wondered whether diffusion of Ca^{2+} through the NPCs might have a key role to play in generating these signals and showed that, indeed, the small flux through NPCs was able to coordinate spike generation even when signalling conditions on either side of the NE were substantially different. If Ca^{2+} was not allowed to pass through NPCs in the model, under those same conditions Ca^{2+} spikes no longer occurred simultaneously on both sides of the NE. Experimental measurements have shown that the nuclear and peri-nuclear Ca^{2+} spikes are generated simultaneously [62], despite differences in diffusion rates for Ca^{2+} in the cytoplasm and nucleoplasm [142] and the numbers of signalling components on the two nuclear membranes [62]. Our modelling has therefore highlighted a possible role of Ca^{2+} diffusion through the NPC during symbiosis signalling.

To confirm this result requires new experimental approaches. Our model predicts that the simultaneous spike generation would be robust to changes in the buffering capacity of the cytoplasm or to different channel distributions on the two membranes. The buffering capacity of the cytoplasm can be artificially changed [114], as could the channel distributions by genetically attaching nuclear localisation or exclusion sequences to the genes of interest (DMI1 or CNGC15 for example). However, this wouldn't eliminate the possibility of some other means of coordination. Until experimental techniques are developed that are able to once and for all establish the Ca^{2+} permeability of the NPC [142], this question will remain open.

The use of a 2D model in Chapter 2 neglected the ability for Ca^{2+} to diffuse into the volume of the cytoplasm/nucleoplasm surrounding or contained by the NE. We showed it was acceptable to make this artificial restriction if care is taken over which parameter sets are chosen. This 2D model could reproduce the overall behaviour at the surface in a full 3D implementation or the behaviour around a single Ca^{2+} release with the right parameters, but

couldn't capture both simultaneously. This result will be of use to those looking to simulate Ca^{2+} signalling in enclosed spaces in which the signalling units are restricted to the surface, for example models of the PM of the cell, the nucleus, or simulation of the cytosolic and ER in animal systems, which can be treated as a spherical system with surface release sites [283, 284].

Now that the symbiotic Ca^{2+} channel has been identified [63], future modelling within this system needs to focus on developing models that incorporate knowledge on how this channel is regulated (see Section 4.4 for further discussion). This process has already started with a compartment model based on the work of Granqvist *et al* [63, 114], but as we have seen in this thesis, the spatial element is important. Combining detailed channel descriptions with full spatial models will allow us to develop a more comprehensive understanding of how these Ca^{2+} signals are generated.

4.3 Systemic Signalling

We explored the propagation of two types of systemic signal in plants in Chapter 3: variation potentials in response to wounding, and Ca^{2+} waves in response to salt stress. The currently accepted conceptual model for how VPs propagate is that a hydraulic wave travels through the xylem, activating electrical signalling in surrounding tissue [135]. But the disparity between the velocities of these two waves led us to investigate further. Our work identified a number of issues with this model. We showed instead that a model in which chemical signals are transported through the xylem to activate electrical signalling in nearby cells is a more consistent explanation of VP propagation, in agreement with [127, 203].

For the Ca^{2+} wave, we considered a number of different models that had been proposed as possible mechanisms underlying its propagation [204] (Figure 3.1). We identified a ROS driven wave as the most likely mechanism using a 1-dimensional FDF model. In particular, we eliminated a TPC1-driven CICR wave due to the gaps that would have to be crossed between neighbouring cells. The existence and requirement of a ROS wave was then confirmed by experiments from our collaborators. Future work in this system would benefit substantially from identification of the other signalling components now known to be required (e.g. a PM-Ca^{2+} channel, or an additional source of ROS).

In constructing our model we did not include plasmodesmata explicitly, merely assuming a means of connecting adjacent cells that had no effect on the diffusion of Ca^{2+}. We wished to only test the possibility of the models working or not, and so didn't need to add in this additional complexity at this stage. Future modelling should take into account more of the details of this system. This will include the plasmodesmata which, as channels between adjacent cells, are similar to the gap junctions of animal systems [285]. The propagation of signals via gap junctions has been modelled by Höfer *et al.* and others [286, 287, 288]. Application of these methods to this system will aid in gaining a more detailed understanding of how these signals cross the cell walls and propagate the wave intercellularly.

4.4 Future Perspectives

4.4.1 CNGCs and Ca^{2+} channel identity

A recurrent theme in the previous sections is a need for a detailed description of the Ca^{2+} (and other) channels involved in the generation of these Ca^{2+} signals. The development of these kinds of models, which have proved so valuable to the animal Ca^{2+} field, in plants has been held back by the challenge of identifying those channels genetically [12, 13, 289]. Only now are we starting to find those missing signalling components. These are not the well studied IP_3R or RyR channels of animal systems, but instead CNGCs, glutamate-like receptors, and TPCs [12, 13] that have not been modelled in detail.

CNGCs represent a diverse class of channel, with 20 different genes in the *Arabidopsis* genome. They have been identified as being involved in gravitropic bending and senescence [290], defence [291], in response to jasmonic acid [292] and the symbiosis signalling process (in *M. truncatula*) [63], as discussed above. They also appear to have a role in systemic signalling in response to flg22 (Simon Gilroy, personal communication). See [223, 289, 293, 294] for reviews.

CNGCs are believed to be activated by binding of cyclic nucleotides cAMP or cGMP, resulting in ionic fluxes of predominantly Ca^{2+} but also K^+ [293]. They respond to raised Ca^{2+} concentrations via binding of Ca^{2+}-bound CaM to a site that overlaps the cyclic nucleotide binding site. Thus, when Ca^{2+} is elevated, CaM displaces the cyclic nucleotide and closes the channel [293]. Within this model there is no obvious scope for CICR type activity, however as highlighted in the discussion of symbiotic Ca^{2+} oscillations, the presence of a partner channel such as DMI1 that is activated by Ca^{2+} might enable CICR to occur in systems utilising CNGCs.

4.4.2 ROS and Ca^{2+} cross-talk

The inter-related nature of ROS and Ca^{2+} signalling is a topic that has been discussed widely in the literature [198, 259, 295, 296, 297]. ROS signalling has been observed in almost every situation that Ca^{2+} signalling has been studied, yet we are only just beginning to study the interaction of these two signalling networks within a modelling framework. ROS is primarily generated through two protein classes, RBOHs and the less well understood peroxidases [298]. RBOHs can be directly regulated by Ca^{2+} [296] while ROS can also trigger Ca^{2+} influx across the PM through channels such as the annexins [239, 296, 299]. In fact, Ordoñez *et al.* [252] showed a role for cyclic nucleotides in modulating the Ca^{2+} response to ROS. Thus, ROS and Ca^{2+} create a linked positive feedback loop whose role is ripe for future study.

In this the response to biological elicitors such as flg22 represents a mathematically unexplored area with great scope for future work. Experimental assays for both ROS and Ca^{2+} have been developed in this system [33], with the recent development of sub-cellular resolution [8]. This system is also able to give rise to systemic signals [198] in a similar way

to salt (Simon Gilroy, personal communication). Extending our models of ROS/Ca^{2+} wave propagation also represents an interesting system for future mathematical developments, for example, the theoretical analysis of a 2 species, coupled, FDF-style system.

4.4.3 Experiment and Theory

It was the aim of this thesis to use intuitive models to advance our knowledge of these Ca^{2+} signalling systems. In Chapter 3 we have shown how our models have directly led to new experimental discoveries and it is our hope that future experiments may extend our investigations of nuclear Ca^{2+} signalling now that the Ca^{2+} channel has been identified. Following the lead exemplified by experimentalists and theoreticians in the animal Ca^{2+} field, future collaborations will be a driving force for progress in the study of plant Ca^{2+} signalling.

List of Abbreviations

The abbreviations that have been used in this thesis are.

ABA	Abscisic Acid
AM	Arbuscular Mycorrhizae
AP	Action Potential
Ca^{2+}	Calcium
CaM	Calmodulin
CaMKII	Calmodulin dependent protein Kinase II
CICR	Calcium Induced Calcium Release
CWC	Calculus of Wrapped Compartments
DPI	Diphenyleneiodonium
ER	Endoplasmic Reticulum
FDF	Fire Diffuse Fire
FRET	Fluorescence Resonance Energy Transfer
GFP	Green Fluorescent Protein
INM	Inner Nuclear Membrane
IP_3R	Inositol-1,4,5-triphosphate Receptors
JA	Jasmonic Acid
La^{2+}	Lanthanum, used as a channel blocker
LCO	Lipochitooligosaccharides
Myc Factor	Mycorrhizal Factor
NADPH	Nicotinamide Adenine Dinucleotide Phosphate-oxidase
NE	Nuclear Envelope
NF	Nod Factor
NPC	Nuclear Pore Complex
ODE	Ordinary Differential Equation
ONM	Outer Nuclear Membrane
PAMPs	Pathogen Associated Molecular Patterns
PD	Plasmodesmata
PM	Plasma Membrane
ROI	Region Of Interest
RICR	ROS-Induced Ca^{2+} Release

RIRR	ROS-Induced ROS Release
RNS	Root Nodule Symbiosis
ROS	Reactive Oxygen Species
RyR	Ryanodine Receptors
SAA	Systemic Acquired Acclimation
SAR	Systemic Acquired Resistance
SERCA	Sarcoplasmic/Endoplasmic Reticulum Calcium ATPase
SV	Slow Vacuolar channel
SYM	Common Symbiotic Pathway
TIP	Tonoplast Intrinsic Proteins
TPC1	Two Pore Channel 1
VP	Variation Potential
WT	Wild Type
YFP	Yellow Fluorescent Protein

Bibliography

[1] F. Dyson, "A meeting with Enrico Fermi," *Nature*, vol. 427, p. 8540, 2004.

[2] The Arabidopsis Genome Initiative, "Analysis of the genome sequence of the flowering plant *Arabidopsis thaliana*," *Nature*, vol. 408, pp. 796–815, 2000.

[3] J. Gunawardena, "Biology is more theoretical than physics," *Molecular Biology of the Cell*, vol. 24, pp. 1827–9, 2013.

[4] G. Dupont, L. Combettes, G. S. Bird, and J. W. Putney, "Calcium Oscillations," *Cold Spring Harbor Perspectives in Biology*, vol. 3, pp. 1–18, 2011.

[5] T. Martins, M. Evans, H. Woolfenden, and R. Morris, "Towards the Physics of Calcium Signalling in Plants," *Plants*, vol. 2, pp. 541–588, 2013.

[6] G. B. Monshausen, M. A. Messerli, and S. Gilroy, "Imaging of the Yellow Cameleon 3.6 indicator reveals that elevations in cytosolic Ca^{2+} follow oscillating increases in growth in root hairs of Arabidopsis," *Plant physiology*, vol. 147, pp. 1690–1698, 2008.

[7] C. N. Kanchiswamy, M. Malnoy, A. Occhipinti, and M. E. Maffei, "Calcium imaging perspectives in plants," *International Journal of Molecular Sciences*, vol. 15, pp. 3842–3859, 2014.

[8] N. F. Keinath, R. Waadt, R. Brugman, J. I. Schroeder, G. Grossmann, K. Schumacher, and M. Krebs, "Live cell imaging with R-GECO1 sheds light on flg22- and chitin-induced transient $[Ca^{2+}]_{cyt}$ patterns in Arabidopsis," *Molecular Plant*, vol. 8, pp. 1188–1200, 2015.

[9] S. Stael, B. Wurzinger, A. Mair, N. Mehlmer, U. C. Vothknecht, and M. Teige, "Plant organellar calcium signalling: an emerging field," *Journal of Experimental Botany*, vol. 63, pp. 1525–1542, 2012.

[10] D. Sanders, C. Brownlee, and J. Harper, "Communicating with calcium," *The Plant cell*, vol. 11, pp. 691–706, 1999.

[11] M. McAinsh and J. Pittman, "Shaping the calcium signature," *New Phytologist*, vol. 181, pp. 275–294, 2009.

[12] D. Sanders, J. Pelloux, C. Brownlee, and J. F. Harper, "Calcium at the crossroads of signaling," *The Plant cell*, vol. 14 Suppl, pp. S401–S417, 2002.

[13] A. N. Dodd, J. Kudla, and D. Sanders, "The Language of Calcium Signaling," *Annual Review of Plant Biology*, vol. 61, pp. 593–620, 2010.

[14] J. Kudla, O. Batistic, and K. Hashimoto, "Calcium Signals: The Lead Currency of Plant Information Processing," *The Plant Cell*, vol. 22, pp. 541–563, 2010.

[15] M. Berridge, P. Lipp, and M. Bootman, "The versatility and universality of calcium signalling," *Nature Reviews Molecular Cell Biology*, vol. 1, pp. 11–21, 2000.

[16] D. E. Clapham, "Calcium Signaling," *Cell*, vol. 131, pp. 1047–1058, 2007.

[17] A. Parekh, "Decoding cytosolic Ca^{2+} oscillations," *Trends in Biochemical Sciences*, vol. 36, pp. 78–87, 2011.

[18] J. Feijò, J. Sainhas, T. Holdaway-Clarke, M. Cordeiro, J. Kunkel, and P. Hepler, "Cellular oscillations and the regulation of growth: the pollen tube paradigm," *Bio Essays*, vol. 23, pp. 86–94, 2001.

[19] A. N. Dodd, M. Gardner, C. Hotta, K. Hubbard, N. Dalchau, J. Love, J.-M. Assie, F. C. Robertson, M. K. Jakobsen, J. Gonçalves, D. Sanders, and A. Webb, "The Arabidopsis circadian clock incorporates a cADPR-based feedback loop," *Science*, vol. 318, pp. 1789–92, 2007.

[20] J. Love, A. N. Dodd, and A. A. R. Webb, "Circadian and diurnal calcium oscillations encode photoperiodic information in Arabidopsis," *Plant Cell*, vol. 16, pp. 956–66, 2004.

[21] W.-G. Choi, M. Toyota, S.-H. Kim, R. Hilleary, and S. Gilroy, "Salt stress-induced Ca^{2+} waves are associated with rapid, long-distance root-to-shoot signaling in plants," *Proceedings of the National Academy of Sciences*, vol. 111, pp. 6497–6502, 2014.

[22] F. E. Tracy, M. Gilliham, A. N. Dodd, A. A. R. Webb, and M. Tester, "NaCl-induced changes in cytosolic free Ca^{2+} in Arabidopsis thaliana are heterogeneous and modified by external ionic composition," *Plant, Cell and Environment*, vol. 31, pp. 1063–1073, 2008.

[23] R. Hedrich and A. Kurkdjian, "Characterization of an anion-permeable channel from sugar beet vacuoles: effect of inhibitors," *The EMBO Journal*, vol. 7, pp. 3661–3666, 1988.

[24] E. Peiter, F. J. M. Maathuis, L. N. Mills, H. Knight, J. Pelloux, A. M. Hetherington, and D. Sanders, "The vacuolar Ca^{2+}-activated channel TPC1 regulates germination and stomatal movement," *Nature*, vol. 434, pp. 325–37, 2005.

[25] V. Kiep, J. Vadassery, J. Lattke, J. P. Maaß, W. Boland, E. Peiter, and A. Mithöfer, "Systemic cytosolic Ca^{2+} elevation is activated upon wounding and herbivory in Arabidopsis," *New Phytologist*, vol. 207, pp. 996–1004, 2015.

[26] A. J. E. van Bel, A. C. U. Furch, T. Will, S. V. Buxa, R. Musetti, and J. B. Hafke, "Spread the news: Systemic dissemination and local impact of Ca^{2+} signals along the phloem pathway," *Journal of Experimental Botany*, vol. 65, pp. 1761–1787, 2014.

[27] T.-H. Kim, M. Bohmer, H. Hu, N. Nishimura, and J. I. Schroeder, "Guard cells signal transduction network: advances in understanding abscisic acid CO_2, and Ca^{2+} signalling," *Annual Review of Plant Biology*, vol. 61, pp. 561–591, 2010.

[28] C. K. Y. Ng, M. R. McAinsh, J. E. Gray, E. Le Hunt, C. P. Leckie, L. Mills, and A. M. Hetherington, "Calcium-based signalling systems in guard cells," *New Phytologist*, vol. 151, pp. 109–120, 2001.

[29] G. J. Allen, S. P. Chu, C. L. Harrington, K. Schumacher, T. Hoffmann, Y. Y. Tang, E. Grill, and J. I. Schroeder, "A defined range of guard cell calcium oscillation parameters encodes stomatal movements," *Nature*, vol. 411, pp. 1053–7, 2001.

[30] J. M. Kwak, I. C. Mori, Z.-M. Pei, N. Leonhardt, M. A. Torres, J. L. Dangl, R. E. Bloom, S. Bodde, J. D. G. Jones, and J. I. Schroeder, "NADPH oxidase AtrbohD and AtrbohF genes function in ROS-dependent ABA signaling in Arabidopsis," *The EMBO journal*, vol. 22, pp. 2623–33, 2003.

[31] A. N. Dodd, M. K. Jakobsen, A. J. Baker, A. Telzerow, S. W. Hou, L. Laplaze, L. Barrot, R. Scott Poethig, J. Haseloff, and A. A. R. Webb, "Time of day modulates low-temperature Ca^{2+} signals in Arabidopsis," *Plant Journal*, vol. 48, pp. 962–973, 2006.

[32] D. Lecourieux, R. Ranjeva, and A. Pugin, "Calcium in plant defence-signalling pathways," *New Phytologist*, vol. 171, pp. 249–269, 2006.

[33] S. Ranf, L. Eschen-Lippold, P. Pecher, J. Lee, and D. Scheel, "Interplay between calcium signalling and early signalling elements during defence responses to microbe- or damage-associated molecular patterns," *Plant Journal*, vol. 68, pp. 100–113, 2011.

[34] K. Thor and E. Peiter, "Cytosolic calcium signals elicited by the pathogen-associated molecular pattern flg22 in stomatal guard cells are of an oscillatory nature," *New Phytologist*, vol. 204, pp. 873–881, 2014.

[35] G. E. D. Oldroyd and J. A. Downie, "Coordinating nodule morphogenesis with rhizobial infection in legumes," *Annual Review of Plant Biology*, vol. 59, pp. 519–46, 2008.

[36] G. E. D. Oldroyd, "Speak, friend, and enter: signalling systems that promote beneficial symbiotic associations in plants," *Nature Reviews Microbiology*, vol. 11, pp. 252–63, 2013.

[37] J. Downie, "Calcium signals in plant immunity: a spiky issue," *New Phytologist*, vol. 204, pp. 733–5, 2014.

[38] F. A. Smith and S. E. Smith, "Structural diversity in (vesicular)-arbuscular mycorrhizal symbioses," *New Phytologist*, vol. 137, pp. 373–388, 1997.

[39] C. P. Humphreys, P. J. Franks, M. Rees, M. I. Bidartondo, J. R. Leake, and D. J. Beerling, "Mutualistic mycorrhiza-like symbiosis in the most ancient group of land plants," *Nature communications*, vol. 1, p. 103, 2010.

[40] M. Harrison, "Signaling in the arbuscular mycorrhizal symbiosis," *Annual Review of Microbiology*, vol. 59, pp. 19–42, 2005.

[41] C. Sbrana and M. Giovannetti, "Chemotropism in the arbuscular mycorrhizal fungus *Glomus mosseae*," *Mycorrhiza*, vol. 15, pp. 539–45, 2005.

[42] A. Besserer, V. Puech-Pagès, P. Kiefer, V. Gomez-Roldan, A. Jauneau, S. Roy, J.-C. Portais, C. Roux, G. Bécard, and N. Séjalon-Delmas, "Strigolactones Stimulate Arbuscular Mycorrhizal Fungi by Activating Mitochondria," *PLoS Biology*, vol. 4, p. e226, 2006.

[43] J. I. Sprent and E. K. James, "Legume Evolution: Where Do Nodules and Mycorrhizas Fit In?," *Plant Physiology*, vol. 144, pp. 575–581, 2007.

[44] C. Kistner and M. Parniske, "Evolution of signal transduction in intracellular symbiosis," *Trends in Plant Science*, vol. 7, pp. 511–18, 2002.

[45] P. Mylona, K. Pawlowski, and T. Bisseling, "Symbiotic Nitrogen Fixation," *The Plant cell*, vol. 7, pp. 869–885, 1995.

[46] B. E. Smith, "Nitrogenase Reveals Its Inner Secrets," *Science*, vol. 297, pp. 1654–55, 2002.

[47] D. E. Canfield, A. N. Glazer, and P. G. Falkowski, "The Evolution and Future of Earth's Nitrogen Cycle," *Science*, vol. 330, pp. 192–196, 2010.

[48] M. Charpentier and G. Oldroyd, "How close are we to nitrogen-fixing cereals?," *Current Opinion in Plant Biology*, vol. 13, pp. 556–64, 2010.

[49] C. Rogers and G. E. D. Oldroyd, "Synthetic biology approaches to engineering the nitrogen symbiosis in cereals," *Journal of Experimental Botany*, vol. 65, pp. 1939–1946, 2014.

[50] S. Radutoiu, L. H. Madsen, E. B. Madsen, H. H. Felle, Y. Umehara, M. Grønlund, S. Sato, Y. Nakamura, S. Tabata, N. Sandal, and J. Stougaard, "Plant recognition of symbiotic bacteria requires two LysM receptor-like kinases," *Nature*, vol. 425, pp. 585–92, 2003.

[51] A. Broghammer, L. Krusell, M. Blaise, J. Sauer, J. T. Sullivan, N. Maolanon, M. Vinther, A. Lorentzen, E. B. Madsen, K. J. Jensen, P. Roepstorff, S. Thirup, C. W. Ronson, M. B. Thygesen, and J. Stougaard, "Legume receptors perceive the rhizobial lipochitin oligosaccharide signal molecules by direct binding," *Proceedings of the National Academy of Sciences of the United States of America*, vol. 109, pp. 13859–64, 2012.

[52] J.-F. Arrighi, A. Barre, B. Ben Amor, A. Bersoult, L. C. Soriano, R. Mirabella, F. de Carvalho-Niebel, E.-P. Journet, M. Ghérardi, T. Huguet, R. Geurts, J. Dénarié, P. Rougé, and C. Gough, "The *Medicago truncatula* lysine motif-receptor-like kinase gene family includes NFP and new nodule-expressed genes," *Plant physiology*, vol. 142, pp. 265–79, 2006.

[53] M. Antolín-Llovera, M. Ried, A. Binder, and M. Parniske, "Receptor kinase signaling pathways in plant-microbe interactions," *Annual Review of Phytopathology*, vol. 50, pp. 451–73, 2012.

[54] M. K. Ried, M. Antolín-Llovera, and M. Parniske, "Spontaneous symbiotic reprogramming of plant roots triggered by receptor-like kinases," *eLife*, vol. 3, pp. 1–17, 2014.

[55] J.-M. Ané, G. B. Kiss, B. K. Riely, R. V. Penmetsa, G. E. D. Oldroyd, C. Ayax, J. Lévy, F. Debellé, J.-M. Baek, P. Kalo, C. Rosenberg, B. A. Roe, S. R. Long, J. Dénarié, and D. R. Cook, "Medicago truncatula DMI1 required for bacterial and fungal symbioses in legumes," *Science*, vol. 303, pp. 1364–7, 2004.

[56] A. Edwards, A. B. Heckmann, F. Yousafzai, G. Duc, and J. A. Downie, "Structural implications of mutations in the pea SYM8 symbiosis gene, the DMI1 ortholog, encoding a predicted ion channel," *Molecular plant-microbe interactions: MPMI*, vol. 20, pp. 1183–91, 2007.

[57] B. K. Riely, G. Lougnon, J.-M. Ané, and D. R. Cook, "The symbiotic ion channel homolog DMI1 is localized in the nuclear membrane of *Medicago truncatula* roots," *The Plant journal*, vol. 49, pp. 208–16, 2007.

[58] M. Charpentier, R. Bredemeier, G. Wanner, N. Takeda, E. Schleiff, and M. Parniske, "Lotus japonicus CASTOR and POLLUX are ion channels essential for perinuclear calcium spiking in legume root endosymbiosis," *The Plant cell*, vol. 20, pp. 3467–79, 2008.

[59] N. Kanamori, L. H. Madsen, S. Radutoiu, M. Frantescu, E. M. H. Quistgaard, H. Miwa, J. A. Downie, E. K. James, H. H. Felle, L. L. Haaning, T. H. Jensen, S. Sato, Y. Nakamura, S. Tabata, N. Sandal, and J. Stougaard, "A nucleoporin is required for induction of Ca^{2+} spiking in legume nodule development and essential for rhizobial and fungal

symbiosis," *Proceedings of the National Academy of Sciences of the United States of America*, vol. 103, pp. 359–64, 2006.

[60] K. Saito, M. Yoshikawa, K. Yano, H. Miwa, H. Uchida, E. Asamizu, S. Sato, S. Tabata, H. Imaizumi-Anraku, Y. Umehara, H. Kouchi, Y. Murooka, K. Szczyglowski, J. A. Downie, M. Parniske, M. Hayashi, and M. Kawaguchi, "NUCLEOPORIN85 is required for calcium spiking, fungal and bacterial symbioses, and seed production in Lotus japonicus," *The Plant cell*, vol. 19, pp. 610–24, 2007.

[61] M. Groth, N. Takeda, J. Perry, H. Uchida, S. Dräxl, A. Brachmann, S. Sato, S. Tabata, M. Kawaguchi, T. L. Wang, and M. Parniske, "NENA, a Lotus japonicus homolog of Sec13, is required for rhizodermal infection by arbuscular mycorrhiza fungi and rhizobia but dispensable for cortical endosymbiotic development," *The Plant cell*, vol. 22, pp. 2509–26, 2010.

[62] W. Capoen, J. Sun, D. Wysham, M. S. Otegui, M. Venkateshwaran, S. Hirsch, H. Miwa, J. A. Downie, R. J. Morris, J.-M. Ané, and G. E. D. Oldroyd, "Nuclear membranes control symbiotic calcium signaling of legumes," *Proceedings of the National Academy of Sciences of the United States of America*, vol. 108, pp. 14348–53, 2011.

[63] M. Charpentier, J. Sun, T. V. Martins, G. V. Radhakrishnan, K. Findlay, E. Soumpourou, J. Thouin, A.-A. Véry, D. Sanders, R. J. Morris, and G. E. D. Oldroyd, "Symbiotic Calcium Oscillations," *Science*, vol. 352, pp. 1102–5, 2016.

[64] J. Lévy, C. Bres, R. Geurts, B. Chalhoub, O. Kulikova, G. Duc, E.-P. Journet, J.-M. Ané, E. Lauber, T. Bisseling, J. Dénarié, C. Rosenberg, and F. Debellé, "A putative Ca^{2+} and calmodulin-dependent protein kinase required for bacterial and fungal symbioses," *Science*, vol. 303, pp. 1361–4, 2004.

[65] R. M. Mitra, C. A. Gleason, A. Edwards, J. Hadfield, J. A. Downie, G. E. D. Oldroyd, and S. R. Long, "A Ca^{2+}/calmodulin-dependent protein kinase required for symbiotic nodule development: gene identification by transcript-based cloning," *Proceedings of the National Academy of Sciences of the United States of America*, vol. 101, pp. 4701–5, 2004.

[66] E. Messinese, J.-H. Mun, L. H. Yeun, D. Jayaraman, P. Rougé, A. Barre, G. Lougnon, S. Schornack, J.-J. Bono, D. R. Cook, and J.-M. Ané, "A novel nuclear protein interacts with the symbiotic DMI3 calcium- and calmodulin-dependent protein kinase of *Medicago truncatula*," *Molecular plant-microbe interactions: MPMI*, vol. 20, pp. 912–21, 2007.

[67] K. Yano, S. Yoshida, J. Müller, S. Singh, M. Banba, K. Vickers, K. Markmann, C. White, B. Schuller, S. Sato, E. Asamizu, S. Tabata, Y. Murooka, J. Perry, T. L. Wang,

M. Kawaguchi, H. Imaizumi-Anraku, M. Hayashi, and M. Parniske, "CYCLOPS, a mediator of symbiotic intracellular accommodation," *Proceedings of the National Academy of Sciences of the United States of America*, vol. 105, pp. 20540–5, 2008.

[68] P. Smit, J. Raedts, V. Portyanko, F. Debellé, C. Gough, T. Bisseling, and R. Geurts, "NSP1 of the GRAS protein family is essential for rhizobial Nod factor-induced transcription," *Science*, vol. 308, pp. 1789–91, 2005.

[69] F. Maillet, V. Poinsot, O. André, V. Puech-Pagès, A. Haouy, M. Gueunier, L. Cromer, D. Giraudet, D. Formey, A. Niebel, E. A. Martinez, H. Driguez, G. Bécard, and J. Dénarié, "Fungal lipochitooligosaccharide symbiotic signals in arbuscular mycorrhiza," *Nature*, vol. 469, pp. 58–63, 2011.

[70] J. Dénarié, F. Debellé, and J.-C. Promé, "Rhizobium lipo-chitooligosaccharide nodulation factors: Signaling molecules mediating recognition and morphogenesis," *Annual Review of Biochemistry*, vol. 65, pp. 503–35, 1996.

[71] X. Perret, C. Staehelin, and W. J. Broughton, "Molecular Basis of Symbiotic Promiscuity," *Microbiology and Molecular Biology Reviews*, vol. 64, 2000.

[72] A. A. N. van Brussel, R. Bakhuizen, P. C. van Spronsen, H. P. Spaink, T. Tak, B. J. J. Lugtenberg, and J. W. Kijne, "Induction of preinfection thread structures in the leguminous host plant by mitogenic lipooligosaccharides of Rhizobium," *Science*, vol. 257, pp. 70–72, 1992.

[73] N. C. A. de Ruijter, T. Bisseling, and A. M. C. Emons, "*Rhizobium* Nod Factors Induce an Increase in Sub-apical Fine Bundles of Actin Filaments in *Vicia sativa* Root Hairs within Minutes," *Molecular Plant-Microbe Interactions: MPMI*, vol. 12, pp. 829–832, 1999.

[74] C. P. Ponting, L. Aravind, J. Schultz, P. Bork, and E. V. Koonin, "Eukaryotic signalling domain homologues in archaea and bacteria. Ancient ancestry and horizontal gene transfer," *Journal of molecular biology*, vol. 289, pp. 729–45, 1999.

[75] E. Limpens, C. Franken, P. Smit, J. Willemse, T. Bisseling, and R. Geurts, "LysM Domain Receptor Kinases Regulating Rhizobial Nod Factor-Induced Infection," *Science*, vol. 302, pp. 630–633, 2003.

[76] P. Smit, E. Limpens, R. Geurts, E. Fedorova, E. Dolgikh, C. Gough, and T. Bisseling, "Medicago LYK3, an entry receptor in rhizobial nodulation factor signaling," *Plant physiology*, vol. 145, pp. 183–191, 2007.

[77] S. Radutoiu, L. H. Madsen, E. B. Madsen, A. Jurkiewicz, E. Fukai, E. M. H. Quistgaard, A. S. Albrektsen, E. K. James, S. Thirup, and J. Stougaard, "LysM domains mediate

lipochitin-oligosaccharide recognition and NFR genes extend the symbiotic host range," *The EMBO journal*, vol. 26, pp. 3923–35, 2007.

[78] S. Bensmihen, F. de Billy, and C. Gough, "Contribution of NFP LysM domains to the recognition of Nod factors during the *Medicago truncatula/Sinorhizobium meliloti* symbiosis," *PLoS ONE*, vol. 6, 2011.

[79] C. Kistner, T. Winzer, A. Pitzschke, L. Mulder, S. Sato, T. Kaneko, S. Tabata, N. Sandal, J. Stougaard, K. J. Webb, K. Szczyglowski, and M. Parniske, "Seven Lotus japonicus genes required for transcriptional reprogramming of the root during fungal and bacterial symbiosis," *The Plant cell*, vol. 17, pp. 2217–2229, 2005.

[80] H. Miwa, J. Sun, G. E. D. Oldroyd, and J. A. Downie, "Analysis of Nod-factor-induced calcium signaling in root hairs of symbiotically defective mutants of Lotus japonicus," *Molecular plant-microbe interactions: MPMI*, vol. 19, pp. 914–23, 2006.

[81] D. W. Ehrhardt, R. Wais, and S. R. Long, "Calcium spiking in plant root hairs responding to Rhizobium nodulation signals," *Cell*, vol. 85, pp. 673–81, 1996.

[82] H. Felle, E. Kondorosi, A. Kondorosi, and M. Schultze, "Nod factors modulate the concentration of cytosolic free calcium differently in growing and non-growing root hairs of *Medicago sativa* L.," *Planta*, vol. 209, pp. 207–12, 1999.

[83] H. Felle, E. Kondorosi, A. Kondorosi, and M. Schultze, "Nod signal-induced plasma membrane potential changes in alfalfa root hairs are differentially sensitive to structural modifications of the lipochitooligosaccharide," *Plant Journal*, vol. 7, pp. 939–47, 1995.

[84] H. Felle, E. Kondorosi, A. Kondorosi, and M. Schultze, "Rapid alkalinization in alfalfa root hairs in response to rhizobial lipochitooligosaccharide signals," *Plant Journal*, vol. 10, pp. 295–301, 1996.

[85] H. Felle, E. Kondorosi, A. Kondorosi, and M. Schultze, "The role of ion fluxes in nod factor signalling in *Medicago sativa*," *Plant Journal*, vol. 13, pp. 455–63, 1998.

[86] M. Charpentier and G. E. D. Oldroyd, "Nuclear calcium signaling in plants," *Plant physiology*, vol. 163, pp. 496–503, 2013.

[87] E. Engstrom, D. Ehrhardt, R. M. Mitra, and S. R. Long, "Pharmacological Analysis of Nod Factor-Induced Calcium Spiking in Medicago truncatula. Evidence for the Requirement of Type IIA Calcium Pumps and Phosphoinositide Signaling 1," *Plant physiology*, vol. 128, pp. 1390–1401, 2002.

[88] D. Charron, J.-L. Pingret, M. Chabaud, E.-P. Journet, and D. G. Barker, "Pharmacological Evidence That Multiple Phospholipid Signaling Pathways Link Rhizobium

Nodulation Factor Perception in *Medicago truncatula* Root Hairs to Intracellular Responses, Including Ca^{2+} Spiking and Specific ENOD Gene Expression," *Plant physiology*, vol. 136, pp. 3582–3593, 2004.

[89] L. Chen, W. Hu, S. Tan, M. Wang, Z. Ma, S. Zhou, X. Deng, Y. Zhang, C. Huang, G. Yang, and G. He, "Genome-Wide Identification and Analysis of MAPK and MAPKK Gene Families in Brachypodium distachyon," *PLoS ONE*, vol. 7, pp. 18–19, 2012.

[90] Z. Kevei, G. Lougnon, P. Mergaert, G. V. Horvath, A. Kereszt, D. Jayaraman, N. Zaman, F. Marcel, K. Regulski, G. B. Kiss, A. Kondorosi, G. Endre, E. Kondorosi, and J. M. Anè, "3-hydroxy-3-methylglutaryl coenzyme A reductase1 interacts with NORK and is crucial for nodulation in Medicago truncatula," *Plant Cell*, vol. 19, pp. 3974–3989, 2007.

[91] S. A. Walker, V. Viprey, and J. A. Downie, "Dissection of nodulation signaling using pea mutants defective for calcium spiking induced by nod factors and chitin oligomers," *Proceedings of the National Academy of Sciences of the United States of America*, vol. 97, pp. 13413–8, 2000.

[92] R. J. Wais, D. H. Keating, and S. R. Long, "Structure-Function Analysis of Nod Factor-Induced Root Hair Calcium Spiking in Rhizobium-Legume Symbiosis," *Plant physiology*, vol. 129, pp. 211–224, 2002.

[93] W. Capoen, J. den Herder, J. Sun, C. Verplancke, A. de Keyser, R. de Rycke, S. Goormachtig, G. Oldroyd, and M. Holsters, "Calcium spiking patterns and the role of the calcium/calmodulin-dependent kinase CCaMK in lateral root base nodulation of *Sesbania rostrata*," *The Plant cell*, vol. 21, pp. 1526–40, 2009.

[94] B. J. Sieberer, M. Chabaud, A. C. Timmers, A. Monin, J. Fournier, and D. G. Barker, "A nuclear-targeted cameleon demonstrates intranuclear Ca^{2+} spiking in *Medicago truncatula* root hairs in response to rhizobial nodulation factors," *Plant physiology*, vol. 151, pp. 1197–206, 2009.

[95] M. Venkateshwaran, A. Cosme, L. Han, M. Banba, K. a. Satyshur, E. Schleiff, M. Parniske, H. Imaizumi-Anraku, and J.-M. Ané, "The recent evolution of a symbiotic ion channel in the legume family altered ion conductance and improved functionality in calcium signaling," *The Plant cell*, vol. 24, pp. 2528–45, 2012.

[96] J. B. Miller, A. Pratap, A. Miyahara, L. Zhou, S. Bornemann, R. J. Morris, and G. E. D. Oldroyd, "Calcium/Calmodulin-dependent protein kinase is negatively and positively regulated by calcium, providing a mechanism for decoding calcium responses during symbiosis signaling," *The Plant cell*, vol. 25, pp. 5053–66, 2013.

[97] T. Hayashi, M. Banba, Y. Shimoda, H. Kouchi, M. Hayashi, and H. Imaizumi-Anraku, "A dominant function of CCaMK in intracellular accommodation of bacterial and fungal endosymbionts," *The Plant Journal*, vol. 63, pp. 141–54, 2010.

[98] C. Gleason, S. Chaudhuri, T. Yang, A. Muñoz, B. W. Poovaiah, and G. E. D. Oldroyd, "Nodulation independent of rhizobia induced by a calcium-activated kinase lacking autoinhibition," *Nature*, vol. 441, pp. 1149–52, 2006.

[99] S. Kosuta, S. Hazledine, J. Sun, H. Miwa, R. J. Morris, J. A. Downie, and G. E. D. Oldroyd, "Differential and chaotic calcium signatures in the symbiosis signaling pathway of legumes," *Proceedings of the National Academy of Sciences of the United States of America*, vol. 105, pp. 9823–8, 2008.

[100] M. Chabaud, A. Genre, B. J. Sieberer, A. Faccio, J. Fournier, M. Novero, D. G. Barker, and P. Bonfante, "Arbuscular mycorrhizal hyphopodia and germinated spore exudates trigger Ca^{2+} spiking in the legume and nonlegume root epidermis," *The New phytologist*, vol. 189, pp. 347–55, 2011.

[101] B. J. Sieberer, M. Chabaud, J. Fournier, A. C. J. Timmers, and D. G. Barker, "A switch in Ca^{2+} spiking signature is concomitant with endosymbiotic microbe entry into cortical root cells of *Medicago truncatula*," *The Plant journal*, vol. 69, pp. 822–30, 2012.

[102] A. Genre, M. Chabaud, and T. Timmers, "Arbuscular mycorrhizal fungi elicit a novel intracellular apparatus in *Medicago truncatula* root epidermal cells before infection," *The Plant Cell*, vol. 17, pp. 3489–3499, 2005.

[103] M. Falcke, "Reading the patterns in living cells: the physics of Ca^{2+} signalling," *Advances in Physics*, vol. 53, pp. 255–440, 2004.

[104] J. Lechleiter, S. Girard, E. Peralta, and D. Clapham, "Spiral calcium wave propagation and annihilation in xenopus laevis oocytes," *Science*, vol. 252, pp. 123–6, 1991.

[105] H. Cheng, M. Lederer, W. Lederer, and M. Cannell, "Calcium sparks and $[Ca^{2+}]_i$ waves in cardiac myocytes," *American Journal of Physiology*, vol. 270, pp. 148–59, 1996.

[106] J. Wagner and J. Keizer, "Effects of rapid buffers on Ca^{2+} diffusion and Ca^{2+} oscillations," *Biophysical journal*, vol. 67, pp. 447–56, 1994.

[107] J. Keizer, G. D. Smith, S. Ponce-Dawson, and J. E. Pearson, "Saltatory propagation of Ca^{2+} waves by Ca^{2+} sparks," *Biophysical Journal*, vol. 75, pp. 595–600, 1998.

[108] J. E. Pearson and S. Ponce-Dawson, "Crisis on skid row," *Physica A: Statistical Mechanics and its Applications*, vol. 257, pp. 141–148, 1998.

[109] S. P. Dawson, J. Keizer, and J. E. Pearson, "Fire-diffuse-fire model of dynamics of intracellular calcium waves," *Proceedings of the National Academy of Sciences of the United States of America*, vol. 96, pp. 6060–3, 1999.

[110] L. Jaffe, "Classes and mechanisms of calcium waves," *Cell Calcium*, vol. 14, pp. 736–45, 1993.

[111] S. Coombes, "The effect of ion pumps on the speed of travelling waves in the fire-diffuse-fire model of Ca^{2+} release," *Bulletin of mathematical biology*, vol. 63, pp. 1–20, 2001.

[112] Y. Timofeeva and S. Coombes, "Wave bifurcation and propagation failure in a model of Ca^{2+} release," *Journal of Mathematical Biology*, vol. 47, pp. 249–269, 2003.

[113] S. Coombes, R. Hinch, and Y. Timofeeva, "Receptors, sparks and waves in a fire-diffuse-fire framework for calcium release," *Progress in biophysics and molecular biology*, vol. 85, pp. 197–216, 2004.

[114] E. Granqvist, D. Wysham, S. Hazledine, W. Kozlowski, J. Sun, M. Charpentier, T. Vaz Martins, P. Haleux, K. Tsaneva-Atanasova, J. A. Downie, G. E. D. Oldroyd, and R. J. Morris, "Buffering capacity explains signal variation in symbiotic calcium oscillations," *Plant physiology*, vol. 160, pp. 2300–2310, 2012.

[115] A. Miyawaki, O. Griesbeck, R. Heim, and R. Y. Tsien, "Dynamic and quantitative Ca^{2+} measurements using improved cameleons," *Proceedings of the National Academy of Sciences of the United States of America*, vol. 96, pp. 2135–40, 1999.

[116] K. Deisseroth, E. K. Heist, and R. W. Tsien, "Translocation of calmodulin to the nucleus supports CREB phosphorylation in hippocampal neurons," *Nature*, vol. 392, pp. 198–202, 1998.

[117] E. Peiter, J. Sun, A. B. Heckmann, M. Venkateshwaran, B. K. Riely, M. S. Otegui, A. Edwards, G. Freshour, M. G. Hahn, D. R. Cook, D. Sanders, G. E. D. Oldroyd, J. A. Downie, and J.-M. Ané, "The Medicago truncatula DMI1 protein modulates cytosolic calcium signaling," *Plant physiology*, vol. 145, pp. 192–203, 2007.

[118] E. Sciacca, S. Spinella, A. Genre, and C. Calcagno, "Analysis of Calcium Spiking in Plant Root Epidermis through CWC Modeling," *Electronic Notes in Theoretical Computer Science*, vol. 277, pp. 65–76, 2011.

[119] M. Coppo, F. Damiani, M. Drocco, E. Grassi, E. Sciacca, S. Spinella, and A. Troina, "Hybrid Calculus of Wrapped Compartments," *Electronic Proceedings in Theoretical Computer Science*, vol. 40, pp. 102–120, 2010.

[120] Terese, *Term Rewriting Systems*. Cambridge University Press, 2003.

[121] E. Jaynes, "Information theory and statistical mechanics," *Physical Review*, vol. 106, p. 620, 1957.

[122] C. Calcagno, M. Coppo, F. Damiani, M. Drocco, E. Sciacca, S. Spinella, and A. Troina, "Modelling Spatial Interactions in the Arbuscular Mycorrhizal Symbiosis using the Calculus of Wrapped Compartments," *Electronic Proceedings in Theoretical Computer Science*, vol. 67, pp. 3–18, 2011.

[123] G. Queisser and G. Wittum, "A method to investigate the diffusion properties of nuclear calcium," *Biological Cybernetics*, vol. 105, pp. 211–216, 2011.

[124] J. Fromm and S. Lautner, "Electrical signals and their physiological significance in plants," *Plant, cell & environment*, vol. 30, pp. 249–57, 2007.

[125] H. H. Felle and M. R. Zimmermann, "Systemic signalling in barley through action potentials," *Planta*, vol. 226, pp. 203–14, 2007.

[126] D. Cosgrove and R. Hedrich, "Stretch-activated chloride, potassium, and calcium channels coexisting in plasma membranes of guard cells of *Vicia faba* L.," *Planta*, vol. 186, pp. 143–53, 1991.

[127] M. Malone, *Advances in Botanical Research*, vol. 22, ch. Rapid, long distance signal transmission in higher plants, pp. 163–228. Academic Press, 1996.

[128] V. Sukhov and V. Vodeneev, "A mathematical model of action potential in cells of vascular plants," *The Journal of membrane biology*, vol. 232, pp. 59–67, 2009.

[129] D. Gradmann and J. Hoffstadt, "Membrane Biology Electrocoupling of Ion Transporters in Plants: Interaction with Internal Ion Concentrations," *Journal of Membrane Biology*, vol. 166, pp. 51–59, 1998.

[130] D. Gradmann, "Impact of Apoplast Volume on Ionic Relations in Plant Cells," *Journal of Membrane Biology*, vol. 184, pp. 61–69, 2001.

[131] V. Sukhov, V. Nerush, L. Orlova, and V. Vodeneev, "Simulation of action potential propagation in plants," *Journal of Theoretical Biology*, vol. 291, pp. 47–55, 2011.

[132] V. Sukhov, E. Akinchits, L. Katicheva, and V. Vodeneev, "Simulation of variation potential in higher plant cells," *Journal of Membrane Biology*, vol. 246, pp. 287–296, 2013.

[133] R. Stahlberg, R. E. Cleland, and E. Van Volkenburgh, "Decrement and amplification of slow wave potentials during their propagation in *Helianthus annuus* L. shoots," *Planta*, vol. 220, pp. 550–8, 2005.

[134] R. Stahlberg and D. J. Cosgrove, "The Propagation of Slow Wave Potentials in Pea Epicotyls," *Plant physiology*, vol. 113, pp. 209–217, 1997.

[135] E. E. Farmer, D. Gasperini, and I. F. Acosta, "The squeeze cell hypothesis for the activation of jasmonate synthesis in response to wounding," *Journal of Physiology*, vol. 204, pp. 282–288, 2014.

[136] M. Rodrigues, D. Gomes, M. Leite, W. Grant, L. Zhang, L. Wing, Y. Cheng, A. Bennett, and M. Nathanson, "Nucleoplasmic calcium is required for cell proliferation," *Journal of Biological Chemistry*, vol. 282, pp. 17061–68, 2007.

[137] W. Echevarría, M. F. Leite, M. Guerra, W. Zipfel, and H. Natanson, "Regulation of calcium signals in the nucleus by a nucleoplasmic reticulum," *Nat Cell Biology*, vol. 5, pp. 440–446, 2003.

[138] C. Mazars, C. Brire, S. Bourque, and P. Thuleau, "Nuclear calcium signaling: an emerging topic in plants," *Biochimie*, vol. 93, pp. 2068–2074, 2011.

[139] J.-P. Mauger, "Role of the nuclear envelope in calcium signalling," *Biology of the cell*, vol. 104, pp. 70–83, 2012.

[140] A. G. Oliveira, E. S. Guimaraes, L. M. Andrade, G. B. Menezes, and M. Fatima Leite, "Decoding Calcium Signaling Across the Nucleus," *Physiology*, vol. 29, pp. 361–368, 2014.

[141] T. Merkle, "Nucleo-cytoplasmic transport of proteins and RNA in plants," *Plant Cell Reports*, vol. 30, pp. 153–176, 2011.

[142] M. D. Bootman, C. Fearnley, I. Smyrnias, F. MacDonald, and H. L. Roderick, "An update on nuclear calcium signalling," *Journal of cell science*, vol. 122, pp. 2337–50, 2009.

[143] C. Perez-terzic, M. Jaconi, and D. E. Clapham, "Nuclear calcium and the regulation of the nuclear pore complex," *BioEssays*, vol. 19, pp. 787–92, 1997.

[144] A. Kramer, Y. Ludwig, V. Shahin, and H. Oberleithner, "A pathway separate from the central channel through the nuclear pore complex for inorganic ions and small macromolecules," *Journal of Biological Chemistry*, vol. 282, pp. 31437–31443, 2007.

[145] V. Shahin, T. Danker, K. Enss, R. Ossig, and H. Oberleithner, "Evidence for Ca^{2+}- and ATP-sensitive peripheral," *Faseb J.*, vol. 15, pp. 1895–1901, 2001.

[146] J. Bustamante, E. Michelette, J. Geibel, D. Dean, J. Hanover, and T. McDonnell, "Calcium, ATP and nuclear pore channel gating," *Pflügers Arch – Eur J Physiol*, vol. 439, pp. 433–444, 2000.

[147] N. Pauly, M. R. Knight, P. Thuleau, A. H. van der Luit, M. Moreau, A. J. Trewavas, R. Ranjeva, and C. Mazars, "Control of free calcium in plant cell nuclei," *Nature*, vol. 405, pp. 754–5, 2000.

[148] T. Danker, V. Shahin, A. Schlune, C. Schäfer, and H. Oberleithner, "Electrophoretic plugging of nuclear pores by using the nuclear hourglass technique," *Journal of Membrane Biology*, vol. 184, pp. 91–99, 2001.

[149] O. Gerasimenko and J. Gerasimenko, "New aspects of nuclear calcium signalling," *Journal of cell science*, vol. 117, pp. 3087–94, 2004.

[150] A. Eder and H. Bading, "Calcium signals can freely cross the nuclear envelope in hippocampal neurons: somatic calcium increases generate nuclear calcium transients," *BMC neuroscience*, vol. 8, p. 57, 2007.

[151] N. Pauly, M. R. Knight, P. Thuleau, A. Graziana, S. Muto, R. Ranjeva, and C. Mazars, "The nucleus together with the cytosol generates patterns of specific cellular calcium signatures in tobacco suspension culture cells," *Cell calcium*, vol. 30, pp. 413–421, 2001.

[152] D. Lecourieux, O. Lamotte, S. Bourque, D. Wendehenne, C. Mazars, R. Ranjeva, and A. Pugin, "Proteinaceous and oligosaccharidic elicitors induce different calcium signatures in the nucleus of tobacco cells," *Cell Calcium*, vol. 38, pp. 527–538, 2005.

[153] C. Lachaud, D. Da Silva, V. Cotelle, P. Thuleau, T. C. Xiong, A. Jauneau, C. Brière, A. Graziana, Y. Bellec, J. D. Faure, R. Ranjeva, and C. Mazars, "Nuclear calcium controls the apoptotic-like cell death induced by D-erythro-sphinganine in tobacco cells," *Cell Calcium*, vol. 47, pp. 92–100, 2010.

[154] T. C. Xiong, S. Coursol, S. Grat, R. Ranjeva, and C. Mazars, "Sphingolipid metabolites selectively elicit increases in nuclear calcium concentration in cell suspension cultures and in isolated nuclei of tobacco," *Cell Calcium*, vol. 43, pp. 29–37, 2008.

[155] A. Walter, C. Mazars, M. Maitrejean, J. Hopke, R. Ranjeva, W. Boland, and A. Mithöfer, "Structural requirements of jasmonates and synthetic analogues as inducers of Ca^{2+} signals in the nucleus and the cytosol of plant cells," *Angewandte Chemie - International Edition*, vol. 46, pp. 4783–4785, 2007.

[156] Y. Timofeeva and S. Coombes, "Directed percolation in a two-dimensional stochastic fire-diffuse-fire model," *Physical Review E*, vol. 70, p. 062901, 2004.

[157] R. Thul, T. Bellamy, H. Roderick, M. Bootman, and S. Coombes, "Calcium Oscillations," *Advances in Experimental Medical Biology*, vol. 641, pp. 1–27, 2008.

[158] R. Thul, K. Thurley, and M. Falcke, "Toward a predictive model of Ca^{2+} puffs," *Chaos*, vol. 19, 2009.

[159] K. Thurley and M. Falcke, "Derivation of Ca^{2+} signals from puff properties reveals that pathway function is robust against cell variability but sensitive for control," *Proceedings of the National Academy of Sciences of the United States of America*, vol. 108, pp. 427–432, 2011.

[160] J. S. Marchant and I. Parker, "Role of elementary Ca^{2+} puffs in generating repetitive Ca^{2+} oscillations," *EMBO Journal*, vol. 20, pp. 65–76, 2001.

[161] W. Press, S. Teukolsky, W. Vetterling, and B. Flannery, *Numerical Recipes*. Cambridge University Press, 3 ed., 2007.

[162] A. Skupin, H. Kettenmann, and M. Falcke, "Calcium signals driven by single channel noise," *PLoS computational biology*, vol. 6, pp. 17–19, 2010.

[163] "Points on a sphere." http://www.softimageblog.com/archives/115. Accessed: 8 October 2013.

[164] G. E. D. Oldroyd and J. A. Downie, "Nuclear calcium changes at the core of symbiosis signalling," *Current opinion in plant biology*, vol. 9, pp. 351–7, 2006.

[165] D. Swainsbury, L. Zhou, G. Oldroyd, and S. Bornemann, "Calcium ion binding properties of *Medicago truncatula* calcium/calmodulin-dependent protein kinase," *Biochemistry*, vol. 51, pp. 6895–6907, 2012.

[166] B. Pando, J. Pearson, and S. Dawson, "Sheet Excitability and Nonlinear Wave Propagation," *Physical Review Letters*, vol. 91, p. 258101, 2003.

[167] K. Riley, M. Hobson, and S. Bence, *Mathematical methodes for physics and engineering*. Cambridge University Press, 3 ed., 2006.

[168] N. L. Allbritton, T. Meyer, and L. Stryer, "Range of messenger action of calcium ion and inositol 1,4,5-trisphosphate," *Science*, vol. 258, pp. 1812–1815, 1992.

[169] K. Maeshima, H. Iino, S. Hihara, and N. Imamoto, "Nuclear size, nuclear pore number and cell cycle," *Nucleus*, vol. 2, pp. 113–118, 2011.

[170] N. Belgareh and V. Doye, "Dynamics of nuclear pore distribution in nucleoporin mutant yeast cells," *J Cell Biol*, vol. 136, pp. 747–759, 1997.

[171] N. Imamoto and T. Funakoshi, "Nuclear pore dynamics during the cell cycle," *Current Opinion in Cell Biology*, vol. 24, pp. 453–459, 2012.

[172] F. Domínguez and F. Cejudo, "A comparison between nuclear dismantling during plant and animal programmed cell death," *Plant Sci.*, vol. 197, pp. 114–121, 2012.

[173] J. Fiserova, E. Kiseleva, and M. Goldberg, "Nuclear envelope and nuclear pore complex structure and organization in tobacco by-2 cells," *The Plant Journal*, vol. 59, pp. 243–255, 2009.

[174] Y. Kinoshita, T. Kalir, P. Dottino, and D. Kohtz, "Nuclear distributions of nup62 and nup214 suggest architectural diversity and spatial patterning among nuclear pore complexes," *PLoS ONE*, vol. 7, p. e36137, 2012.

[175] M. Winey, D. Yarar, T. J. Giddings, and D. Mastronarde, "Nuclear pore complex number and distribution throughout the saccharomyces cerevisiae cell cycle by three-dimensional reconstruction from electron micrographs of nuclear envelopes," *Molecular Biology of the Cell*, vol. 8, pp. 2119–2132, 1997.

[176] J. Boruc, X. Zhou, and I. Meier, "Dynamics of the plant nuclear envelope and nuclear pore," *Plant physiology*, vol. 158, pp. 78–86, 2012.

[177] A. Binder and M. Parniske, "Analysis of the Lotus japonicus nuclear pore NUP107-160 subcomplex reveals pronounced structural plasticity and functional redundancy," *Frontiers in plant science*, vol. 4, p. 552, 2014.

[178] A. Grover, "Targeting of calcium-sensing protein cameleon from cytoplasm to nucleus," *Journal of Plant Biochemistry and Biotechnology*, vol. 24, pp. 365–368, 2015.

[179] G. E. D. Oldroyd, J. D. Murray, P. S. Poole, and J. A. Downie, "The rules of engagement in the legume-rhizobial symbiosis.," *Annual review of genetics*, vol. 45, pp. 119–144, 2011.

[180] P. Mermelstein, K. Deisseroth, N. Dasgupta, A. Isaksen, and R. Tsien, "Calmodulin priming: nuclear translocation of a calmodulin complex and the memory of prior neuronal activity," *Proceedings of the National Academy of Sciences of the United States of America*, vol. 98, pp. 15342–47, 2001.

[181] R. Thorogate and K. Torok, "Ca^{2+}-dependent and -independent mechanisms of calmodulin nuclear translocation," *Journal of Cell Science*, vol. 117, pp. 5923–36, 2004.

[182] X. Wu and D. Bers, "Free and bound intracellular calmodulin measurements in cardiac myocytes," *Cell Calcium*, vol. 41, pp. 353–364, 2007.

[183] P. Kaló, C. Gleason, A. Edwards, J. Marsh, R. M. Mitra, S. Hirsch, J. Jakab, S. Sims, S. R. Long, J. Rogers, G. B. Kiss, J. A. Downie, and G. E. D. Oldroyd, "Nodulation signaling in legumes requires NSP2, a member of the GRAS family of transcriptional regulators," *Science*, vol. 308, pp. 1786–9, 2005.

[184] L. Gerace and B. Burke, "Functional organization of the nuclear envelope," *Annual Review of Cell Biology*, vol. 4, pp. 335–374, 1988.

[185] C. Mazars, S. Bourque, A. Mithöfer, A. Pugin, and R. Ranjeva, "Calcium homeostasis in plant cell nuclei," *The New phytologist*, vol. 181, pp. 261–274, 2009.

[186] A. J. M. Matzke, T. M. Weiger, and M. Matzke, "Ion channels at the nucleus: electrophysiology meets the genome," *Molecular Plant*, vol. 3, pp. 642–652, 2010.

[187] P. Thuleau, C. Brière, and C. Mazars, "Recent advances in plant cell nuclear signaling," *Molecular Plant*, vol. 5, pp. 968–970, 2012.

[188] M. Watahiki, A. Trewavas, and R. Parton, "Fluctuations in the pollen tube tip-focused calcium gradient are not reflected in nuclear calcium level: a comparative analysis using recombinant yellow cameleon calcium reporter," *Sexual Plant Reproduction*, vol. 17, pp. 125–130, 2004.

[189] S. Means, A. J. Smith, J. Shepherd, J. Shadid, J. Fowler, R. J. H. Wojcikiewicz, T. Mazel, G. D. Smith, and B. S. Wilson, "Reaction diffusion modeling of calcium dynamics with realistic ER geometry," *Biophysical journal*, vol. 91, pp. 537–57, 2006.

[190] C. H. T. Kong, D. R. Laver, and M. B. Cannell, "Extraction of Sub-microscopic Ca^{2+} Fluxes from Blurred and Noisy Fluorescent Indicator Images with a Detailed Model Fitting Approach," *PLoS Computational Biology*, vol. 9, p. e1002931, 2013.

[191] S. R. Wente and M. P. Rout, "The nuclear pore complex and nuclear transport.," *Cold Spring Harbor perspectives in biology*, vol. 2, pp. 1–19, 2010.

[192] A. Christmann, E. Grill, and J. Huang, "Hydraulic signals in long-distance signaling," *Current Opinion in Plant Biology*, vol. 16, pp. 293–300, 2013.

[193] S. A. R. Mousavi, A. Chauvin, F. Pascaud, S. Kellenberger, and E. E. Farmer, "GLUTAMATE RECEPTOR-LIKE genes mediate leaf-to-leaf wound signalling," *Nature*, vol. 500, pp. 422–426, 2013.

[194] M. R. Zimmermann, H. Maischak, A. Mithöfer, W. Boland, and H. H. Felle, "System potentials, a novel electrical long-distance signal in plants, induced by wounding," *Plant physiology*, vol. 149, pp. 1593–1600, 2009.

[195] V. Salvador-Recatalà, W. F. Tjallingii, and E. E. Farmer, "Real-time, in vivo intracellular recordings of caterpillar-induced depolarization waves in sieve elements using aphid electrodes," *New Phytologist*, vol. 203, pp. 674–684, 2014.

[196] G. Miller, K. Schlauch, R. Tam, D. Cortes, M. A. Torres, V. Shulaev, J. L. Dangl, and R. Mittler, "The plant NADPH oxidase RBOHD mediates rapid systemic signaling in response to diverse stimuli," *Science signaling*, vol. 2, p. ra45, 2009.

[197] T. C. Xiong, E. Ronzier, F. Sanchez, C. Corratgé-Faillie, C. Mazars, and J.-B. Thibaud, "Imaging long distance propagating calcium signals in intact plant leaves with the BRET-based GFP-aequorin reporter," *Frontiers in plant science*, vol. 5, p. 43, 2014.

[198] U. Dubiella, H. Seybold, G. Durian, E. Komander, R. Lassig, C.-P. Witte, W. X. Schulze, and T. Romeis, "Calcium-dependent protein kinase/NADPH oxidase activation circuit is required for rapid defense signal propagation," *Proceedings of the National Academy of Sciences of the United States of America*, vol. 110, pp. 8744–8749, 2013.

[199] T. Romeis and M. Herde, "From local to global: CDPKs in systemic defense signaling upon microbial and herbivore attack," *Current Opinion in Plant Biology*, vol. 20, pp. 1–10, 2014.

[200] J. Shah, R. Chaturvedi, Z. Chowdhury, B. Venables, and R. A. Petros, "Signaling by small metabolites in systemic acquired resistance," *Plant Journal*, vol. 79, pp. 645–658, 2014.

[201] C. Wang, M. El-Shetehy, M. B. Shine, K. Yu, D. Navarre, D. Wendehenne, A. Kachroo, and P. Kachroo, "Free Radicals Mediate Systemic Acquired Resistance," *Cell Reports*, vol. 7, pp. 348–355, 2014.

[202] D. Wendehenne, Q. ming Gao, A. Kachroo, and P. Kachroo, "Free radical-mediated systemic immunity in plants," *Current Opinion in Plant Biology*, vol. 20, pp. 127–134, 2014.

[203] V. Vodeneev, A. Orlova, E. Morozova, L. Orlova, E. Akinchits, O. Orlova, and V. Sukhov, "The mechanism of propagation of variation potentials in wheat leaves," *Journal of plant physiology*, vol. 169, pp. 949–54, 2012.

[204] S. Gilroy, N. Suzuki, G. Miller, W. G. Choi, M. Toyota, A. R. Devireddy, and R. Mittler, "A tidal wave of signals: calcium and ROS at the forefront of rapid systemic signaling," *Trends in Plant Science*, vol. 19, pp. 623–630, 2014.

[205] L. Steinhorst and J. Kudla, "Calcium and ROS rule the waves of signaling," *Plant physiology*, vol. 163, pp. 471–485, 2013.

[206] L. Steinhorst and J. Kudla, "Signaling in cells and organisms - calcium holds the line," *Current Opinion in Plant Biology*, vol. 22, pp. 14–21, 2014.

[207] A. Christmann, E. W. Weiler, E. Steudle, and E. Grill, "A hydraulic signal in root-to-shoot signalling of water shortage," *Plant Journal*, vol. 52, pp. 167–174, 2007.

[208] P. Oyarce and L. Gurovich, "Evidence for the transmission of information through electric potentials in injured avocado trees," *Journal of Plant Physiology*, vol. 168, pp. 103–108, 2011.

[209] I. Bricchi, A. Occhipinti, C. M. Bertea, S. A. Zebelo, C. Brillada, F. Verrillo, C. De Castro, A. Molinaro, C. Faulkner, A. J. Maule, and M. E. Maffei, "Separation of early and late responses to herbivory in Arabidopsis by changing plasmodesmal function," *Plant Journal*, vol. 73, pp. 14–25, 2013.

[210] R. Stahlberg, R. Cleland, and E. Volkenburgh, *Communication in Plants*, ch. Slow Wave Potentials - a Propagating Electrical Signal Unique to Higher Plants, pp. 291–308. Springer, 2006.

[211] A. L. Hodgkin and A. F. Huxley, "A quantitative description of membrane current and its application to conduction and excitation in nerve," *Journal of Physiology*, vol. 117, pp. 500–544, 1952.

[212] U. Ricca, "Soluzione d'un problema di fisiologia: la propagazione di stimulo nella mimosa," *Nuovo G Bot Ital*, vol. 23, pp. 51–170, 1916.

[213] A. M. Mastro, M. A. Babich, W. D. Taylor, and A. D. Keith, "Diffusion of a small molecule in the cytoplasm of mammalian cells," *Proceedings of the National Academy of Sciences*, vol. 81, pp. 3414–3418, 1984.

[214] J. B. Passioura, "Water transport in and to roots," *Annual Review of Plant Physiology and Plant Molecular Biology*, vol. 39, pp. 245–265, 1988.

[215] M. Ibañes, N. Fàbregas, J. Chory, and A. Caño-Delgado, "Brassinosteroid signaling and auxin transport are required to establish the periodic pattern of Arabidopsis shoot vascular bundles," *Proc. Nat. Acad. Sci. USA.*, vol. 106, pp. 13630–5, 2009.

[216] H. Tian, I. R. Baxter, B. Lahner, A. Reinders, D. E. Salt, and J. M. Ward, "Arabidopsis NPCC6/NaKR1 is a phloem mobile metal binding protein necessary for phloem function and root meristem maintenance.," *The Plant cell*, vol. 22, pp. 3963–79, 2010.

[217] M. E. Westgate, E. Steudle, A. Membranforschung, and K. Jiulich, "Water Transport in the Midrib Tissue of Maize Leaves," *Plant Physiology*, vol. 78, pp. 183–191, 1985.

[218] J. Rhodes, J. Thain, and D. Wildon, "Evidence for Physically Distinct Systemic Signalling Pathways in the Wounded Tomato Plant," *Annals of Botany*, vol. 84, pp. 109–116, 1999.

[219] R. Hedrich and E. Neher, "Cytoplasmic calcium regulates voltage-dependent ion channels in plant vacuoles," *Nature*, vol. 329, pp. 833–836, 1987.

[220] I. Pottosin, T. Wherrett, and S. Shabala, "SV channels dominate the vacuolar Ca^{2+} release during intracellular signaling," *FEBS Letters*, vol. 583, pp. 921–926, 2009.

[221] K. E. Cosker and R. A. Segal, "Neuronal Signaling through Endocytosis," *Cold Spring Harbor perspectives in biology*, vol. 6, p. a020669, 2014.

[222] C. Garcia-Mata, J. Wang, P. Gajdanowicz, W. Gonzalez, A. Hills, N. Donald, J. Riedelsberger, A. Amtmann, I. Dreyer, and M. R. Blatt, "A Minimal Cysteine Motif Required to Activate the SKOR K_+ Channel of Arabidopsis by the Reactive Oxygen Species H_2O_2," *The Journal of Biological Chemistry*, vol. 285, pp. 29286–29294, 2010.

[223] R. Hedrich and I. Marten, "TPC1-SV channels gain shape," *Molecular plant*, vol. 4, pp. 428–41, 2011.

[224] J. Guo, W. Zeng, Q. Chen, C. Lee, L. Chen, Y. Yang, C. Cang, D. Ren, and Y. Jiang, "Structure of the voltage-gated two-pore channel TPC1 from Arabidopsis thaliana," *Nature*, vol. 531, pp. 196–201, 2016.

[225] A. F. Kintzer and R. M. Stroud, "Structure, inhibition and regulation of two-pore channel TPC1 from Arabidopsis thaliana," *Nature*, vol. 531, pp. 258–264, 2016.

[226] I. Pottosin, L. Tikhonova, R. Hedrich, and G. Schönknecht, "Slowly activating vacuolar channels cannot mediate Ca^{2+}-induced Ca^{2+} release," *The Plant journal*, vol. 12, pp. 1387–1398, 1997.

[227] I. I. Pottosin and G. Schönknecht, "Vacuolar calcium channels," *Journal of experimental botany*, vol. 58, pp. 1559–69, 2007.

[228] K. Kikushima, S. Kita, and H. Higuchi, "A non-invasive imaging for the in vivo tracking of high-speed vesicle transport in mouse neutrophils," *Scientific reports*, vol. 3, p. 1913, 2013.

[229] T. Taba, M. Edamatsu, S. Toba, K. Shibata, Y. Imafuku, Y. Toyoshima, K. Tawada, and A. Yamada, "Direction and speed of microtubule movements driven by kinesin motors arranged on catchin thick filaments," *Cell Motil Cytoskeleton*, vol. 10, pp. 816–26, 2008.

[230] J. Bove, B. Vaillancourt, J. Kroeger, P. K. Hepler, P. W. Wiseman, and A. Geitmann, "Magnitude and direction of vesicle dynamics in growing pollen tubes using spatiotemporal image correlation spectroscopy and fluorescence recovery after photobleaching," *Plant physiology*, vol. 147, pp. 1646–1658, 2008.

[231] X. Wang, Y. Teng, Q. Wang, X. Li, X. Sheng, M. Zheng, J. Samaj, F. Baluska, and J. Lin, "Imaging of Dynamic Secretory Vesicles in Living Pollen Tubes of Picea meyeri Using Evanescent," *Plant Physiology*, vol. 141, pp. 1591–1603, 2006.

[232] S. Romagnoli, G. Cai, C. Faleri, E. Yokota, T. Shimmen, and M. Cresti, "Microtubule- and actin filament-dependent motors are distributed on pollen tube mitochondria and contribute differently to their movement," *Plant Cell Physiology*, vol. 48, pp. 345–61, 2007.

[233] S. Stael, B. Wurzinger, A. Mair, N. Mehlmer, U. C. Vothknecht, and M. Teige, "Plant organellar calcium signalling: An emerging field," *Journal of Experimental Botany*, vol. 63, pp. 1525–1542, 2012.

[234] J. Keener and J. Sneyd, *Mathematical Physiology*. Springer, 2 ed., 1998.

[235] M. Sagi and R. Fluhr, "Production of reactive oxygen species by plant NADPH oxidases," *Plant physiology*, vol. 141, pp. 336–340, 2006.

[236] M. A. Torres, J. L. Dangl, and J. D. G. Jones, "Arabidopsis gp91 phox homologues AtrbohD and AtrbohF are required for accumulation of reactive oxygen intermediates in the plant defense response," *Proceedings of the National Academy of Sciences of the United States of America*, vol. 99, pp. 517–522, 2002.

[237] M. Pogány, U. von Rad, S. Grün, A. Dongó, A. Pintye, P. Simoneau, G. Bahnweg, L. Kiss, B. Barna, and J. Durner, "Dual roles of reactive oxygen species and NADPH oxidase RBOHD in an Arabidopsis-Alternaria pathosystem.," *Plant physiology*, vol. 151, pp. 1459–75, 2009.

[238] Y. Zhang, H. Zhu, Q. Zhang, M. Li, M. Yan, R. Wang, L. Wang, R. Welti, W. Zhang, and X. Wang, "Phospholipase dalpha1 and phosphatidic acid regulate NADPH oxidase activity and production of reactive oxygen species in ABA-mediated stomatal closure in Arabidopsis," *The Plant cell*, vol. 21, pp. 2357–77, 2009.

[239] S. L. Richards, A. Laohavisit, J. C. Mortimer, L. Shabala, S. M. Swarbreck, S. Shabala, and J. M. Davies, "Annexin 1 regulates the H_2O_2- induced calcium signature in Arabidopsis thaliana roots," *The Plant Journal*, vol. 77, pp. 136–45, 2014.

[240] H. Hao, L. Fan, T. Chen, R. Li, X. Li, Q. He, M. A. Botella, and J. Lin, "Clathrin and Membrane Microdomains Cooperatively Regulate RbohD Dynamics and Activity in Arabidopsis," *The Plant cell*, vol. 26, pp. 1729–1745, 2014.

[241] A. E. S. Macklon, D. G. Lumsdon, A. Sim, and W. J. McHardy, "Phosphate fluxes, compartmentation and vacuolar speciation in root cortex cells of intact Agrostis capillaris seedlings: effect of non-toxic levels of aluminium," *Journal of experimental botany*, vol. 47, pp. 793–803, 1996.

[242] P. Rezvani Moghaddam and D. Wilman, "Cell wall thickness and cell dimensions in plant parts of eight forage species," *The Journal of Agricultural Science*, vol. 131, pp. 59–67, 1998.

[243] T. Werner, V. Motyka, V. Laucou, R. Smets, H. V. Onckelen, and T. Schmuelling, "Cytokinin-Deficient Transgenic Arabidopsis Plants Show Functions of Cytokinins in the Regulation of Shoot and Root Meristem Activity," *The Plant cell*, vol. 15, pp. 2532–2550, 2003.

[244] W.-J. Guo, R. Nagy, H.-Y. Chen, S. Pfrunder, Y.-C. Yu, D. Santelia, W. B. Frommer, and E. Martinoia, "SWEET17, a Facilitative Transporter, Mediates Fructose Transport across the Tonoplast of Arabidopsis," *Plant Physiology*, vol. 164, pp. 777–789, 2014.

[245] S. Gattolin, M. Sorieul, and L. Frigerio, "Mapping of tonoplast intrinsic proteins in maturing and germinating Arabidopsis seeds reveals dual localization of embryonic TIPs to the tonoplast and plasma membrane," *Molecular Plant*, vol. 4, pp. 180–189, 2011.

[246] P. R. Hunter, C. P. Craddock, S. Di Benedetto, L. M. Roberts, and L. Frigerio, "Fluorescent reporter proteins for the tonoplast and the vacuolar lumen identify a single vacuolar compartment in Arabidopsis cells," *Plant physiology*, vol. 145, pp. 1371–1382, 2007.

[247] C. A. Schneider, W. S. Rasband, and K. W. Eliceiri, "NIH Image to ImageJ: 25 years of image analysis," *Nat Meth*, vol. 9, pp. 671–675, 2012.

[248] B. Kachar, "Direct visualization of organelle movement along actin filaments dissociated from characean algae," *Science*, vol. 227, pp. 1355–7, 1985.

[249] R. E. Goldstein, I. Tuval, and J.-W. van de Meent, "Microfluidics of cytoplasmic streaming and its implications for intracellular transport," *Proc. Nat. Acad. Sci. USA.*, vol. 105, pp. 3663–3667, 2008.

[250] G. B. Monshausen, T. N. Bibikova, M. A. Messerli, C. Shi, and S. Gilroy, "Oscillations in extracellular pH and reactive oxygen species modulate tip growth of Arabidopsis root hairs," *Proc. Nat. Acad. Sci. U.S.A.*, vol. 104, pp. 20996–21001, 2007.

[251] G. B. Monshausen, T. N. Bibikova, M. H. Weisenseel, and S. Gilroy, "Ca^{2+} regulates reactive oxygen species production and pH during mechanosensing in Arabidopsis roots," *Plant Cell*, vol. 21, pp. 2341–2356, 2009.

[252] N. M. Ordoñez, C. Marondedze, L. Thomas, S. Pasqualini, L. Shabala, S. Shabala, and C. Gehring, "Cyclic mononucleotides modulate potassium and calcium flux responses to H_2O_2 in Arabidopsis roots," *FEBS Letters*, vol. 588, pp. 1008–1015, 2014.

[253] J. Foreman, V. Demidchik, J. Bothwell, P. Mylona, H. Miedema, M. Torres, P. Linstead, S. Costa, C. Brownlee, J. Jones, J. Davies, and L. Dolan, "Reactive oxygen species produced by NADPH oxidase regulate plant cell growth," *Nature*, vol. 422, pp. 442–6, 2003.

[254] V. Demidchik, S. N. Shabala, and J. M. Davies, "Spatial variation in H_2O_2 response of Arabidopsis thaliana root epidermal Ca^{2+} flux and plasma membrane Ca^{2+} channels," *Plant Journal*, vol. 49, pp. 377–386, 2007.

[255] D. Beyhl, S. Hörtensteiner, E. Martinoia, E. E. Farmer, J. Fromm, I. Marten, and R. Hedrich, "The fou2 mutation in the major vacuolar cation channel TPC1 confers tolerance to inhibitory luminal calcium.," *The Plant Journal*, vol. 58, pp. 715–23, 2009.

[256] C. Faulkner, "Receptor-mediated signaling at plasmodesmata," *Frontiers in Plant Science*, vol. 4, p. 521, 2013.

[257] Y. Kadota, J. Sklenar, P. Derbyshire, L. Stransfeld, S. Asai, V. Ntoukakis, J. D. Jones, K. Shirasu, F. Menke, A. Jones, and C. Zipfel, "Direct Regulation of the NADPH Oxidase RBOHD by the PRR-Associated Kinase BIK1 during Plant Immunity," *Molecular Cell*, vol. 54, pp. 43–55, 2014.

[258] M. Boudsocq and J. Sheen, "CDPKs in immune and stress signaling," *Trends in plant science*, vol. 18, pp. 30–40, 2013.

[259] S. Gilroy, M. Białasek, N. Suzuki, M. Górecka, R. Devireddy Amith, S. Karpiński, and R. Mittler, "ROS, Calcium and Electric Signals: Key Mediators of Rapid Systemic Signaling in Plants," *Plant Physiology*, p. ra45, 2016.

[260] R. Hedrich, V. Salvador-Recatalà, and I. Dreyer, "Electrical Wiring and Long-Distance Plant Communication," *Trends in Plant Science*, vol. 21, pp. 376–387, 2016.

[261] L. Mignolet-Spruyt, E. Xu, N. Idänheimo, F. Hoeberichts, P. Mühlenbock, M. Brosché, F. Breusegem, and J. Kangasjärvi, "Spreading the news: subcellular and organellar reactive oxygen species production and signalling," *J. Exp. Bot.*, vol. 67, pp. 3855–3872, 2016.

[262] S. Shabala, J. Pang, M. Zhou, L. Shabala, T. A. Cuin, P. Nick, and L. H. Wegner, "Electrical signalling and cytokinins mediate effects of light and root cutting on ion uptake in intact plants," *Plant, Cell and Environment*, vol. 32, pp. 194–207, 2009.

[263] R. R. Lew, "Pressure Regulation of the Electrical Properties of Growing Arabidopsis thaljana L . Root Hairs," *Plant physiology*, vol. 112, pp. 1089–1100, 1996.

[264] T. Sibaoka, "Application of leaf extract causes repetitive action potentials in *Biophytum sensitivum*," *J Plant Res*, vol. 110, pp. 485–487, 1997.

[265] S. Ferrari, D. V. Savatin, F. Sicilia, G. Gramegna, F. Cervone, and G. D. Lorenzo, "Oligogalacturonides: plant damage-associated molecular patterns and regulators of growth and development," *Frontiers in plant science*, vol. 4, p. 49, 2013.

[266] A. G. Volkov, J. C. Foster, K. D. Baker, and V. S. Markin, "Mechanical and electrical anisotropy in Mimosa pudica pulvini," *Plant signaling & behavior*, vol. 5, pp. 1211–1221, 2010.

[267] Z. Zhang, W. Xin, S. Wang, X. Zhang, H. Dai, R. Sun, T. Frazier, B. Zhang, and Q. Wang, "Xylem sap in cotton contains proteins that contribute to environmental stress response and cell wall development," *Function & Integrative Genomics*, vol. 15, pp. 17–26, 2015.

[268] V. Hlaváčková, P. Krchňák, J. Nauš, O. Novák, M. Špundová, and M. Strnad, "Electrical and chemical signals involved in short-term systemic photosynthetic responses of tobacco plants to local burning," *Planta*, vol. 225, pp. 235–244, 2006.

[269] R. Stahlberg and D. J. Cosgrove, "Planta and electrical potentials upon stem excision in pea seedlings," *Planta*, vol. 187, pp. 523–531, 1992.

[270] L. V. Bindschedler, J. Dewdney, K. a. Blee, J. M. Stone, J. Plotnikov, C. Denoux, T. Hayes, C. Gerrish, D. R. Davies, F. M. Ausubel, and G. P. Bolwell, "Peroxidase-dependent apoplastic oxidative burst in Arabidopsis required for pathogen resistance," *Plant J*, vol. 47, pp. 851–863, 2006.

[271] A. Carpaneto, A. M. Cantù, and F. Gambale, "Redox agents regulate ion channel activity in vacuoles from higher plant cells," *FEBS Letters*, vol. 442, pp. 129–132, 1999.

[272] J. Scholz-Starke, A. De Angeli, C. Ferraretto, S. Paluzzi, F. Gambale, and A. Carpaneto, "Redox-dependent modulation of the carrot SV channel by cytosolic pH," *FEBS Letters*, vol. 576, pp. 449–54, 2004.

[273] G. P. Bienert, J. K. Schjoerring, and T. P. Jahn, "Membrane transport of hydrogen peroxide," *Biochimica et biophysica acta*, vol. 1758, pp. 994–1003, 2006.

[274] C. L. Vestergaard, H. Flyvbjerg, and I. M. Møller, "Intracellular signaling by diffusion: can waves of hydrogen peroxide transmit intracellular information in plant cells?," *Front Plant Sci*, vol. 3, p. 295, 2012.

[275] E. Peiter, "The plant vacuole: Emitter and receiver of calcium signals," *Cell Calcium*, vol. 50, pp. 120–128, 2011.

[276] K. Birnbaum, D. Shasha, J. Wang, J. Jung, G. Lambert, D. Galbraith, and P. Benfey, "A gene expression map of the arabidopsis root," *Science*, vol. 302, pp. 1956–60, 2003.

[277] M. Alvarez, R. Pennell, P. Meijer, A. Ishikawa, R. Dixon, and C. Lamb, "Reactive oxygen intermediates mediate a systemic signal network in the establishment of plant immunity," *Cell*, vol. 92, pp. 773–84, 1998.

[278] S. Karpinski, H. Reynolds, B. Karpinska, G. Wingsle, G. Creissen, and P. Mullineaux, "Systemic signaling and acclimation in response to excess excitation energy in arabidopsis," *Science*, vol. 284, pp. 654–57, 1999.

[279] N. Suzuki, G. Miller, C. Salazar, H. A. Mondal, E. Shulaev, D. F. Cortes, J. L. Shuman, X. Luo, J. Shah, K. Schlauch, V. Shulaev, and R. Mittler, "Temporal-spatial interaction between reactive oxygen species and abscisic acid regulates rapid systemic acclimation in plants," *The Plant cell*, vol. 25, pp. 3553–69, 2013.

[280] J. M. Ward and J. I. Schroeder, "Calcium-activated K^+ channels and calcium-induced calcium-release by slow vacuolar ion channels in guard-cell vacuoles implicated in the control of stomatal closure," *Plant Cell*, vol. 6, pp. 669–683, 1994.

[281] G. Allen and D. Sanders, "Control of ionic currents in guard cell vacuoles by cytosolic and luminal calcium," *The Plant Journal*, vol. 10, pp. 1055–1069, 1996.

[282] N. Larisch, S. A. Kirsch, A. Schambony, T. Studtrucker, R. A. Böckmann, and P. Dietrich, "The function of the two-pore channel TPC1 depends on dimerization of its carboxy-terminal helix," *Cellular and Molecular Life Sciences*, pp. 1–17, 2016.

[283] B. P. Olveczky and A. S. Verkman, "Monte Carlo analysis of obstructed diffusion in three dimensions: application to molecular diffusion in organelles," *Biophys J*, vol. 74, pp. 2722–2730, 1998.

[284] K. Bentele and M. Falcke, "Quasi-steady approximation for ion channel currents," *Biophysical journal*, vol. 93, pp. 2597–608, 2007.

[285] D. A. Goodenough and D. L. Paul, "Gap junctions," *Cold Spring Harbor perspectives in biology*, vol. 1, pp. 1–19, 2009.

[286] Höfer, Thomas and Politi, Antonio and Heinrich, Reinhart, "Intercellular Ca^{2+} Wave Propagation through Gap-Junctional Ca^{2+} Diffusion: A Theoretical Study," *Biophysical journal*, vol. 80, pp. 75–87, 2001.

[287] K. Tsaneva-Atanasova, D. I. Yule, and J. Sneyd, "Calcium oscillations in a triplet of pancreatic acinar cells," *Biophysical journal*, vol. 88, pp. 1535–1551, 2005.

[288] J. Harris and Y. Timofeeva, "Intercellular calcium waves in the fire-diffuse-fire framework: Green's function for gap-junctional coupling," *Physical Review E*, vol. 82, p. 051910, 2010.

[289] S. M. Swarbreck, R. Colaco, and J. M. Davies, "Plant Calcium-Permeable Channels," *Plant Physiology*, vol. 163, pp. 514–522, 2013.

[290] W. Urquhart, K. Chin, H. Ung, W. Moeder, and K. Yoshioka, "The cyclic nucleotide-gated channels AtCNGC11 and 12 are involved in multiple Ca^{2+}-dependent physiological responses and act in a synergistic manner," *Journal of Experimental Botany*, vol. 62, pp. 3671–3682, 2011.

[291] Y. Ma, R. K. Walker, Y. C. Zhao, and G. A. Berkowitz, "Linking ligand perception by PEPR pattern recognition receptors to cytosolic Ca^{2+} elevation and downstream immune signaling in plants," *Proc Natl Acad Sci USA*, vol. 109, pp. 19852–19857, 2012.

[292] M. Lu, Y. Zhang, S. Tang, J. Pan, Y. Yu, J. Han, Y. Li, X. Du, Z. Nan, and Q. Sun, "AtCNGC2 is involved in jasmonic acid-induced calcium mobilization," *Journal of Experimental Botany*, vol. 67, pp. 809–819, 2016.

[293] P. Dietrich, U. Anschütz, A. Kugler, and D. Becker, "Physiology and biophysics of plant ligand-gated ion channels," *Plant Biology*, vol. 12, pp. 80–93, 2010.

[294] F. Jammes, H. C. Hu, F. Villiers, R. Bouten, and J. M. Kwak, "Calcium-permeable channels in plant cells," *FEBS Journal*, vol. 278, pp. 4262–4276, 2011.

[295] C. Mazars, P. Thuleau, O. Lamotte, and S. Bourque, "Cross-talk between ROS and calcium in regulation of nuclear activities," *Molecular Plant*, vol. 3, pp. 706–718, 2010.

[296] M. Wrzaczek, M. Brosché, and J. Kangasjärvi, "ROS signaling loops - production, perception, regulation," *Current opinion in plant biology*, vol. 16, pp. 575–82, 2013.

[297] N. Sewelam, K. Kazan, and P. M. Schenk, "Global Plant Stress Signaling: Reactive Oxygen Species at the Cross-Road," *Frontiers in plant science*, vol. 7, p. 187, 2016.

[298] V. Demidchik, "Mechanisms of oxidative stress in plants: From classical chemistry to cell biology," *Environmental and Experimental Botany*, vol. 109, pp. 212–228, 2015.

[299] A. Laohavisit, Z. Shang, L. Rubio, T. A. Cuin, A.-A. Véry, A. Wang, J. C. Mortimer, N. Macpherson, K. M. Coxon, N. H. Battey, C. Brownlee, O. K. Park, H. Sentenac, S. Shabala, A. A. Webb, and J. M. Davies, "*Arabidopsis* Annexin1 Mediates the Radical-Activated Plasma Membrane Ca^{2+}- and K^{+}-Permeable Conductance in Root Cells," *The Plant Cell*, vol. 24, pp. 1522–1533, 2012.